UNIVERSIDAD COMPLUTENSE DE MADRID

FACULTAD DE CIENCIAS FÍSICAS
Departamento de Física Aplicada III
(Electricidad y Electrónica

TESIS DOCTORAL

Medidas espectrales y de conectividad funcional con magnetoencefalografía: fiabilidad y aplicaciones a deterioro cognitivo leve

Magnetoencephalography spectral and functional connectivity measures : reliability and applications in mild cognitive impairment

MEMORIA PARA OPTAR AL GRADO DE DOCTOR

PRESENTADA POR

Pilar Garcés López

Directores

Miguel Sancho Ruiz
Francisco del Pozo Guerrero

Madrid, 2015

UNIVERSIDAD COMPLUTENSE DE MADRID

FACULTAD DE CIENCIAS FÍSICAS

DEPARTAMENTO DE FÍSICA APLICADA III

MEDIDAS ESPECTRALES Y DE CONECTIVIDAD FUNCIONAL CON MAGNETOENCEFALOGRAFÍA. FIABILIDAD Y APLICACIONES A DETERIORO COGNITIVO LEVE.

MAGNETOENCEPHALOGRAPHY SPECTRAL AND FUNCTIONAL CONNECTIVITY MEASURES. RELIABILITY AND APPLICATIONS IN MILD COGNITIVE IMPAIRMENT.

Memoria para optar al grado de doctor presentada por:
Pilar Garcés López

Directores: Miguel Sancho Ruiz
Francisco del Pozo Guerrero

Madrid 2015

Acknowledgments

Thanks to everyone who has contributed to this work. This work results from the collaborative effort of several groups in Madrid and abroad (Frankfurt), involved either in project design, subject evaluation, data acquisition (MEG, MRI, neuropsychology), data analysis or selection and interpretation of results. Thanks to everybody, for sure to all the authors in the papers but also to everyone who has participated or given advice in any way. Thanks to all the study participants who volunteered to contribute to our work and gave their time away to help us.

Gracias a todos los que se han leido y comentado cualquier parte de esta tesis.

Gracias a mis directores. A Miguel y Paco, por darme la oportunidad de hacer esta tesis, y guiarme a lo largo de estos años. Y a Fernando, que también ha dirigido y supervisado todos los estudios que se incluyen aquí.

Gracias al departamento de Física Aplicada III. A Genoveva, por acogerme con tanta amabilidad desde el primer momento, y seguirme cuidando tanto incluso después de acabar el máster. También a los demás del laboratorio de biofísica, Sagrario, Antonio, Azahara, Naza, Pablo, Low, por crear un ambiente tan cálido y tranquilo.

Gracias a todos los miembros del laboratorio de neurociencia cognitiva y computacional. Hemos compartido muchísimas horas, y la mayoría de ellas han sido buenas! Gracias a Bruña, por ser una constante desde el principio del todo, por estar sentado en frente de mí todos los días (a partir de las 12:30), enseñarme tantas cosas, dejarme mirar cómo arregla las cosas, hacerme compañía y aguantar todos los chaparrones que han llegado. A Mari Carmen por dejarme colarme en su proyecto a mitad, aceptar la responsabilidad de mi deadline como si fuera suyo, y su alegría contagiosa cada vez que hay buenos resultados. A Jose por sus ganas de hacer más y más estudios y papers, por tener las puertas abiertas de su despacho y dar muy buen feedback a todas las dudas. A David por las meriendas, y darme apoyo y cariño diariamente. A Gema por ser una crack sin igual y alegrar todos los ambientes. A Gerardo, por todas las conversaciones de camino a casa. Y para no extenderme más,

gracias a TODOS los demás! Hay muchos nombres y muchas historias. Seguro que os voy a echar de menos.

Gracias a mi familia y amigos. Por acompañarme y aguantarme.

Resumen

En los últimas décadas se ha avanzado mucho en la neuroimagen cerebral. Han surgido varias técnicas que miden distintos aspectos de la función cerebral, como el matabolismo, las respuestas hemodinámicas o las corrientes neuronales. Entre ellas, la magnetoencefalografía (MEG) destaca por su alta resolución temporal, que permite inspeccionar la dinámica de la actividad cerebral. En esta tesis estudiamos la utilidad de medidas de potencia y conectividad funcional (FC, *functional connectivity*) de MEG en estado basal en el estudio de deterioro cognitivo leve (DCL) y evaluamos su fiabilidad.

Alzheimer y deterioro cognitivo leve

Alrededor de al 20% de la población mayor de 70 años presenta DCL: su estado cognitivo es peor del que se considera normal para su edad, aunque el deterioro no es tan severo como para ser considerado demencia. Hay varios tipos de DCL, según el (o los) dominio (s) cognitivo (s) afectados. El DCL amnésico es el tipo más frecuente, y también es el tipo de interés en esta tesis, ya que presenta altas tasas de conversión (hasta 45% en 30 meses) a enfermedad de Alzheimer (EA). A su vez, la EA es una enfermedad neurodegenerativa que suele manifestarse primero como un déficit en la memoria a corto plazo, aunque también se caracteriza por deterioro en funciones visio-espaciales, lenguaje, o cambios de humor o personalidad. La EA es hoy en día especialmente relevante, ya que afecta a un 5-7% de la población mayor de 60 años en la actualidad, y se calcula que de aquí a 2050 su tasa de incidencia podría incluso duplicarse. Sin embargo, no hay tratamientos efectivos contra la EA, y ni siquiera están claras sus causas. Por lo tanto, es importante investigar qué cambios ocurren en DCL/EA, ya que esto ayudaría a conocer los procesos que subyacen a la EA. En esta tesis se pretende evaluar la utilidad de la MEG para detectar alteraciones en la actividad electrofisiológica en DCL. Aunque la MEG no es la modalidad de neuroimagen más comúnmente usada en el estudio de DCL/EA, puede ser de mucha utilidad ya que, al contrario que otras técnicas de neuroimagen, es una medida directa de la

actividad neuronal, con una resolución espacial adecuada (entorno a 1cm) y una muy buena resolución temporal (entorno a 1ms), además de ser totalmente no invasiva. Así pues, en esta tesis se evaluaron primero diferencias en el espectro de potencia y en FC en registros MEG en estado de reposo entre sujetos con DCL y controles sanos de la misma edad. Después, se cuantificó la fiabilidad test-retest de la potencia y FC en estado de reposo, para evaluar la potencialidad de estas medidas en la caracterización de sujetos individuales.

MEG

La MEG mide flujos magnéticos en varios sensores repartidos en un casco, sobre el que se apoya la cabeza del sujeto. Estos flujos magnéticos son generados por las pequeñas corrientes neuronales, y son por tanto muy débiles, de forma que la MEG requiere sensores muy precisos, una habitación aislada que apantalle el ruido magnético ambiental, y un preprocesado cuidadoso que elimine ruido ambiental y biológico. Se considera que la MEG es sólo sensible a las corrientes post-sinápticas generadas por la actividad síncrona de cientos de miles de neuronales piramidales, que forman pequeños dipolos de corriente. Estas corrientes (y en consecuencia los campos magnéticos) varían rápidamente con el tiempo, y contienen actividad oscilatoria a distintos ritmos: delta (2-4 Hz), zeta (4-8 Hz), alfa (8-13 Hz), beta (12-30 Hz), y gama (30-45 Hz). Todos estos ritmos están involucrados en una gran variedad de funciones cognitivas y sensoriales. Para extraer esta actividad oscilatoria de los datos MEG, se realizó un procesado de datos, que se describe a continuación. Primero, se eliminó gran parte del ruido (campo magnético no procedente de corrientes neuronales) mediante un filtrado espaciotemporal que separa componentes internas y externas a la cabeza del sujeto (tSSS o *spatiotemporal signal space separation*) y una detección de artefactos oculares, musculares y de salto. Segundo, se procedió a la reconstrucción de fuentes de los datos MEG limpios. Así pues, la MEG mide flujos magnéticos en la superficie de un casco exterior a la cabeza, y es necesaria la resolución de un problema inverso para estimar qué corrientes neuronales generaron esa actividad en sensores. A su vez, el problema inverso requiere resolver un problema directo, que calcula el campo magnético producido en sensores por determinadas corrientes neuronales. El problema directo tiene solución única determinada por las ecuaciones de Maxwell, una vez conocidas las conductividades de los tejidos atravesados. Esto se estimó aplicando un modelo directo a la geometría de las superficies del cerebro, cráneo y cuero cabelludo extraídas de imágenes de resonancia magnética (RM) ponderadas en T1. Una vez resuelto el problema directo, el problema inverso no es inmediato, ya que tiene infinitas soluciones. Es por lo tanto necesario aplicar una hipótesis o elegir un

modelo inverso para restringir este espacio infinito de soluciones. En esta tesis, esto se realizó mediante *beamforming*, El tercer paso consistió en, a partir de la actividad de las corrientes neuronales en espacio de fuentes reconstruidas con *beamforming*, estimar potencia y FC. La potencia se calculó directamente a partir del espectro de potencia de las series temporales en fuentes. La FC, que mide dependencias estadísticas entre las actividades de distintas regiones, se calculó con medidas de sincronización de amplitud y de fase en las series temporales en fuentes para cada uno de los ritmos cerebrales.

Alteraciones en el espectro y la red por defecto en DCL

Para estudiar las alteraciones en el espectro y FC en DCL, se realizaron registros en estado de reposo a sujetos con DCL y controles. Estos datos MEG se usaron después en dos estudios distintos.

- El primer estudio se centra en el pico alfa, que es un marcador comúnmente utilizado en espectros electrofisiológicos. Se ha descrito que el espectro de potencia EEG/MEG está enlentecido en EA, ya que pacientes con EA suelen mostrar más potencia que controles a bandas de frecuencia lentas y menos potencia a bandas de frecuencia altas. Aquí pretendíamos ver si este enlentecimiento está ya de manifiesto en DCL. Para ello, se procesaron los datos MEG siguiendo los pasos descritos anteriormente, y se calculó el espectro de potencia para cada región del atlas Harvard-Oxford. Después, se detectó el pico alfa (su frecuencia y su amplitud) ajustando por mínimos cuadrados el espectro de potencias a una gaussiana sobre una ley de potencia. Finalmente, se compararon la frecuencia y amplitud del pico alfa entre controles y DCL con un modelo ANOVA de 4 factores: diagnóstico, edad, sexo y nivel educativo. Se encontró que la frecuencia del pico alfa era significativamente menor en DCL que en controles en amplias zonas del cerebro, sobretodo en regiones posteriores. Sin embargo, la frecuencia y amplitud del pico alfa dependían también de otros factores como la edad y el sexo. Además, la frecuencia del pico alfa correlacionó positivamente con el volumen de hipocampo, que es un marcador de deterioro comúnmente utilizado en EA. Esto indica que los DCL presentan un enlentecimiento del pico alfa, y que este enlentecimiento es patológico.

- En el segundo estudio nos centramos en FC en la red por defecto (DMN, *default mode network*). Esta red fue descubierta por Raichle et al (2001), y está fuertemente activada en estado de reposo, mientras que se desactiva cuando el sujeto está inmerso en la realización de una tarea. También tiene relevancia

en EA, ya que, por un lado las regiones que la componen como precúneo y cingulado posterior son de las primeras en presentar acumulación de placas de beta-amiloide y bajo metabolismo, y por otro lado varios estudios con RM funcional han encontrado que está más desconectada en EA y en DCL que en controles. Ya que la DMN ha sido principalmente estudiada con RM funcional, que es una medida indirecta de las fluctuaciones hemodinámicas asociadas a la actividad cerebral, en este estudio pretendíamos evaluar las bases electrofisiológicas de las alteraciones de la DMN en DCL a distintas bandas de frecuencia (delta, zeta, alfa, beta, gama). Para ello, se aplicó el esquema de análisis descrito anteriormente, y se calculó la FC entre regiones de la DMN (precúneo, cingulados anterior y posterior y parietal inferior) con la técnica de correlación de envolventes. Además, se calcularon dos tipos de conectividad estructural (dSC y wSC) entre estas mismas regiones, que estimaban el número de tractos que conectan las regiones y la anisotropía fraccional media a lo largo de estos tractos, respectivamente. Los tractos se reconstruyeron con tractografía tipo *streamline* a partir de imágenes de RM ponderadas por difusión. Después, se aplicaron tests de Mann-Whitney para comparar los valores de FC, dSC y wSC entre controles y DCLs. Se encontró que tanto la wSC como la FC en la banda alfa estaban disminuidas en DCL frente a controles.

En ambos estudios encontramos que la MEG es sensible a alteraciones en el estado de reposo de sujetos con DCL: tanto enlentecimiento del pico alfa como disminución de FC en alfa en la DMN. Sin embargo, antes de poder usar estos resultados en un ámbito clínico, es necesario evaluar la fiabilidad de estas medidas de potencia y conectividad.

Fiabilidad de medidas de potencia y conectividad en estado basal en MEG

Los estudios de DCL descritos anteriormente siguen un esquema de análisis habitual en MEG, que consiste en hacer estadística entre grupos o condiciones testeando la hipótesis nula de que no hay diferencias entre las dos poblaciones. Esto sirve para identificar efectos de grupo, pero no da resultados a nivel individual. Antes de dar ese paso, es necesario evaluar la variabilidad intrasujeto y la fiabilidad test-retest de estas medidas. Para ello, se realizaron 3 sesiones de registros MEG en estado basal a 24 sujetos sanos (una a la semana). La fiabilidad de una medida se puede cuantificar a partir de varias mediciones en los mismos sujetos como $\frac{\sigma_r^2}{\sigma_r^2+\sigma_w^2}$, donde σ_r^2 es la varianza real de la medida y σ_w^2 la varianza del error. En un estudio test-retest como el presente, σ_r^2 corresponde a la varianza intersujeto y σ_w^2 a la varianza intrasujeto.

Cualquier variabilidad en la medida de un sujeto se considera por lo tanto error, independientemente de si se debe a ruido en la medición o a un cambio real en la actividad neuronal del sujeto. De esta forma, se analizó la fiabilidad de medidas de potencia y FC por separado mediante el coeficiente de correlación intraclase (ICC, *intraclass correlation coefficient*).

- Primero, se calculó la potencia tanto en sensores como en fuentes en delta, zeta, alfa, beta baja (13-20Hz), beta alta (20-30Hz) y gama (30-45 Hz) para cada sujeto y sesión. Después, se calculó el ICC para cada sensor, fuente, y banda de frecuencia. En general, zeta, alfa y beta baja presentaban altos valores de ICC (ICC>0.7) en amplias zonas de la corteza cerebral. En cambio, delta, beta alta y gama presentaban valores más bajos de ICC (ICC<0.6) en la mayoría de regiones, aunque también alcanzaron ICC altos en zonas concretas, como regiones frontales en delta. Para comprobar si la fiabilidad (y los valores de ICC) dependían de la relación señal a ruido, se estimó la probabilidad condicional de obtener una determinada variabilidad intrasujeto dado un cierto valor de potencia. Se observó que existía una dependencia entre ambas variables, ya que valores de potencia bajos estaban asociados a alta variabilidad intrasujeto. Sin embargo, está relación no era lineal, ya que potencias altas no siempre conllevaban baja variabilidad intrasujeto.

- Segundo, se calculó FC entre 17 nodos y el resto de fuentes repartidas a lo largo de la corteza cerebral, para todas las bandas de frecuencia y cuatro medidas de FC distintas: d-ecor (correlación de envolventes), lc-ecor (correlación de envolventes con corrección por volumen de conducción), PLV (*phase locking value*) y PLI (*phase lag index*). Estos nodos componen 7 redes de reposo (RSN, *resting state network*): visual, sensori-motora, auditiva, DMN, fronto-insular y fronto-parietales izquierda y derecha, y se definieron a partir de la literatura de RSNs con RM funcional. Después, se estimó la fiabilidad de estas medidas con el ICC, y la concordancia intra- e intersujeto en los mapas de FC con el coeficiente W de Kendall. La fiabilidad de los mapas de FC era muy dependiente de la medida utilizada, de la banda de frecuencia y de la región. Los valores de PLV eran en general los más fiables, especialmente en alfa, beta y gama, aunque también se alcanzaron valores altos de ICC con d-ecor y con lc-ecor en beta. Por el contrario, se encontró que el ICC era consistentemente bajo para el PLI. Por otro lado, para todas las medidas, las conexiones intrared eran más fiables que la interred. De hecho, el ICC correlacionaba positivamente con el valor de FC: conexiones más intensas eran más fiables. En cuanto a la concordancia intra-

e intersujeto, se obtuvieron resultados parecidos a los el ICC: se alcanzaron los valores más altos para el PLV; intermedios para d-ecor y PLI y más bajos para lc-ecor. La concordancia intrasujeto era además mayor que la intersujeto.

En conjunto, tanto la potencia como la FC con PLV fueron altamente fiables. Esto indica que ambos tipos de medidas podrían tener utilidad en la caracterización de sujetos individuales. Por ejemplo, se podrían aplicar los resultados de los estudios anteriores para la clasificación entre sujetos con DCL y controles a nivel individual. Sin embargo, la fiabilidad caracteriza a un grupo concreto, ya que depende de la variabilidad intra- e intersujeto, así que sería necesario realizar un estudio de fiabilidad test-retest en DCL y controles de la misma edad, para evaluar si es mayor o menor que en un grupo de controles sanos y jóvenes.

Abstract

Although neuroimaging techniques are rapidly progressing, the accurate and non-invasive imaging of brain function remains a challenge. Imaging modalities emerge from the measurement of distinct aspects of brain function, such as metabolic consumption, hemodynamic responses or neuronal currents. Amongst them, magnetoencephalography (MEG) is a direct measure of neuronal activity which measures tiny magnetic fields that are produced by neuronal currents. MEG offers a great insight into the fast dynamics of the brain, by enabling the mapping of electrophysiological brain rhythms and functional connectivity (FC). Brain rhythms consist in oscillatory activity which ranges from the delta (<4Hz) to fast gamma oscillations (>30Hz), and they are engaged in a variety of cognitive and sensorimotor functions. FC assesses brain integration by measuring statistical dependencies between the activities of distinct brain regions. FC is therefore a measure of information transfer between brain regions, and can be computed separately for the distinct electrophysiological rhythms. The evaluation of resting-state MEG brain rhythms and FC is only possible after a great deal of signal processing, which includes noise reduction techniques, signal segmentation, filtering, source reconstruction, and a FC metric (Chapter 2).

MEG enables the study of several neurological diseases, such as Alzheimer's disease (AD) and mild cognitive impairment (MCI). On the one hand, AD is a neurodegenerative disease which is accompanied by a severe cognitive decline. On the other hand, MCI is characterized by a smaller cognitive decline, which is not severe enough to be classified as dementia. As amnestic MCI patients show both an intermediate cognitive state between healthy subjects and AD patients and high conversion rates to AD, the study of amnestic MCI benefits AD research by casting some light into how the memory impairment develops. This is nowadays especially relevant due to the rapidly increasing prevalence of AD and the lack of understanding of its pathological pathways. In this thesis, we explored the resting state spectral and FC profiles of amnestic MCI patients and age-matched healthy controls. For that, samples from both populations underwent resting state MEG recordings, and their power spectra and

FC were computed in source space. Statistical analysis showed differences between controls and MCIs: slowing of the alpha peak frequency and a decreased FC in the alpha band (Chapter 3).

Although such group statistics reveal alterations in the spectral and FC patterns of MCI, the potential use of these patterns as markers of MCI is not easy to assess. This is a well-known challenge for MEG research, and it is not limited to the study of MCI/AD. In fact, although extensive literature has used MEG spectral and FC measures to distinguish between two conditions or two subject samples, the reliability of such measures remains unclear. The second part of this thesis focuses on this matter. For that, healthy subjects underwent three resting state MEG recordings over three consecutive weeks, and spectral and FC measures were computed for each subject and session. The reliability of such measures was then estimated with the intraclass correlation coeffcient, which accounts for between- and within-subject variability. In general, power and FC values showed medium to good reliability. This was however dependent on the brain region and frequency band (Chapter 4).

Overall, our results indicate that MEG power and FC measures are sensible to early brain alterations, and that these measures are fairly reliable, suggesting that MEG could be employed in the individual characterization of MCI subjects.

Contents

List of Tables

List of Figures

Chapter 1

Introduction to neuroimaging and MCI

The brain is an intricate structure which is responsible for our sensorimotor processing and cognition. Although many of the brain's mysteries remain unresolved, scientific research over the past century has provided much insight into its structure and function. This has been enabled by a variety of neuroimaging techniques. Upon such, magnetoencephalography (MEG) emerges as an ideal technique to non-invasively investigate the fast dynamics of brain activity. Neuroimaging facilitates the investigation of the structural and functional substrate of neurological pathologies such as Alzheimer's disease (AD) and Mild Cognitive Impairment (MCI). In this chapter we present an overview of brain imaging modalities and their findings in the study of MCI and AD.

1.1 Brain imaging

1.1.1 Overview of brain structure and function

The human brain has three main parts: brainstem, cerebellum and cerebrum. First, the brainstem is responsible for mantaining sleep cycle, consciouness and automatic functions such as breathing, heart rate or body temperature. Second, the cerebellum has an important role in motor control and coordination, and maintaining posture and balance. Finally, the cerebrum is responsible for higher functions such as cognition or movement control.

The cerebrum can be separated into two main systems: cerebral cortex and deep structures. Deep structures are located further away from the scalp and include,

among others, thalamus, basal glanglia and amygdala. Within these structures, the thalamus has a crucial role, since it acts as a relay between sensory information, subcortical nuclei and the cerebral cortex. The cerebral cortex consists in a thin sheet (2-4 mm thick) that is folded forming gyri (ridges) and sulci (fissures), so that its great surface (around 1700 cm^2) can be contained within the scalp (see Figure 1.1). It is separated into 2 hemispheres, each one consisting in 4 lobes: occipital, parietal, frontal, and temporal. Within the medial temporal lobe, the hippocampus is a remarkable structure that is widely mentioned throughout this dissertation, as it is decisive for memory and learning, and plays an important role in Alzheimer's disease.

At a cellular level, the brain is mainly constituted of glial cells, which have a variety of functions such as synaptic modulation or structural and metabolic support, and neurons, which are responsible for the transfer of information with electrical and chemical signals. A neuron is built from three main parts: dendrites, soma and axon. A dendrite receives input from another neuron at a synapse, and then this information (either excitation or inhibition) travels through the dendrite in the direction of the soma. The soma or cell body integrates the input from the neuron's dendrites, and triggers an action potential if it reaches enough depolarization. Action potentials propagate very quickly through the axon (1-100 m/s), and reach many other neurons by means of thousands of synapses. This axon may be short and communicate with nearby neurons, but it may also be very long and communicate with neurons in distant brain regions. Large axons are usually covered by a myelin sheath, which speeds the impulse and prevents axonal currents from leaving the axon, and therefore enable action potentials to reach distant targets.

When observing a brain slice, one can rapidly identify three types of tissue: grey matter, white matter and cerebrospinal fluid (CSF). First, grey matter assembles neural nuclei. However, it is not only composed of neural cell bodies, since it also contains glial cells and unmyelinated axons. Second, white matter mainly consists in glial cells and myelinated axons that connect different brain regions. Finally, CSF is found around and inside the brain (in the ventricles) and in the spinal cord. It provides nutrients necessary for the correct brain function, and protects the nervous system by working as a cushion against mechanical damage.

The brain is a highly active organ and consumes around 20% of the body's 0_2, although it only accounts for 2% of the body weight (Clarke and Sokoloff, 1999). It is constantly working, even during sleep or in the absence of externally-driven tasks. Engaging in some task may produce local brain activations and deactivations, but these task-induced changes represent less than 5% of the local metabolic consumption (Raichle and Gusnard, 2002).

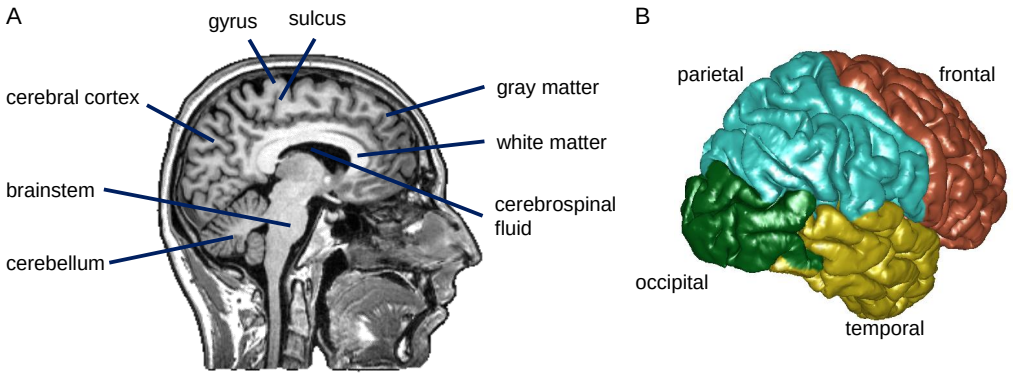

Figure 1.1: Basic brain structure. A. Sagittal slice in a T1-weighted magnetic resonance image, showing different brain structures, such as brainstem, cerebellum, and cerebral cortex. The cerebral cortex is folded into gyri and sulci. Gray matter, white matter and cerebrospinal fluid regions have different intensities. B. Surface of the right cerebral cortex, separated into occipital, parietal, temporal and frontal lobes.

Although the functional organization of the brain is still unclear,many discoveries have been made over the past two centuries. Over the nineteenth and early twentieth century, much knowledge was extracted from brain injury. If damage to a region impairs a certain cognitive or sensory ability, one can argue that this brain region is responsible for this process or, at least, involved in it. This led to the concept of brain segregation, in which regions specialize in particular functions; and an early brain mapping could be inferred from brain damage reports. For instance, Broca noticed that damage to a particular region in the frontal lobe, that was then named Broca's area after him, related consistently to speech impairment in his patients. He concluded that this region is functionally specialized in speech production. The use of evoked responses provided also useful information on brain specialization. For example, the hearing of tones trigger evoked responses in the primary auditory cortex 100 ms after the sound onset, indicating a fixed latency for auditory processing (Roberts and Poeppel, 1996).

The concept of brain segregation is being progressively completed with the concept of brain integration, in which networks rather than isolated regions are involved in distinct brain processes. Any set of interconnected regions could be considered a brain network. A distinction can be made between structural and functional networks. In the first case, regions are anatomically connected, possibly with the use of densely packed axons, or fiber tracts. In the latter, the time dynamics of the regions is somehow linked. Functionally connected regions may exhibit the same pattern of activation or deactivation in response to some stimulus, or show similar dynamics. In both

cases, connectivity, which quantifies the connections or dependencies between two regions, comes in handy to characterize these networks. For instance, the amount of tracts connecting two regions is a valid structural connectivity metric. Functional connectivity may be defined as statistical dependencies between neural, metabolic or hemodynamic activity of two brain regions (Friston, 2011). Functional connectivity can be assessed with a variety of algorithms, as will be introduced in section 2.4.

1.1.2 Structural brain imaging

Structural imaging techniques such as computed tomography (CT) and magnetic resonance imaging (MRI) have variable sensitivity to different tissue types, and can therefore be used to locate and inspect brain structures. CT emits x-rays in many directions to reconstruct a 3D image of the region of interest. Because of its relatively low cost and short scanning times, it is commonly used in the clinical scenario to detect abnormalities such as contusions, bleeding or edemas. MRI offers generally higher sensitivity and contrast for soft tissue, and it does not employ ionizing radiation, but it is also more expensive and takes longer scanning times.

Basics of magnetic resonance imaging (MRI)

MRI devices use strong magnetic fields to align nuclear spins (although only ^{1}H nuclei are considered relevant, due to their abundance in soft tissue), and measure how these spins return to equilibrium after they have been transiently excited (Brown and Semelka, 2003). When placed in a strong magnetic field $\mathbf{B_0} = B_0\mathbf{u_z}$ with $B_0 \approx$ 0.5-7T, hydrogen atoms align in the z-direction (either $+\mathbf{u_z}$, or $-\mathbf{u_z}$), and precess around the z-axis at a rate $\omega_0 = \gamma B_0/2\pi$, where γ is the gyromagnetic ratio ($\gamma \approx$ 42.6 MHz/T for the ^{1}H nucleus). Overall, a net magnetization $\mathbf{M_0} = M_0\mathbf{u_z}$ is established. Then, a radiofrequency (RF) pulse at a frequency ω_0 is applied, which releases energy to the ^{1}H nuclei and enables transitions to excited states. This modifies the net magnetization, so that the longitudinal M_z decreases, whereas a transversal M_{xy} emerges. When the RF pulse is turned off, the nuclei gradually return to equilibrium, thereby releasing RF waves which are detected by receiver coils in the MRI system.

This process of relaxation, which is detected indirectly by measuring RF waves, depends on the proton density and other molecular properties of the target tissue. Relaxation can be separated into longitudinal (along the z-direction) and transversal (in the xy plane) relaxation. Both relaxation processes can be modelled with exponential decays: $M_z(t) = M_0(1 - \exp(-t/T_1))$ and $M_{xy}(t) = M_{xy,max}\exp(-t/T_2)$, where T_1 and T_2 are tissue-specific decay times. Various MRI sequences can be used, depending on

the desired contrast. For instance, T_1-weighted images have great sensitivity to the T_1 longitudinal relaxation time and are of use to distinguish cerebrospinal fluid and white and grey matter. Conversely, T_2-weighted images are sensitive to the T_2 transversal relaxation and are useful to detect soft tissue pathologies.

Diffusion Tensor Imaging (DTI)

MRI can be used to map the diffusion of water molecules within the brain (Le Bihan et al., 2001; Alexander et al., 2007). Diffusion represents the transport of material from one spatial location to another, and can be characterized with Einstein's equation:

$$\langle \Delta u^2 \rangle = 2 D_u \Delta t \tag{1.1}$$

where D_u is the diffusion coefficient along the u-axis and Δu represents the u-displacement over the time Δt. By using specific sequences in the MRI scanner, one obtains diffusion-weighted (DW) 3D images, from which the D_u coefficient for every 3D voxel (i, j, k) along a fixed direction u can be inferred. DW acquisitions consist in several images with varying u-directions. In a homogeneous and isotropic medium, D has the same value over all diffusion directions. For instance, $D \approx 2 \cdot 10^{-3}$ mm^2/s for pure water at 20°C. However, in a general case, D has to be determined for every position or voxel (i, j, k) and every direction (ϕ, θ): $D = D(i, j, k, \phi, \theta)$. This general case can be simplified by using a diffusion tensor, in which the diffusion coefficient at a certain voxel (i, j, k) is modeled as a tensor:

$$\mathbf{D}(i, j.k) = \begin{pmatrix} D_{xx} & D_{yx} & D_{zx} \\ D_{xy} & D_{yy} & D_{zy} \\ D_{xz} & D_{yz} & D_{zz} \end{pmatrix} \tag{1.2}$$

In this model, the diagonal coefficients D_{uu}, $u = x, y, z$ represent the diffusion coefficient along the u-direction, and the off-diagonal coefficients are symmetric $D_{uv} = D_{vu}$. The tensor is diagonalizable:

$$\mathbf{D} = \mathbf{P} \begin{pmatrix} \lambda_1 & 0 & 0 \\ 0 & \lambda_2 & 0 \\ 0 & 0 & \lambda_3 \end{pmatrix} \mathbf{P}^{-1}, \mathbf{P} = \begin{pmatrix} \mathbf{v_1} & \mathbf{v_2} & \mathbf{v_3} \end{pmatrix} \tag{1.3}$$

where $\mathbf{v_u}$ and λ_u are the matrix' eigenvectors and eigenvalues, respectively. The tensor can then be visualized as an ellipsoid with $\mathbf{v_u}$ as principal axes and λ_u as radii. This informs about the region's structure. For example, in a highly isotropic medium diffusion is very similar along all directions ($\lambda_1 \approx \lambda_2 \approx \lambda_3$), and the ellipsoid is rather spherical.

This is usually the case in cerebrospinal fluid and grey matter. However, if diffusion occurs predominantly in one direction ($\lambda_1 \gg \lambda_2, \lambda_3$), the ellipsoid resembles a cigar. This is common in white matter regions, since diffusion is hindered in directions perpendicular to white matter fibers.

Several magnitudes that derive from DTI are commonly used in neuroscience and neurology studies (Le Bihan et al., 2001), such asmean diffusivity (MD) and fractional anisotropy (FA):

$$MD = \frac{1}{3}(\lambda_1 + \lambda_2 + \lambda_3) \tag{1.4}$$

$$FA = \frac{\sqrt{3\left[(\lambda_1 - MD)^2 + (\lambda_2 - MD)^2 + (\lambda_3 - MD)^2\right]}}{\sqrt{2\left[\lambda_1^2 + \lambda_2^2 + \lambda_3^2\right]}} \tag{1.5}$$

DTI can also be used to estimate structural connectivity (SC), with tractography techniques (Mori and van Zijl, 2002; Lazar et al., 2003; Jbabdi and Johansen-Berg, 2011). Assuming that tracts are oriented along the direction of higher diffusion, tracts can be reconstructed with a variety of line propagation techniques. Once they have been estimated, a SC metric can be calculated. For instance, the amount of reconstructed tracts connecting two regions and the FA along these tracts are SC metrics. In this dissertation, both metrics are used to compare SC between MCI patients and controls in section 3.2.

1.1.3 Electrophysiological techniques

Electrophysiological activity is generated by electrical currents in the brain. Measurement techniques differ in the recording site (at the scalp, invasively with electrodes directly at the brain surface or even inserted into a brain structure) and the type of measured signal (either electric potential or magnetic field) (Buzsáki et al., 2012). They all have great temporal resolution (~1) ms, and medium to excellent spatial resolution, as shown in Figure 1.2.

Electroencephalography (EEG)

EEG measures electric potential at the scalp by placing electrodes directly at its surface and applying conducting gel and a slight abrasion to the skin in order to reduce the skin-electrode impedance. There is a wide offer of EEG systems, most systems ranging from 19 to 256 electrodes. EEG has relatively low cost and is frequently used both for

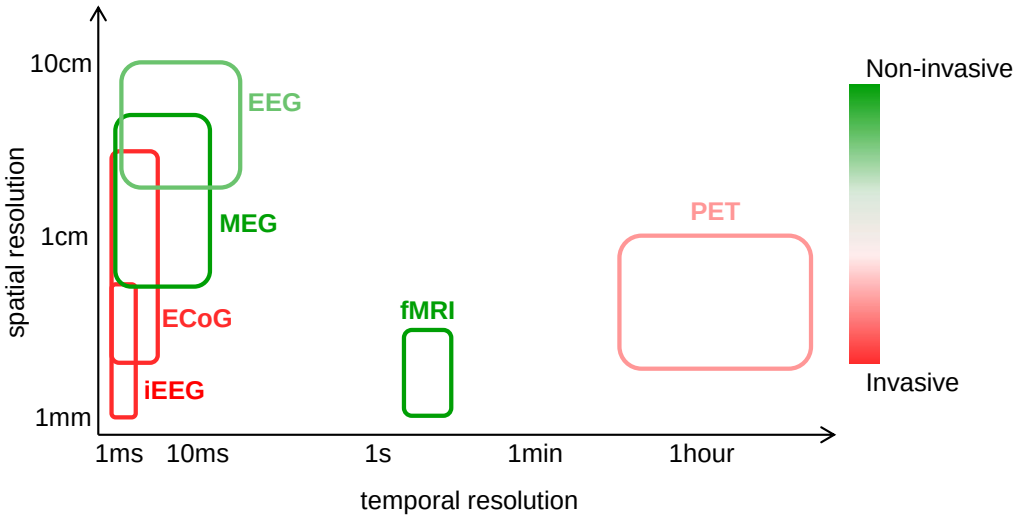

Figure 1.2: Spatial and temporal resolutions of functional neuroimaging modalities. Colors indicate the invasiveness of the technique (red: invasive, green: non-invasive).

research and the diagnosis of several pathologies such as epilepsy, sleep disorders, or coma (Noachtar and Rémi, 2009; Kaplan, 2004).

Magnetoencephalography (MEG)

MEG measures magnetic fields in a helmet-shaped set of sensors. The head has a rather constant magnetic permeability $\mu \approx \mu_0$, but a very variable electrical conductivity $\frac{\sigma(brain)}{\sigma(skull)} > 20$ (Stenroos and Sarvas, 2012), so that magnetic fields are less distorted than electric fields when they reach the scalp. MEG has therefore higher spatial resolution than EEG. MEG systems are further described in section 2.1.

Electrocorticography (ECoG)

To reach higher spatial resolution one may resort to ECoG, which uses subdural electrodes to record electric potentials directly at the surface of the brain. Electric fields do not cross the scalp or the skull, and are therefore less distorted than in EEG. Since it is a highly invasive measurement (it requires a craniotomy), its use in humans is restricted to clinical applications. For instance, some patients suffering from untreatable epilepsy undergo a resection of their epileptic foci. ECoG is of use in this case to obtain the precise localization of the epileptogenic tissue (Nakasatp et al., 1994).

Intracranial encephalography (iEEG)

Even higher spatial resolution can be achieved with iEEG: electrodes are inserted directly into the target brain region in order to measure the local field potential (LFP) (Buzsáki et al., 2012). Modern electrodes contain many close contacts and allow for a precise mapping of the region of interest. iEEG is widespread in animal studies, since it enables a detailed inspection of the functional organization of brain structures. As in the case of ECoG, iEEG with human subjects is restricted to clinical applications.

1.1.4 Other functional imaging techniques

While electrophysiological techniques measure neural activity directly, other functional imaging techniques measure brain functioning indirectly, via hemodynamic or metabolic activity. Positron emission tomography (PET), functional magnetic resonance imaging (fMRI) and functional near-infrared spectroscopy (fNIRS) are included in this group (Dale and Halgren, 2001; Menon, 2001; Uludağ and Roebroeck, 2014). PET detects gamma-rays that result from the annihilation of positrons and electrons, which are triggered by a radioactive tracer. When using fluorodeoxyglucose (FDG) as a tracer, PET gives a 3D image of brain metabolic activity. fMRI detects a blood-oxygen-level dependent signal and thereby measures hemodynamic responses to brain activation, so that it is commonly used to investigate event-related responses and brain networks. fNIRS measures hemodynamic responses by detecting changes in light scattering and absorption. It is non-invasive and has lower cost than other functional neuroimaging techniques, but it is only sensitive to activity close to the scalp surface, since its signal to noise ratio decreases rapidly with distance from the measurement site.

1.2 Introduction to MCI and AD

1.2.1 MCI and AD pathology

Aging is usually accompanied by some cognitive decline, and this is considered normal (Goh et al., 2012; Naveh-Benjamin, 2000). However, MCI individuals show a worse cognitive decline than normal, but not severe enough to be classified as dementia (Petersen, 2001, 2011). MCI could therefore be grasped as an intermediate stage between normal aging and dementia. It is usually classified into two subtypes: amnestic and non-amnestic. While amnestic-MCIs show memory impairment, non-amnestic MCIs show decline in other cognitive functions such as language, attention, visuospatial or

executive functions. MCI can be further subdivided into single-domain or multiple-domain, depending on whether a single or various cognitive functions are affected, respectively.

MCI individuals present higher conversion rates to dementia than their age-matched controls (Petersen and Negash, 2008). Dementia is a wide term that refers to a cognitive decline that is severe enough to interfere with daily activities. It includes a variety of disorders, such as Alzheimer's disease (AD), vascular dementia, dementia with Lewy bodies or frontotemporal dementia. AD is the most prevalent form: it accounts for 60-80% of the cases (Barnes and Yaffe, 2011). It is a chronic neurodegenerative disease, which usually first manifests as short-memory impairment but also includes other symptoms such as deficits in language and visuospatial functions, poor judgment and changes in mood or personality (Alzheimer's Association, 2011). The conversion rate from MCI to AD is high: 10-17% annually vs. 1-4% for age-matched controls (Petersen, 2011; Petersen and Negash, 2008; Landau et al., 2010). Additionally, conversion rates from MCI to AD are higher for amnestic MCI than for non-amnestic MCI, and for multiple-domain MCI than for single-domain MCI (Fischer et al., 2007; Vos et al., 2013). For instance, Fischer et al. (2007) obtained that, after a 30-month follow-up, 48.7% of amnestic MCI and 26.8% of non-amnestic MCI developed AD.

The study of MCI could therefore shed some light into the early stages of AD by informing about how the disease develops. It should nonetheless be mentioned that MCI is not equivalent to early stage AD, as MCI individuals can progress to develop other dementias, stay MCI indefinitely or even revert to a control status. However, since MCI individuals present both an intermediate cognitive status between controls and AD and high conversion rates to AD, they constitute a decent population to investigate early AD-related changes. This is especially relevant because AD is a progressive pathology with no clear and abrupt onset (Albert et al., 2013). In fact, AD-related changes are thought to initiate decades before any clinical symptoms appear (Sheline and Raichle, 2013). Although AD is mainly characterized by the accumulation of amyloid β (Aβ) plaques and neurofibrillary tangles, brain atrophy, neuronal and synaptic loss (Ballard et al., 2011; Verghese et al., 2011), the pathway of the pathology is unclear. AD diagnosis can indeed only be confirmed post-mortem during autopsy.

Moreover, AD-related research is nowadays especially relevant, since it has become one of the most concerning health conditions, both for human and economic reasons (see Figure 1.3). Around 5-7% of the population older than 60 and 15-30% of the population older than 85 are affected with AD (Prince et al., 2013), and often require institutional or home healthcare. What is more, as the world's population ages, AD threatens to spread rapidly. Brookmeyer et al. (2007) predicted that by 2050 1 in 85

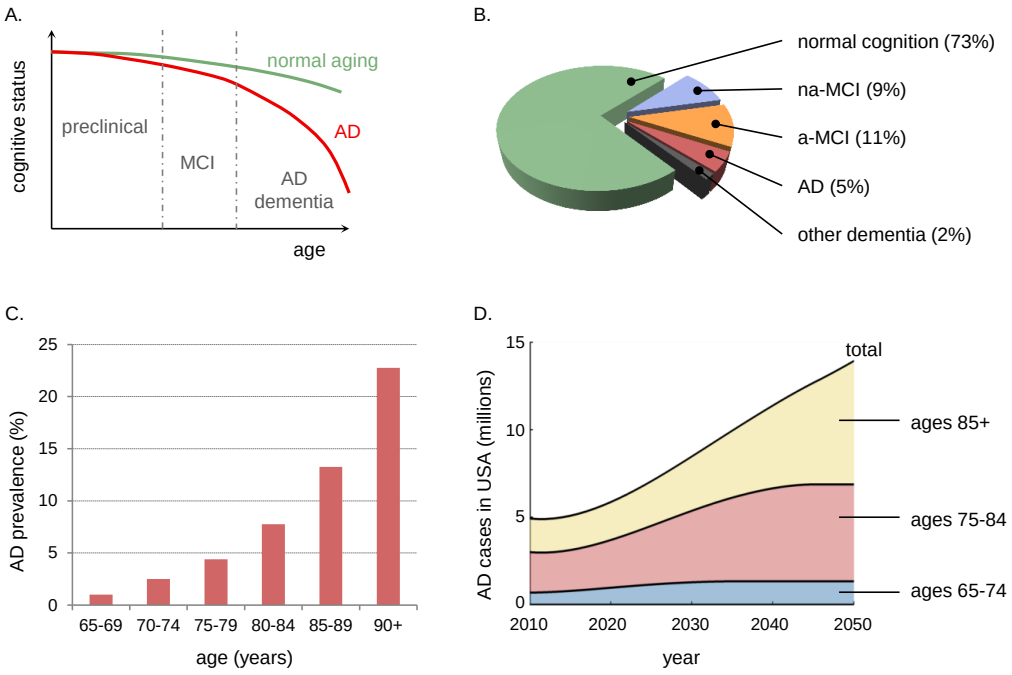

Figure 1.3: Some AD facts. A. AD causes a cognitive decline with age that is worse than in normal aging. Depending on the extent of this cognitive decline, individuals may be classified as either showing no objective cognitive decline (preclinical phase), MCI, or dementia. B. Prevalence of amnestic MCI (a-MCI), non-amnestic MCI (na-MCI), AD and other dementias in a population aged 70 years and above. Prevalence rates are extracted from (Katz et al., 2012). C. AD prevalence for different age groups in Europe, according to (Qiu et al., 2009). D. Prevision of the number of AD patients in USA from 2010 to 2050 for distinct age ranges, according to (Hebert et al., 2013).

people could be affected with AD. Although some promising drugs were developed (Barnes and Yaffe, 2011), they failed in the clinical trials and the existing pharmaceutical treatments for mild to severe AD (Roberson and Mucke, 2006) have a limited efficiency, so that new developments are essential.

We note that the knowledge on MCI and AD is rapidly changing, and the consensus on the proper terminology and diagnostic criteria is often updated. In this dissertation we use the terminology that was valid when the experiments were carried out, although some terms and concepts may be outdated for the reader. In particular, the newest edition of the Diagnostic and Statistical Manual of Mental Disorders (DSM-5) (American Psychiatric Association, 2013), introduced some changes relative to its previous edition (DSM-IV) (American Psychiatric Association, 2000). Roughly, within the DSM-5 the terms mild and major neurocognitive disorders are preferred to MCI and dementia, respectively (Simpson, 2014). This highlights the continuum between both diagnoses. Although the DSM-5 was released before the ending of this dissertation, we decided to maintain the terms MCI and AD throughout this text, because they were the accepted terms when the studies were performed and they were employed in the resulting publications.

1.2.2 In-vivo investigation in MCI/AD

Much research is nowadays invested to face the AD disease: understanding how the pathology initiates and how it progresses could contribute to developing appropriate strategies to deal with it. Current research is targeting AD from different perspectives: animal studies, post-mortem histological studies, computational models, demographic studies, neuroimaging, etc. Although all these approaches have provided interesting information into the matter, we here focus exclusively on the in-vivo investigation of MCI/AD in humans. Different approaches in such studies are illustrated in Figure 1.4 and overviewed in the following.

Cognitive evaluation

A detailed neuropsychological evaluation is essential to diagnose MCI and AD. Episodic-memory impairment is typically associated with AD and MCI due to AD, but other cognitive domains should be examined with the use of appropriate neuropsychological tests, such as language, executive functions, attention, or visuospatial skills (Albert et al., 2013). A detailed cognitive evaluation is also useful in the prognosis, since individuals with higher cognitive impairment tend to convert faster to AD (Dickerson et al., 2007).

Aβ

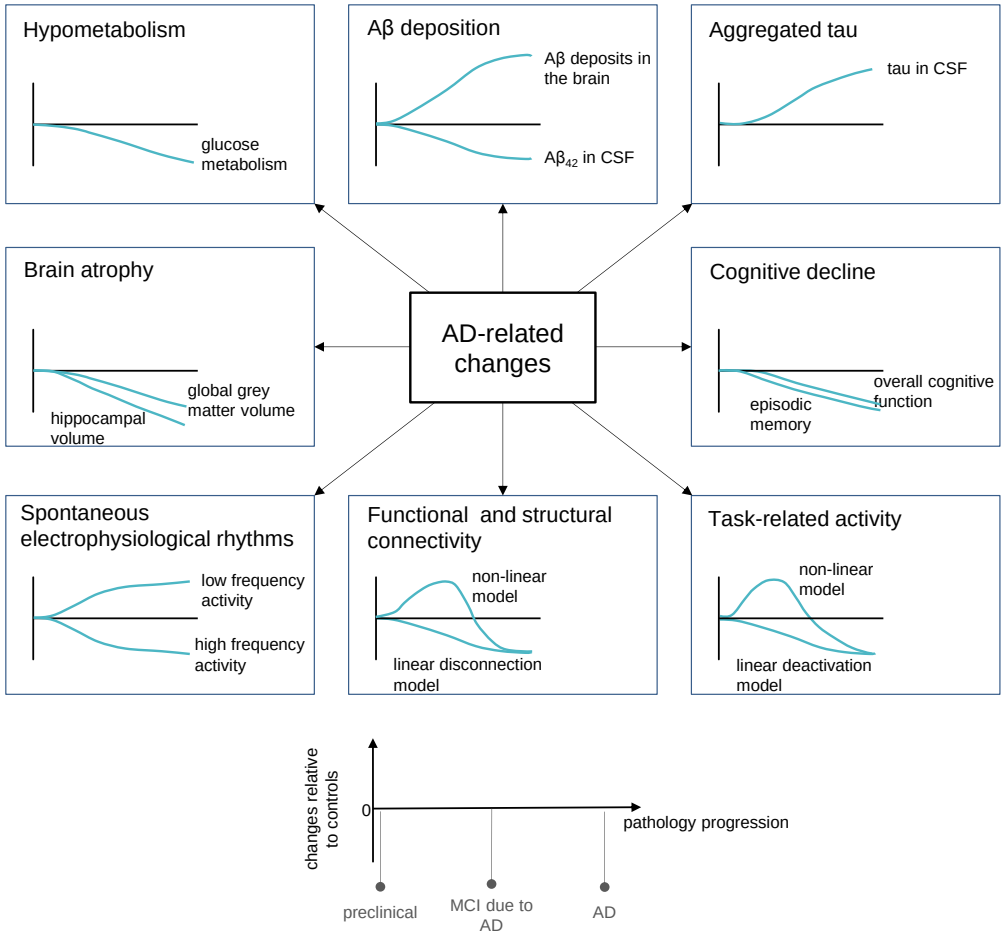

Figure 1.4: Distinct approaches to the in-vivo study of AD. The AD pathology is related to many alterations, which are illustrated in separate rectangles and described in the following. 1- Hypometabolism, which can be evidenced with fluorodeoxyglucose-PET. 2- Amyloid deposits, which can be observed with PET-PIB as increased intensities or as decreased $A\beta_{42}$ concentrations in the cerebrospinal fluid (CSF). 3- Aggregated tau, which can be measured as increased tau concentrations in the CSF. 4- Brain atrophy, specially in medial temporal regions, which can be detected with a T1-weighted MRI. 5- Cognitive decline, which typically first affects episodic memory and executive functions. 6- Slowing of the electrophysiological brain rhythms, which can be evidenced by increased low frequency activity and decreased high frequency activity. 7- Altered functional and structural connectivity. Although AD is consistently associated to a loss in connectivity, it is unclear whether the timeline of this connectivity changes follow a linear decrease or a non-linear trajectory. 8- Task-related activations are altered in AD. Although AD is usually associated with decreased task-related activations, some studies found task-related hyperactivations in MCI, possibly indicating compensatory mechanisms. Based on (Ewers et al., 2011; Jack and Holtzman, 2013).

Aβdeposition is a hallmark of AD. This can be assessed in vivo as either decreased concentrations of $A\beta_{42}$ in the CSF, or as increased intensities in PET imaging when using amyloid-specific agents. For instance, PIB (^{11}C-Pittsburgh Compound B) binds to the amyloid deposits, and enables a 3D image of the amyloid deposits in the brain (Adlard et al., 2014).

Aggregated tau

Aggregated tau protein, in the form of neurofibrillary tangles, is characteristic of AD. Although neurofibrillary tangles are best inspected postmortem during autopsies, they can also be assessed in-vivo as increased levels of total tau and phosphorylated tau in the CSF (Visser et al., 2009; Jack and Holtzman, 2013).

Atrophy

AD is accompanied by a progressive brain atrophy, which generally starts in the entorhinal cortex, and then spreads first to the hippocampus and later to the neocortex. This atrophy can be detected with structural MRI (such as T1-weighted MRI) and quantified as a volume loss. MCIs that convert to AD show greater and accelerated atrophy than non-converting MCIs (Jack et al., 2005, 2008). Particularly, the hippocampal volume has been proven relevant, since it correlates with cognitive decline (Petersen et al., 2000), and predicts conversion from MCI to AD (Apostolova et al., 2006; Jack et al., 2010).

Metabolism

Hypometabolism in temporal and parietal regions is characteristic of AD. It can be measured with ^{18}F-fluorodeoxyglucose-PET and it was found to be a decent predictor of conversion from MCI to AD (Landau et al., 2010).

Intensity of spontaneous electrophysiological rhythms

AD is associated with an increased electrophysiological activity in the lowest frequency bands (delta and theta) and a decreased activity in higher frequency bands such as alpha and beta (Berendse et al., 2000). This “slowing” of the EEG rhythms seems to occur progressively from controls to MCI and then to AD and to correlate with other AD markers such as brain atrophy (Moretti et al., 2012; Babiloni et al., 2013). It does not occur uniformly across all brain regions, as it is accompanied by changes in the topography of the main cortical generators (Osipova et al., 2006). The functional significance of electrophysiological brain rhythms, their quantification from MEG raw data and their alterations in MCI/AD are further discussed in Chapters 2 and 3.

Task-related activations

Neuroimaging of the brain when performing a cognitive task evaluates the neural correlates of the cognitive changes in MCI/AD. As expected, MCI and AD patients have worse performance than controls. More interestingly, some studies found increased activity in MCI in trials with correct responses or in a subgroup of MCI patients with high performance, and decreased activity for wrong responses or worse performance subjects (Celone et al., 2006; Kircher et al., 2007; Chechko et al., 2014). This has been hypothesized to reflect a compensatory mechanism, in which MCI patients require additional activation to reach the same performance level than controls. The task-related activation would then follow a non-linear trajectory as the AD pathology advances, and exhibit first a hyperactivation to achieve a normal performance followed by a hypoactivation when approaching the AD stage.

Functional and structural connectivity

AD is accompanied by a loss in structural connectivity, as revealed by DWI studies (Shao et al., 2012). Functional disconnection was also found in AD for several networks such as the default mode network (DMN), the sensory network or the dorsal attention network (Brier et al., 2012; Greicius et al., 2004). Some studies have suggested that this disconnection occurs progressively (Sheline and Raichle, 2013), while others point out the existence of a transitory hypersynchronization in the MCI stage, possibly reflecting a compensatory mechanism (Bajo et al., 2012; López et al., 2014). Connectivity in MCI is further discussed in Chapter 3.

Genetics

Increased AD risk is associated with some genotypes. Although early onset AD (at ages 30-65) only accounts for a small fraction of the cases, it is worthwhile studying, as it informs about the AD pathways. Such early onset AD is usually caused by mutations that influence either the production or the clearance of Aβ, highlighting the role of Aβ in the AD pathology (Hardy and Selkoe, 2002; Jack and Holtzman, 2013). Additionally, the APOE (apolipoprotein E) gene is attracting widespread interest, since its thee alleles $\epsilon 2$, $\epsilon 3$ and $\epsilon 4$, which are relatively frequent in the population (1-5%, 50-90% and 5-35% of people, respectively), are thought to modulate Aβ deposition and therefore the risk for AD (Verghese et al., 2011). In particular, $\epsilon 4$ is associated with higher risk for AD than $\epsilon 3$, and $\epsilon 3$ with higher risk than $\epsilon 2$. Many neuroimaging studies with MCI or AD include APOE genotype as a variable to investigate its role in the MCI/AD process. For

example, Cuesta et al. (2015) evaluated the effect of diagnosis (MCI/Control) and APOE genotype in resting state functional connectivity.

1.2.3 Towards reliable AD biomarkers

Although all the previous approaches reveal changes in MCI/AD patients relative to age-matched controls, it is still unknown how they fit into a global model of AD. In fact, much research needs yet to be done before achieving a global picture and the accurate characterization of the various stages of the pathology. In particular, work needs to be done in two directions:

Building the timeline of AD

The progress of AD is unclear. Some theories point out that it may be triggered by deposition of Aβ (Sheline and Raichle, 2013), which in turn causes aggregated tau, brain atrophy and other abnormalities reviewed in section 1.2.2. Other theories indicate that neurodegeneration precedes the Aβ deposition. It is also possible that the AD timeline is not fixed, and that different timelines account for different AD etiologies (see Jack and Holtzman (2013) for a review). Early-onset AD is for instance thought to be generated differently than late-onset AD, In any case, establishing the timeline(s) of AD and the causality between its different markers is essential. Big multimodal and longitudinal studies are needed for this purpose.

Establishing reliable biomarkers for specific stages of the AD pathology

AD-related changes can be observed with several approaches: decreased Aβ in the CSF, decreased metabolism in PET images, altered functional connectivity, etc. However, none of these markers constitutes a true biomarker, or a definite indicator of AD. For instance, (Albert et al., 2013) recommend including markers of Aβ and neuronal injury to diagnose MCI due to AD in research studies, but they clarify that these markers only modulate the likelihood that the MCI is due to the AD pathology. In fact, much work must be done before any of these markers becomes a trustworthy AD biomarker: it should first be proven that the underlying alteration is pathognomonic of AD (e.g. that Aβ deposition is a definite indicator of AD), and second, that the measurement instrument and methodology are reliable (e.g. evaluate the precision of the instrument, the magnitude of the systematic and random error, the within and between subject variability, etc.). Furthermore, the sensitivity of the marker to characterize a specific stage of the pathology should be established. For example, early markers of AD may be sensitive to the asymptomatic stage or the MCI stage and remain

stable during the dementia stage, while late markers of AD may only exhibit variations once the dementia stage is reached (Frisoni, 2012).

In this thesis we focus on the second direction. In particular, our goal is to evaluate the potential use of MEG to produce reliable biomarkers of the MCI stage. Although MEG is not the most popular approach to the study of MCI/AD, it could provide promising biomarkers. Contrary to CSF and PET measures, it is completely non-invasive and escapes lumbar punctures and radioactivity side effects. Moreover it provides an interesting insight into brain functioning, since it measures neural activity directly, with excellent temporal resolution. It has additionally been proven to be sensitive to AD-related changes (section 1.2.2). In this work we follow two distinct approaches. We first compare the MEG resting state power spectrum and functional connectivity in MCI patients and their age matched controls, and look for differences between both populations samples (Chapter 3). Then, we quantify the test-retest reliability of MEG spectral and connectivity measures by examining their within- and between-subject variability (Chapter 4).

Chapter 2

MEG measurements and analysis

In Chapter 1 we introduced neuroimaging and formulated our objective to evaluate the potential use of MEG spectral and functional connectivity measures in producing reliable biomarkers of MCI. In this chapter we introduce MEG measurements, electrophysiological activity and the analysis pipeline that is used throughout Chapters 3 and 4. MEG systems measure tiny magnetic fields that result from coherent neural firing. These measurements contain a variety of electrophysiological rhythms, but are also contaminated with unwanted magnetic fields. Although magnetically shielded rooms and the use of gradiometers reduce greatly this noise, MEG recordings remain contaminated with non-brain signals. We deal with this issue when preprocessing: a great amount of noise is eliminated with a signal space separation filter and then ocular, muscular and jump artifacts are located and all artifacted segments are excluded from the subsequent analysis. Once clean segments of data are obtained, we aim at determining the neural currents that generated the sensor-level measured data. This is called source reconstruction, and requires (1) a forward model that determines how fields propagate from an original current to the MEG sensors, and (2) an inverse model that estimates the original current distribution from its resulting MEG measurements. Source reconstruction can then be employed to estimate the power distribution and time dynamics of the distinct electrophysiological brain rhythms. Alternatively, a functional connectivity analysis can be performed, which assesses statistical dependencies between brain regions and examines the coordinated activity of the brain.

2.1 Introduction to MEG

2.1.1 Electrophysiological basis of MEG signals

MEG detects magnetic fields induced by electrical currents in the brain, which can be generated by a variety of different neural processes such as action potentials, synaptic events, post-synaptic potentials, calcium spikes or fluctuations in glia (Buzsáki et al., 2012). However, the main generators of the detectable MEG/EEG signal are thought to be post-synaptic potentials, as the other processes either generate low magnitude fields or they do not add into a measurable signal (Papanicolaou, 2009; Lopes da Silva, 2010). For instance, action potentials are strong and rapid changes in membrane potential that propagate along a neuron's axon, but they are so fast (around 1-2ms) that they are unlikely to synchronize over a population of neurons. Additionally, they can be described as quadrupoles, which produce fields that decay rapidly with distance (proportional to $1/r^3$ vs. proportional to $1/r^3$ for dipolar fields), so that their contribution to EEG/MEG is negligible (Milstein and Koch, 2008).

At a chemical synapse, when an action potential reaches a presynaptic neuron, neurotransmitters that can either excite or inhibit the postsynaptic neuron are released. When an excitatory synapse is activated, positive ions flow inwards the postsynaptic neuron, creating an active sink at the level of the synapse and a membrane depolarization. Conversely, when an inhibitory synapse is activated, either negative ions flow inwards the postsynaptic neuron or positive ions flow outwards the postsynaptic neuron, creating an active source at the level of the synapse and causing a membrane hyperpolarization. In both cases a primary current propagates through the dendrite, and secondary or passive currents flow through the extracellular medium to ensure electroneutrality.

With this procedure, small currents can be generated at the many dendrites of a neuron that propagate towards the soma. According to (Hämäläinen et al., 1993), for each dendrite, the strength of the postsynaptic current decays exponentially as it separates from the synapse, and it can be modeled as a really small dipole, with a dipole moment $Q = \lambda I$, where λ is the constant rate of the exponential decay, which lies typically around 0.1-0.2mm for a cortical neuron, and I is the post-synaptic current, which is usually $10^2 - 10^3$ pA.

The neuron's geometry is now a crucial factor that determines whether these post-synaptic currents add up into a non vanishing total dipole moment. For example, spherically symmetric neurons that can be found in thalamo-cortical modules have dendrites that emanate from the soma in all directions (Buzsáki et al., 2012). Assuming that there is no prominent direction of presynaptic firing for these cells, the small

dendritic currents would be distributed in a spherically symmetric fashion, producing a closed field configuration and no measurable signal. It is considered that the EEG/MEG signals are mainly generated by pyramidal neurons in the cortex (Baillet et al., 2001; Lopes da Silva, 2010). A pyramidal neuron has a long apical dendrite which integrates the currents generated at many synapses (see Figure 2.1). Moreover, pyramidal neurons are arranged in the cerebral cortex in a regular fashion, with apical dendrites oriented parallel to each other and perpendicular to the surface of the cortex. This enables a spatial summation of the apical dendrite currents over neighboring neurons.

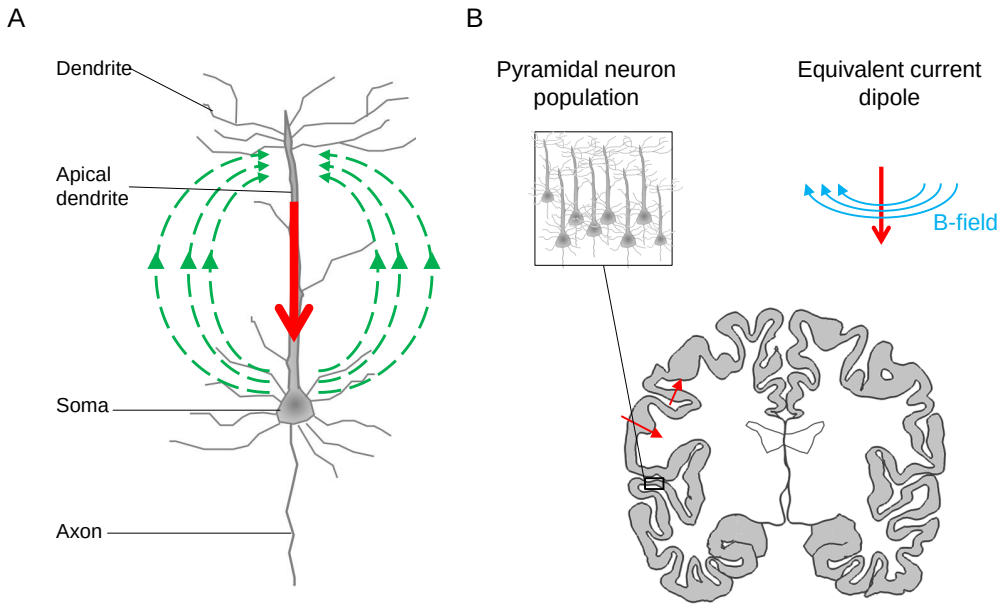

Figure 2.1: Electrophysiological basis of MEG signals. A. Pyramidal neuron, which is composed of many dendrites, a single apical dendrite, a soma and an axon. A primary intracellular current (red) propagates along the apical dendrite and secondary or passive currents (green) flow though the extracellular space. B. A population of pyramidal neurons in the cortex that is activated synchronously produces a net current in the direction of their apical dendrites. This can be modeled as an equivalent current dipole (red): a small current that generates a magnetic field (blue) around its axis.

Apart from this spatial summation, temporal summation is needed in order to produce a measurable signal. This means that MEG measures does not detect the activity of individual neurons. Instead, it measures the activity of a population of neurons that are arranged parallel to each other and excited synchronously. Around

$50 \cdot 10^3$ synchronously firing neurons may be necessary to produce a net current dipole moment that is intense enough to be detected with EEG/MEG (Murakami and Okada, 2006).

2.1.2 Electrophysiological brain rhythms

The coherent neural firing gives rise to a variety of electrophysiological rhythms, which are now introduced. In 1929 Hans Berger discovered prominent oscillations at approximately 10Hz in the brain, which he named alpha oscillations (Berger, 1929). Since then, the oscillatory nature of electrophysiological activity has become evident, and different rhythms have been discovered in human and animal studies, ranging from the infraslow (<1Hz) to the ultrafast (>100Hz). The most commonly employed frequency bands in human cognitive studies are delta (0.5-4Hz), theta (4-7Hz), alpha (8-12Hz), beta (13-30Hz) and gamma (>30Hz) (Lopes da Silva, 2013; Jafarpour et al., 2013; Engel and Fries, 2010), as shown in Figure 2.2. Electrophysiological activity is always oscillatory, even during resting state, sleep, or the performance of externally-driven tasks. However, the intensity and connectivity of brain rhythms change with the condition, so that brain rhythms seem to be functionally distinct and relevant, as is introduced below.

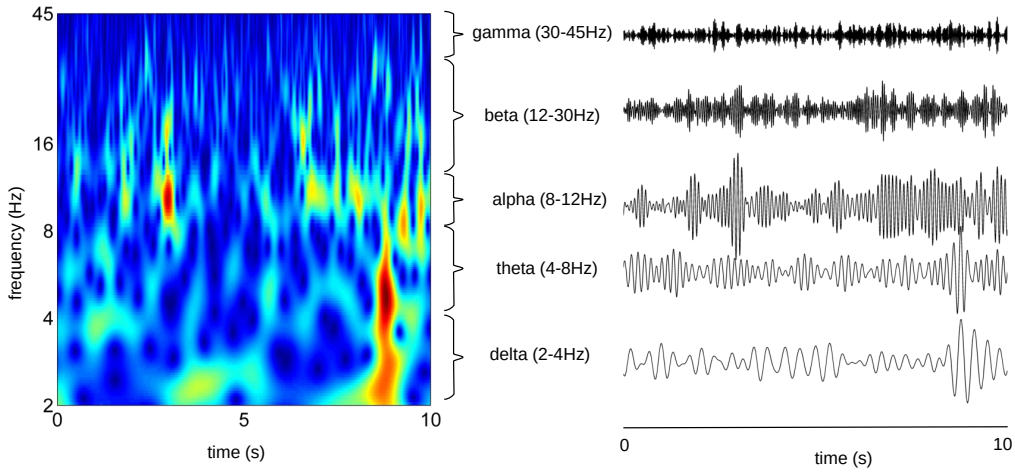

Figure 2.2: Electrophysiological brain rhythms. Spectrogram of a resting state recording. Wavelet power is represented as a function of time and frequency (blue: low power, red: high power). The frequency spectrum consists in separate brain rhythms: delta, theta, alpha, beta and gamma, which have different time-dynamics.

Functional significance

Oscillatory activity at different frequency bands seems to be involved in perceptual, sensorimotor and cognitive functions (Klimesch, 1999; Başar et al., 2001). In general, slower rhythms, such as delta, theta and alpha, which extend over wide cortical regions, have been linked to the coordination and integration of different brain regions in long temporal windows. In contrast, faster rhythms (beta and gamma), are believed to be responsible for a local and faster cortical processing (von Stein and Sarnthein, 2000; Knyazev, 2012; Harmony, 2013). Delta, theta, alpha, beta and gamma oscillations are now separately introduced.

Delta

Delta activity has been involved in basic functions such as deep sleep, heart rate, motivational processes or fetal and infant development (Platt and Riedel, 2011; Jurysta et al., 2005; Scher, 2008; Knyazev, 2007). As these are early processes both phylogenetically and ontogenetically, some authors believe that delta activity could represent evolutionary old processes (Knyazev, 2012). While sleep and sleep disorders are the most popular topics for the study of delta in adult humans, much interest has also been drawn to gestation and early child development. In fact, delta oscillations are dominant during the third trimester of gestation (Scher, 2008), and decrease progressively during childhood (John et al., 1980). Abnormally high delta power in children is indicative of various developmental disorders such as attention-deficit/hyperactivity disorder (Barry et al., 2003). Additionally, delta relates to motivation, with high delta powers found during hunger and drug craving (Knyazev, 2007, 2012).

Aside from these basic functions, delta activity has been considered relevant in cognitive tasks: several studies have found increased delta power both during concentration (i.e. mental calculation, semantic tasks) and in attentional tasks (Fernández et al., 1995; Harmony et al., 1996; Harmony, 2013). High delta power could also indicate different pathological states, such as tissue damage (Gloor et al., 1977; Spironelli and Angrilli, 2009), schizophrenia (Boutros et al., 2008), depression (Korb et al., 2008), Parkinson's disease (Zijlmans et al., 1998) and Alzheimer's disease (Babiloni et al., 2004).

Theta

Theta activity has been predominantly studied in the hippocampus of rodents, since it seems to play an important role in spatial navigation and learning. Theta activity dominates the hippocampal LFP of moving rodents and it increases

during locomotion or orienting (Kahana, 2006). Hippocampal theta, along with the firing of specific neurons called "place cells", encode a moving rat's location (O'Keefe and Recce, 1993; Jensen and Lisman, 2000). In humans, some iEEG studies have shown similar results. Theta activity increased when subjects were engaging in a taxi driver game, in which they virtually drove through a town searching for passengers and delivering them to their destination (Ekstrom et al., 2005).

Theta activity has also been involved in cognitive processing during memory tasks. Theta power and coherence increase in memory tasks during successful encoding and recognition, as shown repeatedly over the past years (Klimesch, 1999; Sederberg et al., 2003; Kahana, 2006; Khader et al., 2010). Additionally, theta coherence correlates with task load (Deiber et al., 2007; Cashdollar et al., 2009).

Alpha

Alpha waves are the first documented brain oscillations. Their discovery dates from the late 1920s, when Hans Berger recorded large oscillations at approximately 10Hz in the brain of his human patients (Berger, 1929). In fact, alpha oscillations are the largest oscillations in the resting state brain, and they have higher amplitude in the occipital lobe when subjects close their eyes. This led scientists to believe that alpha oscillations were a mere representation of the idling brain. However, this vision has rapidly faded, as the role of alpha oscillations in perception and cognition has become clear (Bonnefond and Jensen, 2013; Lopes da Silva, 2013).

Alpha oscillations are involved in the perception of visual stimuli. First of all, alpha power is strongly modulated by eye opening, which triggers a decrease in alpha activity. Moreover, attention to visual stimuli causes changes in alpha activity. When a subject attends to the left hemifield, alpha power decreases in the right occipito-parietal cortex (responsible for the left hemifield) while it increases in the left occipito-parietal cortex (responsible for the right hemifield) (Worden et al., 2000; Rihs et al., 2009). This pattern of alpha power decrease over task-relevant regions and increase over task-irrelevant regions seems to be functionally important, as it relates to task performance (Ergenoglu et al., 2004; Thut et al., 2006) and to neural firing rate (Haegens et al., 2011). This led to the hypothesis that alpha power has an inhibiting role (Lopes da Silva, 2013). Using transcranial magnetic stimulation (TMS) at different frequencies, Romei et al. (2010) could test this hypothesis. Authors found that the detection

of visual stimuli contralateral to the TMS site was impaired when stimulating over occipito-parietal areas at 10Hz, thereby showing that alpha oscillations can cause inhibition over the affected areas.

Beta

Beta band oscillations have been traditionally linked to motor control (Engel and Fries, 2010). First, beta amplitude decreases in the motor cortex prior to and during both voluntary and imagined movements (de Lange et al., 2008), which has found application in the design of brain computer interfaces (Bai et al., 2008; Pasqualotto et al., 2012). This amplitude decrease could be functionally relevant since both high beta amplitude and 20Hz TMS slow down voluntary movements (Gilbertson et al., 2005; Pogosyan et al., 2009). Second, the function of high beta amplitude could be the maintenance of a steady-state motor output, since beta amplitude increases in holding periods and tonic contraction and relates to the performance in postural tasks (Androulidakis et al., 2006; Engel and Fries, 2010).

Beta is believed to have a similar role in cognition (Engel and Fries, 2010). According to this theory, high beta amplitude would contribute to maintaining the ongoing state in perceptual and cognitive tasks. In fact, tasks that are mainly stimulus-driven usually produce a decrease in beta activity while tasks that are rather endogenous relate to beta increases (Iversen et al., 2009). Higher amplitudes were also found to correlate with faster responses to visual stimuli (Kamiński et al., 2012).

Gamma

Gamma activity is thought to represent active sensory and cognitive processing (Jensen et al., 2007; Jerbi et al., 2009). It increases during a variety of tasks, such as auditory (Crone et al., 2001), visual (Hoogenboom et al., 2006), sensorimotor (Aoki et al., 1999), attentional (Sokolov et al., 2004), language (Dalal et al., 2009) or memory (Pesaran et al., 2002) tasks. It also seems to relate to the task demands, and was for instance found to increase with memory load (Howard, 2003). Additionally, gamma usually activates in task-specific small areas, in opposition to slower brain rhythms which show coherent oscillations in widespread regions of the brain (Jerbi et al., 2009).

Mu

Mu rhythm overlaps in frequency with alpha and beta, although historically it has been considered separately. Mu oscillations are found over rolandic regions and decrease with limb movements and tactile stimulation (Tiihonen et al.,

1989; Hari and Salmelin, 1997). Mu has also been often considered in analogy to the posterior alpha rhythm which decreases by eye opening.

Cross-frequency coupling

In previous sections, brain rhythms have been described separately. This reflects the way most studies have been carried out, but it also constitutes a simplified model of the actual neural processes. Not only may different rhythms be responsible for the same function, but their interaction may be essential. This interaction is called cross-frequency coupling (CFC), and is mediated by various processes. Phase-amplitude CFC is particularly important from a physiological perspective (Canolty and Knight, 2010): the phase of lower frequency is thought to modulate the excitability of the region whereas the higher frequency amplitude is thought to represent active neural processing. One popular example is that of theta-gamma CFC in the hippocampus, which seems to relate to memory and learning. It has been found in rats performing a T-maze task during navigation and decision making (Tort et al., 2008), and in humans during maintenance of multiple items in a working memory task (Axmacher et al., 2010).

Biophysical origin

The actual biophysical mechanisms responsible for oscillatory activity are unclear. Some believe that they can be generated locally, while others point out that feedback loops including other regions are necessary to generate them. While some neurons can oscillate intrinsically (Steriade et al., 1990), this is not considered to be the sole responsible for brain oscillations. Different mechanisms account for the distinct brain rhythms, and simulations, in-vitro and in-vivo studies have provided rhythm-specific theories. For instance, gamma oscillations are thought to be generated locally, and to be controlled by GABAergic interneurons (Mann and Paulsen, 2007; Vierling-Claassen et al., 2010). In contrast, larger circuitry is believed to be needed for alpha oscillations. Earlier studies highlighted the role of thalamus as a pacemaker of alpha oscillations (Hughes and Crunelli, 2005), while others have pointed out the existence of cortical generators (Bollimunta et al., 2008). Computational models that include cortical and thalamic nuclei have shown that both thalamo-cortico-thalamic and cortico-cortical circuits are needed to explain alpha amplitude and frequency responses (Hindriks and van Putten, 2013).

2.1.3 MEG systems

An MEG system is a device that captures the magnetic fields produced by the small neuronal currents. This is a tricky task, since the brain magnetic fields are extremely small. On the one hand, the brain and the MEG system have to be shielded from the huge ambient magnetic fields, using a magnetically shielded room. These ambient magnetic fields are in fact $10^4 - 10^{10}$ times higher than brain fields. On the other hand, usual magnetic sensors are not adequate for this task, since they are not sensitive to such small variations in magnetic field. Cohen performed in 1968 the first successful MEG recording using a 1-million turn coil at different head positions (Cohen, 1968). Although he did not reach a good sensitivity, he was able to detect human alpha oscillations, which are the strongest oscillations in resting state condition, when subjects close their eyes. MEG technology has rapidly evolved ever since, and modern MEG systems have achieved much better sensitivity using SQUID (superconducting quantum interference device) based sensors.

Magnetically shielded room

Neural magnetic fields are several orders of magnitude weaker than ambient magnetic fields. These ambient fields include the Earth's magnetic field and the ones produced by different mechanical or electrical devices that can be found in modern buildings (i.e. motor, air conditioning, etc.), as shown in Figure 2.3. Therefore, in order to measure the weak neural fields, the MEG system needs to be shielded from ambient fields. This is done by placing the MEG system inside a magnetically shielded room (MSR). It is to note that the MSR does not eliminate completely interfering magnetic fields. Firstly, some external fields penetrate the MSR walls. For instance, MEG spectra show a strong peak at 50Hz and harmonics, which originates in the power line. Secondly, some interfering fields are generated inside the MSR. In fact, biological activity such as eye movements, muscular activity or heart beating generates magnetic fields. This is controlled for in the preprocessing stage of the MEG analysis.

MEG sensors

SQUID Kamerlingh Onnes discovered superconductivity in 1911 when examining the variation in electrical resistance of mercury at low temperatures. He found that, under a critical temperature T_c, mercury reached a state with null resistance (Kamerlingh Onnes, 1911). In 1933 Meissner and Ochsenfeld discovered that this superconducting state is also a state of perfect diamagnetism (Meissner and Ochsenfeld, 1933). This means that the magnetic field inside of a superconducting element is

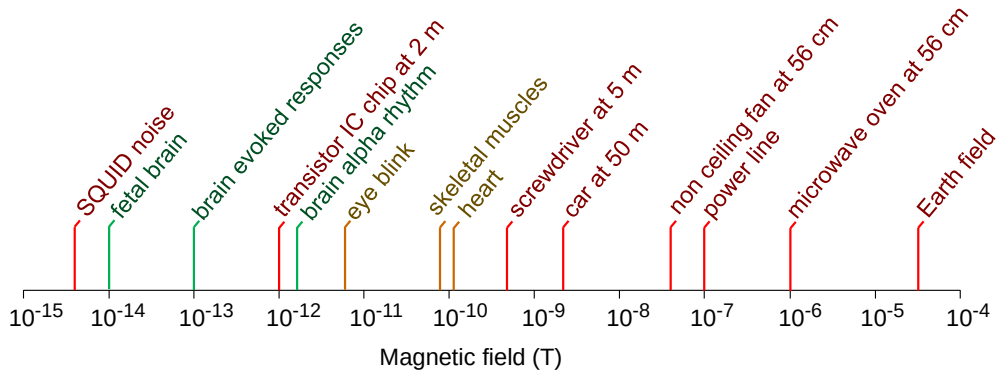

Figure 2.3: Intensity of environmental and biological magnetic fields. Neural magnetic fields are represented in green, biological interfering fields in orange and ambient fields in red. Intensity values are extracted from (Hämäläinen et al., 1993; Vrba, 2002; Fishbine, 2003; Portier and Wolfe, 1998).

zero. In fact, if a superconducting element is placed in an external magnetic field, an everlasting current circulates at the material's surface and shields its interior, provided that temperature, magnetic field and intensity do not exceed critical values (T_c, B_c and I_c) that would destroy the superconducting state. Superconductivity can be used to measure very small magnetic fields with the use of SQUIDs, which can be conceived as devices that convert magnetic flux to voltage. Modern MEG systems use DC SQUIDs that consist in a loop of superconducting element (i.e. niobium) that is separated into two parts united by weak links or Josephson junctions. If a constant bias current I_b enters the superconducting loop, it creates a voltage across it that oscillates with increasing magnetic flux across the loop (Jenks et al., 1997). This $V = f(B)$ dependence is indirectly employed in a negative feedback configuration that maintains a fixed operating point in the SQUID. The feedback loop compensates the external magnetic field and provides an estimation of its value (Vrba and Robinson, 2001; Parkkonen, 2010).

Magnetometers and gradiometers The SQUID does not measure directly the magnetic field outside the head. The magnetic field is first detected by a pick-up coil that has larger area than the SQUID (and thus larger flux and larger signal to noise ratio). First, neural magnetic fields reach this superconducting pick-up coil, and shielding currents are created that then generate a magnetic flux across the SQUID loop. Therefore, the SQUID receives a signal that is proportional to the magnetic flux across the pick-up coil. For a coil in the xy plane, the whole pick-up coil + SQUID + negative feed-

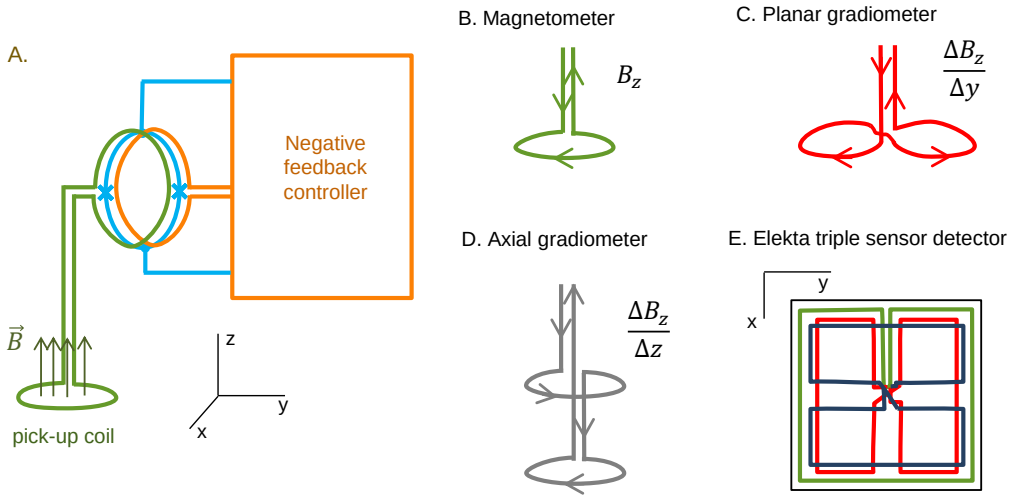

Figure 2.4: MEG sensors. A: Brain magnetic fields are measured with a pick-up coil (green). Magnetic flux is transformed and applied into the SQUID (blue). A negative feedback controller (orange) generates a correcting magnetic field that keeps the SQUID at a certain operating point. B: A magnetometer consists in a pick-up coil and measures the magnetic flux $\Phi = \oint \mathbf{B} \cdot d\mathbf{s} \propto B_z$. C: A planar gradiometer measures spatial derivative of the flux in a transversal direction x or y. D: An axial gradiometer measures spatial derivative of the magnetic flux in the longitudinal z-direction. E: Elekta triple sensor unit combines a magnetometer (green), a planar gradiometer in the y-direction (red) and a planar gradiometer in the x-direction (blue). Modified from (Elekta-Neuromag, 2005)

back system measures then a signal proportional to the flux $\Phi = \oint \mathbf{B} \cdot d\mathbf{s} \approx B_z \cdot S$, where S is the area of the pickup coil. This is however not the only possible configuration. Other sensors called gradiometers measure spatial derivatives of B_z, by using a pickup and a compensating coil (see Figure 2.4). This is useful since the spatial derivative of B_z is less sensitive than B_z to distant magnetic sources, such as non-biological sources (i.e. power line, air conditioning) or muscular and heart activity. If both coils are placed in two parallel planes along the z-axis, $\frac{\Delta B_z}{\Delta z}$ is measured, and the sensor is called axial gradiometer. If both coils are placed in the same xy plane, $\frac{\Delta B_z}{\Delta x}$ or $\frac{\Delta B_z}{\Delta y}$ are measured, and the sensor is called planar gradiometer.

Cryogenics

To reach their superconducting state, MEG sensors are placed inside a Dewar flask filled with liquid helium at its boiling temperature (4.2K). The Dewar flask is thermally insulated, so that the outside of the MEG helmet remains at room temperature. He-

lium is refilled periodically (i.e. once a week) to compensate for helium gas constantly flowing out of the flask, which accounts for the high economical cost of MEG recordings.

Description of our MEG system

All MEG experiments in this dissertation were performed with an Elekta Neuromag Vectorview System with 306 sensors (see Figure 2.5). It has 102 detector units spread in a whole head MEG helmet and separated on average 34 mm. Each detector unit contains one magnetometer and two planar gradiometers in orthogonal directions (see Figure 2.4-E). The system is shielded from external fields with a Vacuumschmelze (Hanau, Germany) MSR. The system enables the continuous determination of the head position relative to the sensor array (and therefore the possibility to correct for movements). For that, three anatomical reference points are located that define the head reference frame: nasion and left- and right- preauricular points. Then, four coils are attached to the scalp and their position relative to these three reference points is determined with a Polhemus digitizer (FASTRAK®) prior to the MEG recording. These coils produce sinusoidal magnetic fields at distinct frequencies, so that the MEG measurements at these particular frequencies can be used to continuously estimate the position of the coils relative to the MEG sensor array (Uutela et al., 2001). This ultimately means that one can continuously switch from device to head coordinate frame, and vice versa.

2.2 Preprocessing of MEG raw data

2.2.1 Signal space separation (SSS)

The signal space separation algorithm (SSS) roughly separates magnetic fields originating from inside and outside the head, and is applied in a first denoising step to MEG raw data. SSS and its spatiotemporal version tSSS are implemented in the Maxfilter software (Elekta Oy, Helsinki, Finland) and they are routinely applied to MEG data recorded with Elekta systems. Their rationale is now briefly described, following (Taulu, 2008; Taulu and Kajola, 2005).

First, we assume the presence of three separate volumes: (see Figure 2.6): (1) an inner volume containing the currents $\boldsymbol{j}_{in}$, (2) an intermediate volume which includes the MEG sensors and is current-free and (3) an outer volume containing currents $\boldsymbol{j}_{out}$.

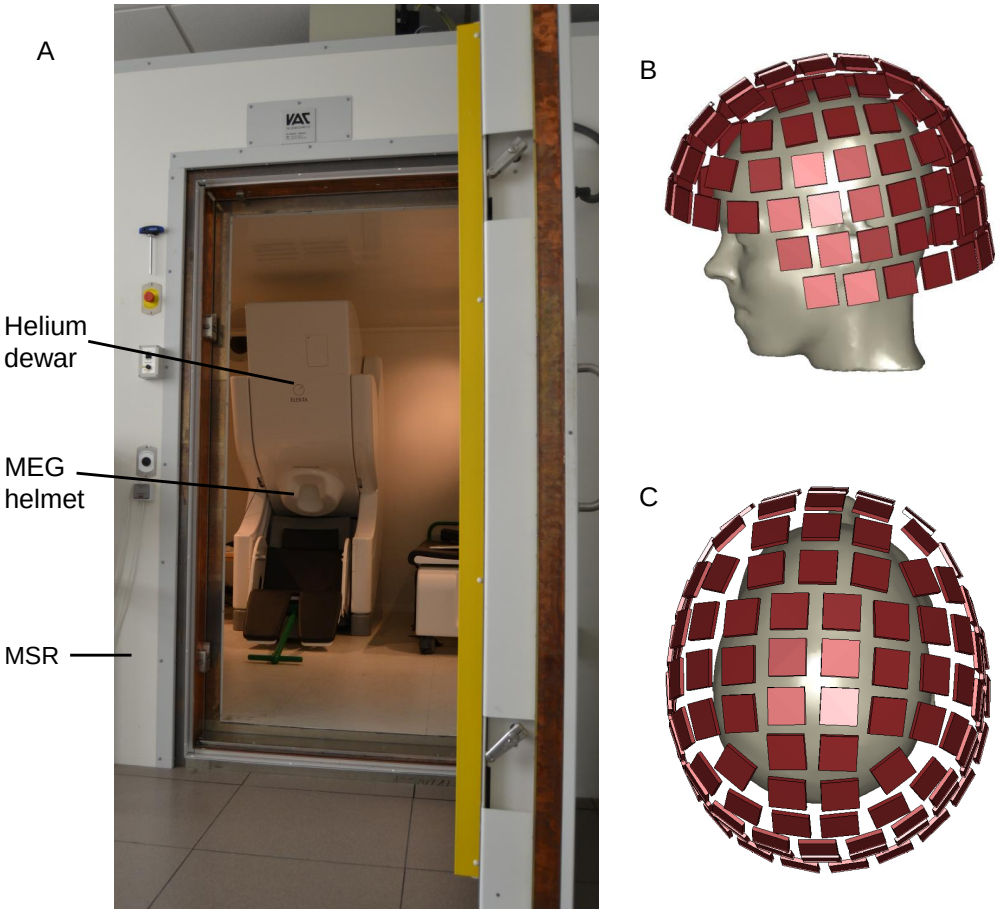

Figure 2.5: Elekta Neuromag Vectorview system. A. The MEG helmet is surrounded by liquid helium contained in a Dewar flask. The whole system is placed inside a MSR (magnetically shielded room). B,C. MEG sensor layout viewed from the side (B) and from the top (C). Each red square represents a triple sensor containing a magnetometer and two planar gradiometers.

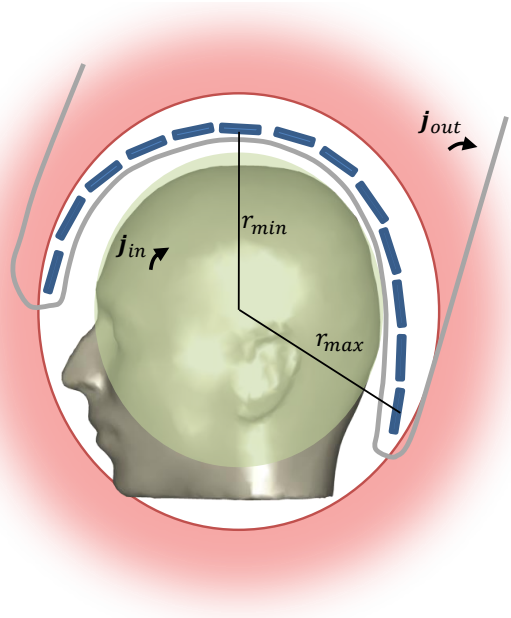

Figure 2.6: Illustration of the SSS method. Three distinct volumes are defined, using a reference point at the center of the head (or at the center of the MEG helmet). r_{min} and r_{max} are defined as the minimum and maximum distances between this reference point and the MEG sensors. Brain currents $\boldsymbol{j}_{in}$ are assumed to lie inside a sphere $r < r_{min}$, and external currents $\boldsymbol{j}_{out}$ are assumed to lie in the volume $r > r_{max}$. No currents should exist in the intermediate volume $r_{min} < r < r_{max}$. Adapted from (Elekta-Neuromag, 2005).

Then, the magnetic field $\mathbf{B}(\boldsymbol{r})$ at a source-free sensor position $\boldsymbol{r}$ is:

$$\boldsymbol{B}(\boldsymbol{r}) = \boldsymbol{B}_{in}(\boldsymbol{r}) + \boldsymbol{B}_{out}(\boldsymbol{r}) \tag{2.1}$$

where $\boldsymbol{B}_{in}$ and $\boldsymbol{B}_{out}$ are the magnetic fields generated by $\boldsymbol{j}_{in}$ and $\boldsymbol{j}_{out}$ respectively.

As proven in (Taulu and Kajola, 2005), under the quasi-static approximation, $\boldsymbol{B}_{in}$ and $\boldsymbol{B}_{out}$ at a sensor position $\boldsymbol{r}$ can be written as series expansions in spherical coordinates:

$$\boldsymbol{B}_{in}(\boldsymbol{r}) = -\mu_0 \sum_{l=0}^{\infty} \sum_{m=-l}^{l} \alpha_{lm} \frac{\boldsymbol{\nu}_{lm}(\theta,\varphi)}{r^{l+2}} \tag{2.2}$$

$$\boldsymbol{B}_{in}(\boldsymbol{r}) = -\mu_0 \sum_{l=0}^{\infty} \sum_{m=-l}^{l} \beta_{lm} r^{l-1} \boldsymbol{\omega}_{lm}(\theta,\varphi) \tag{2.3}$$

where $\boldsymbol{\nu}_{lm}(\theta,\varphi)$ and $\boldsymbol{\omega}_{lm}(\theta,\varphi)$ are modified vector spherical harmonics.

By truncating the previous series expansions to $l \leq L_{in}$ in (2.2) and $l \leq L_{out}$ in (2.3) and applying the previous formulae at all the sensor locations, the $N_{coils} \times 1$ matrix $\boldsymbol{\phi}$ containing the magnetic flux at the sensor locations can be written as:

$$\boldsymbol{\phi} \approx \sum_{l=1}^{L_{in}} \sum_{m=-l}^{l} \alpha_{lm} \boldsymbol{a}_{lm} + \sum_{l=1}^{L_{out}} \sum_{m=-l}^{l} \beta_{lm} \boldsymbol{b}_{lm} \tag{2.4}$$

where $\boldsymbol{a}_{lm}$ and $\boldsymbol{b}_{lm}$ are $N_{coils} \times 1$ vectors that result from applying (2.2) and (2.3) to the sensor positions. This summation contains

$$n = (L_{in} + 1)^2 + (L_{out} + 1)^2 - 2 \tag{2.5}$$

terms. L_{in}=8 and L_{out}=3 are used as default values in Maxfilter, since they are considered to produce a negligible residual (Taulu and Kajola, 2005; Taulu et al., 2005). The summation (2.4) can be written in matrix form:

$$\boldsymbol{\phi} \approx \boldsymbol{S}\boldsymbol{x} = \begin{bmatrix} \boldsymbol{S}_{in} & \boldsymbol{S}_{out} \end{bmatrix} \begin{bmatrix} \boldsymbol{x}_{in} \\ \boldsymbol{x}_{out} \end{bmatrix} \tag{2.6}$$

where $\boldsymbol{S}$ is a $N_{coils} \times n$ matrix which contains $\boldsymbol{a}_{lm}$ and $\boldsymbol{b}_{lm}$ for the (l, m) pairs, and $\boldsymbol{x}_{in}$ and $\boldsymbol{x}_{out}$ are vectors which contain the α_{lm} and β_{lm} coefficients.

Once $\boldsymbol{S}$ is computed from the sensors' coordinates, $\boldsymbol{x}$ can be estimated as:

$$\hat{\boldsymbol{x}} = \begin{bmatrix} \boldsymbol{x}_{in} \\ \boldsymbol{x}_{out} \end{bmatrix} = \boldsymbol{S}^{-1}\boldsymbol{\phi} \tag{2.7}$$

Finally, a cleaner version of the MEG measurements, without the external contribution of $\boldsymbol{j}_{out}$, is:

$$\hat{\boldsymbol{\phi}}_{in} = \boldsymbol{S}_{in}\hat{\boldsymbol{x}}_{in} \tag{2.8}$$

Another version of the SSS, called spatiotemporal-SSS or tSSS, further refines the previous model by adding the time dimension, so that errors in the SSS model can be detected as strong correlations between inside and outside components (Taulu and Simola, 2006). The rationale behind this is that if deviations $\boldsymbol{\phi}_\epsilon$ from (2.6) are included, $\boldsymbol{\phi} = \boldsymbol{S}\boldsymbol{x} + \boldsymbol{\phi}_\epsilon$, and then the estimation of $\boldsymbol{x}$ becomes:

$$\hat{\boldsymbol{x}} = \boldsymbol{S}^{-1}\boldsymbol{\phi} = \boldsymbol{S}^{-1}\boldsymbol{S}\boldsymbol{x} + \boldsymbol{S}^{-1}\boldsymbol{\phi}_\epsilon = \boldsymbol{x} + \begin{bmatrix} \boldsymbol{x}_{in,\epsilon} \\ \boldsymbol{x}_{out,\epsilon} \end{bmatrix} \tag{2.9}$$

Since $\boldsymbol{x}_{in,\epsilon}$ and $\boldsymbol{x}_{out,\epsilon}$ originate from the same $\boldsymbol{\phi}_\epsilon$, they are expected to be temporally

correlated, while the true $\boldsymbol{x}_{in}$ and $\boldsymbol{x}_{out}$ are temporally independent and uncorrelated.

tSSS has been applied to MEG recordings in all experiments presented in the following chapters, using the default Maxfilter parameters. This tSSS also allows for movement compensation, by continuously tracking the position of the head relative to the MEG sensor array and projecting the signals into the original sensor positions. Therefore, MEG sensor positions can be considered as fixed throughout the MEG measurements. Beforehand, the MEG sensor data are visually inspected for broken and noisy channels, and bad channels are excluded from the estimation of the SSS components. However, SSS components are projected to all MEG sensors, and all 306 sensors can be used in the subsequent analysis.

2.2.2 Artifact detection

After the tSSS filtering, MEG measurements are scanned for artifacts. This procedure can be done automatically, visually or combining both methods. Artifacts may arise from biological (eye movements, blinking, or contraction of cardiac and skeletal muscles) or external sources (fields originating outside the MEG, or electronic artifacts in the MEG system).

Artifact prevention is crucial to achieve good quality MEG recordings. Firstly, subjects should remove all objects containing ferromagnetic particles before entering the MSR. These include evident metal objects (phones, keys, rings, etc.) and also products that are apparently non-metallic but contain tiny ferromagnetic particles, such as some sorts of make-up and clothing. Therefore, subjects with permanent metals in their bodies (non-removable dental work, pacemakers, metal implants or even some sorts of tattoos) should be excluded from MEG studies. Secondly, subjects should be instructed to sit quietly and relaxed throughout the measurements, and avoid tensing their muscles (especially jaw and shoulders) or moving.

However, even when dealing with appropriate metal-free subjects that sit completely relaxed, some artifacts arise in MEG signals. These artifacts have to be located (for instance automatically with the FieldTrip software (Oostenveld et al., 2011)) and excluded from any subsequent analysis.

Ocular artifacts

Ocular artifacts produce fatal interference in MEG signals, since eye movements and blinking generate strong magnetic fields. They are usually easily distinguished in MEG frontal sensors. However, to detect them more accurately, electrooculogram (EOG) signal can be measured by placing two electrodes surrounding one eye (above and below for vertical EOG, and to the left and right

side for horizontal EOG) and a third electrode as ground (usually at the earlobe). Deviations in the amplitude of the EOG channel indicate the presence of ocular artifacts.

Muscular artifacts

The contraction of skeletal muscles produces disturbing magnetic fields, which manifest as high frequency activity especially when muscles lie close to the MEG sensor array. Muscular artifacts may for instance be detected as time intervals with higher amplitude than usual in the 110-140 Hz range.

Sensor artifacts

MEG sensors may transiently malfunction, creating artificial jumps in MEG signals. These artifacts are easily identified visually as abrupt changes in sensor measurements. Quantitatively, jumps may be seen as extreme values in the derivative of a smoothed MEG signal.

External artifacts

The tSSS filtering does not completely remove the fields generated outside the MSR. For instance, the power line at 50 Hz (or 60 Hz in some countries) contaminates MEG signals. For this reason, spectral content at 50 Hz and harmonics is not used in MEG analysis, either by focusing in a band that does not contain these frequencies (i.e. from 1 to 40 Hz), or by using broader frequency range for analysis but applying notch filters at 50, 100 and 150 Hz to eliminate the power line noise. Additionally, low frequency content of MEG recordings (i.e. <1 Hz) is highly contaminated, and is usually filtered out from the MEG data analysis. Movements of large ferromagnetic objects in the neighborhood of the MEG system (elevators, car, chairs, etc.) may produce such intense low frequency noise.

2.3 Source reconstruction

MEG preprocessing yields clean MEG sensor fields that are generated by neural currents. The next step in our MEG analysis pipeline is called source reconstruction, and consists in determining the dynamics and topography of these neural currents, as illustrated in Figure 2.7. Source reconstruction is an inverse problem: it consists in estimating the distribution of currents within the brain volume that generated a given set of MEG experimental measurements. This inverse problem cannot be solved directly. In fact, it requires solving the forward problem beforehand: find the

MEG sensor measurements that result from a given distribution of neural currents. In this section, inverse and forward problems are introduced, as well as some common models to solve them.

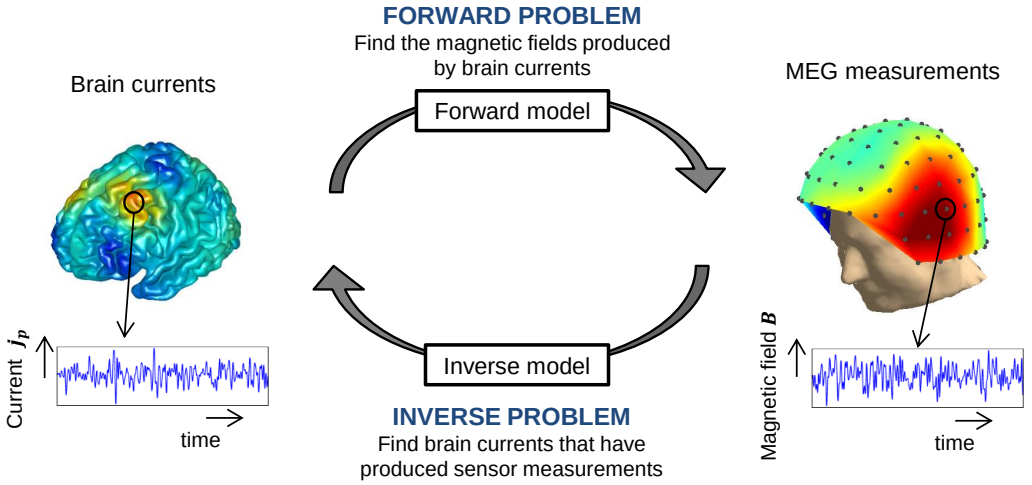

Figure 2.7: Forward and inverse problems. The forward problem finds the magnetic field produced by a known distribution of brain currents, while the inverse problem finds the brain currents that originated the MEG measurements.

2.3.1 General formulation

The relation between brain currents and magnetic fields is governed by Maxwell's equations. For EEG/MEG analysis, a few assumptions are employed to obtain a set of simplified equations that relate neural currents and EEG/MEG sensor measurements. In this text, vectors and matrices are represented with bold characters and scalars with plain characters.

Assumption 1: Brain currents and field measurements have low frequency (< 150 Hz) and travel short distances (< 50 cm), so that the quasi-static approximation of Maxwell's and continuity equations are valid (Heller and van Hulsteyn, 1992; Hämäläinen et al., 1993). Under this assumption, Ampère's Law can be written as:

$$\nabla \times \boldsymbol{B}(\boldsymbol{r}) = \mu_0 \left(\boldsymbol{j}(\boldsymbol{r}) + \epsilon \frac{\partial \boldsymbol{E}(\boldsymbol{r})}{\partial t} \right) \approx \mu_0 \boldsymbol{j}(\boldsymbol{r}) \tag{2.10}$$

where $\boldsymbol{B}(\boldsymbol{r})$, $\boldsymbol{E}(\boldsymbol{r})$ and $\boldsymbol{j}(\boldsymbol{r})$ are the magnetic field, electric field and current density at point $\boldsymbol{r}$, respectively, $\mu_0 = 4\pi \dot{1}0^{-7}$Tm/A is the vacuum permeability and ϵ is the tissue permittivity. All media involved are non-magnetic (i.e. brain, skull, scalp), so

that $\mu(\boldsymbol{r}) = \mu_0$ is assumed for any $\boldsymbol{r}$. Biot Savart's law is therefore also valid:

$$\boldsymbol{B}(\boldsymbol{r}) = \frac{\mu_0}{4\pi} \int_G \boldsymbol{j}(\boldsymbol{r}') \times \frac{\boldsymbol{r} - \boldsymbol{r}'}{|\boldsymbol{r} - \boldsymbol{r}'|^3} d^3 r' \tag{2.11}$$

where G is a closed volume that encloses currents $\boldsymbol{j}(\boldsymbol{r}')$.

Under the quasi-static approximation, the time derivative in Faraday's law is also negligible:

$$\nabla \times \boldsymbol{E}(\boldsymbol{r}) = -\frac{\partial \boldsymbol{B}(\boldsymbol{r})}{\partial t} \approx 0 \tag{2.12}$$

One can therefore relate $\boldsymbol{E}(\boldsymbol{r})$ and the electric potential $V(\boldsymbol{r})$ by:

$$\boldsymbol{E}(\boldsymbol{r}) = -\nabla V(\boldsymbol{r}) \tag{2.13}$$

Finally, in the quasi-static approximation the continuity equation is:

$$\nabla \cdot \boldsymbol{j}(\boldsymbol{r}) = -\frac{\partial \rho}{\partial t} \approx 0 \tag{2.14}$$

In the EEG/MEG inverse problem, $\boldsymbol{j}(\boldsymbol{r}')$ is not directly the current source of interest. Instead, it represents the total current, which has a primary and a volume component:

$$\boldsymbol{j}(\boldsymbol{r}') = \boldsymbol{j}_p(\boldsymbol{r}') + \boldsymbol{j}_{vol}(\boldsymbol{r}') \tag{2.15}$$

$\boldsymbol{j}_p(\boldsymbol{r}')$ is the primary cellular current, which comprises the currents inside the neuron and across its membrane, and reflects the neural activity that we intend to reconstruct. In contrast, $\boldsymbol{j}_{vol}(\boldsymbol{r}') = \sigma(\boldsymbol{r}')\boldsymbol{E}(\boldsymbol{r}')$ is the return ohmic current and results from the macroscopic electric field $\boldsymbol{E}(\boldsymbol{r}')$.

Inserting (2.13) and (2.15) into (2.11) and (2.14), one obtains two main equations (Mosher et al., 1999; Stenroos and Sarvas, 2012):

$$\boldsymbol{B}(\boldsymbol{r}) = \frac{\mu_0}{4\pi} \int_G \left(\boldsymbol{j}_p(\boldsymbol{r}') - \sigma(\boldsymbol{r}')\nabla V(\boldsymbol{r}')\right) \times \frac{\boldsymbol{r} - \boldsymbol{r}'}{|\boldsymbol{r} - \boldsymbol{r}'|^3} d^3 r' \tag{2.16}$$

$$\nabla \cdot \left(\sigma(\boldsymbol{r}')\nabla V(\boldsymbol{r}')\right) = \nabla \cdot \boldsymbol{j}_p(\boldsymbol{r}') \tag{2.17}$$

G is often called the volume conductor, and encloses all currents $\boldsymbol{j}(\boldsymbol{r}')$. It is usually considered to be the head, assuming thereby that no currents reach the neck.

Solving the forward problem means calculating $\boldsymbol{B}(\boldsymbol{r})$ for a given distribution of $\boldsymbol{j}_p(\boldsymbol{r}')$. To do that, one can use equations (2.16) and (2.17), once the conductivity distribution $\sigma(\boldsymbol{r}')$ is known. In other words, one has to model the head and its conductivity

profile first, insert it into equations (2.16) and (2.17), and then use a numerical method to solve the problem.

The problem is then simplified by adding a further assumption:

Assumption 2: The primary current $\boldsymbol{j}_p(\boldsymbol{r}')$ can be modelled by N_{dip} point-like current dipoles with moments $\boldsymbol{q}_k$, $k = 1,2,\ldots,N_{dip}$ at positions $\boldsymbol{r}_k$.

$$\boldsymbol{j}_p(\boldsymbol{r}') = \sum_{k=1}^{N_{dip}} \boldsymbol{q}_k \delta(\boldsymbol{r}' - \boldsymbol{r}_k) \tag{2.18}$$

One can solve equations (2.16) and (2.17) for a single unit dipole at a given position $\boldsymbol{r}_k$, and then calculate the total field $\boldsymbol{B}(\boldsymbol{r})$ with the superposition principle. In fact, the goal of the forward problem is to find the 3×1 vectors $\boldsymbol{L}_{ik}$, called leadfields, that relate dipole k and sensor measurement i:

$$m_i(t) = \sum_{k=1}^{N_{dip}} \boldsymbol{L}_{ik} \boldsymbol{q}_k(t), \quad i = 1,2,\ldots,N_{sensors} \tag{2.19}$$

m_i relates directly to the magnetic field $\boldsymbol{B}(\boldsymbol{r})$ at the MEG sensor position. For magnetometers, $m_i = \int_S \boldsymbol{B}(\boldsymbol{r}) \cdot d\boldsymbol{s} \approx B_z(\boldsymbol{r}) \cdot S$, where S is the small surface of the pick-up coil. For gradiometers, $m_i = \int_{S_1} \boldsymbol{B}(\boldsymbol{r}) \cdot d\boldsymbol{s} - \int_{S_2} \boldsymbol{B}(\boldsymbol{r}) \cdot d\boldsymbol{s} \approx B_z(\boldsymbol{r}_1) \cdot S_1 - B_z(\boldsymbol{r}_2) \cdot S_2$, where S_1 and S_2 are the surfaces of the i-th gradiometer's pick-up coils, with center at positions $\boldsymbol{r}_1$ and $\boldsymbol{r}_2$.

(2.19) is usually expressed with matrices $\boldsymbol{M}$, $\boldsymbol{L}$ and $\boldsymbol{Q}$:

$$\boldsymbol{M} = \boldsymbol{L}\boldsymbol{Q} \tag{2.20}$$

where

$$\boldsymbol{M} = \begin{bmatrix} m_1(t = t_1) & \cdots & m_1(t = t_T) \\ \vdots & \ddots & \vdots \\ m_{N_{sensors}}(t = t_1) & \cdots & m_{N_{sensors}}(t = t_T) \end{bmatrix} \tag{2.21}$$

is a $N_{sensors} \times N_T$ matrix which contains the MEG measurements for all time samples $t = t_1, \cdots, t = t_T$,

$$\boldsymbol{L} = \begin{bmatrix} L_{1,1} & \cdots & L_{1,N_{dip}} \\ \vdots & \ddots & \vdots \\ L_{N_{sensors},1} & \cdots & L_{N_{sensors},N_{dip}} \end{bmatrix} \tag{2.22}$$

is the $N_{sensors} \times N_{dip}$ leadfield matrix and

$$\boldsymbol{Q} = \begin{bmatrix} q_1(t=t_1) & \cdots & q_1(t=t_T) \\ \vdots & \ddots & \vdots \\ q_{N_{dip}}(t=t_1) & \cdots & q_{N_{dip}}(t=t_T) \end{bmatrix} \tag{2.23}$$

is the $N_{dip} \times N_T$ dipole matrix. With this notation, elements of matrix $\boldsymbol{Q}$ are scalar, so that if the dipole orientation is not fixed, 3 dipoles per source location with orthogonal directions have to be included separately.

2.3.2 Forward problem

Equations (2.16) and (2.17) show that the forward problem can only be solved once the conductivity map $\sigma(\boldsymbol{r}')$ is known. Conductivity values for different tissue types have been evaluated with in-vivo and in-vitro experiments (Haueisen and Knösche, 2014). Table 2.1 contains conductivity values of relevant tissue types. We note that in this table (and in most forward models) $\sigma(\boldsymbol{r}')$ is assumed to be isotropic, although this is not strictly the case, especially in white matter regions with highly anisotropic fibers. To build a forward model one should ideally locate precisely each tissue type within each individual (and relative to the MEG sensor array), and assign a conductivity value to it. Luckily, in equation (2.16) the contribution of $\sigma(\boldsymbol{r}')\nabla V(\boldsymbol{r}')$ is smaller than that of $\boldsymbol{j}_p(\boldsymbol{r}')$, so that errors in conductivity modelling do not have a fatal impact on the calculation of $\boldsymbol{B}(\boldsymbol{r})$. In fact, coarse models with isotropic conductivities and rough geometries are surprisingly accurate. The volume conductor is commonly modelled as an N-shell volume, with shells of homogeneous and isotropic conductivity. For instance, in a 1-shell model, the space inside the skull represents the volume conductor, which is considered to be homogeneous. This is possible because the skull has much lower conductivity than the tissues it encloses (Table 2.1), so that in a rough approximation one can assume that no currents cross the inner skull surface. More realistic models include scalp, skull or cerebrospinal fluid as separate shells.

Spherical model

The head volume conductor can be modeled as a homogeneous sphere, which is fitted to the inner skull surface, as shown in Figure 2.8. In this simplified spherical model, the forward problem has an analytical solution (Sarvas, 1987):

$$\boldsymbol{B}(\boldsymbol{r}, \boldsymbol{r}_k) = \frac{\mu_0}{4\pi} \cdot \frac{F(\boldsymbol{r}, \boldsymbol{r}_k)\boldsymbol{q}_k \times \boldsymbol{r}_k - \left(\boldsymbol{q}_k \times \boldsymbol{r}_k \cdot \boldsymbol{r}\right) \nabla F(\boldsymbol{r}, \boldsymbol{r}_k)}{F^2(\boldsymbol{r}, \boldsymbol{r}_k)} \tag{2.24}$$

Table 2.1: Isotropic electrical conductivity values of head tissue types. Values are extracted from (Haueisen and Knösche, 2014; Dannhauer et al., 2011), and correspond to low frequency conductivities.

	Electrical conductivity (S/m)
Gray matter	0.3
White matter	0.2
Cerebrospinal fluid	1.79
Average brain	0.33
Compact bone	0.0064
Spongy bone	0.029
Fat	0.05
Scalp	0.43

with

$$F(\boldsymbol{r}, \boldsymbol{r}_k) = d\left(rd + r^2 + (\boldsymbol{r}_k \cdot \boldsymbol{r})\right) \tag{2.25}$$

and

$$F(\boldsymbol{r}, \boldsymbol{r}_k) = \left(\frac{d^2}{r} + \frac{\boldsymbol{d}\cdot\boldsymbol{r}}{d} + 2d + 2r\right)\boldsymbol{r} - \left(d + 2r + \frac{\boldsymbol{d}\cdot\boldsymbol{r}}{d}\right)\boldsymbol{r}_k \tag{2.26}$$

where $\boldsymbol{r}$ is the measurement position,$\boldsymbol{r}_k$ is the position of dipole k and $\boldsymbol{d} = \boldsymbol{r} - \boldsymbol{r}_k$ separates dipole and measurement point.

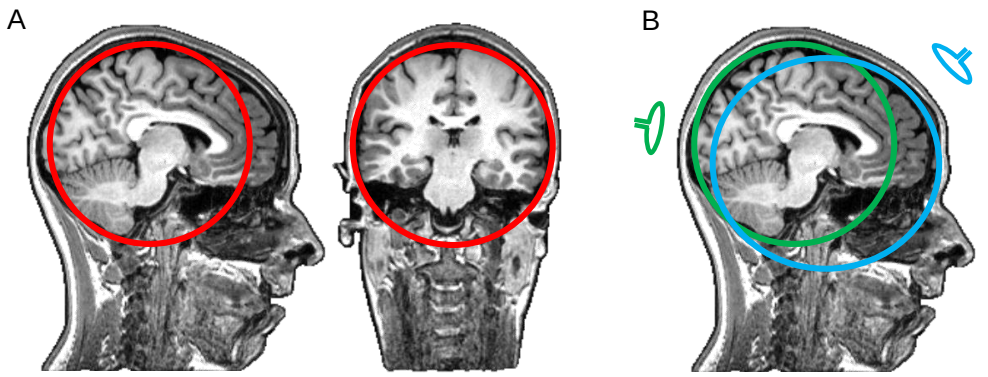

Figure 2.8: Spherical forward model. A. In the single sphere model, a sphere is fitted to the inner skull surface. B. In the local spheres model, a sphere is fitted to a portion of the inner skull surface that lies close to the MEG sensor of interest.

It is interesting to note that (2.24) does not depend on the radius of the sphere, as long as the dipole is inside the sphere and the measurement point in its exterior.

Additionally, the dependence of $\boldsymbol{B}(\boldsymbol{r}.\boldsymbol{r}_k)$ with the orientation of dipoles $\boldsymbol{r}_k$ is easy to grasp from (2.24). On the one hand, for radially oriented dipoles, $\boldsymbol{q} \parallel \boldsymbol{r}_k$ and $\boldsymbol{q} \times \boldsymbol{r}_k = 0$, so that there is no external magnetic fields: $\boldsymbol{B}(\boldsymbol{r}.\boldsymbol{r}_k) = 0$. On the other hand, for dipoles that are tangential to the sphere surface (which ideally represents the inner skull surface), $\|\boldsymbol{q} \times \boldsymbol{r}_k\| = \|\boldsymbol{q}\| \cdot \|\boldsymbol{r}_k\|$ and $\boldsymbol{B}(\boldsymbol{r}.\boldsymbol{r}_k)$ is strongest.

Although it constitutes a very simplistic approximation, the spherical model is adequate for many applications in MEG and standard subjects. Inaccuracies are higher in frontal and temporal regions, which deviate strongly from the global sphere fit. Huang et al. (1999) introduced a local spheres model which achieved higher accuracy than the single sphere model by fitting a different sphere for each MEG sensor. A set of overlapping spheres are then generated that reproduce the geometry of the head near the MEG sensor.

Single shell model with Nolte method

The Nolte method (also called corrected-sphere model) uses a single-shell volume conductor with arbitrary geometry (Nolte, 2003) and calculates the magnetic field by adding correcting terms to the spherical solution (2.24). Nolte proved that, in the quasi-static approximation, the leadfields of two single-shell volume conductors differ by the gradient of a scalar function. In particular, the leadfield $\boldsymbol{L}(\boldsymbol{r}, \boldsymbol{r}')$ for a given MEG sensor at position $\boldsymbol{r}$ and a dipole at position $\boldsymbol{r}'$ can be written as:

$$\boldsymbol{L}(\boldsymbol{r}, \boldsymbol{r}') = \boldsymbol{L}_{sphere}(\boldsymbol{r}, \boldsymbol{r}') - \nabla U(\boldsymbol{r}') \tag{2.27}$$

for a given measurement position $\boldsymbol{r}$, where $L_{sphere}(\boldsymbol{r}, \boldsymbol{r}')$ is the solution of the forward problem with a single-sphere model and $U(\boldsymbol{r}')$ is a harmonic function, chosen such that $L(\boldsymbol{r}, \boldsymbol{r}')$ is tangential to the volume conductor at its surface. It is useful to consider $U(\boldsymbol{r}')$ as a series expansion:

$$U(\boldsymbol{r}') = \sum_{m=1}^{M} a_m U_m(\boldsymbol{r}') \tag{2.28}$$

where $U_m(\boldsymbol{r}')$, $m = 1, 2, \cdots, M$ are basis harmonic functions. For instance, spherical harmonics are adequate $U_m(\boldsymbol{r}')$ functions. Then, calculating the leadfield requires finding the coefficients a_m that satisfy the boundary condition:

$$\boldsymbol{n}(\boldsymbol{r}') \cdot \left(L_{sphere}(\boldsymbol{r}, \boldsymbol{r}') - \nabla U(\boldsymbol{r}') \right) = 0 \tag{2.29}$$

for all $\boldsymbol{r}'$ on the shell's surface. To find the a_m that best satisfy (2.29), one defines P points in the inner skull surface and finds the optimal a_m values by minimizing the

error of the boundary condition at these P points:

$$\min \sum_{p=1}^{P} \left[\boldsymbol{n}(\boldsymbol{r}_p) \cdot \boldsymbol{L}_{sphere}(\boldsymbol{r}_p) - \sum_{m=1}^{M} \left(a_m \boldsymbol{n}(\boldsymbol{r}_p) U_m(\boldsymbol{r}_p) \right) \right]^2 \tag{2.30}$$

In summary, for each MEG sensor, one should: (1) find the coefficients a_m that minimize (2.30) and (2) evaluate the leadfield with (2.27) for all source dipoles at positions $\boldsymbol{r}' = \boldsymbol{r}_k$, $k = 1, 2, \cdots, N_{dip}$.

Boundary element method (BEM)

If the volume conductor is modeled as a piecewise homogeneous and isotropic volume of arbitrary geometry, the forward problem can be solved with BEM (Mosher et al., 1999; Stenroos and Sarvas, 2012). For that, equations (2.16) and (2.17) are first transformed into integral equations at the boundary surfaces between the volume conductor's shells. Then, these surfaces are discretized into small surface elements (usually triangles) and the forward problem is reduced to a system of linear equations. BEM solutions take remarkably longer computation times than analytical spherical or Nolte methods. This was historically considered an important drawback for BEM. However, this is no longer a big issue, as BEM calculations may only last for a few minutes in modern computers.

1-shell and 3-shell models are the most popular. While 1-shell models consider that the volume inside the skull is homogeneous and that currents $\boldsymbol{j}(\boldsymbol{r}')$ do not cross the inner skull boundary, 3-shell models include skull and scalp as separate shells within the volume conductor (see Figure 2.9). Other more detailed models include additional layers such as cerebrospinal fluid or a distinction between hard bone and spongy bone (Stenroos et al., 2014).

Finite element Method(FEM)

While the methods presented before were restricted to piecewise homogeneous volume conductors, FEM can handle more realistic and complicated models. The volume conductor is discretized into a 3D mesh of small volumes, or elements (Haueisen and Knösche, 2014). Each of these elements is characterized by a local conductivity tensor. One advantage of FEM is therefore the possibility to include anisotropic conductivity models. Although FEM enables very detailed and realistic solutions, it is rarely used in EEG/MEG, despite recent efforts to include FEM solvers in free EEG/MEG software (Ziegler et al., 2014).

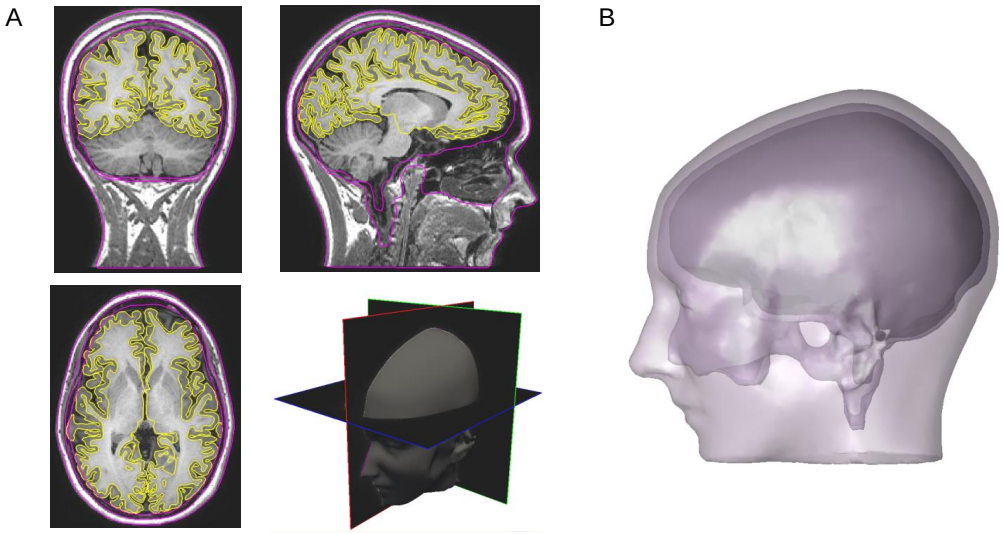

Figure 2.9: Boundary surfaces produced by MRI segmentation. A. Surfaces are overlaid into a subject's MRI. White matter and pial surfaces produced by Freesurfer software are displayed in yellow. Inner skull, outer skull and skin surfaces produced by NFT software are represented in pink. B. 3D view of the inner skull, outer skull and scalp surfaces that can be used as input to the 3-shell BEM solution of the forward problem.

Choosing the right forward model

Choosing an appropriate forward solution is crucial for performing a decent source reconstruction. Extremely detailed and realistic solutions involving anisotropic models with 3D FEM meshes could seem like the most accurate ones. However, this is only true if the conductivity profile in the head is accurately known for each small volume, which is rarely the case. Therefore, piecewise homogeneous models are employed for nearly all applications. While various studies have compared forward models, it is still unclear which is the best one (Hämäläinen and Sarvas, 1987, 1989; Huang et al., 1999; Lalancette et al., 2011; Acar and Makeig, 2013; Stenroos et al., 2014). In general, although spherical models work quite decently for MEG, they are outperformed by realistically shaped models, based on the subject-specific anatomy. Moreover, 3-shell BEM models were found to produce slightly more accurate leadfields than 1-shell models (either 1-shell BEM or Nolte method) (Stenroos et al., 2014). In Appendix C we compared single sphere, local spheres, Nolte, 1-shell BEM and 3-shell BEM models, and obtained results comparable to (Stenroos et al., 2014): 3-shell BEM, 1-shell BEM and Nolte methods produced similar results and the spherical models differed from the realistically-shaped ones, especially in medial temporal regions. We conclude that

3-shell BEM, 1-shell BEM and Nolte offer decent solutions for the forward problem, and that 3-shell BEM is probably the most accurate one. 3-shell BEM was therefore used in Chapter 4. Nevertheless, the forward solutions in Chapter 3, which were computed before the publication of (Stenroos et al., 2014) and the computation of Appendix C, were performed with Nolte method, which was the recommended option for MEG in FieldTrip software (Oostenveld et al., 2011).

Finally, the choice of the right forward model depends on the study's resources. If a T1-weighted MRI is available for each subject, it is best use Nolte method or BEM. In fact, tissue surfaces can be extracted from a T1-weighted image using any segmentation software, such as Freesurfer (Fischl and Dale, 2000; Fischl et al., 2002), SPM (Penny et al., 2011), FieldTrip or NFT (Neuroelectromagnetic Forward Modeling Toolbox) (Acar and Makeig, 2010). In contrast, if no MRI is available, a good estimation of the leadfield can be obtained with the local-spheres method. The headshape, which is routinely digitalized before MEG scans, can be used to determine the spheres. This is possible because (2.24) does not depend on the radius of the sphere, so that one can fit a sphere to the headshape instead of the inner skull surface and use it directly in (2.24), assuming thereby that the spherical fits to the headshape and the inner skull are concentric.

2.3.3 Inverse problem

Solving the forward problem yields the value of the leadfield matrix $\boldsymbol{L}_{ik}$ in (2.19). Once $\boldsymbol{L}_{ik}$ is known, the inverse problem can be tackled, in which one attempts to derive the brain currents $\boldsymbol{q}_k(t)$, $k = 1,2,\cdots,N_{dip}$ from the MEG measurements $m_i(t)$, $i = 1,2,\cdots,N_{sensors}$:

$$\boldsymbol{q}_k(t) = f\left(\{m_i(t), \boldsymbol{L}_{ik}\}, \quad i = 1,\cdots,N_{sensors}\right) \tag{2.31}$$

This is a tricky task, since infinite functions f explain the MEG sensor measurements and verify equation (2.19). The inverse problem has therefore infinite solutions and is said to be ill-posed. This has been known since 1853, when Helmholtz stated that infinite distribution of currents in a conductor produce the same fields and potentials at its surface (Helmholtz, 1853). Then, in order to solve the inverse problem, additional hypotheses should be introduced to select a single solution f. The validity of the inverse solution depends then on the validity of these hypotheses in the specific MEG experiment. Different hypotheses have been proposed over the past years, and each of them has led to a source reconstruction method. In the following, we describe three of the most popular techniques and focus on beamforming, which is used in Chapters 3 and 4. We note however that other models, such as MUSIC (Mosher and

Leahy, 1998) or LORETA (Pascual-Marqui et al., 1994), have been proposed as inverse models and are commonly used in some research centers.

Dipole fitting

The oldest and perhaps simplest hypothesis is that MEG activity is created from only a few dipoles (typically less than 5). Under this hypothesis, the inverse problem becomes well-conditioned, and the dipole positions $\boldsymbol{r}_k$ and activations $\boldsymbol{q}_k(t)$ can be obtained for all modelled dipoles $k = 1, 2, \cdots, N_{dip}$. For each dipole, 6 values have to be estimated: its 3D location $\boldsymbol{r}_k$, its orientation (θ_k, φ_k) and its moment q_k. This is usually solved as an optimization problem, which consists in finding the set of values $\{\boldsymbol{r}_k, \theta_k, \varphi_k, q_k\}$ that minimize the error between the actual measurements $\boldsymbol{M}$ and the predicted measurements $\boldsymbol{LQ}$ (Baillet et al., 2001; Darvas et al., 2004):

$$\min_{\{\boldsymbol{r}_k, \theta_k, \varphi_k, q_k\}} \left|\left|\boldsymbol{M} - \boldsymbol{L}(\boldsymbol{r}_k, \theta_k, \varphi_k)\boldsymbol{Q}\right|\right|^2 \tag{2.32}$$

This is a non-linear optimization problem, and it has to be solved carefully to avoid terminating at a local minimum. To deal with this problem, it can be combined with global optimization methods such as genetic algorithms or simulated annealing (Uutela et al., 1998; Khosla et al., 1997). Dipole fitting can be performed either separately for each time point, or jointly for a time interval (Wood, 1982; Baillet et al., 2001), yielding either free moving dipoles or dipoles with fixed position and time-dependent activation. Although dipole fitting is a simplistic model, it has proven to be adequate for source reconstruction of evoked responses, such as auditory and somatosensory responses (Salmelin, 2010).

Minimum norm estimates (MNE) and minimum current estimates (MCE)

Imaging methods such as minimum norm or minimum current estimates (MNE or MCE, respectively) estimate dipole moments at a set of fixed source positions that cover the entire brain activation area (Baillet et al., 2001). This source space may result from the tessellation of the subject's cortical surface or from a regular grid of 3D points that are spread over the subject's gray matter. If the subject's MRI is not available, its cortical surface and gray matter cannot be located, and the source space may be defined in a template space such as MNI space (see 2.3.4). The orientation of these source positions may be fixed (for instance perpendicularly to the cortical surface), or span 3 possible directions x, y, z. In all cases the source space consists in a few thousands dipoles, while MEG measurements are sampled at a few hundred sensors,

so that the source reconstruction problem is severely underdetermined.

Constraints or *a priori* information must then be included to find a unique solution. Although a Bayesian framework is commonly introduced to describe MNE and MCE, they are easier to grasp as the solution of a simple minimization problem (Gramfort et al., 2012):

$$\min_{\boldsymbol{Q}} \left[f_1(\boldsymbol{Q}) + \lambda f_2(\boldsymbol{Q}) \right] \tag{2.33}$$

The cost function is then composed of two terms $f_1(\boldsymbol{Q})$ and $f_2(\boldsymbol{Q})$ which are weighted by the regularization parameter $\lambda > 0$:

- $f_1(\boldsymbol{Q})$ measures how well source estimations fit the model, or how much the estimated fields $\boldsymbol{LQ}$ deviate from the actual MEG measurements $\boldsymbol{M}$.
- $f_2(\boldsymbol{Q})$ is a regularization or penalty term, and introduces *a priori* information. f_2 is necessary to ensure that the ill-posed inverse problem has a unique solution.

For the basic MNE and MCE, $f_1(\boldsymbol{Q}) = ||\boldsymbol{M} - \boldsymbol{LQ}||$ and $f_2(\boldsymbol{Q}) = ||\boldsymbol{Q}||$, where $||\cdots||$ refers to the L2 norm for MNE and to the L1 norm for MCE (Uutela et al., 1999). The L2 norm results generally in smeared solutions, while the L1 norm produces sparse source activations (Darvas et al., 2004). With this approach, source estimations are biased towards superficial sources, since deeper sources require stronger activation than superficial sources to produce the same field intensity in MEG sensors. To deal with this bias, depth-weighting factors or noise normalization may be introduced in the MNE and MCE solutions (Lin et al., 2006; Hauk et al., 2011).

Beamforming

Beamformers are adaptive spatial filters (Sekihara and Nagarajan, 2008). They are called spatial filters because the source activity $\boldsymbol{q}(\boldsymbol{r}, t)$ at a source position $\boldsymbol{r}$ is estimated as a linear combination of sensor measurements $\boldsymbol{M}(t)$:

$$\boldsymbol{q}(\boldsymbol{r}, t) = \boldsymbol{w}^T(\boldsymbol{r})\boldsymbol{M}(t) \tag{2.34}$$

where the $N_{sensors} \times 3$ weights $\boldsymbol{w}(\boldsymbol{r})$ are computed independently from all other sources $\boldsymbol{r}' \neq \boldsymbol{r}$. $\boldsymbol{w}(\boldsymbol{r})$ depends not only on the source position $\boldsymbol{r}$ and its corresponding leadfield $\boldsymbol{L}(\boldsymbol{r})$, but also on the measurements $\boldsymbol{M}$: beamformers are therefore called adaptive spatial filters.

For the beamforming formulation, the data covariance matrix $\boldsymbol{R_M}(N_{sensors} \times$

$N_{sensors}$) is introduced:

$$\boldsymbol{R_M} = \frac{1}{N_T}\boldsymbol{M}\boldsymbol{M}^T = \begin{bmatrix} \langle m_1(t)^2 \rangle & \cdots & \langle m_1(t) \cdot m_{N_{sensors}}(t) \rangle \\ \vdots & \ddots & \vdots \\ \langle m_{N_{sensors}}(t) \cdot m_1(t) \rangle & \cdots & \langle m_{N_{sensors}}(t)^2 \rangle \end{bmatrix} \tag{2.35}$$

We note that the covariance is not defined here in the usual way, which removes signal average prior to multiplication with other signals. However, this is irrelevant since magnetic fields and source activations are considered to have zero average.

Source variance $\boldsymbol{V}(\boldsymbol{r})$ (also referred to as power) can then be expressed as:

$$\boldsymbol{V}(\boldsymbol{r}) = \boldsymbol{q}(\boldsymbol{r},t)\boldsymbol{q}^T(\boldsymbol{r},t) = \boldsymbol{w}^T(\boldsymbol{r})\boldsymbol{R_M}\boldsymbol{w}(\boldsymbol{r}) \tag{2.36}$$

Ideally, the filter $\boldsymbol{w}(\boldsymbol{r})$ should be defined to enable that signals coming from location $\boldsymbol{r}$ pass, while signals coming from any other location are blocked. In other words, an ideal spatial filter should satisfy:

$$\boldsymbol{w}^T(\boldsymbol{r})\boldsymbol{L}(\boldsymbol{r}') = \begin{cases} \boldsymbol{I}, & \text{for } \boldsymbol{r} = \boldsymbol{r}'. \\ \boldsymbol{0}, & \text{for } \boldsymbol{r} \neq \boldsymbol{r}'. \end{cases} \tag{2.37}$$

where $\boldsymbol{L}(\boldsymbol{r}')$ is the $N_{sensors} \times 3$ leadfield matrix for a source at position $\boldsymbol{r}'$.

Such a filter cannot be built in practice, and more permissive constraints are used to derive real beamformers. For instance, the linearly constrained minimum variance (LCMV) beamformer results from minimizing source power while keeping unit gain at the source position (Van Veen et al., 1997):

$$\min_{\boldsymbol{w}(\boldsymbol{r})} \text{trace}\left(\boldsymbol{w}^T(\boldsymbol{r})\boldsymbol{R_M}\boldsymbol{w}(\boldsymbol{r})\right), \quad \text{subject to } \boldsymbol{w}^T(\boldsymbol{r})\boldsymbol{L}(\boldsymbol{r}) = \boldsymbol{I} \tag{2.38}$$

This minimization problem can be solved with Lagrange multipliers, and the weight $\boldsymbol{w}(\boldsymbol{r})$ becomes:

$$\boldsymbol{w}(\boldsymbol{r}) = \boldsymbol{R_M}^{-1}\boldsymbol{L}(\boldsymbol{r})\left[\boldsymbol{L}^T(\boldsymbol{r})\boldsymbol{R_M}^{-1}\boldsymbol{L}(\boldsymbol{r})\right]^{-1} \tag{2.39}$$

The source power is then:

$$\boldsymbol{V}(\boldsymbol{r}) = \boldsymbol{w}^T(\boldsymbol{r})\boldsymbol{R_M}\boldsymbol{w}(\boldsymbol{r}) = \left[\boldsymbol{L}^T(\boldsymbol{r})\boldsymbol{R_M}^{-1}\boldsymbol{L}(\boldsymbol{r})\right]^{-1} \tag{2.40}$$

Weights $\boldsymbol{w}(\boldsymbol{r})$ and power $\boldsymbol{V}(\boldsymbol{r})$ can then be computed at a set of predefined locations $\boldsymbol{r}$ in order to produce a whole brain image of source power or of source time-courses

with (2.34).

We note that beamforming solutions are derived under a few assumptions (Sekihara and Nagarajan, 2008):

- Sources are uncorrelated. This means that source time series should be linearly independent.
- There are less active sources than MEG sensors: $N_{sensors} > N_{sources}$.
- MEG sensors capture only a small amount of noise, and this noise is uncorrelated.

However, beamformers may still perform adequately if these conditions are not strictly satisfied. For instance, in an experiment with a phantom device, Belardinelli et al. (2012) proved that only extremely high source correlations (>0.95) resulted in a poor spatial resolution (>1.5 cm). Additionally, since beamformers do not attempt to explain the entire measurements $\boldsymbol{M}(t)$ (contrary to dipole fitting or MNE), they are particularly robust to noisy interference as cardiac artifacts (Brookes et al., 2011a). In fact, beamformers have been recommended for the source-space analysis of functional connectivity of resting state data (Hillebrand et al., 2005; Brookes et al., 2011a; Schoffelen and Gross, 2009; Brookes et al., 2011b; Hillebrand et al., 2012; Hipp et al., 2012). They were therefore used throughout Chapters 3 and 4 for source reconstruction.

Matrix regularization The accuracy of the beamforming solution in (2.39) and (2.40) depends on the accuracy of the estimation of the data covariance matrix $\boldsymbol{R_M}$ and its inverse $\boldsymbol{R_M}^{-1}$. First of all, $\boldsymbol{R_M}$ as estimated from (2.35) differs from the true covariance matrix. This estimation error decreases with measurement time and signal bandwidth (Brookes et al., 2008), so that before applying beamforming we should ensure that enough time samples are available to produce a decent covariance matrix. Secondly, $\boldsymbol{R_M}$ should be invertible. This is not the case if the matrix is rank deficient (e.g. after SSS has been applied). In such cases a regularization factor is included, and $\boldsymbol{R_M}^{-1}$ is replaced in (2.39) and (2.40) by:

$$\boldsymbol{R_M}^{-1} \rightarrow \left[\boldsymbol{R_M} + \mu\sigma^2\boldsymbol{I}\right]^{-1} \tag{2.41}$$

where μ is called the regularization parameter and σ quantifies the white noise at the MEG sensors. σ may be extracted from empty room recordings or estimated as the smallest singular value of $\boldsymbol{R_M}$. This regularization procedure is equivalent to adding some uncorrelated noise to the MEG recordings. It is helpful because it reduces the

condition number of $\boldsymbol{R_M}$ but also produces a smearing in the source reconstruction. The value of regularization parameter must then result from a trade-off between both considerations.

Source orientation We have previously employed a vector formulation: source activities $\boldsymbol{q}(\boldsymbol{r},t) : 3 \times 1$ are described as vectors with (x,y,z) components. Alternatively, a scalar formulation fixes the source orientation, and the source activity becomes scalar $q(\boldsymbol{r},t) : 1 \times 1$. For instance, if the source locations are placed over the cortical surface, one can assume that their dipoles are oriented perpendicularly to this surface and choose a scalar beamforming solution. In this case, the solution to the unit-gain beamformer (2.38) is (Sekihara and Nagarajan, 2008):

$$\boldsymbol{w}(\boldsymbol{r}) = \frac{\boldsymbol{R_M}^{-1}\boldsymbol{L}(\boldsymbol{r})}{\boldsymbol{L}^T(\boldsymbol{r})\boldsymbol{R_M}^{-1}\boldsymbol{L}(\boldsymbol{r})} \tag{2.42}$$

where $\boldsymbol{w}(\boldsymbol{r}) : N_{sensors} \times 1$ has now a single dimension and $\boldsymbol{L}(\boldsymbol{r}) : N_{sensors} \times 1$ is the leadfield for position $\boldsymbol{r}$ and the previously determined orientation.

It is generally not recommended to use this scalar formulation directly: even if detailed geometrical information of the cortical surface is available, co-registration errors between MEG sensor positions and the source mesh may yield to considerable errors in the estimation of the source orientation. However, even when choosing the vector beamformer option, we still want to get rid of the orientation parameter and obtain a scalar source power $\boldsymbol{V}(\boldsymbol{r})$ and a single time-course per source location $\boldsymbol{r}$.

The global source power at $\boldsymbol{r}$ can be directly computed by combining all orientations as:

$$\boldsymbol{V}(\boldsymbol{r}) = \text{trace}\left[\boldsymbol{w}^T(\boldsymbol{r})\boldsymbol{R_M}\boldsymbol{w}(\boldsymbol{r})\right] \tag{2.43}$$

Another option is finding a data-driven optimal orientation $\boldsymbol{\eta}_{opt}(\boldsymbol{r})$ and use it to project source power and time-series. This option is used in Chapters 3 and 4, since we aimed at obtaining not only power values but also time series. This $\boldsymbol{\eta}_{opt}(\boldsymbol{r})$ can be extracted from maximizing the power in direction $\boldsymbol{\eta}(\boldsymbol{r})$:

$$\max_{\boldsymbol{\eta}(\boldsymbol{r})} \boldsymbol{\eta}^T(\boldsymbol{r})\boldsymbol{V}(\boldsymbol{r})\boldsymbol{\eta}(\boldsymbol{r}) \tag{2.44}$$

For the LCMV beamformer, this is reduced to (Sekihara and Nagarajan, 2008):

$$\begin{aligned}\max_{\boldsymbol{\eta}(\boldsymbol{r})} \boldsymbol{\eta}^T(\boldsymbol{r})\left[\boldsymbol{L}^T(\boldsymbol{r})\boldsymbol{R_M}^{-1}\boldsymbol{L}(\boldsymbol{r})\right]^{-1}\boldsymbol{\eta}(\boldsymbol{r}) &= \theta_{max}\left(\left[\boldsymbol{L}^T(\boldsymbol{r})\boldsymbol{R_M}^{-1}\boldsymbol{L}(\boldsymbol{r})\right]^{-1}\right) \\ &= \theta_{min}\left(\boldsymbol{L}^T(\boldsymbol{r})\boldsymbol{R_M}^{-1}\boldsymbol{L}(\boldsymbol{r})\right)\end{aligned} \tag{2.45}$$

where $\theta_{max}(\cdots)$ is the eigenvector with maximum eigenvalue of matrix $(\cdots)$ and $\theta_{min}(\cdots)$ is the eigenvector with minimum eigenvalue of matrix $(\cdots)$.

Finally, the weight matrix is projected along this optimal direction:

$$\boldsymbol{w}_{\boldsymbol{\eta}(\boldsymbol{r})}(\boldsymbol{r}) = \boldsymbol{w}(\boldsymbol{r})\boldsymbol{\eta}(\boldsymbol{r}) \tag{2.46}$$

and the new weight vector $\boldsymbol{w}_{\boldsymbol{\eta}(\boldsymbol{r})}$ is used in (2.34) and (2.36) to compute source time series and power.

Frequency resolution Frequency resolution can be introduced into the source reconstruction with either:

- filtering the measurement data $\boldsymbol{M}(t)$ into the target frequency band and then employing a time-domain beamformer (such as LCMV).
- using a frequency domain beamformer, as explained in the following.

Frequency-domain beamformers rely on the cross-spectrum matrix $\boldsymbol{C}(f)$ rather than on the covariance matrix:

$$\boldsymbol{C}(f) = \boldsymbol{G}(f)\boldsymbol{G}^H(f) \tag{2.47}$$

where H denotes the Hermitian transpose (transpose + complex conjugate) and $\boldsymbol{G}(f)$ is the $N_{sensors} \times 1$ vector containing the Fourier transform $g_i(f)$, $i = 1,2,\cdots,N_{sensors}$ of the MEG measurements $m_i(t)$, $i = 1,2,\cdots,N_{sensors}$.

$$\boldsymbol{G}(f) = \begin{bmatrix} g_1(f) \\ \cdots \\ g_{N_{sensors}}(f) \end{bmatrix} \tag{2.48}$$

Similarly as for its time-domain counterpart, for a frequency-resolved filter the source activity is given by:

$$\boldsymbol{q}(\boldsymbol{r}, f) = \boldsymbol{w}^H(\boldsymbol{r}, f)\boldsymbol{G}(\boldsymbol{f}) \tag{2.49}$$

The weights $\boldsymbol{w}(\boldsymbol{r}, f)$ can be obtained by imposing the desired constraints. The unit gain minimum variance filter results in the following optimization problem:

$$\min_{\boldsymbol{w}(\boldsymbol{r},f)} \text{trace}\left(\boldsymbol{w}^H(\boldsymbol{r}, f)\boldsymbol{C}(f)\boldsymbol{w}(\boldsymbol{r}, f)\right), \quad \text{subject to } \boldsymbol{w}^H(\boldsymbol{r}, f)\boldsymbol{L}(\boldsymbol{r}) = \boldsymbol{I} \tag{2.50}$$

which has the solution (Gross et al., 2001; Sekihara and Nagarajan, 2008)

$$\boldsymbol{w}(\boldsymbol{r}, f) = \boldsymbol{C}(f)^{-1}\boldsymbol{L}(\boldsymbol{r})\left[\boldsymbol{L}^{T}(\boldsymbol{r})\boldsymbol{C}(f)^{-1}\boldsymbol{L}(\boldsymbol{r})\right]^{-1} \tag{2.51}$$

Then, inserting this solution into (2.49), source activity and power can be computed at any desired position $\boldsymbol{r}$ and frequency f.

To study a given frequency band BW instead of a particular frequency f, a cross-spectrum matrix $C_{BW}(f)$ which covers the desired frequency range can be used in the previous equations. $C_{BW}(f)$ may be defined as:

$$C_{BW}(f) = \sum_{f \in BW} \boldsymbol{G}(f)\boldsymbol{G}^{H}(f) \tag{2.52}$$

Alternatively, more sophisticated spectral estimation methods can be employed to estimate $C_{BW}(f)$, such a multi tapers or wavelets.

2.3.4 Group analyses

After performing MEG source reconstruction, we want to compare or combine the results from all the study participants. However, before tackling any statistical analysis, we should make sure that the source reconstruction can be compared across subjects. Both source locations and source activation values should be comparable across individuals. This is now further explained.

Spatial matching

To compare source reconstructions from multiple subjects, the correspondence between source locations in any pair of subjects should be established. In other words, for any source location $\boldsymbol{r}_i$ in subject i, the source location $\boldsymbol{r}_j$ in subject j that corresponds to the same structure should be found. This is commonly achieved via a reference or template space, such as the MNI (Montreal Neurological Institute) space (Evans et al., 2012). MNI space was created from a large series of MRI images from healthy controls and constitutes a general and reference space. Some normalization routines are available in software such as SPM can determine the correspondence between subject and MNI space by matching the template MNI T1-weighted image and the subject's T1-weighted volume:

$$\boldsymbol{r}_{MNI} = \boldsymbol{f}_i(\boldsymbol{r}_i), \quad i = 1, 2, \cdots, N_{subjects} \tag{2.53}$$

where $\boldsymbol{f}_i$ depends on the individual, and may be a simple affine transformation or a more complicated non-linear transformation.

Once the transformation from each subject to MNI space $\boldsymbol{f}_i$, $i = 1,2,\cdots,N_{subjects}$ is known, the location correspondence between two subjects i and j can be obtained via:

$$\boldsymbol{r}_i = \boldsymbol{f}_i^{-1}\left[\boldsymbol{f}_j(\boldsymbol{r}_j)\right] \tag{2.54}$$

Therefore, one may create the source meshes separately for each subject, and then compare their source reconstructions by calculating the correspondence between source locations and interpolating. As illustrated in Figure 2.10, a more straightforward alternative is to define the source meshes in MNI space, transform this template mesh to subject's space with (2.53) and use this transformed mesh in subject space for source reconstruction. In this case, source k in subject i can be directly compared with source k in subject j, since source k corresponds to the same MNI location for all subjects. This approach was followed in section 3.1.

Additionally, when performing MEG group analyses, it is often of use to assign anatomical labels to source activations, or to group results into anatomical brain regions. For both cases one may resort to a brain atlas. Many atlases have been built over the past years (Evans et al., 2012), such as the Harvard-Oxford probabilistic atlas (Desikan et al., 2006), the AAL atlas (Tzourio-Mazoyer et al., 2002) or the Desikan-Killiany and Dextrieux atlases in Freesurfer (Fischl et al., 2002, 2004). While the Harvard-Oxford and the AAL atlases assign anatomical labels (and a probability value for the Harvard-Oxford) to MNI coordinates, Freesurfer's cortical parcellation routine employs both geometrical information from the subject's gyri and sulci and a training set model to separate the cortical surface into atlas regions.

Intensity normalization

Source reconstruction yields the time dynamics $\boldsymbol{q}_k(t)$ of all dipoles included in the source model. Although absolute units such as Am could be assigned to the $\boldsymbol{q}_k(t)$ solutions, these $\boldsymbol{q}_k(t)$ values should often not be inserted directly in a statistical analysis. In fact, the source reconstruction algorithm may introduce some bias. For instance, beamforming overestimates source power in the center of the brain, which has a low magnitude leadfield and low signal to noise ratio (Hall et al., 2013; Luckhoo et al., 2014). A common workaround to this is to use a relative $\boldsymbol{q}_k(t)$, using either a baseline or source activation from a different condition to normalize its value.

However, a normalization condition is difficult to obtain for resting state. This is often not an issue, since for some purposes a rescaling of the source intensity

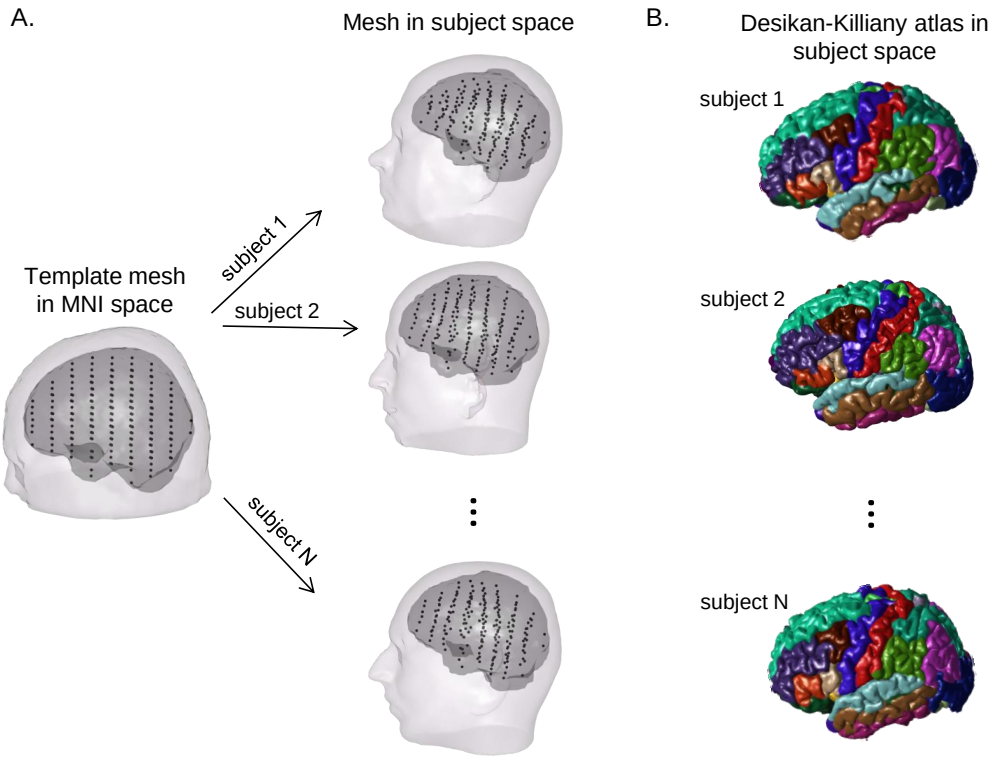

Figure 2.10: Combining spatial information from different subjects. A. A regular template mesh with 2cm spacing is created in MNI space, and then it is transformed into subject space with a non-linear normalization routine from SPM software. If this mesh is used for MEG source reconstruction, source locations can be compared across subjects, since they correspond to the same MNI coordinates. B. Source locations are grouped into regions using the Desikan-Killiany atlas implemented in Freesurfer. Each color corresponds to an atlas region.

is irrelevant. For instance, powerspectra are often normalized with the broadband power, yielding relative power estimates (section 3.1). Additionally, most functional connectivity (FC) algorithms are insensitive to rescaling in their input, so that $\boldsymbol{q}_k(t)$ can usually be employed directly in an FC analysis. However, normalization is necessary when aiming at obtaining absolute resting-state power, and power values $V(\boldsymbol{r})$ are replaced by their normalized version:

$$Z(\boldsymbol{r}) = \frac{V(\boldsymbol{r})}{N(\boldsymbol{r})} \tag{2.55}$$

where $N(\boldsymbol{r})$ represents the power of the noise estimates, and is obtained by replacing the resting state covariance $\boldsymbol{R_M}$ in (2.36) with a noise covariance. The noise covariance is often a diagonal matrix, assuming thereby uncorrelated noise (Luckhoo et al., 2014), but it can also be calculated from actual MEG data (such as an empty room recordings). We followed this second option for the normalization of absolute power estimates in Chapter 4.

2.4 Functional connectivity (FC)

Correct brain functioning requires the coordinated activity of distinct brain areas (Singer, 1999; Varela et al., 2001; Fries, 2005). Such brain integration is studied by structural, functional and effective connectivity (SC, FC and EC, respectively). SC targets the anatomical substrate of the connectivity, and can be assessed for instance with diffusion weighted imaging (DWI) (3.2). FC measures statistical dependencies between the activity of separate brain regions (Friston, 2011) and can be assessed with any functional imaging modality, such as fMRI or MEG. While with fMRI data FC is almost exclusively calculated with covariance between slow BOLD signals, a variety of FC measures are used with MEG data. Finally, EC studies the influence of one region on another, and distinguishes between unidirectional and bidirectional information flow. This section targets FC: we introduce some FC measures and detail how they are applied to MEG source space data.

2.4.1 FC measures

Essentially, any measure that captures some sort of coupling between two time series is a valid FC metric. As reviewed in (Pereda et al., 2005; Sakkalis, 2011; Niso et al., 2013), many algorithms have been used to quantify FC. We briefly overview here some families of connectivity measures, and then describe with further details the implementation of phase and amplitude synchronization, since they are relevant for

the remaining chapters of this thesis. For that, let us first define two time series $x(t)$ and $y(t)$, that are sampled simultaneously at a given frequency, producing two vectors: $\boldsymbol{x} = [x_1, x_2, \cdots, x_n]$ and $\boldsymbol{y} = [y_1, y_2, \cdots, y_n]$.

- *Linear connectivity.* Correlation (or cross-correlation) is the most straightforward measure of coupling. It measures the degree of linear dependency between $\boldsymbol{x}$ and $\boldsymbol{y}$:

$$r_{xy} = \frac{\sum_{k=1}^{n} (x_k - \bar{x})(y_k - \bar{y})}{\sqrt{\sum_{k=1}^{n} (x_k - \bar{x})^2} \cdot \sqrt{\sum_{k=1}^{n} (y_k - \bar{y})^2}} \tag{2.56}$$

  where $\bar{x}$ and $\bar{y}$ denote signal averages. $r_{xy} = \pm 1$ for completely linearly related variables $\boldsymbol{x}$ and $\boldsymbol{y}$ and r_{xy} reaches 0 for linearly independent variables. The frequency-domain counterpart of the correlation is the coherence:

$$\kappa_{xy}(f) = \sqrt{\frac{\left|\langle C_{xy}(f)\rangle\right|^2}{\left|\langle C_{xx}(f)\rangle\right| \cdot \left|\langle C_{yy}(f)\rangle\right|}} \tag{2.57}$$

  where $C_{xy}(f)$ is the cross-spectrum between $x(t)$ and $y(t)$ and $\langle \cdots \rangle$ indicates that the cross-spectra are averaged over segments or time windows.

- *Phase and envelope synchronization.* Oscillatory signals can be separated into phase and envelope. While the phase indicates the moment within the cycle and is measured as an angle $]-\pi, \pi]$, the envelope (or amplitude) represents the power. Synchronization can be assessed with both phase and envelope.

- *Information theory techniques.* Information can be quantified with Shannon entropy, which can be computed for $\boldsymbol{x}$ and $\boldsymbol{y}$ separately, and for both signals jointly. This can be used to determine the amount of information that is shared between $\boldsymbol{x}$ and $\boldsymbol{y}$ (by means of mutual information) and even estimate the direction of the information flow (Sakkalis, 2011).

- *Generalized synchronization.* Generalized synchronization captures coupling between the states of two systems, based on various underlying connectivity models. Synchronization likelihood, which relies on the detection simultaneous patterns in two time series, is the most popular generalized synchronization technique. (Niso et al., 2013).

Extracting phase and envelope

A narrow-band oscillatory neural signal $x(t)$ can be conceived as having phase $\varphi_x(t)$ and envelope $A_x(t)$ (Rosenblum and Pikovsky, 2003). The phase indicates the moment within a cycle and the envelope relates to the amplitude or strength of the oscillations. This is usually represented in a 2D polar coordinate plot, in which angles and radii correspond to $\varphi_x(t)$ and $A_x(t)$, respectively (see Figure 2.11). Envelopes and phases are usually extracted with either Hilbert of wavelet transforms. While the wavelet transform allows for a flexible and complete time-frequency representation of $x(t)$, Hilbert transform is simpler, but only is only meaningful for narrow-band oscillatory signals. In Chapters 3 and 4 we employed Hilbert transform, since the signals of interest were narrow-band (filtered in classical frequency bands) and Hilbert is a simpler and parameter-free approach which gives equivalent results to wavelet (Le Van Quyen et al., 2001).

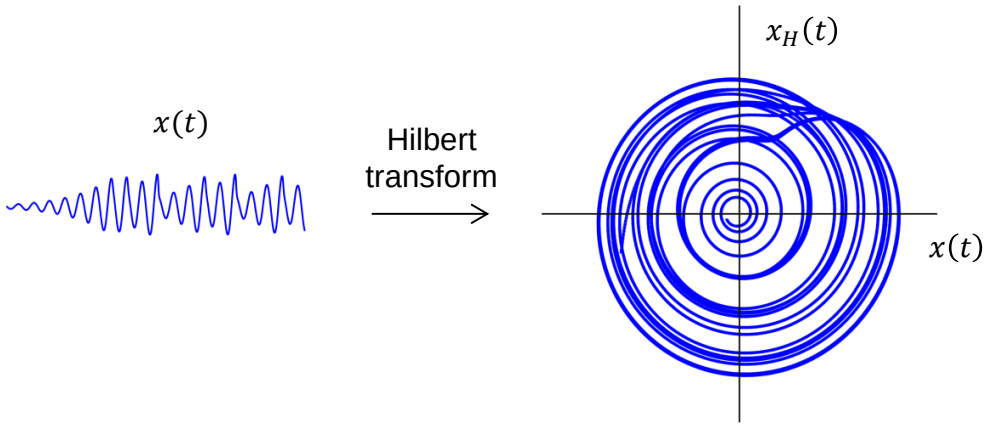

Figure 2.11: Phase and envelope of an oscillatory signal. An oscillatory signal $x(t)$ can be separated into phase $\varphi_x(t)$ and envelope $A_x(t)$. The right plot is obtained when plotting $x(t)$ and its Hilbert transform $x_H(t)$ in the x and y axis, respectively. In this representation, for every time point t, $\varphi_x(t)$ is the angle with the positive x axis and $A_x(t)$ is the distance to the origin.

$\varphi_x(t)$ and $A_x(t)$ are extracted as argument and modulus of the complex analytical signal (Rosenblum et al., 2001)

$$\zeta(t) = x(t) + i x_H(t) = A_x(t) e^{i\varphi_x(t)} \tag{2.58}$$

where $x_H(t)$ is the Hilbert transform of $x(t)$ and is defined as:

$$x_H(t) = \frac{1}{\pi} P.V. \int_{-\infty}^{+\infty} \frac{x(t)}{t-\tau} d\tau \tag{2.59}$$

and *P.V.* refers to the Cauchy principal value. Although this could seem a rather long calculation, it can be easily and rapidly computed when using the Fourier transform to switch between time and frequency domains (Marple, 1999).

Phase synchronization

Strictly, phase synchronization between $x(t)$ and $y(t)$ occurs when their phases $\varphi_x(t)$ and $\varphi_y(t)$ are locked:

$$l\varphi_x(t) - m\varphi_y(t) = constant \tag{2.60}$$

where l and m are two integer numbers that specify the type of coupling. The most common synchronization is $l = m = 1$, and indicates that $x(t)$ and $y(t)$ are separated by a fixed phase. In other words, $\varphi_x(t)$ can be deduced from $\varphi_y(t)$, and vice versa.

Such strict phase locking is in practice not fulfilled, and phase synchronization algorithms search for more flexible couplings. For instance, phase locking value (PLV) measures how much the phase difference differs from a random uniform distribution (Lachaux et al., 1999)

$$\mathrm{PLV}_{xy} = \frac{1}{n}\left|\sum_{k=1}^{n} \exp\left[i\left(\varphi_{x,k} - \varphi_{y,k}\right)\right]\right| \tag{2.61}$$

PLV_{xy} varies between 1 for a constant phase difference and 0 for a randomly distributed phase difference (within $]-\pi,\pi]$). Its calculation is illustrated in Figure 2.12.

An alternative algorithm is the Phase Lag Index (PLI), which is insensitive to zero and π phase differences (Stam et al., 2007):

$$\mathrm{PLI}_{xy} = \frac{1}{n}\left|\sum_{k=1}^{n} \mathrm{sign}\left[\sin\left(\varphi_{x,k} - \varphi_{y,k}\right)\right]\right| \tag{2.62}$$

PLI_{xy} also varies between 0 (no synchronization or synchronization centred around 0 or $\pm\pi$) and 1 (maximal synchronization). It quantifies the asymmetry in the phase difference over the upper and lower half-unit circle ($]0,\pi]$ and $]-\pi,0]$, respectively). For instance, $\mathrm{PLI}_{xy} = 1$ if $\varphi_x - \varphi_y$ always remains in the $[0,\pi]$ interval.

Envelope correlation

As explained in section 2.4.1, envelopes $A_x(t)$ and $A_y(t)$ (also called amplitudes) can be extracted from the modulus of the analytical signal. They represent the power or strength of the source activation, and vary more slowly than the phases $\varphi_x(t)$ and $\varphi_y(t)$, typically over seconds (see Figure 2.12). This means that, although the original

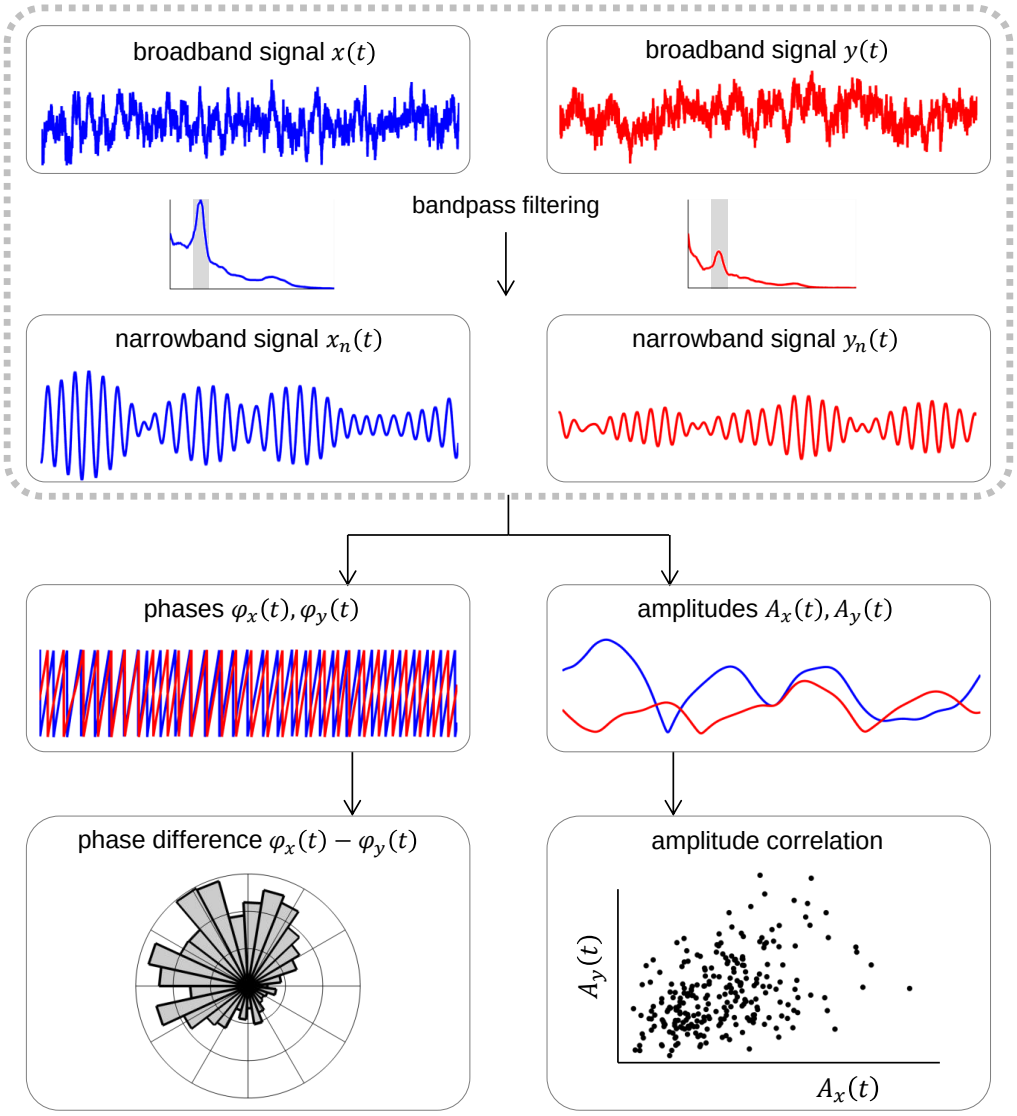

Figure 2.12: Phase and envelope synchronization. First, two broadband time series $x(t)$ and $y(t)$ are filtered into the frequency band of interest and produce narrowband signals $x_n(t)$ and $y_n(t)$. Then, phases and envelopes are extracted from $x_n(t)$ and $y_n(t)$. Phase synchronization is computed from the phases $\varphi_x(t)$ and $\varphi_y(t)$. For instance, PLV derives from the phase difference $\varphi_x(t) - \varphi_y(t)$. Envelope synchronization (such as envelope correlation) derives from $A_x(t)$ and $A_y(t)$.

time series $x(t)$ and $y(t)$ result in discretized envelope and phase vectors of same length, the envelopes contain effectively less time-related variations. In fact, envelopes are often smoothed and downsampled before being included in any connectivity algorithm (Brookes et al., 2011a). Envelope synchronization is usually assessed with the correlation coefficient between $A_x(t)$ and $A_y(t)$, which captures simultaneous power increases/decreases between $x(t)$ and $y(t)$. Envelope correlations are particularly relevant, since they seem to be closely related to fMRI bold fluctuations, and they were used to successfully extract MEG resting state networks (Brookes et al., 2011a,b; Maldjian et al., 2014). Section 3.2, employs therefore envelope correlation to investigate electrophysiological alterations in a well-known fMRI network in a sample of MCI patients and controls.

2.4.2 Applying FC to source space MEG data

Previous FC metrics can be applied to pairs of sources, to produce either:

- $N_{sources} \times N_{sources}$ FC matrices when applied to all pair of sources.
- $1 \times N_{sources}$ FC vectors when selecting a given source as a seed and computing FC with all other sources. This is called seed-based connectivity.
- $N_{ROIs} \times N_{ROIs}$ FC matrices when grouping the source space into regions of interest (ROIs).

Volume conduction

Even when working in source space, the reconstructed source time-series contain some undesired volume conduction or source leakage. This means that the source reconstruction at position $\boldsymbol{r}_j$ is influenced by the activity at position $\boldsymbol{r}_k$. This effect is notably important if $\boldsymbol{r}_j$ and $\boldsymbol{r}_k$ are spatially close, but it also depends on the signal to noise ratio of the specific region and on the validity of the hypotheses that were used in the inverse modelling. Let us consider these three effects separately (Brookes et al., 2014):

- *Distance.* Source leakage is especially relevant for neighboring sources. For this reason, displays of seed-based connectivity before leakage correction show a blur of high connectivity around the seed-point (Maldjian et al., 2014). This could also be grasped as a limitation in the spatial resolution in the source reconstruction (1-2cm).

- *Signal to noise ratio.* Source leakage is larger for sources with low signal to noise ratio. For instance, deep regions are recorded with lower signal to noise ratio than superficial regions in MEG, and their source reconstruction is therefore blurrier.

- *Inverse modelling.* All inverse models hypothesize some properties about the source activity to yield a unique solution to the inverse problem. For instance, beamformer assumes that sources are uncorrelated. Then, the more correlated two sources are, the greater the blur in their beamforming reconstruction.

Even after the previous risk factors for volume conduction have been identified, it is not possible to exactly determine the extent of the volume conduction without knowing the true source activations. However, it can be indirectly assessed with the beamforming weights correlation:

$$\text{corr}\left(\boldsymbol{w}(\boldsymbol{r}_j), \boldsymbol{w}(\boldsymbol{r}_k)\right) \tag{2.63}$$

In fact, if two source locations have highly correlated weights, the reconstructed time series are also highly correlated. In the opposite case, if two source locations have weakly correlated weights but their corresponding reconstructed time series are correlated, it is unlikely that this high correlation results from volume conduction. Although this does not constitute an accurate measure of source leakage, it is a useful estimate. In section 3.2, we intend to compare FC between MCI patients and controls. For that we compute envelope correlation as a FC metric and then compare weights correlation in both groups to ensure that the FC differences between MCI and controls do not result from volume conduction.

For other applications one may want to eliminate the volume conduction bias from the FC metric. For instance, one may want to display a seed-based connectivity map without a big blur at the seed point. A possible solution is to employ a FC metric that is insensitive to zero-lag synchronization, such as PLI or imaginary coherence (Pereda et al., 2005). The rationale behind this is that volume conduction is zero-lag: a source at $\boldsymbol{r}_j$ leaks instantly to another source at $\boldsymbol{r}_k$. However, these metrics are far from ideal since they discard both artifactual and true zero-lag interactions. An alternative is to perform some kind of orthogonalization in order to eliminate the contribution from one source in $\boldsymbol{r}_j$ to the other in $\boldsymbol{r}_k$. When using envelope correlation, this orthogonalization can be performed in the time (Brookes et al., 2012) or in the frequency domain (Hipp et al., 2012).The time domain orthogonalization uses a linear regression between each pair of sources in $\boldsymbol{r}_j$ and $\boldsymbol{r}_k$. In other words, prior to envelope correlation, the source time series $x(\boldsymbol{r}_j, t)$ is replaced by its orthogonalized

version:

$$x_{R,k}(\boldsymbol{r}_j, t) = x(\boldsymbol{r}_j, t) - \beta x(\boldsymbol{r}_k, t) \tag{2.64}$$

where β is the linear regression coefficient between $x(\boldsymbol{r}_j, t)$ and $x(\boldsymbol{r}_k, t)$. This leakage-corrected envelope correlation (lc-ecor) is employed in Chapter 4, and compared to the non-corrected or direct version (d-ecor).

Grouping FC into regions of interest (ROIs)

Source models typically include thousands of dipolar sources spread all over the brain, so that computing FC between each pair of modeled dipoles produces huge $N_{sources} \times N_{sources}$ FC matrices that are difficult to manipulate and interpret. Hence, sources are often grouped into ROIs, producing smaller $N_{ROIs} \times N_{ROIs}$ matrices. As explained in section 2.3.4, these ROIs may simply correspond to regions in a standard atlas, so that the FC matrix is comparable across individuals.

Let us define two ROIs m and n, which contain M and N sources respectively. To estimate FC between ROIS m and n, we can use any of these two options:

- Calculate FC for all pair of sources and combine all $M \times N$ FC estimates into a single FC(ROI=m,ROI=n) value. For instance, using the average value between all pairs of sources:

$$\text{FC}(\text{ROI} = m, \text{ROI} = n) = \text{mean}\big(\text{FC}(\text{source} = i, \text{source} = j)\big) \tag{2.65}$$

  where $i \in \text{ROI} = m$ and $j \in \text{ROI} = n$

- Select a representative time-series for ROIs m and n and then calculate FC between these two time series (Hillebrand et al., 2012). These representative time-series may simply be the source activity of a selected source within the ROIs, such as the source that has highest correlation with its ROI neighbors.

Although both options could seem radically different, they produce similar results. In fact, atlases divide the cortex into 80-100 ROIs, and this number is close to the number of inside components in the tSSS expansion. This means that, on average, source reconstructions within a single ROI are very similar. In Chapters 3 and 4 we employed the second option, because it is much faster to compute and produced good results in its testing phase.

Chapter 3

Resting state spectral and functional connectivity alterations in amnestic-MCI

In Chapter 1 we introduced various neuroimaging techniques and their use in the study of MCI and AD. Then, in Chapter 2 we introduced the MEG technology and the analysis techniques for MEG raw data. In this Chapter we search for abnormalities in the resting state power spectrum and functional connectivity of amnestic-MCI patients. For that, MEG recordings were performed in MCI patients and age matched controls. Then, spectrum and connectivity values were compared in both populations. Here we present two studies that are adapted from their original publications version in (Garcés et al., 2013, 2014).

3.1 Study I. Brain-wide slowing of spontaneous alpha rhythms in MCI

3.1.1 Introduction

As introduced in Chapter 1, electrophysiological rhythms have been found relevant in AD. In particular, both EEG and MEG studies have shown a slowing of the oscillatory rhythms in AD (Huang et al., 2000; Berendse et al., 2000). MCI patients exhibit a reduced mean frequency score in MEG power spectra (Fernández et al., 2006), indicating that the AD-related oscillatory slowing may have its onset in the predementia stage. Additionally, specific spectral profiles have been considered as pathological

biomarkers. For example, an increased delta and a decreased alpha1 power were found to be related to a lower cortical grey matter volume (Babiloni et al., 2013). It has also been reported that changes in the high alpha / low alpha ratio or in the theta / gamma ratio are associated with the cognitive status, conversion to AD, hippocampal and amygdalar atrophy or grey matter changes (Moretti et al., 2011, 2012, 2009a).

An essential property of the electrophysiological spectra is the dominant alpha rhythm or alpha peak. Alpha oscillations have been measured over wide regions of the exposed human cortex (Jasper and Penfield, 1949). Sensor-level EEG studies have found that their frequency rises from childhood to adolescence or young adulthood, and then decreases slowly with age (Chiang et al., 2011). Abnormally low alpha peak frequencies can be found in demented patients (Samson-Dollfus et al., 1997). Some studies of MCI have used the posterior dominant frequency to perform spectral analysis. For instance, Moretti et al. (2011, 2012, 2009a) used the individual alpha peak to define individual frequency ranges for theta, alpha, and beta bands. Babiloni et al. (2009, 2013) considered the alpha peak frequency as a covariate when performing statistical analysis. Nevertheless, although utilized as an intermediate step in the analysis pipeline of many studies, the importance of alpha peak amplitude and frequency values *per se* to define neurophysiological characteristics in MCI has been scarcely investigated.

Here we investigated the spatial distribution of resting state alpha peak frequency and amplitude over the whole brain for MCI patients and age-matched healthy controls. To this aim, beamforming was used to estimate MEG spectral parameters for the alpha peak (frequency and amplitude) in source space. Also, we analyzed how these parameters were modulated by age and sex for each brain region. Finally, we examined the relation between peak parameters and hippocampal volume, which is commonly used as a structural biomarker of AD (Dubois et al., 2007).

3.1.2 Materials and methods

Subjects

27 patients with a diagnosis of amnestic-MCI and 24 controls were included in this study. Table 3.1 summarizes their characteristics. MCI patients were recruited at the Geriatric and Neurological Units of the “Hospital Universitario San Carlos”, Madrid, Spain, where they were diagnosed by clinical experts. As introduced in (Grundman et al., 2004), inclusion criteria for MCI comprised: (1) memory complaint confirmed by an informant, (2) normal cognitive function, (3) no or minimal impairment in activities of daily living, (4) abnormal memory function, (5) not being sufficiently

impaired to meet the criteria for dementia.

Table 3.1: Subjects characteristics. Data are given as mean ± standard deviation. M = males, F = females. Educational level was grouped into five levels: 1: Illiterate, 2: Primary studies, 3: Elemental studies, 4: High school studies, 5: University studies. MMSE = Mini Mental State Examination score. Hippocampal volume was normalized with the overall intracranial volume.

Age (years)	Gender (F/M)	Educational level	MMSE	Hippocampal volume	
				Left	Right
Control (n=24)					
71.8 ± 3.6	18/6	3.8 ± 1.3	29.3 ± 0.9	$(2.62 \pm 0.37) \cdot 10^{-3}$	$(2.59 \pm 0.28) \cdot 10^{-3}$
MCI (n=27)					
71.8 ± 3.6	13/14	2.7 ± 1.3	27.5 ± 2.2	$(2.1 \pm 0.41) \cdot 10^{-3}$	$(2.08 \pm 0.49) \cdot 10^{-3}$

Additionally, all subjects were in good health and had no history of psychiatric or neurological disorders. They underwent an MRI brain scan to rule out infection, infarction or focal lesions. Subjects meeting any of the following criteria were excluded from the study: Hachinski score (Rosen et al., 1980) higher than 4, geriatric depression scale score (Yesavage et al., 1982) higher than 14, alcoholism, chronic use of anxiolytics, neuroleptics, narcotics, anticonvulsants, or sedative hypnotics. Additionally, MCI patients underwent an exam to rule out possible causes of cognitive decline such as B12 vitamin deficit, thyroid problems, syphilis, or HIV. Drugs that could affect MEG measurements such as cholinesterase inhibitors were removed 48 hours before the MEG scan. The investigation was approved by the local Ethics Committee.

MEG recordings

Three-minute MEG resting state recordings were acquired at the Center for Biomedical Technology (Madrid, Spain) with the Elekta Vectorview system described in section 2.1.3. During the measurements, subjects sat with their eyes closed and were instructed to remain calm and move as little as possible. Each subject's head was digitized in 3D with a Fastrak Polhemus system and four coils were attached to the forehead and mastoids, so that the head position with respect to the MEG helmet was continuously determined. Activity in electrooculogram channels was also recorded to keep track of ocular artefacts. Signals were sampled at 1000 Hz with an online filter of

bandwidth 0.1-330 Hz. A tSSS (section 2.2.1) was then applied with Maxfilter software (version 2.2., Elekta Neuromag) to remove external noise.

MRI acquisition

3D T1 weighted anatomical brain MRI scans were collected with a General Electric 1.5T magnetic resonance scanner, using a high-resolution antenna and a homogenization PURE filter (Fast Spoiled Gradient Echo (FSPGR) sequence with parameters: TR/TE/TI = 11.2/4.2/450 ms; flip angle 12º; 1 mm slice thickness, a 256x256 matrix and FOV 25 cm). For volumetric analysis, Freesurfer software package (version 5.1.0) and its automated sub-cortical segmentation tool (Fischl et al., 2002) were employed. For the source analysis, the reference system of the T1 volumes was transformed manually using 3 fiducial points and headshape, until a good match between MEG and T1 coordinates was reached.

Source analysis

Data analysis was done using both FieldTrip software (Oostenveld et al., 2011) and in-house scripts.

MEG preprocessing For the definition of artefact-free epochs, the continuous MEG resting state recording was split into non-overlapping segments of 4 seconds. Segments with ocular, jump or muscular artefacts were identified and discarded. Per subject, a minimum of 20 artefact-free segments (80 seconds) remained (controls: (25.7±4.8), MCI: (24.6±6.6)). After filtering of the continuous original data using a finite impulse response filter of order 1000 and a bandwidth of 1-30Hz, the artifact-free segments of the data identified in the previous step were extracted for further analysis

Headmodels First, a regular grid of 2459 points with 1cm spacing was created in the template Montreal Neurological Institute (MNI) brain. This set of points was transformed to subject's space using a linear normalization between the native T1 image and a standard T1 in MNI space with 2mm resolution. This grid constituted the source locations. The forward model was solved with Nolte method (section 2.3.2).

Beamforming Source reconstruction was performed with linearly constrained minimum variance (LCMV) beamformer (section 2.3.3). For each subject, the covariance matrix was averaged over all trials to compute the spatial filter's coefficients, and

then these coefficients were applied to individual trials, obtaining a time series per segment and source location. This reconstruction was performed for magnetometers and gradiometers separately, yielding two different source estimates per subject.

Spectral analysis

Power spectra were obtained from the time series via a multitaper method with discrete prolate spheroidal sequences as tapers and 1 Hz smoothing for frequencies between 2 and 30 Hz, with a 0.25 Hz step. These spectra were averaged over trials and normalized with the sum of the spectral power in the range [2-30] Hz. Then, an average power spectrum per region of interest (ROI) and subject was obtained. 88 ROIs were used in this study and they were defined in MNI space using the Harvard-Oxford probabilistic atlas (Desikan et al., 2006), as implemented in the fMRIb Software Library (FSL) (Jenkinson et al., 2012). 37 cortical and 7 subcortical ROIs per hemisphere were included (merging subdivisions within gyri in the Harvard-Oxford atlas).

Then, to extract alpha peak parameters, experimental spectra were fitted with a non-linear least-square procedure to:

$$\log\big(P(f)\big) = B - C \cdot \log(f) + A \cdot \exp\left(\frac{-(f - f_p)^2}{\Delta^2}\right) \tag{3.1}$$

where A, B, C, Δ and f_p are adjustable parameters and a wide range (4-13 Hz) is used for the fitting. Such a Gaussian peak fit with power-law background has been proven useful for alpha rhythm detection in EEG (Lodder and van Putten, 2011; Chiang et al., 2008).

With this procedure, a peak per ROI was identified separately for the reconstructions based on magnetometers and gradiometers. Then, magnetometer and gradiometer data were combined. Thus, the final peak amplitude and frequency per ROI and subject was calculated by averaging the peak values obtained for both types of sensors. In order to optimize the reliability of the alpha peak estimation, two criteria were considered: Peaks with (1) high inter-trial amplitude variability for any sensor type or (2) a frequency difference between the magnetometer and the gradiometer fit bigger than 1Hz, were considered spurious and removed from the subsequent statistical analysis.

Statistical analysis

Peak amplitudes and frequencies were compared with univariate ANOVA tests, separately for each ROI. Shapiro-Wilk and Levene tests were used to ensure normality

of the data and equal variances across groups. For the peak amplitude, the transformation $x \rightarrow \log(x/(1-x))$ was applied prior to statistical analysis to obtain values following a normal distribution. A 4-way ANOVA analysis was performed considering diagnosis, age, sex and educational level as factors to investigate differences between controls and MCIs and the influence of age and sex on the alpha peak. Finally, we examined whether peak parameters depended on hippocampal volume (which was normalized with the overall intracranial volume). For that, we computed the Pearson correlation coefficient between peak amplitude or frequency and hippocampal volume across all subjects, for every ROI separately. To establish the statistical significance of these correlations, an 4-way ANOVA test with hippocampal volume, age, sex and educational level as factors was used, taking all subjects (Control and MCI) as a single group.

The p-values of all ANOVA tests were corrected for multiple comparisons with a procedure based on clustering and permutations, as introduced by (Maris and Oostenveld, 2007). For that, spatially adjacent ROIs with p<0.05 were first grouped into clusters. Then, the obtained peak values (frequency or amplitude) were 2000 times randomly assigned to the original groups. The sum of F-values over each cluster in the original dataset was compared with the same measure in the randomized data. For each cluster, the proportion of randomizations with F-values higher than the ones in the original data corresponded to the final p-value.

3.1.3 Results

Peak fitting

Peaks were successfully identified for most ROIs and subjects, especially in posterior and temporal ROIs. Overall, the peak was harder to find in anterior areas of the brain, since for around 10-15% of the subjects the criteria for robustness introduced before were not fulfilled in frontal ROIs. On the whole, a peak was fit in 80±14 ROIs (given as mean±std) for the control group and in 85±5 ROIs for the MCI group. For the following ROIs, less than 85% of the subjects showed a robust peak: right paracingulate gyrus, right frontal operculum cortex, right inferior and middle frontal gyri, both superior frontal gyri, both supplementary motor cortices and right pallidum. These ROIs were not considered for statistical analysis. The average peak frequency over all ROIs was 9.68±0.71 Hz for controls and 9.05±0.90 Hz for MCIs and the average normalized amplitude was $(2.57 \pm 0.59) \cdot 10^{-2}$ for controls and $(2.70 \pm 0.49) \cdot 10^{-2}$ for MCIs.

Control vs. MCI

Both groups presented a similar spatial distribution of peak parameters, with higher amplitude and frequency in posterior ROIs, as shown in Figure 3.1. However, peak frequencies were higher in controls than in MCIs, especially over parietal and temporal ROIs, where differences were statistically significant ($p<0.05$). Amplitudes were similar in controls and MCIs, although values tended to be higher in MCIs, but this was significant only for six temporal and medial ROIs. As amplitude and frequency values are usually inversely related in electrophysiological power spectra, the amplitude increase in MCIs could be just a consequence of the frequency decrease. To investigate this effect, amplitude values were plotted as a function of frequency (Figure 3.1C). For controls, amplitudes were higher within the 9-11Hz frequency range, while for MCIs this range seemed to be broader, with high magnitude alpha peaks from 7 to 11 Hz. On the whole, this leads to the idea that alpha peak frequency is reduced in MCI.

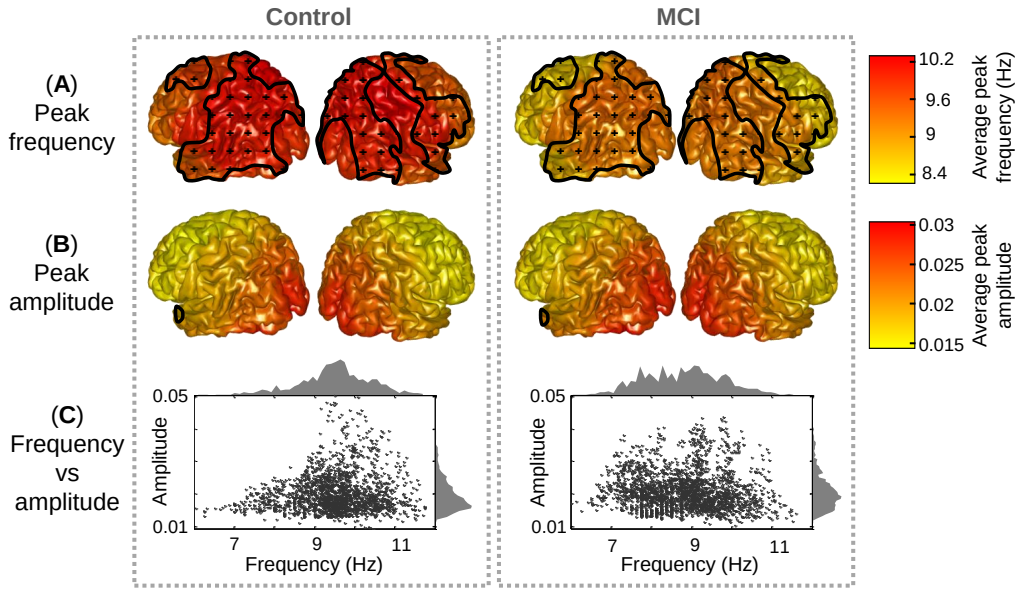

Figure 3.1: Peak distribution in controls and MCIs. Peak (A) frequency and (B) amplitude grand averages for controls and MCIs. Clusters with significant differences between controls and MCIs ($p<0.05$) are enclosed with black lines and scattered with black crosses. (C) represents a scatter plot of the peak parameters (frequency and amplitude) for every ROI and subject. Frequency and amplitude histograms are projected into the y and x axis respectively.

Age and sex influence

Sex and age did not exert a significant influence on peak amplitude, while significant effects were found for the peak frequency. Figure 3.2 displays sex differences and age correlations for peak frequency in Controls and MCIs separately. Peak frequency was higher for females than for males both in controls and MCIs. This trend was present over the whole brain, although only statistically significant ($p<0.05$) over some posterior and right frontal ROIs. Additionally, peak frequency was found to correlate negatively with age. This correlation was strongest in frontal ROIs, where a significant effect ($p<0.05$) was found.

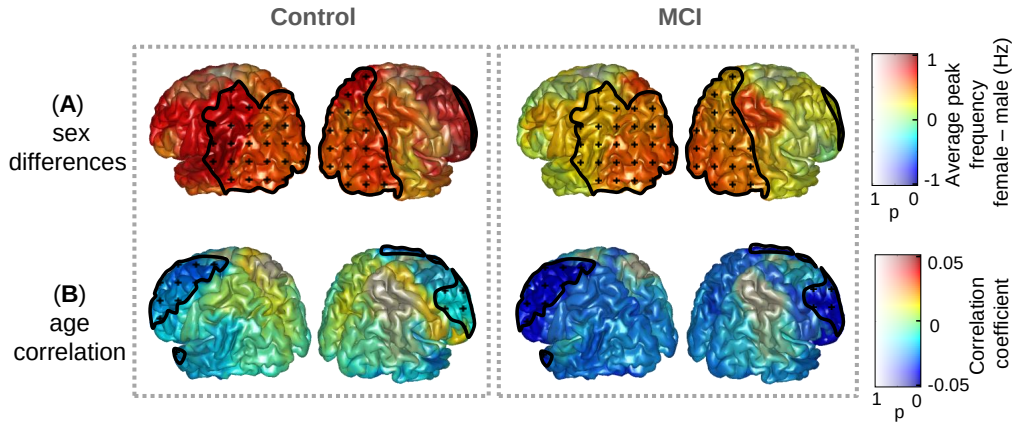

Figure 3.2: Influence of age and sex on peak frequency in controls and MCIs. (A) Peak frequency difference of grand averages: females – males (B) Correlation coefficient between age and peak frequency. Clusters with significant effect of age or sex upon peak frequencies ($p<0.05$) are enclosed with black lines and scattered with black crosses. Additionally, the p-value specifies the transparency of the plotted intensities: a region with p-value of 0 shows a full opaque color, whereas a region with p-value of 1 is transparent.

Hippocampal volume

To further assess whether differences in peak parameters could be considered as a pathological sign, the dependence of peak amplitude and frequency values with hippocampal volume was examined. Results are illustrated in Figure 3.3. Peak frequency correlated positively with hippocampal volume, reaching correlation values up to 0.6, which denote a strong association between both measures. This trend was significant ($p<0.05$) over most of the postrolandic ROIs of the brain and implies that a slowing in the main alpha rhythm is related with a greater atrophy in the medial temporal lobe.

The opposite effect was found for the peak amplitude, which correlated negatively with hippocampal volume over the whole brain, especially over occipital and frontal ROIs, where the trend was significant (p<0.05).

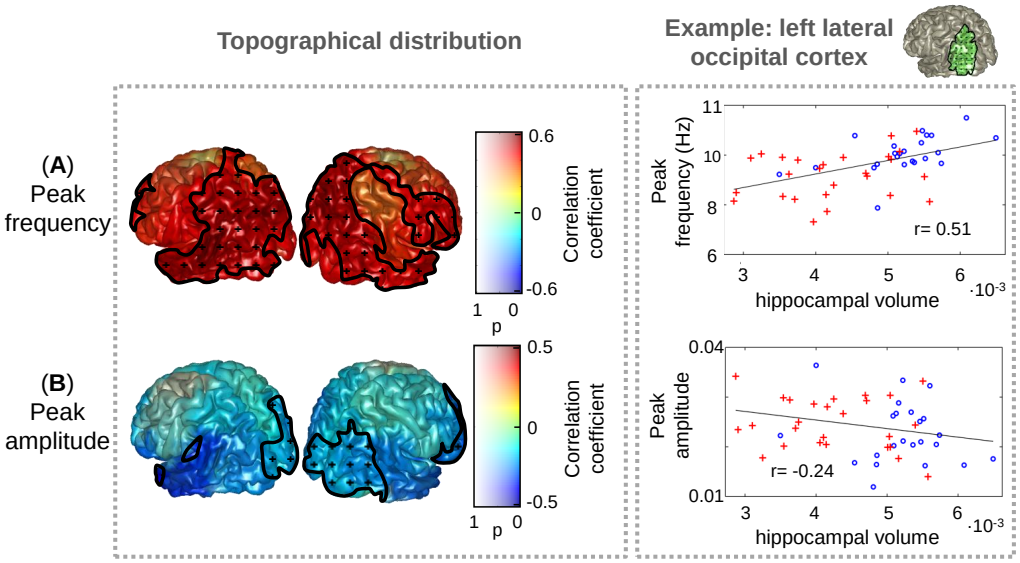

Figure 3.3: Peak frequency and amplitude correlations with hippocampal volume. The distribution of correlation coefficient between peak (A) frequency and (B) amplitude with hippocampal volume (normalized with intracranial volume) for all subjects (Controls and MCIs) is shown. Clusters with significant effect of hippocampal volume (p<0.05) are marked as in Figure 3.2. As an example, scatter plots of the average peak frequency and amplitude over posterior ROIs as a function of hippocampal volume are displayed in the right side. The included ROIs are plotted in green in the upper right side of the figure. Controls are represented as blue circles and MCIs as red crosses.

3.1.4 Discussion

Here the alpha peak parameters (frequency and amplitude) were investigated in a sample of MCI patients and controls. Differences between both groups were examined, as well as the influence of age and sex, and the correlation between peak parameters and hippocampal volume. To attain such goal, a novel method was introduced, that combined beamforming for reconstruction of the power spectra in the source space, and a fitting algorithm that has been successfully used for peak identification with scalp EEG recordings in sensor space (Chiang et al., 2011; Lodder and van Putten, 2011).

The alpha peak was robustly identified in most regions and subjects. This is not the

first attempt to assess the alpha peak spatial distribution of frequency and amplitude values in resting state, since clusters of alpha peaks in EEG recordings within a large sample of healthy population have been analyzed in sensor space (Chiang et al., 2011). However, in the present study the MEG source space analysis allows a better understanding of the spatial distribution of this dominant alpha rhythm. Most studies of pathological aging have only focused on the posterior alpha peak (Osipova et al., 2006). Here we intentionally decided to consider sources of alpha rhythm other than the posterior ones, since alpha rhythms have been detected over wide regions of the brain (for a review, see Nunez et al. (2001)).

One of the main findings of our study is that the alpha rhythm of MCIs is slower when compared with a control population, especially over posterior regions. This is not surprising, since abnormally low alpha peak frequencies in AD have already been described (Passero et al., 1995). In the MCI literature less attention has been drawn to the alpha peak, but a reduced mean frequency score has been reported (Fernández et al., 2006). To gain further insight into the meaning of these peak alterations, their relationship with the hippocampal volume was considered. In fact, atrophy in medial temporal structures such as the hippocampus is a pathological marker of AD (Dubois et al., 2007; Prestia et al., 2013) . Some studies have related a lower hippocampal volume to a higher delta and theta dipole density in AD (Fernández et al., 2003), lower power in the 8-10.5 Hz range (Babiloni et al., 2009), and an increase in the alpha3/alpha2 ratio (Moretti et al., 2009b). Our results show that hippocampal volumes correlated positively with peak frequencies in temporo-parieto-occipital regions of the brain and negatively with peak amplitude in occipital and frontal regions. This contributes to the idea that the peak frequency slowing is associated with a degenerative process, evolving in parallel with the loss of hippocampal volume. Two different hypotheses have been introduced over the past years to explain the increased low frequency power in AD and MCI. It could be explained through either (1) a slowing down or (2) a redistribution of the oscillatory sources in the theta-alpha frequency range (Osipova et al., 2005, 2006). This study supports the first hypothesis, although bigger samples and an analysis of the possible spatial shift of the sources would be needed to make stronger statements and investigate the second hypothesis.

The exact physiological origin of alpha rhythm remains unclear. Some studies indicate a prominent role of the thalamus (Hughes and Crunelli, 2005; Lőrincz et al., 2009; Bollimunta et al., 2011), while others point out the existence of cortical generators (Flint and Connors, 1996; Bollimunta et al., 2008). With a thalamo-cortical model of EEG generation, Hindriks and van Putten (2013) established that the resonance properties of cortico-thalamo-cortical, intra-cortical and feedforward circuits deter-

mine alpha responses. They found that both a decreased firing of excitatory neuronal populations and an increased firing rate in inhibitory neuronal populations related to a decrease in alpha frequency. This modulation was particularly intense in the intracortical circuit: a decreased delay in this circuit produced a strong frequency slowing. Moreover, a decrease in the number of active synapses in thalamic nuclei could also explain an alpha power shift towards lower frequencies, as proved in a recent study with a thalamico-cortical-thalamic neural mass model (Bhattacharya et al., 2011). This model showed that the alpha frequency shift is especially sensitive to damage in inhibitory interneurons in the thalamus. Within this theory, the MCI alpha slowing found in this study would suggest that a synaptic damage is already present in the MCI stage. This in turn could be related with Aβ, since its deposition has been shown to contribute to synaptic loss in AD (Reddy and Beal, 2008; Bate and Williams, 2011).

Additionally, the peak frequency is not determined exclusively by the pathology, but also depends on other factors like age or sex. In fact, we found a frequency decrease with age, and higher frequency values in females than in males. Such trends have been previously found in studies with large healthy samples (Chiang et al., 2011). In our study, we report that this trend is maintained in MCI patients. Most studies of sex differences in the alpha band have focused on childhood and young age, with mixed outcomes, some of them finding higher frequencies and earlier maturation in girls than boys (Petersén and Eeg-Olofsson, 1971). Our results also show higher frequencies in females than in males, although within a completely different age profile. Dustman et al. (1993) found that a slowing of alpha rhythms and an increase in delta, theta and beta activity are common age-associated changes in EEG spectra. This means that the alpha slowing is normal in healthy aging, and suggests that the MCI disease speeds up the natural aging process.

The methodological procedure followed here enabled the examination of amplitude and frequency shifts of the alpha peak. It combined beamforming of MEG resting state data, alpha peak fitting and ANOVA tests for statistical analysis, corrected for multiple comparisons with a procedure including clustering and permutations. Although it was tested with a rather small sample of subjects, it revealed a slowing of the alpha oscillatory sources in MCI and established that age, sex and hippocampal volume affect peak amplitude and frequency. However, larger samples would be needed to confirm these effects and to evaluate others, such as an interaction between age, sex, or educational level. Additionally, longitudinal follow-up studies could provide insight into the evolution of the slowing process and the onset of the AD-related pathology.

3.2 Study II. The default mode network is functionally and structurally disrupted in MCI

3.2.1 Introduction

Recent literature has identified that the Default Mode Network (DMN) is involved in the AD pathology. This network was first introduced by Raichle et al. (2001) and has garnered increasing attention from the neuroscience and neurology communities ever since (see Rosazza and Minati (2011) for a review). It is highly active during an idle state and deactivates during task performance. It includes brain regions such as the precuneus, posterior and anterior cingulate, and the inferior parietal cortex (Greicius et al., 2003; Raichle and Snyder, 2007; Buckner et al., 2008). The precuneus and posterior cingulate cortex have been found to be relevant in AD as they show decreased metabolic activity (Matsuda, 2001) and accumulate Aβplaques at an early stage in the disease (Mintun et al., 2006). DMN alterations such as decreased activity and connectivity have been reported in AD and MCI (Greicius et al., 2004; Rombouts et al., 2005; Qi et al., 2010; Sorg et al., 2007; Jones et al., 2011; Agosta et al., 2012). Furthermore, these alterations were found to be related to the severity of the disease and its progression (Petrella et al., 2011; Brier et al., 2012).

To date, fMRI is the most widespread technique used to explore the DMN in MCI or AD. Blood-oxygenation-level-dependent (BOLD) fMRI signals measure hemodynamic responses to neuronal activity with great spatial resolution and have led to the discovery of multiple resting state networks, including the DMN. Other imaging modalities can also provide insight into DMN integrity in MCI: structural MRI reveals brain atrophy; DTI reconstructs white matter tracts; PET detects metabolic activity or Aβplaques and MEG/EEG measure magnetic/electric fields generated by neural currents. Based on this fact, researchers have combined fMRI (often controlling for brain atrophy with T1-weighted structural MRI) with other neuroimaging modalities such as PET (Hedden et al., 2009; Sperling et al., 2009; Sheline et al., 2010) and DTI (Wee et al., 2012), or DTI with PET (Bozoki et al., 2012) to investigate DMN functional and structural connectivity impairment in AD and MCI.

While fMRI and PET give an indirect estimation of neural activity, EEG/MEG are direct measures of neural firing. Therefore, these neurophysiological techniques enable us to gain a better understanding of the time-frequency dynamics of the DMN, providing us with useful information as to how its regions are connected at different frequency bands. Complementary structural information about DMN connectivity is given by DTI, as it enables the modelling of the white matter connections that support the network. Using this technique, we can compute direct or weighted structural con-

nectivity measures that estimate the number of tracts connecting two regions and the integrity of anatomical connections, respectively. However, thus far, the combination of MEG and DTI has not been used to unravel DMN abnormalities in MCI. In this study, we investigated the DMN in MCI patients compared to age-matched controls using resting-state MEG and DTI data to extract both functional and structural networks. Our purpose was to determine the functional connections that are altered in MCI relative to controls at different frequency bands, and how this relates to the underlying structural network. For that, source space MEG functional connectivity (FC) was computed and two different structural connectivity (SC) measures were used to evaluate whether the amount of tracts or their integrity influence the organization of the functional networks. Our initial hypothesis is that both functional and structural connections will be significantly impaired in MCI patients and there will be a strong correlation between FC and SC abnormalities.

3.2.2 Materials and methods

Subjects

This study included 26 patients with a diagnosis of amnestic-MCI and 31 age-matched controls. MCI patients were diagnosed as in the previous study (section 3.1), following (Grundman et al., 2004). Table 3.2 summarizes the subject's characteristics.

Table 3.2: Subject characteristics. Data are given as mean ± standard deviation. M = males, F = females, Educational level was grouped into five levels: 1: Illiterate, 2: Primary studies, 3: Elemental studies, 4: High school studies, 5: University studies. MMSE = Mini Mental State Examination score. Controls and MCIs differed in MMSE (p=0.0012) and educational level (p=0.03), and did not differ in age (p=0.39) or sex (p=0.44).

	n	Age (years)	Gender (F/M)	Educational level	MMSE
Control	31	70.8 ± 4.2	21/10	3.5 ± 1.2	29.5 ± 0.7
MCI	26	72.5 ± 6.7	15/11	2.8 ± 1.3	27.7 ± 2.4

MEG and MRI acquisition

Resting-state MEG recordings and T1-weighted MRI images were acquired as the in previous study (section 3.1.2). Diffusion weighted images (DWI) were acquired with a single shot echo planar imaging sequence with the following parameters: TE/TR 96.1/12000 ms; NEX 3 for increasing the SNR; 2.4 mm slice thickness, 128x128 matrix

and 30.7 cm FOV yielding an isotropic voxel of 2.4 mm; 1 image with no diffusion sensitization (i.e., T2-weighted b0 image) and 25 DWI (b=900 s/mm^2).

Definition of the regions of interest

For this bimodal connectivity analysis, we defined Regions of Interest (ROIs) in the individual's structural T1 volume using the Freesurfer (version 5.1.0) cortical parcellation in 66 regions (Desikan et al., 2006), such as in (Hagmann et al., 2008; Honey et al., 2009). We selected four ROIs per hemisphere, which are the most common brain structures included in the DMN (Greicius et al., 2003; Raichle and Snyder, 2007; Buckner et al., 2008): precuneus (lPr and rPr), anterior cingulate (lAC and rAC), posterior cingulate (lPC and rPC) and inferior parietal (lIP and rIP).

MEG functional connectivity (FC)

MEG preprocessing and source reconstruction were performed with FieldTrip software (Oostenveld et al., 2011).

Source reconstruction First, ocular, jump and muscular artefacts were identified and located in the 3 minute resting state recordings. Then, the continuous resting time-series were segmented into artefact-free segments of 4 seconds. All subjects had a minimum of 16 artefact-free segments (control: (27.5±5.9), MCI: (27.2±6.1)). Data was filtered in the 1-45Hz band for spectral analysis and in delta (2-4Hz), theta (4-8Hz), alpha (8-12Hz), low beta (12-20Hz), high beta (20-30Hz) and gamma (30-45Hz) bands and for the functional connectivity analysis. To do so while avoiding edge effects, the continuous 3 minute data was first filtered with a finite impulse response filter of order 1000, and then the artefact-free segments were extracted for further analysis.

Source locations were defined in the subject's space using the cortical segmentation produced by Freesurfer. A regular mesh of points with 1cm spacing was created inside each ROI. The number of source locations depended on individual's data (control: (124±14), MCI: (118±15)). The forward model was solved with a realistic single-shell model (Nolte, 2003).

Source reconstruction was performed with Linearly Constrained Minimum Variance beamformer (section 2.3.3) separately for each frequency band. For each subject, the average covariance matrix over all trials was used to compute the spatial filter's coefficients, and then these coefficients were applied to individual trials, obtaining a time series per segment and source location. To avoid mixing MEG sensors with

different sensitivities or resorting to scaling, only magnetometers were used for this source reconstruction step. We must note, however, that gradiometer information is indirectly present as both magnetometers and gradiometers were used in the tsss filtering.

Preliminary power spectrum analysis The goal of this work was to study FC in classical frequency bands, defined with fixed frequency limits. Prior to that, we tested if power spectrum was altered in the MCI sample in these frequency bands. Power spectra were obtained from the time series via a multitaper method with discrete prolate spheroidal sequences as tapers and 1 Hz smoothing for frequencies between 2 and 45 Hz, with a 0.25 Hz step. Average spectra over trials were used and normalized with the sum of the spectral power in the 2-45 Hz range. Then, an average power spectrum per ROI and subject was obtained. Power was averaged per frequency band and Mann-Whitney tests were performed to compare power values between controls and MCIs. Alpha peaks were computed as in section 3.1.2 to evaluate a possible slowing of the spectra.

Functional connectivity FC was obtained from the source reconstruction with the amplitude correlation method (Brookes et al., 2011a). For this, the amplitude of the bandpass filtered time series was extracted with Hilbert transforms and correlation coefficients between the amplitude of all source locations were computed. Then, connectivity values were averaged over links connecting the same ROIs, producing an average 8×8 connectivity matrix per subject. Additionally, we calculated the correlation between beamformer weights in both groups in order to have an estimate of volume conduction.

Structural connectivity

Diffusion weighted images were pre-processed with FMRIB's Diffusion Toolbox (FDT[1]). Pre-processing consisted of eddy-current correction, motion correction and removal of non-brain tissue using the robust Brain Extraction Tool (Smith, 2002). Diffusion Toolkit (DTK[2]) was used to fit the diffusion tensor model. We used tensorline tractography (Lazar et al., 2003) to estimate the fiber tracts between the selected ROIs. Stopping criteria for the streamlines propagation were a maximum angle of 35° between consecutive steps and a lower threshold of fractional anisotropy of 0.2 (Johansen-Berg et al., 2004). A streamline was considered a connection between two ROIs if it

[1] http://fsl.fmrib.ox.ac.uk/fsl/fslwiki/FslOverview/
[2] http://www.trackvis.org

entered at least one voxel of each ROI. We then computed two different SC estimates: direct SC (dSC) and weighted SC (wSC). dSC was defined as the number of streamlines connecting a given pair of ROIs and represents the number of tracts that connect two ROIs. wSC is weighted with fractional anisotropy (FA) and evaluates the integrity of the structural connection:

$$\text{wSC} = \frac{1}{N}\sum_{n=1}^{N}\frac{1}{V_n}\sum_{v=1}^{V_n}\text{FA}_{n,v} \tag{3.2}$$

where N =dSC is the number of streamlines connecting a pair of ROIs, $v = 1 \dots V_n$ is the set of voxels that are crossed by a given streamline n and $\text{FA}_{n,v}$ is the FA in the voxel v of the streamline n.

Statistical analysis

To examine the differences between controls and MCIs in spectral power and FC or SC we used non-parametric Mann-Whitney tests. In all cases, in order to correct for multiple comparisons we followed a permutation approach which was introduced in (Maris and Oostenveld, 2007). First, the original values were 2000 times randomly assigned to the original groups (controls and MCIs) and a Mann-Whitney test was performed for each randomization. Then, the U-value in the original dataset was compared to the ones obtained with the randomized data. The final p-value was defined as the proportion of permutations with U-values higher than the one in the original data.

3.2.3 Results

MEG power spectrum

Preliminary spectral analyses were carried out to determine whether power spectrum was altered in MCI. MCIs tended to have higher spectral power in the theta band, and lower power in the beta and gamma bands, but no significant differences were obtained. Alpha peak frequency was lower for MCIs than for controls in all ROIs, although differences were only significant for the inferior parietal cortex bilaterally ($p<0.05$).

Functional connectivity

MEG FC networks differed significantly between controls and MCIs in the alpha band, while no differences were found for the delta, theta, beta and gamma bands. Table 3.3

contains the p-values of the statistical analysis for each link and frequency band. In the alpha band, FC was lower in the MCI group, especially in links including Pr and IP, as displayed in Figure 3.4. To determine whether volume conduction could be causing these differences, we calculated the correlation between beamforming weights, which is an estimate of source leakage. If two source locations have similar weights (or a high correlation between their weights), the reconstructed time series would be highly correlated. In the opposite case, if two source locations have a low weight correlation but the corresponding reconstructed time series are correlated, it is unlikely that the high FC results from volume conduction. Beamformer weights did not differ between controls and MCIs in any frequency band, which makes it unlikely that the FC differences were caused by volume conduction.

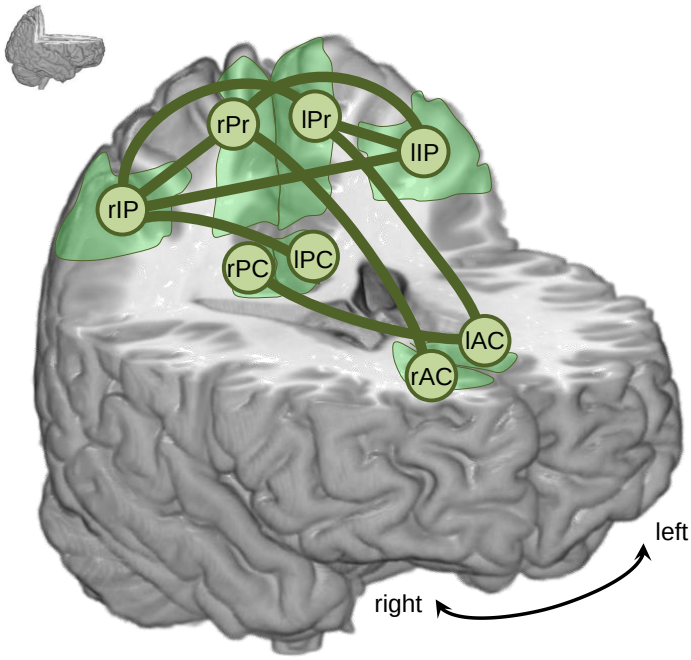

Figure 3.4: FC differences between controls and MCIs in the alpha band. Green links display connections with a significant decrease in MEG FC in the MCI group ($p<0.05$). ROIs are represented as circles (Pr: Precuneus, IP: Inferior parietal, PC: Posterior cingulate, AC: Anterior cingulate, l: left, r: right).

Structural connectivity

Streamlines connecting all ROIs were reconstructed with tensorline tractography, yielding a dSC measure. Thousands of streamlines were found between most ROIs

Table 3.3: FC and SC differences between controls and MCIs. p-values are indicated for each link, after correction for multiple comparisons. Significant p-values ($p<0.05$) are shown in bold. All significant differences corresponded to MCI<control. For structural connectivity, n.i. indicates that this link was not included in the statistical analysis. (Pr: Precuneus, IP: Inferior parietal, PC: Posterior cingulate, AC: Anterior cingulate, l: left, r: right).

Link	FC						SC
	Delta	Theta	Alpha	Low beta	High beta	Gamma	
lPr - rPr	0.32	0.40	0.24	0.29	0.24	0.34	0.06
lPr - lPC	0.18	0.19	0.15	0.12	0.55	0.20	0.10
lPr - rPC	0.73	0.56	0.78	0.37	0.35	0.55	**0.005**
lPr - lIP	0.44	0.32	**0.004**	0.46	0.42	0.65	0.13
lPr - rIP	0.26	0.87	**0.012**	0.19	0.74	0.54	**0.024**
lPr - lAC	0.68	0.46	**0.014**	0.97	0.34	0.35	0.26
lPr - rAC	0.68	0.69	0.08	0.82	0.77	0.72	n.i.
rPr - lPC	0.23	0.23	0.15	0.09	0.16	0.08	0.052
rPr - rPC	0.99	0.96	0.47	0.85	0.85	0.82	0.15
rPr - lIP	0.87	0.77	**0.003**	0.06	0.29	0.29	**0.014**
rPr - rIP	0.09	0.21	**0.002**	0.08	0.72	0.65	0.072
rPr - lAC	0.18	0.71	**0.008**	0.68	0.60	0.18	n.i.
rPr - rAC	0.82	0.35	0.29	0.25	0.59	0.12	0.17
lPC - rPC	0.75	0.43	0.73	0.29	0.42	0.59	**0.007**
lPC - lIP	0.30	0.61	0.45	0.78	0.78	0.93	**0.008**
lPC - rIP	0.90	0.99	**0.004**	0.12	0.89	0.87	**0.029**
lPC - lAC	0.17	0.42	0.30	0.92	0.22	0.89	0.49
lPC - rAC	0.71	0.59	0.07	0.85	0.23	0.25	n.i.
rPC - lIP	0.36	0.51	0.34	0.13	0.38	0.97	**0.002**
rPC - rIP	0.88	0.83	0.09	0.19	0.79	0.89	**0.041**
rPC - lAC	0.27	0.22	**0.003**	0.84	0.38	0.13	n.i.
rPC - rAC	0.52	0.97	0.38	0.85	0.41	0.82	0.75
lIP - rIP	0.83	0.58	**0.009**	0.21	0.32	0.85	0.11
lIP - lAC	0.54	0.55	0.40	0.27	1.00	0.85	n.i.
lIP - rAC	0.60	0.51	0.93	0.29	0.87	0.78	n.i.
rIP - lAC	0.84	0.72	0.06	0.97	0.85	0.08	n.i.
rIP - rAC	0.30	0.26	0.50	0.67	0.65	0.38	n.i.
lAC - rAC	0.79	0.74	0.94	0.98	0.94	0.94	**0.031**

(on average over all links and subjects, dSC = 4413 ± 5594 tracts, given as mean ± std). Higher dSC values (~ 10^4) were obtained between pairs of neighboring regions (such as lPr–rPr, lAC–rAC or lPC-rPC). Conversely, lower dSC values were found (~ 10^2) for some long distance connections such as AC-Pr and AC-IP. Small amounts of reconstructed tracts, especially in long connections, can be caused by the inherent limitations of the DTI and tractography techniques: fiber crossing, fanning or kissing impair the accuracy of the tractography. To control for this effect, links between ROIs were not included in the statistical analysis if, for at least three subjects, less than 100 streamlines were reconstructed (dSC<100). Following this criterion, the following 8 links were removed from the statistical analysis: lAC–lIP, lAC–rIP, rAC–lIP, rAC–rIP, lAC–rPr, rAC–lPr, lAC-rPC and rAC-lPC. For the remaining links, we compared dSC and wSC (the mean FA along the reconstructed tracts) between controls and MCIs. No differences were found for dSC ($p<0.05$). However, wSC was significantly lower in the MCI group than in the control group ($p<0.05$), especially in links involving IP and PC, as displayed in Figure 3.5. P-values for each link are included in Table 3.3.

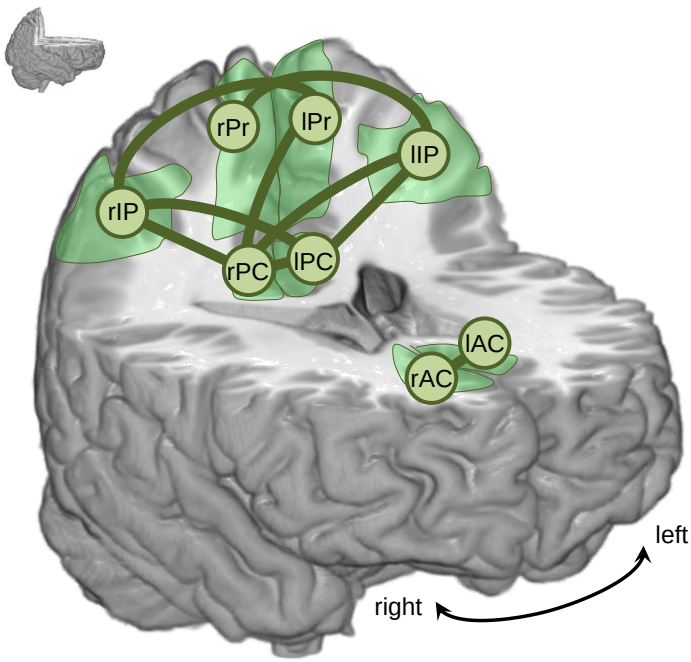

Figure 3.5: SC differences between controls and MCIs. Green links display connections with a significant decrease in wSC in the MCI group ($p<0.05$). ROIs are represented as circles (Pr: Precuneus, IP: Inferior parietal, PC: Posterior cingulate, AC: Anterior cingulate, l: left, r: right).

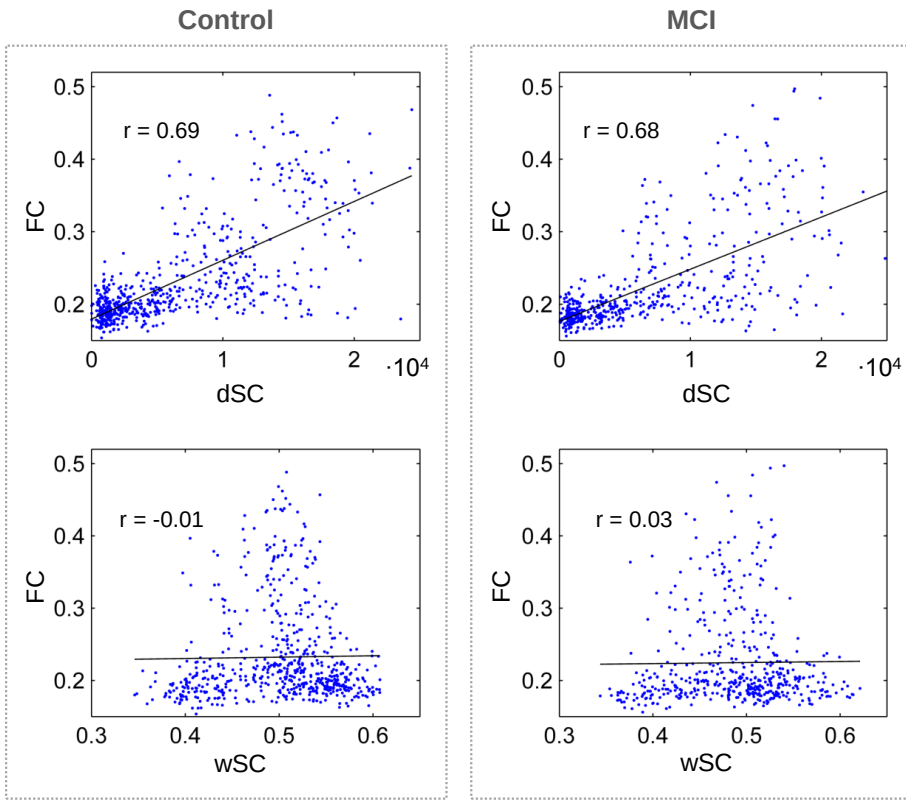

Figure 3.6: Relation between SC and FC. FC is plotted as a function of SC for all subjects and pairs of ROIs, separately for controls and MCIs (in the left and right column respectively). The dependence with the direct SC (dSC) is shown in the top row, and the dependence with fractional anisotropy weighted SC (wSC) is shown in the bottom row. The Spearman correlation coefficient between FC and SC is plotted along in each case.

Correlation between FC and SC

To determine the relationship between FC and SC, we examined how FC values changed with dSC and wSC for all links and subjects with Spearman correlations, as shown in Figure 3.6. All links between ROIs with dSC > 100 were employed in the correlation. FC and dSC were positively correlated in both MCIs ($r = 0.68$, $p < 10^{-5}$) and controls ($r = 0.69$, $p < 10^{-5}$), and high values of FC corresponded with high dSC values. FC and wSC were not significantly correlated for MCIs ($r = 0.03$, $p = 0.48$) or controls ($r = -0.01$, $p = 0.84$). For both dSC and wSC, the dependency pattern was similar for controls and MCIs.

3.2.4 Discussion

In this study, we examined FC and SC within the DMN in a sample of MCI patients and healthy elderly subjects. FC derived from MEG source space reconstruction of resting state data, and SC was extracted from tensorline tractography of DTI images. Three main findings were obtained. Firstly, the DMN was functionally disrupted in the MCI group, specifically in the alpha band, as shown by a decreased FC relative to controls. Secondly, the DMN was also structurally damaged in the MCI group, as indicated by a reduction in FA along the reconstructed white matter pathways connecting DMN regions. Lastly, FC and dSC measures were related, while no significant correlation was obtained for wSC.

The overall results are in line with some previous studies in MCI. Functional disruption of the DMN in MCI has already been reported in fMRI experiments (Sorg et al., 2007; Agosta et al., 2012). Recent reports indicate that lower FC values relate to a worse performance in cognitive tests, a higher conversion rate from MCI to AD (Binnewijzend et al., 2012) or to AD progression (Damoiseaux et al., 2012). Thus, FC appears to offer valuable information in MCI-AD continuum. Using fMRI, Sambataro et al. (2010) observed that FC in the DMN decreased with age along with task performance in a sample of healthy young and old subjects.

Our MEG findings confirm and extend the notion that the DMN is functionally impaired in MCI, and show that this FC disruption occurs specifically in the alpha frequency band, while no differences were found in delta, theta, beta or gamma frequency bands. Alpha band alterations are in fact well-known in MCI and they have been shown to relate for instance to the stability of the clinical condition (Babiloni et al., 2011) or amygdalo-hippocampal atrophy (Moretti et al., 2009b). Additionally, the alpha band seems to be the most relevant frequency band in the DMN, even in healthy subjects. For instance, Brookes et al. (2011b) performed an independent component analysis to extract resting state networks from MEG data, and achieved a great similarity for the DMN between fMRI and MEG data filtered in the alpha band. Knyazev et al. (2011) identified the DMN exclusively in the alpha band using EEG activity during rest and during the performance of a cognitive task, and Mayhew et al. (2013) demonstrated an interaction between alpha power and fMRI responses in the DMN. For this study, this could imply that the coupling between DMN regions is impaired in MCI in its main working rhythm (alpha), while their FC remains unaffected for the other frequency bands.

With regard to SC, anatomical disconnection or loss of white matter integrity (often assessed through FA) has been repeatedly observed in MCI, especially in cingulum fibers (Kiuchi et al., 2009; Bozoki et al., 2012). These white matter abnormalities

have been considered relevant, as they have been associated with performance in neuropsychological tests (Fellgiebel et al., 2005) or conversion rate to AD (Fu et al., 2013). We also noted that differences between controls and MCIs in SC were only significant for wSC but not for dSC. This indicates that SC disruption of the DMN in MCI may be mainly attributed to an abnormal structural integrity of tracts rather than to a reduction of the number of streamlines connecting DMN regions. Therefore, FA along reconstructed tracts appears to have a higher sensibility to detect this disruption than the dSC index.

We observed that dSC correlated positively with FC, while no significant correlation was found for wSC and FC. This suggests that the FC measure is more dependent on the amount of tracts connecting two ROIs than on the integrity or FA of these tracts. Other studies had also found positive correlations between SC and fMRI FC in the DMN (Honey et al., 2009; Khalsa et al., 2014), although this is to our knowledge the first study that combines MEG FC and SC in MCI patients. Additionally, we found that the topographic pattern of network disruption in MCI was similar for FC and SC. FC and SC were reduced in MCI patients in the posterior part of the DMN, particularly affecting links connecting IP with Pr or PC. While FC between anterior cingulate and the posterior part of the DMN was reduced in MCI, no differences could be seen with SC, although this may be attributed to limitations in the tractography technique (Jbabdi and Johansen-Berg, 2011; Jones et al., 2013).

The exact physiological mechanisms that underlie functional and structural disconnections are unknown. However, some bimodal PIB-PET - fMRI studies have provided an insight into the matter: reduced FC seems to relate to Aβin healthy controls and AD patients (Hedden et al., 2009; Sperling et al., 2009; Sheline et al., 2010). Similar findings have been obtained in transgenic mice with an optical intrinsic signal imaging technique (Bero et al., 2012). The present MEG study provides additional information to this functional disruption seen in MCI: it is strongest in the alpha band. Interestingly, alpha rhythms are especially sensitive to the number of active synapses and firing rate in cortical and thalamic neuronal populations (Bhattacharya et al., 2011; Hindriks and van Putten, 2013), and Aβdeposition has been shown to contribute to synaptic loss in AD (Reddy and Beal, 2008; Bate and Williams, 2011). With regard to the structural white matter abnormalities, although they are often attributed to Wallerian degeneration (Bozzali, 2002), some studies point out that Aβdeposition could be involved as well (Serra et al., 2010).

It is important to note that this study is subjected to some methodological and experimental limitations. Firstly, quantifying FC from resting state MEG data is not trivial. Here, we used beamforming for source space reconstruction and amplitude

correlation as a FC metric. This amplitude correlation algorithm has a clear drawback: it is sensitive to volume conduction. Other methods such as Phase Lag Index (Stam et al., 2007) overcome this problem since they are not affected by zero-phase lag interactions. However, they have the disadvantage of discarding true zero-phase lag interactions. Given that the amplitude correlation method has been proven to be suitable for reproducing fMRI networks (Brookes et al., 2011a), we chose this method to asses FC within the DMN network: the DMN was in fact discovered and mainly explored in the fMRI community. However, taking into account that volume conduction could contaminate this FC metric, we used the weight correlation as an estimate of volume conduction to ensure that differences between groups were not caused by this factor. Secondly, quantifying structural connectivity is also a delicate task: tractography techniques are prone to errors, especially when fibers cross, kiss or bend (Jbabdi and Johansen-Berg, 2011; Jones et al., 2013). Long distance connections tend to be biased due to error accumulation and are therefore difficult to evaluate. Thus, we decided not to include connections with a small amount of reconstructed fibers into the statistical analysis. Thirdly, we employed anatomically defined ROIs to study the DMN. We relied on the literature and selected 8 ROIs that are commonly included in the DMN, and thereby assumed that these ROIs really form the DMN in our sample. However, it would be interesting to explore the spatial extent of the DMN in a MCI sample with MEG at different frequency bands, possibly with an independent component analysis (Brookes et al., 2011b; Luckhoo et al., 2012) or combining resting state with task activity (Petrella et al., 2011; Wang et al., 2013).

3.3 Conclusions

In conclusion, our studies revealed some abnormalities in the resting state activity of amnestic-MCI patients, when compared to age-matched controls. First, the alpha peak was altered in the MCI sample: MCIs presented lower peak frequencies. This slowing correlated with the degree of hippocampal atrophy, highlighting its pathological meaning. Second, the DMN was functionally disrupted in MCI subjects in the alpha band and also structurally disconnected, as indicated by a reduction in FA in the tracts connecting different DMN regions. These findings are in agreement with previous fMRI and DTI experiments and indicate that MEG is sensitive to early functional connectivity abnormalities that occur in MCI disease. Before attempting to use these MEG differences as a clinical tool, their reliability should be established. In fact, we cannot speculate about the potential use of MEG measures as biomarkers of amnestic MCI before evaluating their test-retest reliability. This is further discussed in

the next Chapter.

Chapter 4

Reliability of MEG functional connectivity and spectral estimates

In the previous chapter we investigated differences between MCI patients and controls in spectral and FC estimates measured with MEG. For that we followed a common analysis approach: comparing the scores of two populations (MCI patients and controls) against the null-hypothesis that they are extracted from identical distributions. Although this reveals differences between both populations, it fails to provide results at the individual level. In fact, before MEG is used to provide conclusions for individual subjects, the reliability of MEG measurements should be assessed. This is the goal of this chapter. To estimate MEG test-retest reliability, we recorded three sessions of MEG resting state data per subject, and we evaluated the intraclass correlation coefficient, the within- and the between-subject reliability in power and FC estimates.

4.1 Introduction to reliability

4.1.1 Some definitions

Before tackling the study of reliability of MEG spectral and connectivity measures, let us define some related concepts: accuracy, precision, agreement, reliability, repeatability and reproducibility, based on (Barnhart et al., 2007; JCGM, 2008; Bartlett and Frost, 2008).

Accuracy and precision

On the one hand, the accuracy of a measurement refers to the closeness between the measurement and the true value of the targeted quantity. On the other hand,

precision refers to the closeness between replicate measurements of the same targeted quantity (Barnhart et al., 2007; JCGM, 2008). However, there is some confusion about the use of both terms in the literature. In fact, accuracy is sometimes used to designate systematic error and precision for random error, and both terms are occasionally used indistinctly.

Repeatability and reproducibility

Repeatability refers to the closeness between measurements results that were obtained under the same exact conditions (Barnhart et al., 2007; Bartlett and Frost, 2008). It is therefore virtually impossible to perform repeatability studies, since any variation in the object/subject to be measured, instrumentation or environmental factors from measurement to measurement cancels the repeatability conditions. This is especially critical with human subjects, which present some inherent variability over time.

In contrast, reproducibility requires less strict conditions. It refers to the closeness between measurement results that were obtained under simply similar conditions. Usually one wants to investigate the reproducibility of some results when changing a given condition, such as the instrumentation (i.e. MEG system) or the analysis method (i.e. beamforming vs. minimum norm), and keeping the remaining conditions as constant as possible. The ultimate goal of all research is to be reproducible. Ideally, results obtained with a given subject sample, imaging system, analysis method and laboratory should be reproducible with a similar subject sample, an equivalent imaging system and a different analysis method in any other laboratory. This is however a very ambitious goal, especially nowadays in MEG research. Before confronting the reproducibility of MEG studies results, we should explore its reliability, as introduced below.

Agreement and reliability

The agreement between two results simply refers to the closeness between them, or the degree to which they are identical (Bartlett and Frost, 2008; Gisev et al., 2013). Reliability is a more complicated concept, which relates to the variability of the measurement values (or scores) and errors. Although absolute estimates of reliability are occasionally used, reliability is usually considered as a relative quantity, which can be defined as (Weir, 2005):

$$\text{reliability} = \frac{\sigma_r^2}{\sigma_r^2 + \sigma_w^2} \tag{4.1}$$

where σ_r^2 and σ_w^2 represent the true score variance and the error variance, respectively. Reliability ranges therefore from 0 (no reliability) to 1 (perfect reliability), and various measurements are required to estimate it. Depending on the conditions on which these measurements are performed, different reliability types can be distinguished (Scholtes et al., 2011):

- *Internal consistency:* it is only applicable when the score consists in different items, which in turn reflect distinct constructs. It refers to the consistency or interrelatedness between these items.
- *Inter-rater reliability:* it is applicable when the same target scores are obtained by different raters.
- *Intra-rater reliability:* it is applicable when the scores are obtained by the same rater at different times.
- *Test-retest reliability:* the scores are obtained with the same objects (or subjects) at different instances.

In neuroimaging, we focus on test-retest reliability, which is estimated by carrying out various measurement sessions for each subject. Let us call x_{ij} the measured (or observed) score for subject i in session j. For instance, x_{ij} can designate the resting state alpha power in the precuneus for subject i and session j. Then, reliability is defined as (Weir, 2005; Bartlett and Frost, 2008; Scholtes et al., 2011):

$$\text{reliability} = \frac{\sigma_{x,i}^2}{\sigma_{x,i}^2 + \sigma_w^2} \tag{4.2}$$

where $\sigma_{x,i}^2$ corresponds to the true between-subject variance, and the measurement error w is defined as:

$$x_{i,j} = x_{true,i} + w_{i,j} \tag{4.3}$$

We assume thereby that a true quantity $x_{true,i}$ exists for each subject i, and we call error any deviation between $x_{i,j}$ and $x_{true,i}$. This deviation may be caused by the instrumentation (e.g. MEG sensors deviating from their ideal working point), the measurement situation (e.g. varying magnetic fields interfering in the MEG measurement, acoustic noise that could induce interfering brain activity in the subject, etc.) or the subject itself (varying brain activity from session to session, changes in cognitive status, etc.).

It is important to note that reliability is population-specific: it relates to the ability of the score x to distinguish between subjects in a given group. In fact, it increases

with the between subject variability. This means that, for a fixed error variance σ_w^2, the more heterogeneous the subject sample, the higher the reliability.

4.1.2 Quantifying test-retest reliability and agreement

Intraclass correlation coefficient (ICC)

The intraclass correlation (or intraclass correlation coefficient, ICC) is the most commonly employed reliability estimate when dealing with interval and ratio values. It evaluates between-subject variance $\sigma_{x,i}^2$ and error variance σ_w^2 from a measurement sample, and then uses equation (4.2) to quantify reliability. Various ICC types exist, depending on the model used to estimate $\sigma_{x,i}^2$ and σ_w^2. In this text, we focus on the ICC type 1-1 described in (McGraw and Wong, 1996; Shrout and Fleiss, 1979; Weir, 2005), which applies to our study of the test-retest reliability of MEG estimates. This model is based on a one-way random effects model, in which the ordering of j is assumed to be irrelevant. This is equivalent to assuming that there is no systematic error between observations, or that subjects do not change consistently across MEG sessions.

Let us consider the measurements x_{ij}, where $i = 1,2,\cdots,n$ represents the subject index and $j = 1,2,\cdots,k$ represents the observation index (or session number). We suppose therefore that all subjects have been measured an equal amount of times (k). In our random effects model, x_{ij} can be written as:

$$x_{ij} = \mu + r_i + w_{ij} \tag{4.4}$$

where μ is the population mean, r_i accounts for the deviation between the population mean and the subject true score, and w_{ij} are the residuals or errors. r_i and w_{ij} are assumed to be independent and normally distributed, following $r_i \sim N(0,\sigma_r^2)$ and $w_{ij} \sim N(0,\sigma_w^2)$. We then introduce two sums of squares terms:

$$SSR = \sum_{i=1}^{n} (\bar{x_{i\cdot}} - \bar{x_{\cdot\cdot}})^2 \tag{4.5}$$

$$SSW = \sum_{i=1}^{n}\sum_{j=1}^{k} \left(x_{ij} - \bar{x_{i\cdot}}\right)^2 \tag{4.6}$$

which have $n-1$ and $(k-1)n$ degrees of freedom, respectively. Their corresponding mean squares values are:

$$MSR = \frac{SSR}{n-1} \tag{4.7}$$

$$MSW = \frac{SSW}{n(k-1)} \tag{4.8}$$

and have the following expected values (Shrout and Fleiss, 1979)

$$E(MSR) = \sigma_w^2 + k\sigma_r^2 \tag{4.9}$$

$$E(MSW) = \sigma_w^2 \tag{4.10}$$

One can therefore estimate reliability as in (4.2) with MSR and MSW with the following ICC:

$$\rho = \frac{MSR - MSW}{MSR + (k-1)MSW} \tag{4.11}$$

Additionally, we can test the null hypothesis $H_0 : \rho = \rho_0$ against the alternative $\rho > \rho_0$ by defining the F-value:

$$\mathrm{F}_0 = \frac{MSR}{MSW} \cdot \frac{1-\rho_0}{1-(k-1)\rho_0} \tag{4.12}$$

which follows an F-distribution with $n-1$ and $n(k-1)$ degrees of freedom, and computing the corresponding p-value. When testing for $H_0 : \rho = 0$, F_0 simplifies to $\mathrm{F}_0 = MSR/MSW$, and the (1-α) confidence interval for the ICC estimate is (Shrout and Fleiss, 1979):

$$\frac{F_L - 1}{F_L + (k-1)} < ICC < \frac{F_U - 1}{F_U + (k-1)} \tag{4.13}$$

where $F_L = F_0 / F_{1-\alpha/2}(n-1, n(k-1))$, $F_U = F_0 \cdot F_{1-\alpha/2}(n(k-1), n-1)$ and $F_{1-\alpha/2}(\nu_1, \nu_2)$ refers to the $(1-\alpha)\cdot 100$th percentile of an F-distribution with ν_1 and ν_2 degrees of freedom.

Other methods

Although the ICC is the most standard method to quantify reliability, other methods can be employed to evaluate either reliability or agreement. We introduce some of them in the following:

- *Pearson correlation coefficient.* It has been historically employed in some reliability studies, although it is usually not recommended (Bland and Altman, 2010). It is not a reliability or agreement measure *per se*, instead it tests for a linear dependency between two sets of measurement scores: $\{x_{ij}\}$, $i = 1, \cdots, n$, $j = j_1, j_2$.

- *Standard error of measurement.* It is an absolute measure of reliability and indicates the expected error from session to session (or trial to trial). It can be

estimated from the ICC as $\mathrm{SD}(1-\rho)$, where SD is the standard deviation over all measurements (Bland and Altman, 2010). It is of use to estimate the confidence interval of a subject's true score from its measurements.

- *Bland-Altman plot.* It is commonly used to visualize the agreement between two sets of measurements. It displays a scatter plot of the difference between the scores obtained in the two sets versus their average value (Myles and Cui, 2007), along with horizontal lines for mean difference and 95% limits of agreement. It is for instance useful for the careful inspection of the results obtained using two different methodologies.

- *Coefficient of variation.* It measures the relative variability in the measurements scores x_{ij} as:

$$CV = \frac{1}{n}\sum_{i=1}^{n}\frac{\mathrm{SD}\left(x_{ij}\right)\big|_{j=1,\cdots,k}}{mean\left(x_{ij}\right)\big|_{j=1,\cdots,k}} \tag{4.14}$$

  where the same notation as before was used (Shechtman, 2013). Contrary to the ICC, which compares within- and between-subject variability, the coefficient of variation focuses on the relative within-subject variability.

- *Cluster overlap.* It has been used in test-retest fMRI experiments to investigate the reliability of task-related activations. It can be calculated as:

$$R_{overlap} = 2\frac{V_{overlap}}{V_1 + V_2} \tag{4.15}$$

  where V_1 and V_2 are the activation volumes in measurements 1 and 2 and $V_{overlap}$ is the volume that is activated in both measurements (Bennett and Miller, 2010). It requires therefore the definition of a threshold to separate the total brain volume into active and inactive voxels.

- *Kendall's coefficient of concordance.* Kendall's W was originally proposed to measure the agreement amongst several judges who assign ranks to a single set of objects (Legendre, 2005). It was also applied to the present study of quantifying the between-subject and within-subject agreement of FC maps. This is further explained in section 4.3.

4.1.3 Study design

To evaluate the test-retest reliability of resting-state MEG spectral and FC measurements, we performed the following experiment. Three MEG resting state sessions

were recorded from 24 healthy subjects. We selected a test-retest interval of one week, which was long enough to ensure that subsequent sessions were not affected by the previous one (e.g. fatigue effects), but short enough for the subjects to change considerably from one session to the other (Scholtes et al., 2011). Additionally, recordings were performed on the same time of the day to minimize the impact of circadian rhythms. Then, we evaluated within- and between-subject variability in MEG power and FC estimates for distinct brain rhythms (delta, theta, alpha, beta and gamma).

4.2 Study I. Reliability of resting state power

4.2.1 Introduction

MEG/EEG resting-state spectral measures have been applied to a multitude of studies, including both healthy and pathological states. The work introduced in section 3.1, which compared source space power spectra between MCI patients and controls, is an example of such a study. MEG/EEG spectral measures have however been applied to many other fields, such as developmental disorders like autism (Cornew et al., 2012), psychiatric disorders like schizophrenia (Fehr et al., 2001) and neurodegenerative diseases such as Alzheimer's disease (Fernández et al., 2006) or multiple sclerosis (Van Der Meer et al., 2013). MEG/EEG power can also be employed in monitoring longitudinal changes in population groups, such as Parkinson's disease (Olde Dubbelink et al., 2013). Similarly, sensor space MEG power could assist in evaluating the effect of drug treatments, for instance in children with attention deficit with hyperactivity disorder (Wienbruch et al., 2005).

However, spectral measures need to be proven reliable before they can be routinely employed in drug testing or health status monitoring. To this date, reliability studies have been only performed with sensor space EEG, usually concluding that sensor space EEG power is highly reliable (Fingelkurts et al., 2006; McEvoy et al., 2000). Results were however dependent on the frequency band, and reliability was found to be highest for theta, alpha and beta bands and lowest for delta and gamma bands (Burgess and Gruzelier, 1993; Cannon et al., 2012; Gasser et al., 1985; Gudmundsson et al., 2007; Kondacs and Szabó, 1999; McEvoy et al., 2000; Pollock et al., 1991). The reliability was also dependent on the sensor location. Fingelkurts et al. (2006) described a decrease in reliability from frontal to occipital EEG sensors, while others found higher reliability in occipital than in frontal sensors (Gudmundsson et al., 2007; McEvoy et al., 2000). Results are therefore inconclusive, and source space reliability studies could contribute to clarifying this issue. Although source space reliability has already been explored in evoked somatosensory and auditory responses (Atcherson et al., 2006; Schaefer et al.,

2002), it is is undetermined in resting state. Cannon et al. (2012) provided the only attempt to the source space reliability of resting state, although their analysis was restricted to eight regions of interest. In consequence, the reliability of source space MEG/EEG estimates remains unclear.

Here we provide the first test-retest reliability assessment of MEG resting state power at both sensor and source space. To achieve this aim, three weekly resting state MEG recordings were acquired from 24 healthy individuals. Then, power at classical frequency bands (delta, theta, alpha, low beta, high beta and gamma) was calculated at sensor space and at source space after beamforming source reconstruction. ICC, within- and between-subject variability were then computed to evaluate reliability.

4.2.2 Materials and methods

Subjects

Twenty-four healthy volunteers (14 females, 10 males; mean age 28.9 years; range 20–41; 2 left-handed) with normal or corrected-to-normal vision participated in this experiment. They did not present history of psychiatric, neurologic or endocrine diseases. They were informed about the aims of the study and signed a written informed consent before participating.

MEG acquisition and preprocessing

As introduced in section 4.1.3, subjects underwent three MEG sessions at the Center for Biomedical Technology (Madrid, Spain) with a test-retest interval of seven days and the MEG system described in section 2.1.3. For each subject and session, four minutes of eyes open resting state, four minutes of eyes closed resting state and two minutes of empty room were recorded. A vertical electrooculogram was also recorded to keep track of ocular artefacts. MEG data were sampled at 1000 Hz with an online filter of bandwidth 0.1-330 Hz. tSSS (section 2.2.1) was then applied with Maxfilter software (version 2.2., Elekta Neuromag) to remove external noise. Jumps, muscular and ocular artifacts were automatically detected with FieldTrip. Resting state data was then split into artifact-free epochs of 4 seconds, yielding 26.8 ± 6.3 (mean ± standard deviation) clean trials in eyes open condition, 29.9 ± 3.6 clean trials for the eyes closed condition, and 21.3 ± 8.5 clean trials for the empty room data.

Sensor space reliability

Power spectra were obtained for all artifact-free epochs with a multi-taper method using discrete prolate spheroidal sequence tapers and 1 Hz smoothing, as implemented in FieldTrip. Then, the average power values in delta (2-4 Hz), theta (4-8 Hz), alpha (8-13 Hz), low beta (13-20 Hz), high beta (20-30 Hz) and gamma (30-45 Hz) were obtained by averaging power estimates over trials. The mean alpha frequency was calculated as the center of gravity of the power spectrum within the 8-13 Hz range, following (Klimesch, 1999). This was performed for every MEG sensor, subject, session and condition separately. Next, for each condition, frequency band and sensor, reliability was assessed with the ICC, following (4.11).

Source reconstruction

To ensure an accurate source and forward modelling, source reconstruction was only performed for 16/24 subjects, for which a T1-weighted MRI was available. For these subjects source locations were placed regularly over their cortical surface with 6mm spacing using Freesurfer (version 5.1.0, Fischl et al. (2002); Ségonne et al. (2007)) and MNE softwares (Gramfort et al., 2014). The forward model was solved with a 3-shell BEM: inner skull, outer skull and skin surfaces were extracted from the subject's MRI with NFT software (Acar and Makeig, 2010) and leadfields were computed with MNE.

Then, the absolute power for each source location and frequency band was computed with a frequency-domain beamformer (see section 2.3.3). To avoid mixing sensor information with different noise profiles or resort to an arbitrary scaling, we performed source reconstruction with magnetometer and gradiometer data separately. This chapter presents the source space reliability obtained with magnetometers, although gradiometer data yielded similar results which can be found in Appendix D. We note that magnetometer and gradiometer data are not independent measures after preprocessing, since they both are employed in the tSSS filtering, and thus result from the back-projection of the same inside components.

As required in the beamformer computation, sensor space cross-spectral density matrices were first computed for each frequency band using FieldTrip. Then, beamformer filters $\boldsymbol{w}(\boldsymbol{r}_i, f_b)$ ($N_{sensors} \times 3$ matrices) were computed for each source location $\boldsymbol{r}_i$ and frequency band f_b, following (2.51) and using 5% regularization and an unconstrained source orientation. The power for each source location $\boldsymbol{r}_i$ and frequency band f_b was then defined as:

$$V\left(\boldsymbol{r}_i, f_b\right) = \theta_{max}\left(\boldsymbol{w}^H\left(\boldsymbol{r}_i, f_b\right)\boldsymbol{C}(f_b)\boldsymbol{w}\left(\boldsymbol{r}_i, f_b\right)\right) \tag{4.16}$$

where $\boldsymbol{C}(f_b)$, superscript H and $\theta_{max}(\cdots)$ refer to the cross-spectral density matrix for frequency band f_b, the Hermitian transpose and the maximum eigenvalue of a matrix $(\cdots)$, respectively.

However, $V(\boldsymbol{r}_i, f_b)$ was not employed directly in the reliability analysis. In fact, beamforming estimates are biased, particularly towards the center of the brain, where the signal-to-noise ratio of MEG signals is lowest. Therefore, the following normalized power estimates were used:

$$Z(\boldsymbol{r}_i, f_b) = \frac{V(\boldsymbol{r}_i, f_b)}{N(\boldsymbol{r}_i, f_b)} \tag{4.17}$$

where $N(\boldsymbol{r}_i, f_b)$ is a noise estimate in source space, and is obtained by employing (4.16) and substituting the original cross-spectral density matrix $\boldsymbol{C}(f_b)$ with the empty room cross-spectral density matrix $\boldsymbol{C}_N(f_b)$. Although the noise is sometimes assumed to be independent and uncorrelated across sensors (yielding a diagonal $\boldsymbol{C}_N(f_b)$), we considered that this assumption reflects poorly the specific noise characteristics of our data. For instance, we preprocessed the raw MEG recordings with a tSSS filtering, which reduces the dimensionality of the data. Therefore, we decided to compute $\boldsymbol{C}_N(f_b)$ from the empty-room recordings following the same analysis pipeline than for the resting-state data: tSSS, artifact detection, segmentation into clean epochs and spectral estimation.

Finally, the noise-normalized power estimates $Z(\boldsymbol{r}_i, f_b)$ were transformed into MNI space. First, a template mesh of source locations was created from the subjects with Freesurfer. Then, $Z(\boldsymbol{r}_i, f_b)$ was transformed from the subject's to the standard surface and a smoothing with a 15mm moving average filter was applied. Overall, this yielded $N_{subjects} \times N_{sessions} = 16 \times 3$ power estimates for each template source location, frequency band and condition. We note that these power values were computed for each subject and session separately. Reliability was then assessed with the ICC.

Additionally, relative powers were calculated for each frequency band. For that, beamformer filters $\boldsymbol{w}(\boldsymbol{r}_i)$ were computed with the average cross-spectral density matrices over the entire 2-45 Hz range, and then applied to individual-band cross-spectral density matrices $\boldsymbol{C}(f_b)$ as in (4.16). Then, the relative power of each frequency band was obtained by dividing the band power $V(\boldsymbol{r}_i, f_b)$ with the total power over all frequency bands.

Within-subject variability vs. source power

To test whether within-subject variability is dependent on the source intensity, we evaluated the joint distribution of both magnitudes. For a given subject, source position and frequency band, the representative power was simply defined as the average

source power over the three MEG sessions:

$$\bar{Z} = mean(Z_s)|_{s=1,2,3} \tag{4.18}$$

where Z_s represents the source power for a session s. The corresponding within subject variability was defined as the relative inter-session variations:

$$\Delta z = \frac{std(Z_s)|_{s=1,2,3}}{\bar{Z}} \tag{4.19}$$

Further, for a given frequency band, we computed the bivariate histogram of $\bar{Z}$ and Δz across all subjects and source positions. Then, in order to estimate the conditional probability distribution of Δz given $\bar{Z}$, we normalized the histogram by the sum of its counts for each $\bar{Z}$ bin separately.

4.2.3 Results

Sensor space reliability

We first estimated sensor space power reliability in eyes open, eyes closed and empty room conditions. Table 4.1 shows ICC values for the average power over five helmet areas for all the frequency bands. Overall, ICC values ranged from 0.48 to 0.95 in resting state. As expected, the empty room ICC values were appreciably lower. Figure 4.1 displays the sensor space ICC distribution. In general, power in sensors covering the parieto-occipital area of the scalp remained fairly reliable for all the frequency bands.

Reliability varied somewhat across the frequency bands and the scalp areas. Delta power showed the highest ICC values in frontal and parietal areas. Theta power remained highly reliable (range 0.74-0.86) except in the frontal area in the eyes open condition (ICC=0.54). In turn, alpha power showed the highest ICC (range 0.83-0.95) in all sensor areas. Moreover, ICC values were slightly higher in the eyes closed condition. Low beta power presented high ICC values (range 0.74-0.91), especially in the occipital and parietal areas. ICC values in high beta were slightly smaller (range 0.70-0.89) than in low beta, especially in the frontal and temporal sensors, although the ICC distribution was quite similar. Finally, gamma power showed the lowest ICC across all the frequency bands, and only the sensors covering the parietal area of the scalp showed fairly ICC>0.6.

Table 4.1: ICC of the average power over five MEG sensor regions for each frequency band and condition. The right column contains the ICC of the MAF (mean alpha frequency).

		Delta	Theta	Alpha	Low beta	High beta	Gamma	MAF
Eyes open	Occipital	0.52	0.79	0.86	0.86	0.75	0.64	0.91
	Left temporal	0.72	0.75	0.92	0.85	0.85	0.59	0.85
	Right temporal	0.79	0.76	0.83	0.82	0.79	0.59	0.89
	Parietal	0.76	0.85	0.86	0.86	0.85	0.77	0.93
	Frontal	0.78	0.82	0.85	0.76	0.74	0.48	0.70
Eyes closed	Occipital	0.78	0.86	0.94	0.91	0.89	0.59	0.88
	Left temporal	0.69	0.74	0.92	0.87	0.75	0.50	0.87
	Right temporal	0.55	0.83	0.95	0.83	0.75	0.49	0.89
	Parietal	0.66	0.82	0.93	0.85	0.79	0.63	0.90
	Frontal	0.90	0.54	0.84	0.74	0.70	0.53	0.82
Empty room	Occipital	0.02	0.19	0.38	0.42	0.17	0.34	-0.09
	Left temporal	0.06	0.01	0.03	0.07	-0.01	0.08	-0.08
	Right temporal	-0.01	-0.01	0.05	0.14	0.02	0.17	-0.03
	Parietal	-0.07	-0.07	-0.02	-0.01	0.01	-0.00	-0.15
	Frontal	-0.09	-0.11	-0.05	-0.01	-0.04	-0.03	0.03

Source space reliability

ICC was calculated for the power estimates of each source location and frequency band, and represented in Figures 4.2 and 4.3 for eyes open and eyes closed condition, respectively. In general, these source space results were similar to the previously described sensor space ones. On the one hand, highest ICC values were obtained in widespread regions for alpha, low beta and theta bands. On the other hand, for delta, high beta and gamma bands, reliability was medium to low (ICC<0.6) for most brain areas, although high ICC values (ICC>0.6) were found in restricted brain regions.

Delta power yielded mainly medium to low reliability, although high ICC was found in some frontal regions such as superior and orbitofrontal cortices. In turn, ICC was high (ICC>0.7) for theta in regions surrounding the central sulcus such as superior parietal and superior frontal gyrus, paracentral and posterior cingulate. Note that parahippocampal gyrus showed high ICC values in the eyes open condition, whereas it decreased along with other temporal regions in the eyes closed one. Similarly as in the sensor space analysis, alpha power showed high ICC for most brain areas, especially in frontal and parietal cortices. High ICC regions were however more spatially restricted in the eyes closed condition. For low beta, highest reliability was reached in the left

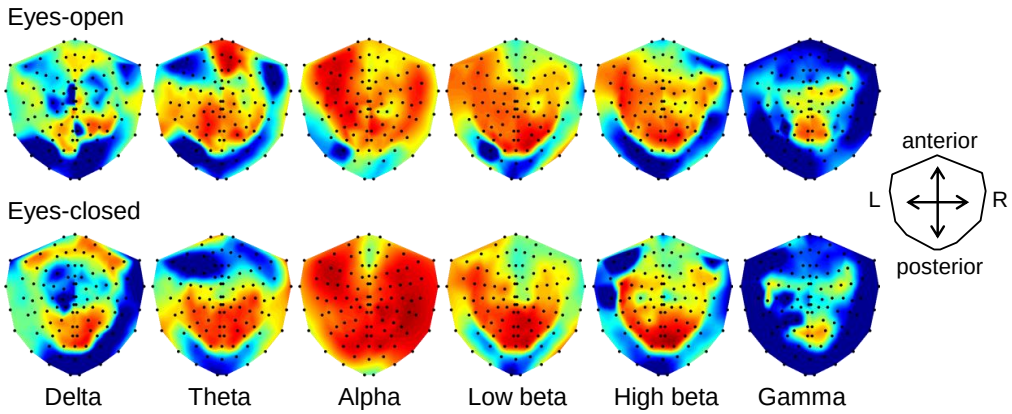

Figure 4.1: Topography of the intraclass correlation coefficient (ICC) of sensor space power for each resting state condition, frequency band, sensor.

parietal, precuneus and the isthmus of the cingulate gyrus. The power reliability distribution seemed to be more anterior and bilateral in the eyes closed condition, especially in the medial orbitofrontal, superior frontal and paracentral gyri. High beta and gamma were the frequency bands with fewer regions with high reliability. The former showed medium to low ICC values except in precuneus, paracentral and parahippocampal gyrus in the eyes open condition (ICC>0.6). Power in gamma band showed widespread low ICC values, except in the left precentral gyrus in the eyes open condition (ICC>0.7).

Absolute vs. relative power

While previous results referred to absolute power estimates, ICC was also computed for relative power. Sensor space relative power yielded overall high reliability (ICC>0.7) for all frequency bands (Table D.1 in Appendix D). The ICC distribution was similar than for the absolute power, although higher values (ICC=0.8-0.9) were reached in high beta and gamma bands. Source space reliability was appreciably higher for relative than for absolute power. ICC distributions for the relative power are displayed in the Figures D.1 and D.2 in Appendix D (note that the colorbars span higher ICC values than for the absolute power). For instance, ICC values for high beta were higher in more regions than for the absolute power. However, relative power in delta and theta showed smaller ICC values than absolute power in some regions such as the frontal cortex. On the whole, whereas for the absolute power high ICC values were restricted to specific regions, ICC for relative power estimates seemed to present broader patterns, especially in low beta and high beta. Relative power in parietal and occipital cortices

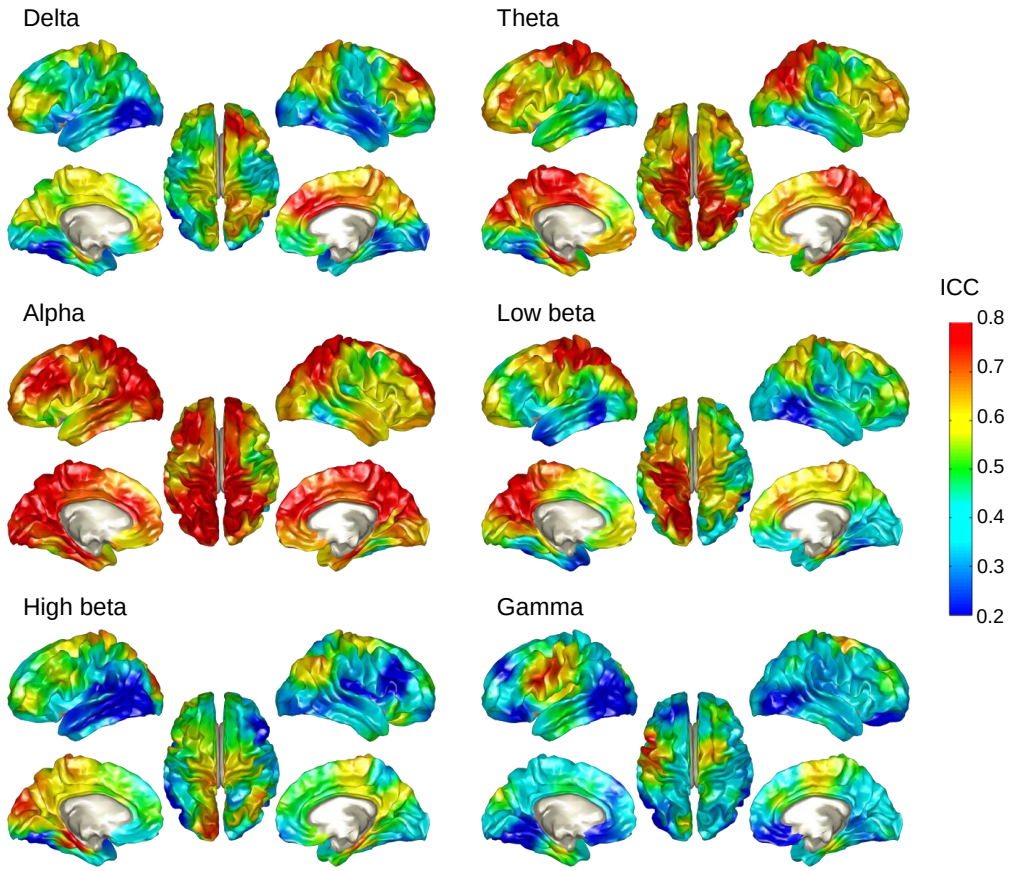

Figure 4.2: ICC of source space power for the resting state eyes open condition. ICC values were computed for each source location and frequency band separately.

was fairly reliable even when low ICC was obtained for absolute power, such as the right cuneus in low beta.

Dependence between within-subject variability and source power

To determine whether the within-subject variability depends on the source power, the joint distribution of within-subject variability and average power for each frequency band is displayed in Figures 4.2 and 4.3 for eyes open and eyes closed condition, respectively. In general, low power levels result in high within-subject variability. This trend was present in all frequency bands, and was particularly evident in gamma, where power values were small (<2) throughout the brain. However, the relation be-

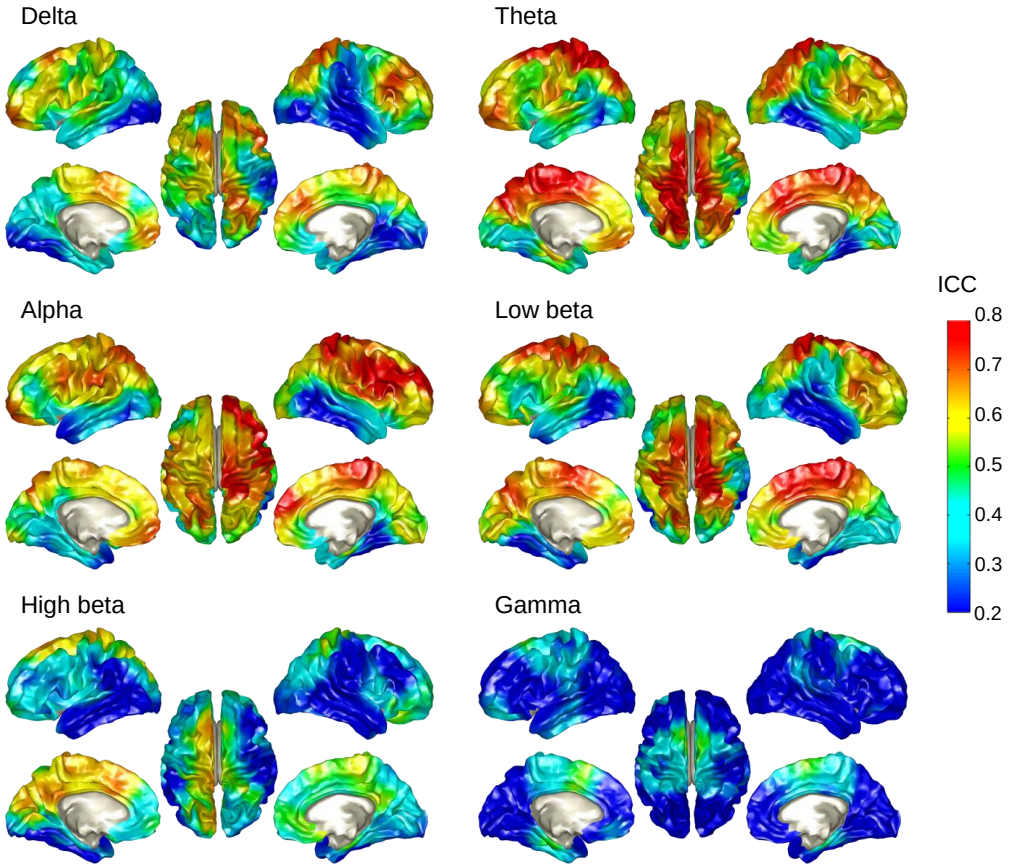

Figure 4.3: ICC of source space power for the resting state eyes closed condition. ICC values were computed for each source location and frequency band separately.

tween power and within-subject variability was not linear. In fact, although power and within subject variability were inversely related for low power values, this tendency was not maintained for moderate to high power values (3-6), for which within-subject variability remained rather constant. In addition, the lowest within-subject variability was not invariably found for highest power values. For instance, in alpha band eyes closed condition, high power values (8-11) resulted in higher within-subject variability than moderate power values (3-8). Overall, this indicates that, although a general inverse relation was found between within-subject variability and power values, within-subject variability did not exclusively result from power intensity.

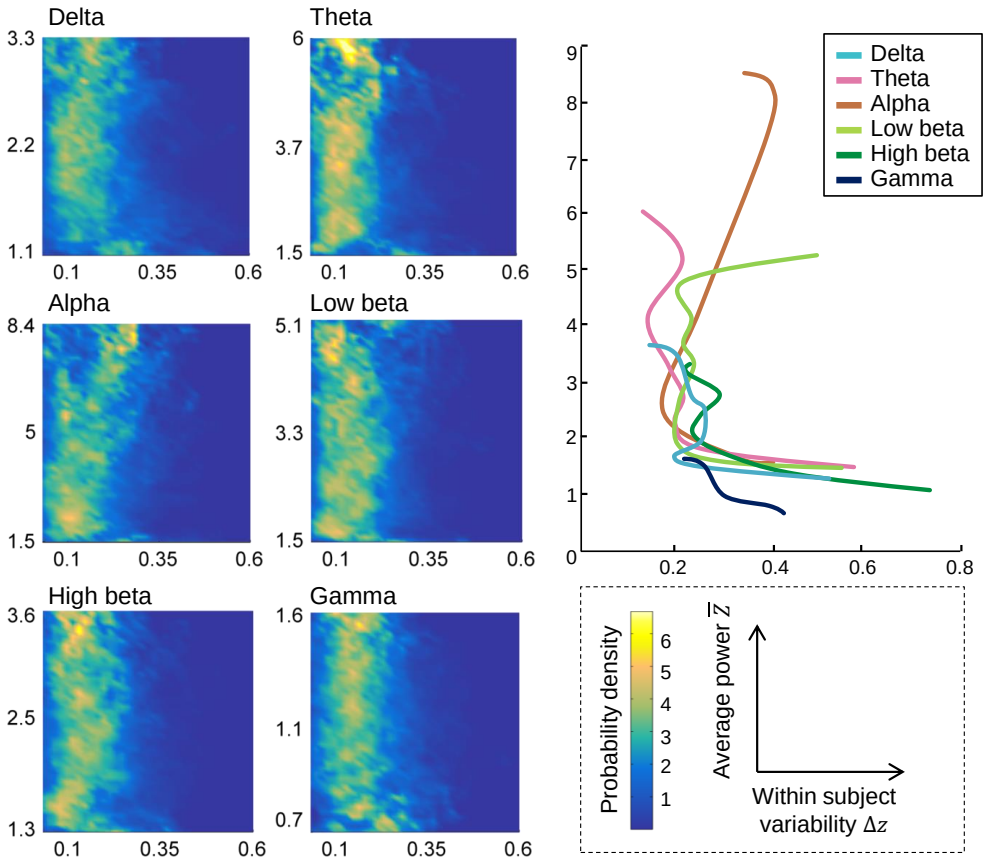

Figure 4.4: Dependence of within-subject variability with the average power, for the resting state eyes open condition. The surface plots estimate the conditional probability of obtaining a given relative within-subject variability Δz for a source power $\bar{Z}$. The right plot represents the average within-subject variability as a function of the source power $\bar{Z}$.

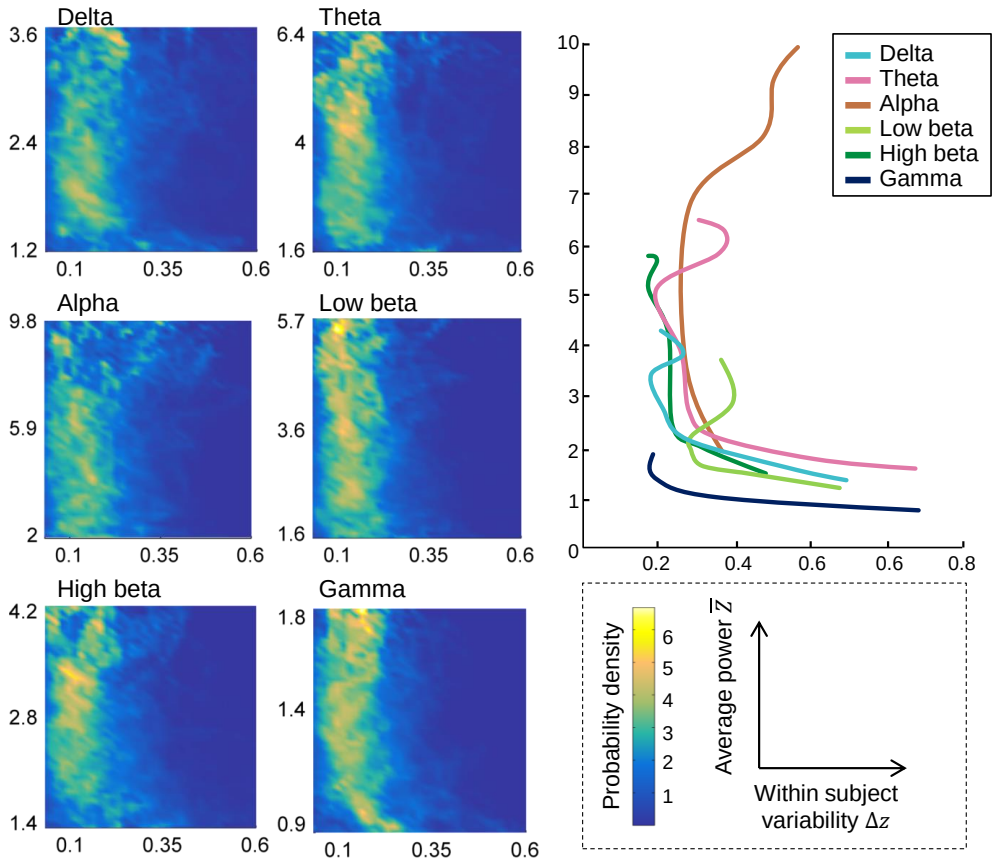

Figure 4.5: Dependence of within-subject variability with the average power, for the resting state eyes closed condition. The surface plots estimate the conditional probability of obtaining a given relative within-subject variability Δz for a source power $\bar{Z}$. The right plot represents the average within-subject variability as a function of the source power $\bar{Z}$.

4.2.4 Discussion

In this work, we examined the test-retest reliability of MEG resting state power in classical frequency bands at sensor and source space. To achieve this aim, three weekly MEG recordings were performed and the ICCs of power values at each sensor and source location were calculated. Moreover, to evaluate how power intensity modulates reliability, we explored the relation between source power and within-subject variability for each frequency band. To our knowledge, this is the first attempt to evaluate the reliability of source space MEG resting state power. We obtained two main findings. On the one hand, theta, alpha and low beta were the most reliable brain rhythms at sensor and source space, in contrast to high beta and gamma power, which showed poor reliability. On the other hand, within-subject variability was partially dependent on power intensities, as shown by the inverse relation found between both magnitudes.

Our results are in line with previous sensor space EEG test-retest literature, which also found reliable theta, alpha and beta power estimates (Gasser et al., 1985; Kondacs and Szabó, 1999; McEvoy et al., 2000). Amongst them, highest reliability was obtained in alpha in groups of children or young adults and in theta when including healthy elderly people (Gudmundsson et al., 2007). Further, gamma and delta power presented low to moderate reliability (ICC<0.7 generally), which is also in agreement with previous EEG studies (Gasser et al., 1985; Gudmundsson et al., 2007; Kondacs and Szabó, 1999; Pollock et al., 1991).

Additionally, reliability differed between absolute and relative power estimates. In line with previous EEG studies (Gudmundsson et al., 2007; Kondacs and Szabó, 1999; Pollock et al., 1991), sensor space reliability was generally similar for absolute than for relative power in theta, alpha, and beta bands, although relative power yielded lower ICC in alpha and higher ICC in high beta and gamma. Since relative power values are normalized with the overall power, which is dominated by the high intensities in theta and alpha bands, it is possible that the relative power in gamma became reliable because of the high reliability of theta and alpha bands. Source space results followed nonetheless a different trend: higher ICC values were generally found for relative than for absolute power for all frequency bands. This could be attributed to the source reconstruction process. Beamformer solutions are in fact biased, especially in regions with low signal to noise ratio (Sekihara and Nagarajan, 2008). Beamfomer intensities are therefore usually not directly employed in any statistical analysis: they are rather normalized with another condition or with a noise estimate (Luckhoo et al., 2014). Although this is often performed by assuming uncorrelated noise, we used empty room recordings, since they are a more realistic estimate of the noise present in the MEG data. Empty room data fail however to account for biological noise emerging

from the subject. Relative power escapes this issue by normalizing source intensities with the overall source power, thereby avoiding any *a priori* assumptions on the noise characteristics. Nevertheless, relative powers are also more unspecific, as they mix intensities from all frequency bands, and they do not enable the separate inspection of brain rhythms. For instance, changes in the relative power of low intensity frequency bands (high beta or gamma), could be overshadowed by small variations in alpha or theta bands.

Additionally, the signal-to-noise ratio (SNR) of power estimates may be partially responsible for the variability in its reliability across brain regions and rhythms. This was previously proposed to explain the low reliability of delta band power (Deuker et al., 2009; Gasser et al., 1985; Pollock et al., 1991), as delta measurements are greatly affected by environmental and biological noise. In this work we demonstrated that the reliability of power estimates was modulated by the signal intensity. Low power was in fact related to high within-subject variability. This was particularly evident in the gamma band, which presented low power throughout the brain. However, power intensity was not entirely responsible for its reliability, since source locations with highest power did not consistently present the lowest within-subject variability. For instance, the alpha power in occipital regions was more intense and yet less reliable during the eyes closed than during the eyes open condition, as it presented both higher intensities and higher within-subject variability.

Moreover, reliability might result from the inherent nature of brain oscillations. For instance, although the biophysical original of alpha oscillations is not completely clear, some studies have pointed out that it could be paced by the thalamus (Buzsáki and Moser, 2013; Hughes and Crunelli, 2005), contributing therefore to creating stable oscillations and a high test-retest reliability. As for the other brain rhythms, the highest reliability was in general found in those regions where the brain rhythm had been previously described as dominant (Hillebrand et al., 2005). For example, theta power presented high ICC around the central sulcus and the parahippocampal gyrus, thus coinciding with previous literature which identified theta oscillations in the hippocampus (Buzsáki, 2002) and midfrontal regions such as the dorsal anterior cingulate cortex (Cavanagh and Frank, 2014; Congedo et al., 2010; Wang, 2010). Furthermore, low beta power showed high reliability in frontal regions such as the superior frontal or the paracentral gyrus. In agreement, beta rhythm has been typically identified in the primary motor cortex (Wang, 2010) and frontal regions related to the inhibitory control of movement (Sauseng and Klimesch, 2008). Finally, gamma oscillations are associated with high level processing such as perceptual binding, episodic memory retrieval or working memory (Jensen et al., 2007), and adapt rapidly to the presence

of incoming events or stimuli. Therefore, although gamma power presented low ICC in resting state, it could be expected to have higher reliability during a controlled task. This effect was previously found for FC measures (Deuker et al., 2009).

4.3 Study II. Reliability of resting state FC

4.3.1 Introduction

Since Biswal et al. (1995) observed highly correlated brain activity between bilateral motor cortices, resting state brain networks (RSNs) have become increasingly popular (van den Heuvel and Hulshoff Pol, 2010). They consist in separate brain regions that spontaneously exhibit coordinated activity and are engaged in distinct sensory or cognitive functions, such as visual or motor processes, attention or executive control (Rosazza and Minati, 2011). These networks are usually characterized with FC (section 2.4), which can be seen a mechanism of information transfer between a network's nodes, and has been proven to be indicative of an individual's brain functioning. In fact, it was shown to account for inter-subject variability in task performance (Baldassarre et al., 2012; Yamashita et al., 2015) and to distinguish between healthy and pathological populations, such as schizophrenia (Lynall et al., 2010) or Alzheimer's disease (Damoiseaux et al., 2012; Greicius et al., 2004).

RSNs have been traditionally examined with fMRI as correlations between blood-oxygenated-level-dependent (BOLD) signals. While fMRI is of great use in the exploration of human brain function, slowly fluctuating BOLD signals constitute only an indirect measure of brain activity. Therefore, over the past few years, attention has been drawn to the electrophysiological basis of RSN. In fact, although MEG is often overshadowed by the high spatial resolution of fMRI, MEG provides an excellent insight into the time-frequency dynamics of brain activity. It is indeed a direct measure of neuronal firing and offers unmatched temporal resolution in non-invasive neuroimaging. RSNs have been successfully reproduced with MEG by computing source space FC and using either independent component analysis (ICA) (Brookes et al., 2011b; Hall et al., 2013; Luckhoo et al., 2012) or seed-based connectivity (Brookes et al., 2011a; de Pasquale et al., 2010; Hipp et al., 2012; Wens et al., 2014). While ICA RSNs are built by temporally concatenating source reconstructions along subjects (Brookes et al., 2011b), seed-based connectivity is applied individually after the a priori selection of some seed locations.

Overall, this indicates that RSNs can be robustly extracted with MEG. However, the subjects' cognitive or emotional state and measurement noise could affect FC estimates, and it is unclear to what extent MEG-derived RSNs are representative of

an individual. This prevents the potential use of MEG RSN in the characterization of individual subjects, or in the proper classification between healthy and pathological populations. Therefore, the reliability of FC estimates needs to be carefully examined. In fact, only a handful of studies have tackled test-retest reliability of MEG/EEG FC (Deuker et al., 2009; Jin et al., 2011; Hardmeier et al., 2014), and they were restricted to sensor space, therefore failing to provide the spatial resolution necessary for the evaluation of RSNs. To our knowledge, no study has quantified test-retest reliability on FC estimates of MEG RSNs.

In the present work we investigated the test-retest reliability of MEG RSNs. For that, MEG resting state recordings were pooled from the study presented in section 4.2 (Sixteen subjects scanned three times with a one-week test-retest interval). Then, source reconstruction of the sensor space data was performed with beamforming, and FC was computed with four metrics (envelope correlation or d-ecor, envelope correlation with source leakage correction or lc-ecor, PLV and PLI) using the nodes of 7 well-known RSNs (visual, motor, auditory, DMN, fronto-parietal or FP, insular) as seeds. Test-retest reliability was then assessed with ICC for within-network FC and seed-based FC.

4.3.2 Materials and methods

Subjects and MEG acquisition

16 healthy subjects were included in this analysis (age 30.4 ± 5.8, 10 women), Subjects underwent three MEG sessions of resting-state (two conditions: 4min eyes open, 4 min eyes closed) with an Elekta Vectorview system. Details on data acquisition can be found in section 4.2.2.

Source reconstruction

Similarly as in section 4.2.2, jump, muscle and ocular artifacts were located with FieldTrip, and non-overlapping artifact-free 6-second epochs were located in the continuous resting state recordings. This yielded 24.3 ± 5.7 clean epochs for the eyes open condition and 26.8 ± 4.7 clean epochs for the eyes closed condition. Then, MEG data were filtered into delta (2-4 Hz), theta (4-8 Hz), alpha (8-13 Hz), beta (13-30 Hz) and gamma (30-45 Hz) frequency bands with a finite impulse response (FIR) filter of order 1000, and down-sampled to a 250Hz rate.

Source and forward models were built as in the previous study (section 4.2.2): source locations were spread over the cortical surface and the forward problem was solved with a 3-shell BEM. However, here we employed the time-domain beamformer

LCMV instead a frequency domain beamformer, since we aimed at computing FC between source time-series. Beamforming filters were computed using equation (2.39) and all clean trials in the covariance calculation. These filters were then applied to the continuous resting state data, yielding a 4-min time series per source location. To avoid edge artefacts, source time series were not split into clean trials before the FC computation. Source reconstruction was performed for every frequency band, condition, subject and session separately.

FC computation

FC was computed between source time-series using four different metrics, which were introduced in section 2.4:

- *Envelope correlation (d-ecor):* Pearson correlation between the envelopes of the source time series.
- *Envelope correlation with leakage correction (lc-ecor):* similar to d-ecor, but includes a regression of the source time series prior to the envelope computation, following equation (2.64).
- *PLV:* a classical measure of phase synchronization (equation (2.61)).
- *PLI:* another measure of phase synchronization, which is insensitive to zero and π phase differences (equation (2.62)) .

Envelopes and phases were extracted from the Hilbert transform of the source time series and then envelopes were smoothed with a 0.5 second moving average filter. To avoid edge artefacts, envelopes and phases were estimated in the whole 4-min time series, but correlations, PLV and PLI were only computed for the previously determined 6-second clean trials. FC values were averaged over trials to produce a final FC estimate per pair of source locations, condition, frequency band, subject and session.

Within-network reliability

FC was first assessed between the nodes of 7 RSNs: visual, sensorimotor, auditory, DMN, left FP, right FP and fronto-insular networks. These nodes were defined in MNI space (see Table 4.2 for their coordinates) and transformed into subject space with a homogeneous transformation extracted from Freesurfer's cortical segmentation process. The FC between two nodes was defined as the average FC between all sources

Table 4.2: MNI coordinates of the nodes forming the resting state networks (RSNs). MNI coordinates are obtained from the fMRI RSNs released by Laird et al. (2011) and Smith et al. (2009). Labels are assigned with FSL atlas tools (Desikan et al., 2006; Eickhoff et al., 2005; Jenkinson et al., 2012). DMN: default mode network, FP: fronto-parietal, BA: Broadmann area.

Network	Node	MNI coordinate			BA
		x	y	z	
Visual	Left visual cortex	-41	-77	3	19
	Right visual cortex	41	-72	1	19
Sensorimotor	Left primary somatosensory cortex	-38	-27	52	1
	Right primary somatosensory cortex	40	-25	50	1
Auditory	Left primary auditory cortex	-55	-21	7	41
	Right primary auditory cortex	57	-20	7	41
DMN	Precuneus	1	-57	28	31
	Left inferior parietal	-45	-65	30	39
	Right inferior parietal	52	-60	26	39
	Anterior cingulate	2	42	7	32
Left FP	Left angular gyrus	-40	-58	56	39
	Left middle frontal gyrus	-42	28	23	9
Right FP	Right angular gyrus	53	-50	43	39
	Right middle frontal gyrus	45	28	26	9
Fronto-insular	Left insula	-38	16	2	13
	Right insula	38	16	2	13
	Median cingulate	-2	12	40	32

located within 1cm from the nodes' positions. Then, test-retest reliability for every link, frequency band and condition was computed with the ICC.

Reliability of seed-based FC maps

Whole brain FC maps were computed from every seed in Table 4.2 to the remaining source locations. Then, they were transformed into a template mesh in MNI space with $N_{sources} = 4739$ sources generated with Freesurfer from the subjects' cortical segmentations. FC values were then spatially smoothed with a 15mm moving average filter, yielding $N_{subjects} \times N_{sessions} = 16 \times 3$ FC estimates for each target template source location, seed, frequency band, FC metric and condition. The reliability of the FC estimates was then assessed with the ICC. Additionally, in order to explore whether ICC values depended on the FC strength, joint histograms of both magnitudes were computed. Histograms were normalized with the product of total histogram count and bin width.

Within- and between-subject agreement of seed-based FC maps

For a given condition, FC metric, frequency band and seed location, seed-based FC maps were sorted across template source locations l and transformed into ranks r_{ijl} ($1 \leq r_{ijl} \leq N_{sources}$), for every subject i and session j separately. Then, the agreement between two sessions j_1 and j_2 (or within-subject agreement) was assessed with Kendall's W (Legendre, 2005)

$$W_w = \frac{12 \sum_{l=1}^{N_{sources}} \left(A_{il} - \bar{A}_i\right)^2}{2^3 \left(N_{sources}^3 - N_{sources}\right)} \tag{4.20}$$

where $A_{il} = \sum_{j=\{j_1,j_2\}} r_{ijl}$ and $\bar{A}_i = \frac{1}{N_{sources}} \sum_{l=1}^{N_{sources}} A_{il}$. Analogously, the agreement between two subjects i_1 and i_2 (or between-subject agreement) was assessed with:

$$W_b = \frac{12 \sum_{l=1}^{N_{sources}} \left(B_{jl} - \bar{B}_j\right)^2}{2^3 \left(N_{sources}^3 - N_{sources}\right)} \tag{4.21}$$

where $B_{jl} = \sum_{i=\{i_1,i_2\}} r_{ijl}$ and $\bar{B}_j = \frac{1}{N_{sources}} \sum_{l=1}^{N_{sources}} B_{jl}$. W ranges from 0 to 1 and reaches 1 when the ranks obtained in two sessions/subjects are in perfect agreement. Wilcoxon ranksum tests were performed to compare within- and between-subject W values, and false discovery rate (q=0.05) was applied to correct for multiple comparisons (Benjamini and Yekutieli, 2001).

4.3.3 Results

Within-network reliability

The reliability of FC for links connecting RSNs regions was assessed with the ICC. Results are listed in Table 4.3 for the resting state eyes closed condition, and Table E.1 for the resting-state eyes open condition. ICC values were dependent both on the FC metric and frequency band. Highest ICC values were found for PLV, usually ranging from 0.7 to 0.9. PLV ICC varied across frequency bands, and it was generally larger in alpha, beta and gamma bands. High ICC values (>0.7) were however also found in delta and theta bands for the sensorimotor network and the DMN. d-ecor and lc-ecor presented greater variability across frequency bands than PLV. The ICC of both FC metrics topped in the beta band (ICC=0.43-0.77 for d-ecor and ICC=0.72-0.63 for lc-ecor), while medium to low ICC (<0.5) was found for delta, theta, and gamma bands. Although ICC was rather low in the alpha band, high values (>0.7) were found with d-ecor in the visual and sensorimotor networks. Finally ICC values were considerably low for the PLI in all frequency bands and networks, and rarely exceeded 0.45.

Reliability of seed-based FC maps

FC was computed from each seed to the remaining source locations for each condition, frequency band and FC metric separately. Then, the ICC of the FC values was computed for each link. Average ICC values over all source locations for each seed are listed in Table 4.4. ICC was lower than for the within-network FC (Table 4.3), indicating greater within- than between-network reliability. Moreover, the variability over frequency bands and FC metrics was similar than in the within-network analysis. First, highest values (ICC>0.6) were found for PLV, especially in alpha, beta and gamma bands. Second, ICC values for d-ecor and lc-ecor peaked in the beta band (0.27-0.53), and remained low for the remaining frequency bands (<0.36). Of note, ICC was slightly higher for d-ecor than for lc-ecor. Third, average ICC was fairly poor for PLI (<0.14).

ICC values were unevenly distributed across brain regions. As an example, beta band ICC and average FC maps for three selected seeds are displayed for lc-ecor in Figure 4.6 and for PLV in Figure 4.7 (corresponding figures for d-ecor and PLI can be found in Appendix E). Average FC was higher between regions belonging to the same network. For instance, seeds in sensory networks (visual, somatosensory and auditory cortices) were strongly connected to their homologous contralateral areas. This was less evident for DMN, FP and fronto-insular networks. For instance strong precuneus/anterior cingulate FC was only appreciable for PLV and d-ecor. ICC maps resembled average FC maps, showing high ICC for links between homologous sensory

Table 4.3: ICC of the within-network FC for the resting-state eyes closed condition. ICC values are computed for every frequency band, FC metric and RSN separately. For RSNs with more than two nodes (DMN and fronto-insular), the average ICC across links within the network is displayed.

	Network	Visual	Sensori-motor	Auditory	DMN	Left FP	Right FP	Fronto-insular
d-ecor	Delta	0.45	0.48	0.18	0.18	0.17	0.28	0.05
	Theta	0.56	0.62	0.08	0.30	0.10	0.22	0.12
	Alpha	0.73	0.73	0.58	0.38	0.34	0.32	0.14
	Beta	0.60	0.70	0.45	0.43	0.52	0.77	0.57
	Gamma	0.38	0.37	0.41	0.38	0.24	0.32	0.11
lc-ecor	Delta	0.34	0.46	0.41	0.16	0.03	0.42	0.11
	Theta	0.46	0.27	0.36	0.31	0.22	0.15	-0.01
	Alpha	0.27	0.38	0.07	0.39	0.02	0.47	0.21
	Beta	0.63	0.53	0.49	0.44	0.44	0.60	0.42
	Gamma	0.17	0.34	0.34	0.22	0.24	0.15	0.07
PLV	Delta	0.59	0.88	0.72	0.79	0.31	0.44	0.68
	Theta	0.73	0.87	0.63	0.79	0.39	0.68	0.70
	Alpha	0.85	0.94	0.59	0.76	0.80	0.49	0.62
	Beta	0.82	0.88	0.70	0.81	0.77	0.77	0.74
	Gamma	0.83	0.81	0.66	0.87	0.70	0.91	0.83
PLI	Delta	0.28	0.05	0.30	0.44	-0.02	0.32	0.41
	Theta	0.29	-0.31	0.26	0.46	0.05	0.32	0.40
	Alpha	0.43	-0.07	-0.28	0.38	0.22	0.21	0.46
	Beta	0.05	0.17	0.07	0.44	0.17	0.14	0.53
	Gamma	0.16	0.01	0.23	0.28	0.12	0.03	0.49

Table 4.4: Average ICC values of seed based FC maps for the resting-state eyes closed condition. ICC values are computed for every seed, FC metric and frequency band separately. Values are displayed as mean (standard deviation).

		Delta	Theta	Alpha	Beta	Gamma
Left visual	d-ecor	0.16 (0.26)	0.17 (0.28)	0.27 (0.29)	0.42 (0.22)	0.20 (0.26)
	lc-ecor	-0.01 (0.15)	-0.01 (0.14)	0.20 (0.17)	0.32 (0.15)	0.07 (0.16)
	PLV	0.44 (0.27)	0.56 (0.24)	0.63 (0.19)	0.76 (0.14)	0.80 (0.11)
	PLI	0.08 (0.17)	0.05 (0.15)	0.14 (0.15)	0.10 (0.16)	0.08 (0.17)
Left somato-sensory	d-ecor	0.12 (0.26)	0.19 (0.27)	0.31 (0.27)	0.52 (0.20)	0.18 (0.28)
	lc-ecor	0.04 (0.14)	-0.02 (0.13)	0.28 (0.18)	0.52 (0.14)	0.09 (0.17)
	PLV	0.49 (0.27)	0.59 (0.25)	0.67 (0.22)	0.75 (0.16)	0.73 (0.19)
	PLI	0.06 (0.13)	0.06 (0.16)	0.08 (0.17)	0.10 (0.17)	0.11 (0.17)
Left auditory	d-ecor	0.18 (0.27)	0.24 (0.28)	0.36 (0.24)	0.50 (0.19)	0.23 (0.29)
	lc-ecor	0.03 (0.13)	0.03 (0.14)	0.19 (0.14)	0.46 (0.12)	0.03 (0.14)
	PLV	0.56 (0.23)	0.62 (0.21)	0.72 (0.16)	0.75 (0.15)	0.77 (0.16)
	PLI	0.09 (0.15)	0.10 (0.15)	0.13 (0.16)	0.06 (0.16)	0.06 (0.15)
Precuneus	d-ecor	0.15 (0.27)	0.18 (0.26)	0.29 (0.25)	0.46 (0.18)	0.24 (0.28)
	lc-ecor	0.01 (0.14)	0.02 (0.14)	0.22 (0.16)	0.27 (0.14)	0.03 (0.15)
	PLV	0.48 (0.25)	0.62 (0.22)	0.69 (0.17)	0.79 (0.12)	0.82 (0.11)
	PLI	0.09 (0.17)	0.10 (0.16)	0.12 (0.15)	0.14 (0.17)	0.10 (0.17)
Left middle frontal	d-ecor	0.03 (0.23)	0.09 (0.23)	0.19 (0.25)	0.45 (0.18)	0.07 (0.24)
	lc-ecor	0.02 (0.15)	-0.00 (0.13)	0.11 (0.14)	0.53 (0.15)	-0.04 (0.14)
	PLV	0.33 (0.27)	0.47 (0.26)	0.63 (0.22)	0.67 (0.17)	0.65 (0.19)
	PLI	0.05 (0.14)	0.04 (0.14)	0.12 (0.14)	0.09 (0.16)	0.07 (0.17)
Right middle frontal	d-ecor	0.08 (0.24)	0.10 (0.23)	0.18 (0.25)	0.49 (0.17)	0.16 (0.28)
	lc-ecor	-0.01 (0.14)	-0.03 (0.13)	0.12 (0.16)	0.34 (0.13)	-0.02 (0.14)
	PLV	0.34 (0.27)	0.50 (0.25)	0.60 (0.21)	0.73 (0.14)	0.75 (0.17)
	PLI	0.08 (0.16)	0.07 (0.15)	0.12 (0.16)	0.11 (0.17)	0.04 (0.15)
Median cingulate	d-ecor	0.08 (0.25)	0.09 (0.25)	0.25 (0.25)	0.47 (0.19)	0.15 (0.26)
	lc-ecor	0.03 (0.15)	0.04 (0.13)	0.20 (0.16)	0.39 (0.15)	-0.02 (0.15)
	PLV	0.35 (0.29)	0.50 (0.26)	0.63 (0.22)	0.75 (0.14)	0.76 (0.15)
	PLI	0.12 (0.16)	0.08 (0.19)	0.19 (0.19)	0.12 (0.20)	0.13 (0.18)

areas. DMN and FP networks presented lower ICC than sensory networks for all FC metrics. Moreover, FC increased along with ICC values for d-ecor, lc-ecor and PLV, as revealed by the joint distribution of both magnitudes. This relation was however not linear, especially for FC metrics without zero-lag correction (PLV and d-ecor), for which the ICC increased first rapidly along with FC values and then saturated for medium to high FC (Figure 4.7 and Figure E.1).

Within- and between-subject agreement of seed-based FC maps

The within- and between-subject agreement of seed-based FC maps was computed with Kendall's W from pairwise maps of a single and distinct subjects. W values for every frequency band, FC metric and seed are listed in Table 4.5. High within- and between-subject W indicate low within-subject variability and robust networks across subjects, respectively. Additionally, high within- relative to between-subject W contributes to high reliability. First, highest within- and between-subject W values were found for PLV (0.68-0.96). Moreover, within-subject W was generally significantly higher than between-subject W for PLV (19% increment on average), and W values tended to increase with increasing frequencies. Second, similar W values were found for d-ecor and PLI, although d-ecor tended to present slightly higher W. For both metrics, W was medium to high (0.57-0.80), and within-subject W was higher than between-subject W (5% difference on average). Finally, lc-ecor presented low W (0.49-0.59) and also little variability across frequency bands and seeds. Additionally, within-subject W was only marginally higher than between-subject W for lc-ecor (1% higher on average), and differences between both W estimates failed to reach significance for most frequencies and seeds. Of note, W values for the seeds in visual, sensorimotor, auditory cortices and precuneus were generally higher than for the frontal seeds selected from fronto-parietal and fronto-insular RSNs.

Table 4.5: Kendall's W of within and between-subject agreement between pairwise seed-based FC maps. Average Kendall's W for within-subject (w) and between-subject (b) agreement are listed for each frequency band, seed and FC metric. The standard deviation of W is displayed in parenthesis below its average value. Asterisks denote significant differences between within- and between-subject W (Wilcoxon ranksum test, corrected with false discovery rate and q=0.05).

		Delta		Theta		Alpha		Beta		Gamma	
		w	b	w	b	w	b	w	b	w	b
Left visual	d-ecor	0.64 (0.06)	0.62 (0.04)	0.67* (0.06)	0.64 (0.05)	0.70* (0.07)	0.67 (0.05)	0.74* (0.08)	0.69 (0.06)	0.69* (0.06)	0.65 (0.05)
	lc-ecor	0.50	0.49	0.50	0.50	0.52	0.51	0.56*	0.53	0.53*	0.50

		Delta		Theta		Alpha		Beta		Gamma	
		w	b	w	b	w	b	w	b	w	b
		(0.06)	(0.05)	(0.05)	(0.05)	(0.06)	(0.06)	(0.07)	(0.07)	(0.05)	(0.05)
	PLV	0.83*	0.73	0.87*	0.75	0.88*	0.75	0.94*	0.78	0.95*	0.76
		(0.05)	(0.07)	(0.07)	(0.08)	(0.05)	(0.07)	(0.04)	(0.09)	(0.03)	(0.08)
	PLI	0.65	0.63	0.65*	0.63	0.69*	0.65	0.67*	0.65	0.68*	0.65
		(0.07)	(0.06)	(0.06)	(0.07)	(0.06)	(0.06)	(0.06)	(0.06)	(0.07)	(0.07)
Left	d-ecor	0.64*	0.62	0.66*	0.62	0.71*	0.65	0.79*	0.74	0.68*	0.64
somato		(0.06)	(0.05)	(0.06)	(0.05)	(0.05)	(0.05)	(0.08)	(0.07)	(0.06)	(0.04)
sensory	lc-ecor	0.52	0.50	0.49	0.50	0.51	0.50	0.59	0.55	0.51	0.51
		(0.05)	(0.05)	(0.05)	(0.05)	(0.07)	(0.06)	(0.12)	(0.09)	(0.06)	(0.05)
	PLV	0.84*	0.72	0.87*	0.73	0.91*	0.77	0.94*	0.77	0.93*	0.75
		(0.06)	(0.06)	(0.05)	(0.07)	(0.04)	(0.07)	(0.04)	(0.06)	(0.04)	(0.06)
	PLI	0.66	0.64	0.64*	0.62	0.65	0.63	0.65*	0.61	0.66*	0.62
		(0.06)	(0.07)	(0.05)	(0.06)	(0.06)	(0.06)	(0.07)	(0.06)	(0.06)	(0.06)
Left	d-ecor	0.70*	0.68	0.73*	0.69	0.76*	0.71	0.78*	0.72	0.71*	0.67
auditory		(0.06)	(0.05)	(0.05)	(0.05)	(0.06)	(0.06)	(0.06)	(0.06)	(0.06)	(0.05)
	lc-ecor	0.50	0.50	0.51	0.50	0.51	0.50	0.54	0.52	0.49	0.50
		(0.05)	(0.05)	(0.05)	(0.05)	(0.05)	(0.05)	(0.08)	(0.07)	(0.05)	(0.05)
	PLV	0.91*	0.80	0.93*	0.82	0.95*	0.83	0.96*	0.82	0.96*	0.81
		(0.03)	(0.06)	(0.02)	(0.05)	(0.02)	(0.05)	(0.03)	(0.05)	(0.02)	(0.06)
	PLI	0.66*	0.63	0.66*	0.63	0.69*	0.65	0.65*	0.63	0.66*	0.63
		(0.06)	(0.06)	(0.06)	(0.06)	(0.06)	(0.05)	(0.06)	(0.06)	(0.06)	(0.06)
Precuneus	d-ecor	0.68*	0.65	0.71*	0.69	0.75*	0.71	0.80*	0.75	0.74*	0.70
		(0.05)	(0.04)	(0.05)	(0.05)	(0.05)	(0.05)	(0.05)	(0.06)	(0.06)	(0.05)
	lc-ecor	0.51	0.50	0.49	0.50	0.54*	0.51	0.57*	0.53	0.50	0.50
		(0.05)	(0.05)	(0.05)	(0.05)	(0.06)	(0.05)	(0.10)	(0.08)	(0.05)	(0.05)
	PLV	0.87*	0.77	0.92*	0.80	0.93*	0.79	0.96*	0.84	0.96*	0.83
		(0.04)	(0.05)	(0.04)	(0.06)	(0.03)	(0.05)	(0.03)	(0.06)	(0.03)	(0.06)
	PLI	0.70*	0.66	0.72*	0.69	0.70*	0.68	0.75*	0.72	0.74*	0.72
		(0.06)	(0.06)	(0.11)	(0.10)	(0.11)	(0.10)	(0.06)	(0.05)	(0.06)	(0.05)
Left	d-ecor	0.58	0.58	0.61*	0.59	0.63*	0.60	0.70*	0.64	0.61	0.60
middle		(0.05)	(0.05)	(0.06)	(0.05)	(0.05)	(0.05)	(0.08)	(0.08)	(0.05)	(0.04)
frontal	lc-ecor	0.50	0.50	0.49	0.50	0.50	0.51	0.55*	0.51	0.50	0.50
		(0.05)	(0.05)	(0.04)	(0.05)	(0.06)	(0.05)	(0.09)	(0.08)	(0.04)	(0.05)
	PLV	0.77*	0.67	0.82*	0.69	0.86*	0.68	0.91*	0.72	0.90*	0.74
		(0.06)	(0.05)	(0.05)	(0.06)	(0.05)	(0.07)	(0.04)	(0.09)	(0.05)	(0.09)
	PLI	0.62*	0.60	0.62	0.61	0.65*	0.61	0.65*	0.62	0.63*	0.61
		(0.05)	(0.05)	(0.05)	(0.06)	(0.06)	(0.06)	(0.07)	(0.05)	(0.06)	(0.06)
Right	d-ecor	0.59	0.59	0.61	0.59	0.63	0.60	0.70*	0.65	0.64*	0.61

		Delta		Theta		Alpha		Beta		Gamma	
		w	b	w	b	w	b	w	b	w	b
middle		(0.05)	(0.05)	(0.06)	(0.05)	(0.06)	(0.05)	(0.08)	(0.07)	(0.05)	(0.06)
frontal	lc-ecor	0.49	0.50	0.51	0.50	0.50	0.50	0.53	0.52	0.50	0.50
		(0.06)	(0.05)	(0.06)	(0.05)	(0.05)	(0.05)	(0.09)	(0.07)	(0.05)	(0.05)
	PLV	0.77*	0.68	0.82*	0.68	0.86*	0.70	0.91*	0.72	0.91*	0.74
		(0.05)	(0.06)	(0.06)	(0.07)	(0.06)	(0.07)	(0.06)	(0.10)	(0.07)	(0.10)
	PLI	0.63*	0.60	0.60	0.59	0.63*	0.60	0.62*	0.58	0.64*	0.61
		(0.06)	(0.06)	(0.05)	(0.06)	(0.07)	(0.06)	(0.07)	(0.06)	(0.06)	(0.06)
Median	d-ecor	0.61	0.61	0.62	0.61	0.67*	0.63	0.75*	0.70	0.66*	0.63
cingulate		(0.04)	(0.04)	(0.05)	(0.04)	(0.05)	(0.05)	(0.07)	(0.07)	(0.05)	(0.05)
	lc-ecor	0.50	0.50	0.49	0.50	0.51	0.49	0.55	0.53	0.49	0.51
		(0.05)	(0.05)	(0.06)	(0.05)	(0.06)	(0.05)	(0.10)	(0.08)	(0.05)	(0.05)
	PLV	0.79*	0.71	0.84*	0.72	0.88*	0.73	0.93*	0.76	0.94*	0.77
		(0.05)	(0.06)	(0.04)	(0.06)	(0.04)	(0.06)	(0.02)	(0.06)	(0.03)	(0.06)
	PLI	0.64*	0.57	0.63*	0.58	0.68*	0.60	0.63*	0.59	0.64*	0.59
		(0.09)	(0.10)	(0.05)	(0.09)	(0.08)	(0.12)	(0.09)	(0.11)	(0.10)	(0.12)

4.3.4 Discussion

In this work, we assessed the test-retest reliability of 7 MEG RSNs by exploring within- and between-subject variability of FC values in a cohort of 16 subjects. First, node coordinates for each RSN were defined based on previously released fMRI RSNs (Laird et al., 2011; Smith et al., 2009). Then, source space FC was computed between each node (or seed) and the remaining RSN nodes (within-network) and all source locations using four distinct FC metrics: d-ecor, lc-ecor, PLV and PLI. Within- and between-subject variability was employed to assess reliability and agreement of the FC maps. First, reliability was quantified with the ICC, yielding overall medium to high values (ICC>0.5). ICC values depended however greatly on the FC and frequency band, and highest values were found for PLV in alpha, beta and gamma bands and for d-ecor and lc-ecor in beta band. Moreover, within-network FC was found to be more reliable than between-network FC. Second, within- and between-subject agreement was evaluated with Kendall's coefficient of concordance W. W values ranged from medium to high (0.5-0.97) depending on the frequency band and the FC metric. W was highest with PLV and lowest with lc-ecor. Additionally, within-subject W was generally significantly higher than between-subject FC.

To our knowledge, this constitutes the first test-retest reliability study of MEG source space FC. Test-retest reliability of FC has however already been explored with sensor space MEG/EEG and fMRI. Deuker et al. (2009) and Jin et al. (2011) employed

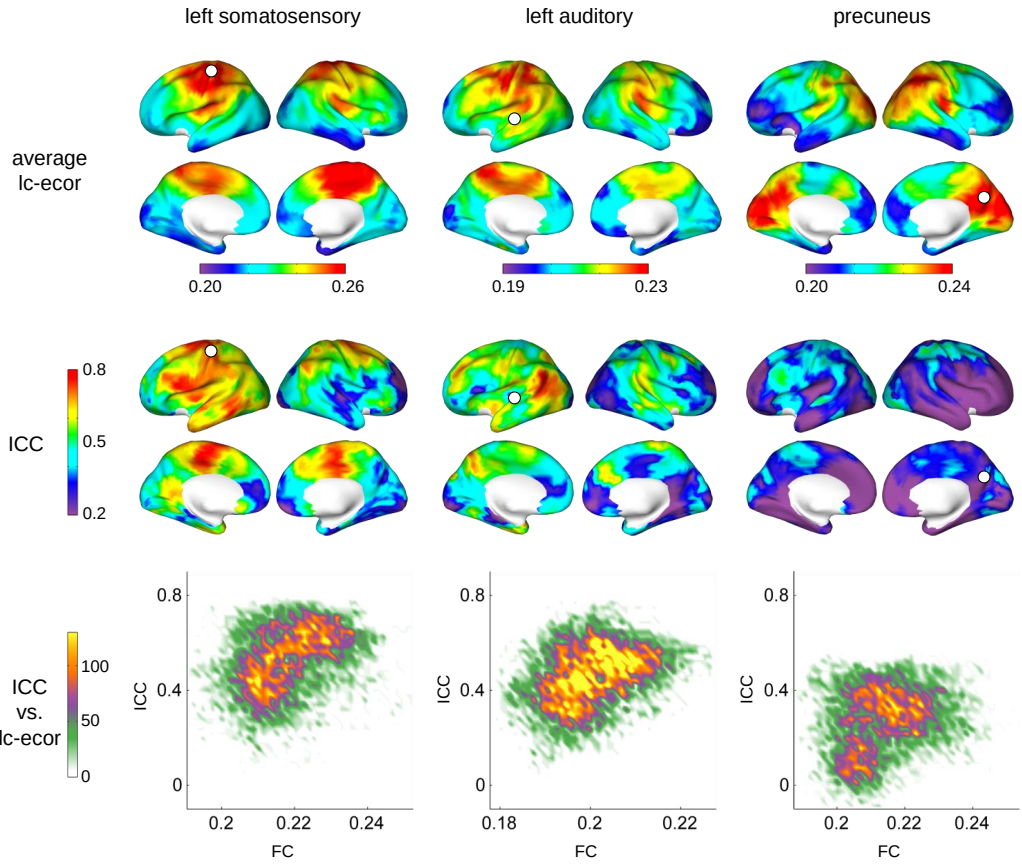

Figure 4.6: FC and ICC for beta band resting-state eyes closed and lc-ecor. For three selected seeds (left primary somatosensory, left primary auditory and precuneus), average FC maps (1st row), ICC (2nd row) and the normalized joint histogram of ICC and FC values (3rd row) are displayed. FC maps are averaged over all sessions and subjects. The seed location is indicated with a white circle. For better visualization, the template brain surface was inflated with Caret software (Van Essen et al., 2001).

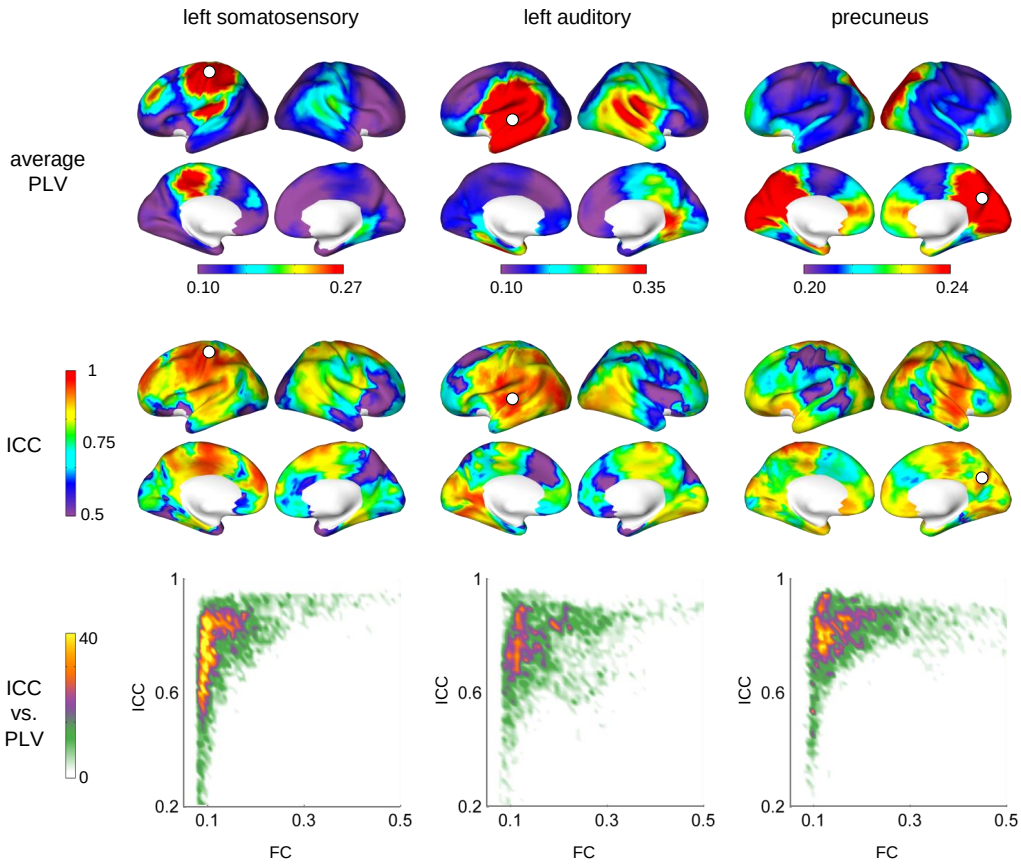

Figure 4.7: FC and ICC for beta band resting-state eyes closed and PLV. For three selected seeds (left primary somatosensory, left primary auditory and precuneus), average FC maps (1st row), ICC (2nd row) and the normalized joint histogram of ICC and FC values (3rd row) are displayed. FC maps are averaged over all sessions and subjects. The seed location is indicated with a white circle.

the ICC to estimate the reliability of resting-state graph metrics derived from MEG sensor space mutual information. While Jin et al. (2011) found medium ICC (0.4-0.65) for alpha and beta bands and lower ICC for theta and gamma bands, Deuker et al. (2009) obtained low ICC (0-0.5) for all frequency bands but alpha (0.5-0.8). Interestingly, the ICC of graph metrics during a working memory task was found to be higher than during resting-state. Using EEG and sensor space PLI, Hardmeier et al. (2014) obtained good reliability (ICC range: 0.5-0.8) for graph metrics in theta, alpha and beta bands. Test-retest studies of sensor space graph metrics have therefore obtained divergent results, although they cannot be easily compared because of differences in the processing methodology, the choice of FC metric and the test-retest interval. Using resting-state fMRI, Shehzad et al. (2009) could directly inspect the test-retest reliability of RSNs by computing FC between regions of interest selected from the fMRI literature. They overall obtained low reliability (average ICC=0.10-0.40), although higher ICC values were found when considering significant correlations exclusively. This is in agreement with our results and suggests that strong connections are more reliable. Although not focusing on reliability, Wens et al. (2014) studied short-term within-subject variability in MEG FC with 4 subjects that underwent 20 scans sessions in a single day. After selecting three seeds in visual, auditory and sensorimotor cortices, they evaluated the spatial similarity between FC maps. They finally recommended between 2 to 11 sessions to produce a robust subject average, depending on the network. Moreover, in line with our work, they obtained that the sensorimotor network presented the highest within-subject similarity, and hence required the least sessions to produce good subject-representative average FC maps.

An interesting result in our work is the frequency specificity of the reliability of RSNs. With PLV, RSNs reached medium to good reliability for all frequency bands, but highest ICC values were consistently found in alpha, beta and gamma bands. In the previously commented graph metrics studies (Deuker et al., 2009; Jin et al., 2011; Hardmeier et al., 2014), reliability was generally highest for alpha, reasonably good for theta and beta, and quite low for gamma. Although we cannot establish any direct analogy between our approach and sensor space graph metrics, given that high frequency oscillations are supposed to be more local than low frequency oscillations (Buzsáki and Draguhn, 2004), we could speculate that we found higher gamma band reliability because gamma network properties are not well captured with sensor space FC. When using d-ecor and lc-ecor, reliability varied greatly amongst frequency bands and was higher in beta. This finding is not particularly surprising, since MEG RNS have been predominantly studied with envelope correlation in the beta band. In fact, although the seminal work of (Brookes et al., 2011b,a; de Pasquale et al., 2010; Hipp

et al., 2012) investigated RSNs with envelope correlation at several frequency bands, they concluded that most networks were best extracted in the beta band, and alpha band in (de Pasquale et al., 2010) and in (Brookes et al., 2011b) for the DMN.

Additionally, we found that the choice of FC metric greatly influenced reliability. ICC was highest for PLV, medium for d-ecor and lc-ecor, and lowest for PLI, indicating that PLV estimates are the most reliable ones. Recent literature of MEG RSNs has however predominantly used d-ecor and lc-ecor. Envelope correlation has in fact produced FC maps which resemble the ones obtained with fMRI (Brookes et al., 2011b; de Pasquale et al., 2010, 2012). Further, lc-ecor refines d-ecor by eliminating zero-lag volume conduction effects, using either time-domain (Brookes et al., 2012) or frequency domain (Hipp et al., 2012; Wens et al., 2014) orthogonalization. In our work, lc-ecor yielded similar average FC maps than in the previously commented studies. With lc-ecor, homologous areas in sensory networks were strongly connected and, contrary to PLV or d-ecor, the neighborhood of the seed did not present artefactual high values. Our results suggest nonetheless, that, although lc-ecor produces meaningful and unbiased FC maps, PLV estimates are more reliable. Furthermore, phase and amplitude synchronization represent different mechanisms of information transfer, so that the choice of FC metric should depend on the underlying FC model (Fell and Axmacher, 2011).

4.4 Conclusions

In conclusion, we provided the first source space test-retest reliability study of resting state MEG power and FC estimates. We found that such measures reach high reliability, which encourages their use in assessing the changes produced by drug treatments, neuropsychological rehabilitation, degenerative diseases or developmental trajectories. We evaluated the effect of a number of factors on reliability –frequency band, brain region, FC metric– which might guide researchers and clinicians to obtain reliable results in future MEG studies. Reliability was defined here as a relative quantity (Weir, 2005), which represents the fraction of the measurement variability that is accounted for by between-subject variability. Under this model, any within-subject variability constitutes a measurement error, regardless of whether it results from the MEG system, external or biological noise in the subject, the data processing pipeline, or a real change in the power intensity or the coupling strength between the two brain regions. We can therefore not conclude that power or FC estimates with highest reliability are the most accurate or the most valid ones. It could as well be possible that the within-subject variability was caused from a true variability in the neuronal firing

or coupling strength. Besides, increasing between-subject variability in FC estimates results in increasing reliability. Reliability is in fact a useful quantity to assess how good individuals can be identified within a group using power or FC values.

Chapter 5

Conclusions and future directions

5.1 Main conclusions

In this thesis, we followed two main lines:

- In Chapter 3, we characterized resting state spectral and FC profiles in MCI. Resting state MEG was recorded in a sample of MCI patients and age-matched controls. Then, the activity of some regions of interest was reconstructed with beamforming. The source-space time series were employed to estimate both the spectral content of brain currents and FC between DMN regions. The statistical analysis comparing controls and MCI patients revealed abnormalities in the MCI group. MCIs presented both a widespread slowing in the alpha rhythm, as evidenced by a decrease of the alpha peak frequency, and a decreased FC in the DMN in this same frequency band. Both findings point out that alpha rhythms are involved in the MCI pathology: they become slower and functionally disconnected. Moreover, these electrophysiological differences were found to occur along with structural changes which are commonly associated with AD: hippocampal volume loss and decrease of white matter fractional anisotropy. This suggests that the alpha slowing and disconnection in the DMN could be indicative of the neurodegeneration associated with the MCI-AD continuum.

- In Chapter 4, we evaluated the test-retest reliability of MEG power and FC estimates. In fact, MEG power and FC are mostly used for group-level analyses between various sets of individuals or various conditions. This was the case of the previous studies on MCI introduced in Chapter 3: statistical analysis revealed differences between controls and MCIs, but no conclusions could be drawn at the individual level, since measurement noise and within-subject

variability is undetermined. This hinders the use of MEG in clinical applications and in the characterization of individual subjects. To tackle this issue, a cohort of healthy subjects underwent three MEG resting state recordings with a one week test-retest interval. Source reconstruction was performed and power and FC were calculated. The reliability of both measures was assessed with the ICC. First, power reliability varied amongst brain regions and frequency bands. It was generally high for theta, alpha and beta bands (ICC>0.7), and lower for delta and gamma bands. Furthermore, within-subject variability correlated negatively with source intensity, although the dependence between both magnitudes was not linear. In fact, while highest within-subject variability was consistently found for low power sources, the lowest within-subject variability was not normally found for the highest power sources. Secondly, the reliability of FC estimates connecting seeds of interest and the remaining source locations was assessed, for four FC metrics: d-corr, lc-corr, PLV and PLI. Seeds represented the nodes of 7 well-known RSNs (visual, sensorimotor, auditory, DMN, left FP, right FP and fronto-insular), and were extracted from the resting state literature. Reliability varied across frequency bands, source locations and FC metrics. PLV estimates were found to be highly reliable, often exhibiting ICC>0.8, especially in alpha, beta and gamma frequency bands. D-corr and lc-corr were generally quite unreliable (ICC<0.4), except for the beta band, for which ICC values of 0.6-0.7 were reached. PLI yielded the least reliable FC estimates, which rarely exceeded ICC=0.4. Moreover, ICC correlated with the average FC, so that strongest connections tended to be more reliable for all FC metrics.

Overall, we found that MCI is accompanied by changes in resting state MEG power spectrum and FC, and that these power and FC measures are fairly reliable in healthy subjects. This suggests that resting-state MEG alterations could be detected at the individual level, and potentially employed in a clinical scenario.

5.2 Limitations

Our results are dependent on the employed MEG data processing methodology. Despite recent efforts to establish general guidelines for MEG research (Gross et al., 2013), there are multitude of analysis techniques for each processing step (preprocessing, source reconstruction, FC computation, etc.), and no consensus has been reached on which are the most appropriate ones. In this work, we used beamforming for source reconstruction, following extensive MEG resting state literature (Hillebrand et al., 2005; Brookes et al., 2011a; Schoffelen and Gross, 2009; Brookes et al., 2011b;

Hillebrand et al., 2012; Hipp et al., 2012). We note however that some groups prefer minimum norm solutions (de Pasquale et al., 2012; Wens et al., 2014). As for the choice of FC metric, we selected envelope correlation in Chapter 3 because this metric had been previously employed in the successful reconstruction of resting state networks using MEG data (Brookes et al., 2011a,b; Maldjian et al., 2014). However, in Chapter 4 we explored reliability with four FC metrics. Higher ICC values were found for PLV, so that rerunning the analysis in Chapter 3 with PLV seems worthwhile. Furthermore, bigger sample sizes in all the included studies would contribute to increasing the robustness of the results.

5.3 Suggestions for future work

The work presented in this thesis sheds some light into the spectral and FC alterations in MCI and their reliability. However, many related research lines remain unexplored, and could be addressed in future studies. We suggest some of them in the following.

- *Reliability in MCI.* Reliability depends on the subject sample, as it accounts both for within- and between-subject variability. This means the reliability of MEG power and FC measures could differ when measured in a sample of healthy young subjects and in a sample of MCI patients. On the one hand, if MCI subjects were to be more variable across time than young healthy individuals (higher within-subject variability), reliability in the MCI group would be smaller than the one estimated in Chapter 3. On the other hand, if MCIs were to be more heterogeneous than young heathy subjects (higher between-subject variability), reliability in the MCI group would be higher than in Chapter 3.

- *Longitudinal studies.* Clinical and MEG follow-ups could provide information on the clinical significance of the results. In fact, MCI individuals can either progress to develop dementia, remain MCI or revert to control. It could be expected that these three outcomes were characterized by distinct MEG spectral or FC patterns. A longitudinal study could therefore contribute to evaluating whether MEG spectral and FC patterns could have any use in the prognosis of the cognitive decline. Of note, longitudinal studies could be perceived as a test-retest study with a test-retest interval that is long enough for substantial changes in the individuals' cognitive state to take place.

- *Use of classifiers.* If proven reliable, the power and FC patterns distinguishing MCIs and controls could be employed for building classifiers, possibly with the

use of machine learning techniques. This would ideally be performed with a big dataset of MEG resting state recordings from MCIs and controls, which would be split into big training and testing sets and yield robust classifiers and accuracy estimations.

Appendix A

List of publications

- Garcés, P., Vicente, R., Wibral, M., Pineda-Pardo, J.Á., López, M.E., Aurtenetxe, S., Marcos, A., de Andrés, M.E., Yus, M., Sancho, M., Maestú, F., Fernández, A. (2013). Brain-wide slowing of spontaneous alpha rhythms in mild cognitive impairment. *Frontiers in Aging Neuroscience*, 5.

- Garcés, P., Pineda-Pardo, J.A., Canuet, L., Aurtenetxe, S., López, M.E., Marcos, A., Yus, M., Llanero-Luque, M., Del-Pozo, F., Sancho, M., Maestú, F. (2014). The Default Mode Network is functionally and structurally disrupted in amnestic mild cognitive impairment - a bimodal MEG-DTI study. *NeuroImage Clinical*, 6:214–21.

- López, M.E., Garcés, P., Cuesta, P., Castellanos, N.P., Aurtenetxe, S., Bajo, R., Marcos, A., Montenegro, M., Yubero, R., del Pozo, F., Sancho, M., Maestú, F. (2014). Synchronization during an internally directed cognitive state in healthy aging and mild cognitive impairment: a MEG study. *Age (Dordr)*, 36(3):1389-1406.

- Pineda-Pardo, J.A., Garcés, P., López, M.E., Aurtenetxe, S., Cuesta, P., Marcos, A., Montejo, P., Yus, M., Hernández-Tamames, J.A., del Pozo, F., Becker, J.T., Maestú, F. (2014). White matter damage disorganizes brain functional networks in amnestic mild cognitive impairment. *Brain Connectivity*, 4:312–22.

- Cuesta, P., Garcés, P., Castellanos, N.P., López, M.E., Aurtenetxe, S., Bajo, R., Pineda-Pardo, J.A., Bruña, R., Marín, A.G., Delgado, M., Barabash, A., Ancín, I., Cabranes, J.A., Fernandez, A., Del Pozo, F., Sancho, M., Marcos, A., Nakamura, A., Maestú, F. (2015). Influence of the APOE $\epsilon 4$ Allele and Mild Cognitive Impairment Diagnosis in the Disruption of the MEG Resting State Functional Connectivity in Sources Space. *Journal of Alzheimer's Disease*, 44(2):493–505

- López, M.E., Cuesta, P., Garcés, P., Castellanos, P.N., Aurtenetxe, S., Bajo, R., Marcos, A., Delgado, M.L., Montejo, P., López-Pantoja, J.L., Maestú, F., Fernandez, A. (2014). MEG spectral analysis in subtypes of mild cognitive impairment. *Age (Dordr)*, 36:1092-1112.

Appendix B

Acronyms

Aβ	Amyloid beta
AC	Anterior cingulate
AD	Alzheimer's disease
APOE	Apolipoprotein E
BEM	Boundary element method
BOLD	Blood oxygen level-dependent
CFC	Cross-frequency coupling
CSF	Cerebrospinal fluid
d-ecor	Envelope correlation (without leakage correction)
DMN	Default mode network
dSC	Direct structural connectivity
DTI	Diffusion tensor imaging
DWI	Diffusion weighted imaging
EC	Effective connectivity
EEG	Electroencephalography
FA	Fractional anisotropy

FC	Functional connectivity
FEM	Finite element method
FIR	Finite impulse response
fMRI	Functional magnetic resonance imaging
FP	Fronto-parietal
ICA	Independent component analysis
ICC	Intraclass correlation coefficient
IP	Inferior parietal
lc-ecor	Envelope correlation with leakage correction
LCMV	Linearly constrained minimum variance beamformer
MCE	Minimum current estimate
MCI	Mild cognitive impairment
MEG	Magnetoencephalography
MNE	Minimum norm estimate
MRI	Magnetic resonance imaging
MSR	Magnetically shielded room
PC	Posterior cingulate
PET	Positron emission tomography
PLI	Phase lag index
PLV	Phase locking value
Pr	Precuneus
ROI	Region of interest
RSN	Resting state network
SC	Structural connectivity

SNR	Signal to noise ratio
SQUID	Superconducting quantum interference device
SSS	Signal space separation
tSSS	Spatiotemporal SSS
wSC	Weighted structural connectivity

Appendix C

Forward model comparison

An exploratory analysis was performed to compare different forward solutions and assess their relative validity. For that, leadfield matrices were computed with five forward models that were introduced in section 2.3.2: single sphere, local spheres, Nolte, 1-shell BEM and 3-shell BEM. All forward models derived from the same original geometries: inner skull, outer skull and scalp surfaces which were extracted from the individuals' MRI with NFT (Neuroelectromagnetic Forward Modeling Toolbox) (Acar and Makeig, 2010) and realigned to the MEG coordinate system with MNE software (Gramfort et al., 2014). These surfaces were then employed into five forward solution calculations:

Single sphere model

A sphere was fitted to inner skull surface and Sarva's analytical solution (2.24) was applied. This was performed with FieldTrip (Oostenveld et al., 2011).

Local spheres model

For each MEG sensor, a sphere was fitted to the points of the inner skull surface that lied closer than 10 cm to that sensor, and then Sarva's formula was applied. This was performed with FieldTrip, following (Huang et al., 1999).

Nolte or corrected-sphere model

Nolte or corrected-sphere model: Following (Nolte, 2003), this forward solution started from the single sphere solution and then additional terms were added to account for the full geometry of the inner skull surface. This was also performed with FieldTrip.

1-shell BEM

The inner skull mesh consisted of 7000 small triangles, which were used to

reduce the forward solution into a system of equations. This was solved with MNE software.

3-shell BEM

Analogous to 1-shell BEM, but the volume conductor includes also skull and scalp compartments, so that outer skull and scalp surfaces were also employed.

For all five models, the forward calculations were performed for the same source locations: a mesh with 6mm spacing that covered the subjects' cortical surface. These source locations were extracted from Freesurfer+MNE. Then, for each model, the leadfield can be stored as a 3D matrix: $N_{channels} \times N_{sources} \times 3$. The third dimension corresponds to 3 directions (x, y, z) for the dipole moment.

At first sight, leadfield matrices were similar for all five models. In fact, for a given channel, the distribution of leadfield values over the cortical surface for all models looks alike. For instance, one can barely appreciate any difference between forward solutions when looking at the distribution of leadfield values for a given subject and channel, as shown in Figure C.1-A. However, these differences become evident when plotting the difference between forward solutions, as in Figure C.1-B. For this channel, the average relative difference to BEM3 model were 8.4%, 12.3%, 14.3% and 20.9% for BEM1, Nolte, local spheres and single sphere respectively

To evaluate these differences, we performed a pairwise comparison of the relative error between forward solutions. Figure C.2 condenses these results in a violin plot of the pairwise relative errors: the higher the density near 0 (or area in the violin plot near 0), the smaller the relative error. The closest pairs of forward solutions were BEM3-BEM1, followed by BEM3-Nolte, BEM1-Nolte, and Nolte-local spheres.

To further inspect the spatial dependence of these differences, we employed Freesurfer's Desikan-Killiany atlas (Fischl et al., 2004) and grouped the leadfield matrix into 34 anatomical regions. Then, correlation coefficients between leadfield values for each pair of forward models were computed separately for each region, as summarized in Table C.1. High correlation values were found between BEM3, BEM1 and Nolte models. Local spheres and single sphere models were highly correlated with the other models for some regions such as paracentral, inferior parietal, superior parietal or Precuneus, presumably because the inner skull surface close to these regions fits well to a sphere. Conversely, the lowest correlation values were found in orbital and medial temporal regions, probably because geometry of volume conductor near these regions deviates strongly from the spherical fit.

Overall, we conclude that all models worked reasonably well (or at least similarly). In fact, at first sight, the leadfield distribution over the cortical surface was very similar

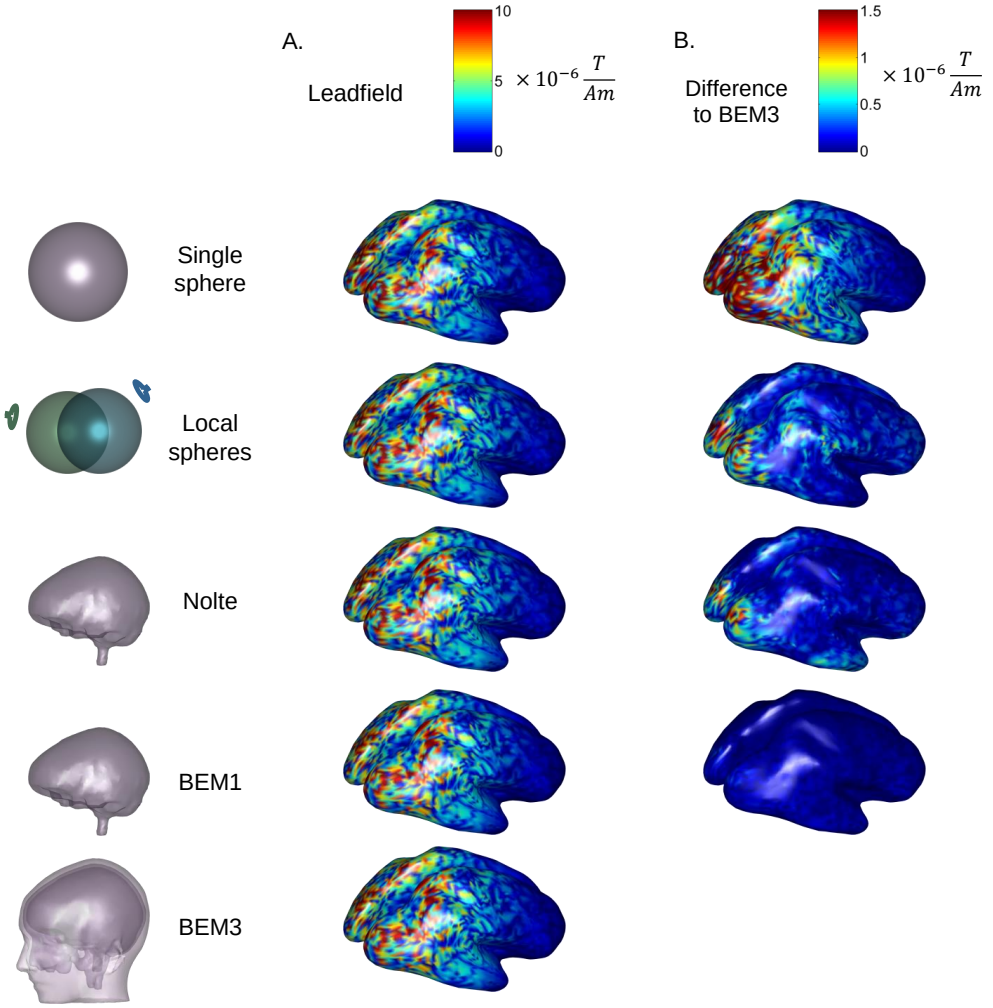

Figure C.1: Leadfield distribution for a given subject and occipital channel. Each row corresponds to a different forward model:. A. Distribution of leadfield values over the cortical surface. The leadfield is projected in a direction normal to the cortical surface (which represents the direction of the pyramidal neurons). B. absolute value of the difference between all solutions and BEM3. Note that the colorbar in B has a different scale: values are smaller than in A.

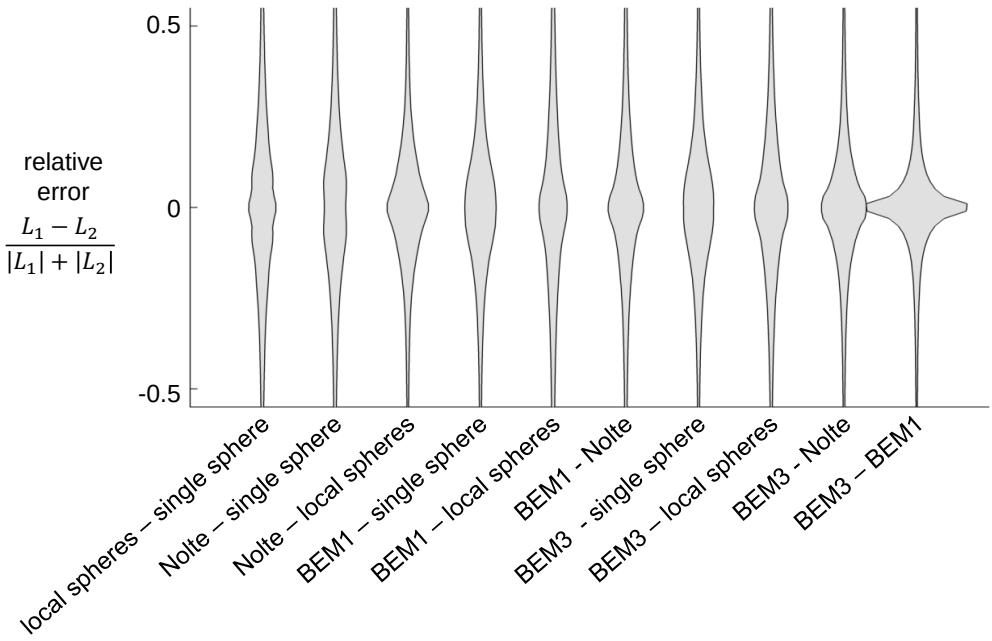

Figure C.2: Relative error between forward solutions. The relative error between leadfield matrices was computed for all pairs of forward solutions, using all MEG magnetometers and source locations. These values are displayed in a violin plot, which represents the distribution of relative error values.

for all five models. However, a more careful inspection revealed some differences between forward solutions, which were in some cases not negligible. These differences were highest for frontal and medial temporal regions. Nolte, BEM1 and BEM3 performed similarly, so they all seem good choices for the forward model. Of note, (Stenroos et al., 2014) obtained similar conclusions. However, BEM3 seems a safer choice, especially when interested in orbital or medial temporal regions.

Table C.1: Correlation between leadfields obtained with five forward models for 34 regions of interest. All sources included in the regions of interest and all MEG magnetometers were used to compute the correlations. For easier visualization, correlation values higher than 0.98 are highlighted in bold green and correlation values lower than 0.8 are highlighted in bold red. Singles: single sphere, Locals, local spheres, STS: Superior Temporal Sulcus.

	Locals Nolte	Nolte Singles	Nolte Locals	BEM1 Singles	BEM1 Locals	BEM1 Nolte	BEM3 Singles	BEM3 Locals	BEM3 Nolte	BEM3 BEM1
Banks of the STS	0.94	0.96	**0.98**	**0.98**	0.94	0.95	**0.98**	0.97	**0.98**	**0.99**
Caudal anterior cingulate	**0.78**	**0.75**	0.95	0.91	0.9	0.89	0.88	0.94	0.94	**0.98**
Caudal middle frontal	0.95	0.95	0.98	0.97	0.96	0.98	0.97	0.98	**0.99**	**0.99**
Cuneus	0.95	0.96	**0.99**	0.97	0.97	**0.98**	0.97	**0.98**	**0.99**	**1.00**
Entorhinal	**0.78**	**0.65**	0.85	0.92	**0.67**	**0.45**	0.97	**0.79**	**0.61**	0.97
Fusiform	0.86	0.85	0.95	0.94	**0.79**	**0.76**	0.96	0.89	0.88	0.97
Inferior Parietal	0.97	0.98	**0.99**	**0.98**	0.97	**0.99**	**0.98**	**0.98**	**0.99**	**1.00**
Inferior Temporal	0.89	0.87	0.95	0.95	0.85	0.82	0.96	0.92	0.9	0.98
Isthmus cingulate	0.85	0.87	0.96	0.93	0.88	0.89	0.92	0.95	0.96	0.97
Lateral occipital	0.96	0.97	**0.98**	0.98	0.95	0.97	0.98	0.97	**0.99**	**0.99**
Lateral orbitofrontal	0.91	0.84	0.96	0.88	**0.74**	**0.66**	0.95	0.89	0.84	0.95
Lingual	0.92	0.94	0.98	0.98	0.91	0.93	0.98	0.96	0.98	**0.98**
Medial orbitofrontal	0.92	0.88	0.97	0.92	**0.77**	**0.70**	0.98	0.91	0.87	0.95
Middle temporal	0.92	0.92	0.97	0.96	0.89	0.89	0.97	0.95	0.95	**0.98**
Parahippocampal	**0.78**	**0.77**	0.93	0.88	**0.60**	**0.49**	0.96	0.82	**0.75**	0.93
Paracentral	0.98	0.98	**0.99**	**0.99**	0.98	**0.99**	**0.98**	**0.99**	**1.00**	**1.00**
Pars opercularis	0.9	0.88	0.96	0.94	0.91	0.92	0.94	0.95	0.97	**0.99**
Pars orbitalis	0.91	0.85	0.95	0.85	**0.76**	**0.75**	0.89	0.87	0.88	0.96
Pars triangularis	0.9	0.83	0.93	0.85	0.85	0.87	0.86	0.91	0.94	0.98
Pericalcarine	0.94	0.96	**0.98**	**0.98**	0.95	0.97	0.98	0.98	**0.99**	**0.99**

	Locals Nolte	Nolte Sin-gles	Nolte Locals	BEM1 Sin-gles	BEM1 Locals	BEM1 Nolte	BEM3 Sin-gles	BEM3 Locals	BEM3 Nolte	BEM3 BEM1
Postcentral	0.96	0.97	**0.98**	**0.98**	0.96	0.98	**0.98**	0.97	**0.99**	**1.00**
Posterior cingulate	0.9	0.94	0.97	0.95	0.93	0.96	0.95	0.96	**0.98**	**0.99**
Precentral	0.95	0.96	0.98	**0.98**	0.95	0.97	0.98	0.97	**0.98**	**0.98**
Precuneus	0.96	0.97	**0.99**	**0.98**	0.97	**0.98**	0.98	**0.98**	**0.99**	**1.00**
Rostral anterior cingulate	0.89	0.83	0.96	0.95	0.84	**0.78**	0.95	0.94	0.91	0.96
Rostral middle frontal	0.93	0.88	0.96	0.9	0.9	0.92	0.9	0.95	0.97	0.98
Superior frontal	0.93	0.9	0.97	0.93	0.95	0.97	0.92	0.97	**0.99**	**0.99**
Superior parietal	0.98	**0.98**	**0.99**	**0.99**	**0.98**	**0.99**	**0.98**	**0.99**	**1.00**	**1.00**
Superior temporal	0.89	0.9	0.97	0.97	0.87	0.87	0.97	0.94	0.94	**0.98**
Supramarginal	0.96	0.97	0.98	**0.98**	0.95	0.98	**0.98**	0.97	**0.99**	**0.99**
Frontal pole	0.95	0.89	0.96	0.94	0.87	0.82	0.96	0.95	0.93	0.95
Temporal pole	0.88	**0.75**	0.9	0.91	**0.73**	**0.54**	0.96	0.87	**0.72**	0.96
Transverse temporal	0.88	0.92	0.97	0.98	0.87	0.9	0.97	0.93	0.96	**0.98**
Insula	**0.72**	**0.72**	0.93	0.93	**0.72**	**0.72**	0.92	0.86	0.87	0.96

Appendix D

Supplementary results on the reliability of power estimates

This appendix contains supplementary results of the study of the reliability of resting state power estimates introduced in section 4.2. While the main results presented in section 4.2 referred to absolute power estimated with magnetometer data, ICC values for relative power and gradiometer data are presented here.

Table D.1: ICC of the relative average power over five MEG sensor regions, for each frequency band and condition. The right column contains the ICC of the MAF (mean alpha frequency).

		Delta	Theta	Alpha	Low beta	High beta	Gamma	MAF
Eyes open	Occipital	0.46	0.81	0.82	0.91	0.87	0.71	0.90
	Left temporal	0.42	0.80	0.81	0.90	0.89	0.68	0.85
	Right temporal	0.35	0.81	0.78	0.88	0.83	0.73	0.88
	Parietal	0.48	0.87	0.87	0.94	0.92	0.66	0.93
	Frontal	0.35	0.80	0.83	0.82	0.80	0.78	0.68
Eyes closed	Occipital	0.62	0.70	0.89	0.90	0.87	0.83	0.88
	Left temporal	0.75	0.79	0.92	0.94	0.87	0.84	0.86
	Right temporal	0.70	0.70	0.91	0.91	0.92	0.86	0.88
	Parietal	0.83	0.80	0.94	0.92	0.95	0.88	0.90
	Frontal	0.76	0.61	0.96	0.94	0.90	0.91	0.83
Empty room	Occipital	0.01	0.07	0.05	-0.00	0.11	0.08	-0.09
	Left temporal	0.05	0.13	0.12	0.11	0.04	0.06	-0.10
	Right temporal	0.00	0.09	0.12	-0.09	0.13	-0.03	-0.07
	Parietal	-0.03	0.09	0.08	0.02	0.27	-0.09	-0.15
	Frontal	0.12	0.00	0.26	0.22	0.12	0.11	0.02

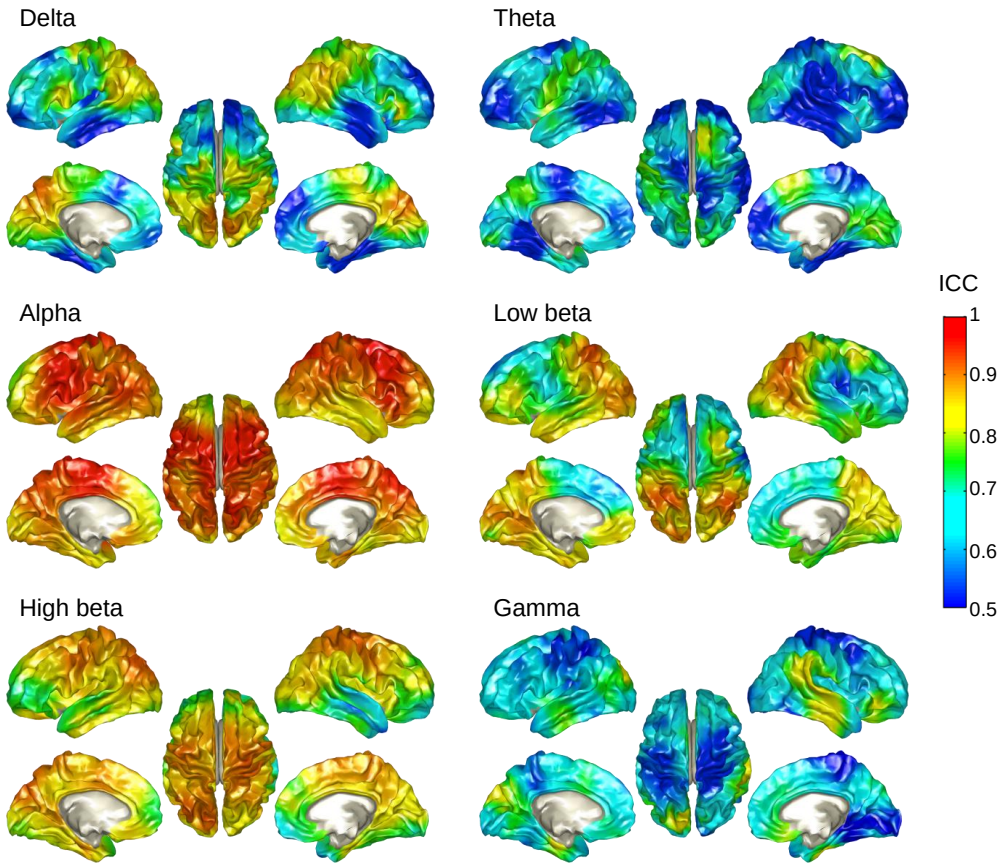

Figure D.1: ICC of source space relative power for the resting state eyes open condition. ICC values were computed for each source location and frequency band separately.

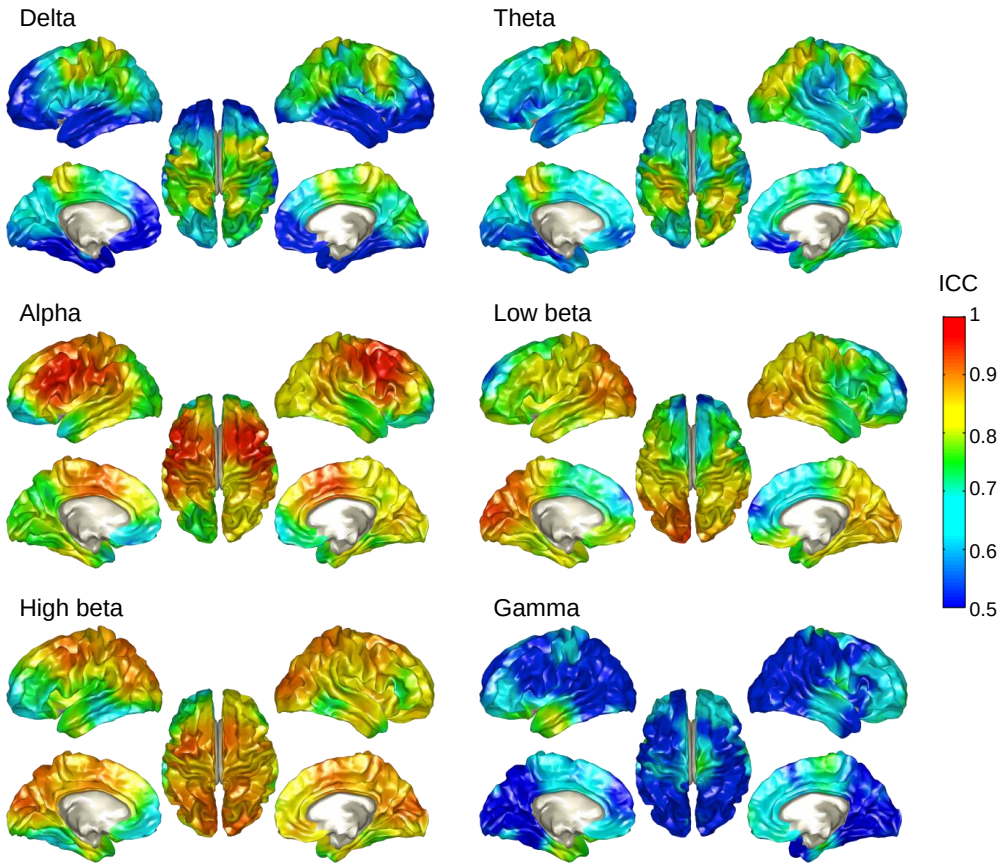

Figure D.2: ICC of source space relative power for the resting state eyes closed condition. ICC values were computed for each source location and frequency band separately.

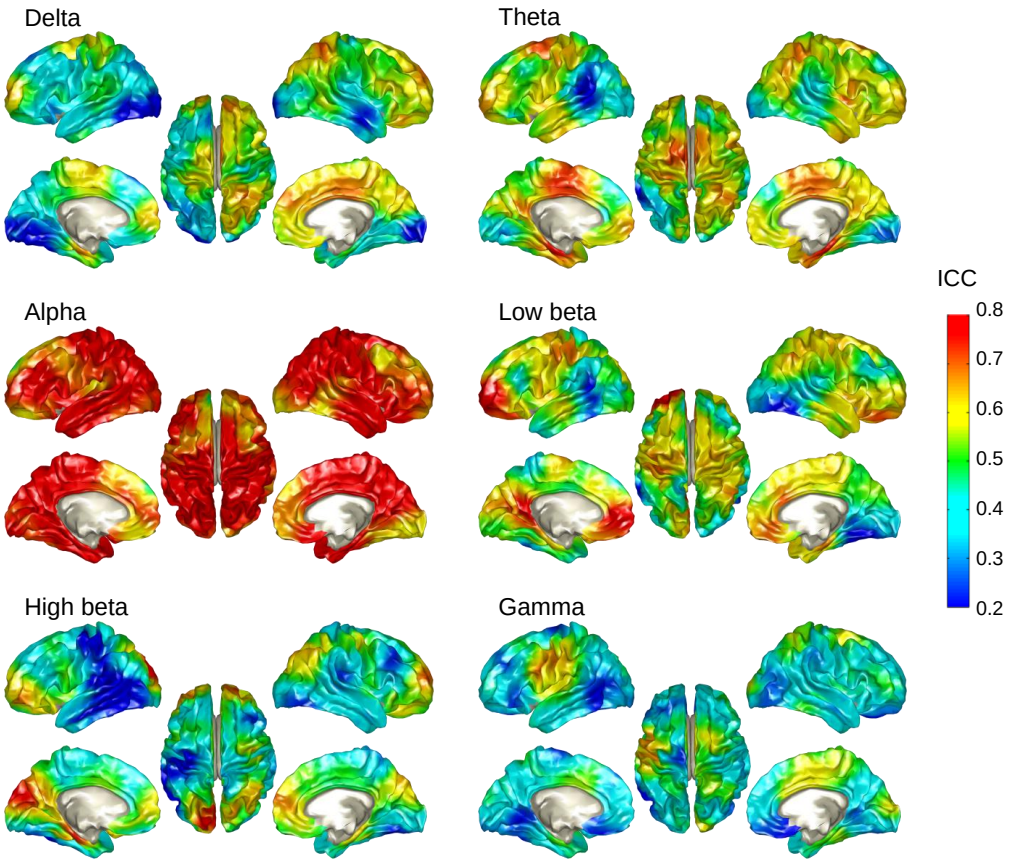

Figure D.3: ICC of source space power estimated with planar gradiometers for the resting state eyes open condition. ICC values were computed for each source location and frequency band separately.

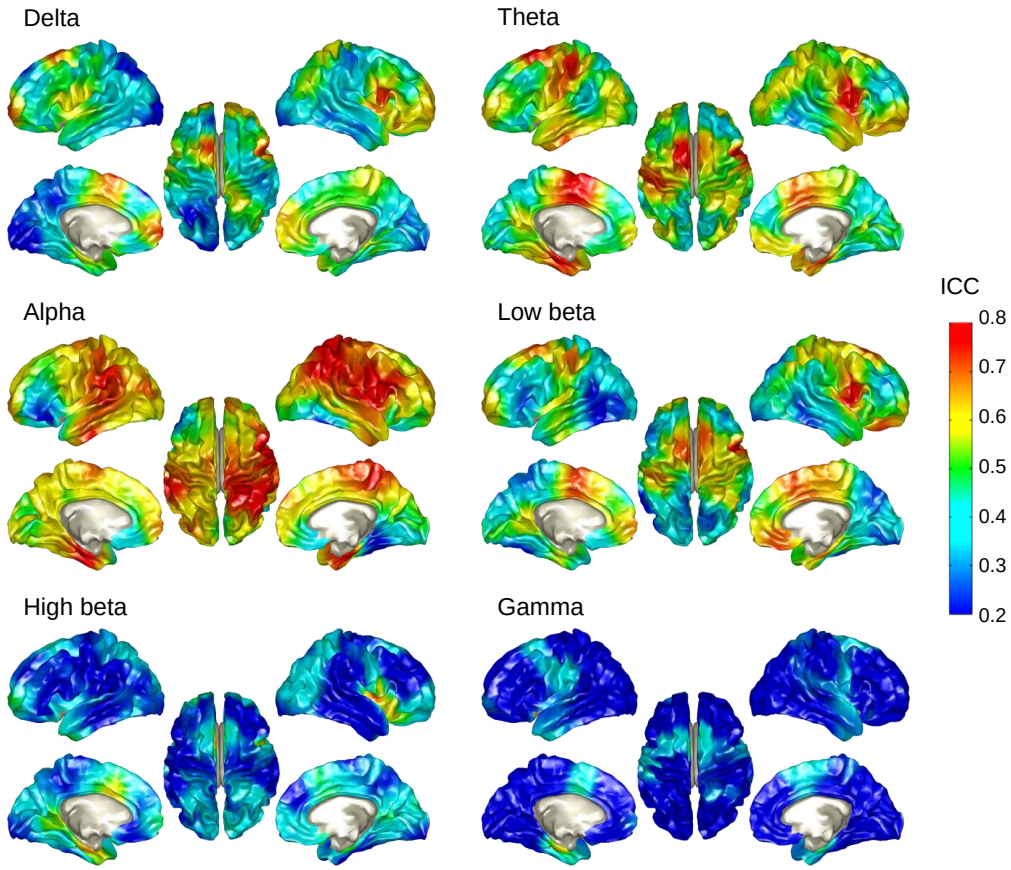

Figure D.4: ICC of source space power estimated with planar gradiometers for the resting state eyes closed condition. ICC values were computed for each source location and frequency band separately.

Appendix E

Supplementary results on the reliability of FC estimates

This appendix contains supplementary results of the study of the reliability of resting state FC estimates introduced in section 4.3. First, Table E.1 lists ICC values of the within-network ICC, using the resting state eyes open condition. Then, Figures E.1 and E.2 display average FC and ICC for three selected seeds, using d-ecor and PLI, respectively.

Table E.1: ICC of the within-network FC for the resting-state eyes open condition. ICC values are computed for every frequency band, FC metric and RSN separately. For RSNs with more than two nodes (DMN and fronto-insular), the average ICC across links within the network is displayed.

	network	visual	sensori-motor	auditory	DMN	left FP	right FP	fronto-insular
d-ecor	delta	0.34	0.52	0.62	0.27	0.35	0.19	0.12
	theta	0.40	0.40	0.20	0.22	0.28	0.20	0.07
	alpha	0.59	0.77	0.31	0.33	0.01	0.42	0.10
	beta	0.36	0.63	0.25	0.39	0.43	0.57	0.36
	gamma	0.20	0.48	0.24	0.22	0.03	0.49	0.05
lc-ecor	delta	-0.02	0.27	0.24	0.17	-0.02	0.18	-0.01
	theta	0.14	0.25	-0.01	0.26	0.36	0.11	0.02
	alpha	0.03	0.32	0.15	0.23	0.28	0.47	0.06
	beta	0.21	0.57	0.00	0.27	0.27	0.34	0.20
	gamma	0.11	0.21	-0.11	0.19	0.05	0.30	-0.11
PLV	delta	0.78	0.83	0.53	0.73	0.48	0.52	0.64
	theta	0.85	0.88	0.66	0.78	0.00	0.71	0.70
	alpha	0.90	0.92	0.60	0.77	0.80	0.67	0.66
	beta	0.91	0.92	0.69	0.85	0.77	0.70	0.73
	gamma	0.87	0.83	0.71	0.88	0.69	0.91	0.81
PLI	delta	0.07	0.48	-0.03	0.34	0.38	-0.05	0.44
	theta	-0.04	0.32	-0.17	0.27	0.07	-0.19	0.36
	alpha	0.19	-0.05	0.10	0.39	0.13	0.04	0.41
	beta	0.49	0.28	0.32	0.38	0.21	-0.14	0.45
	gamma	0.13	0.24	-0.10	0.48	0.04	0.11	0.44

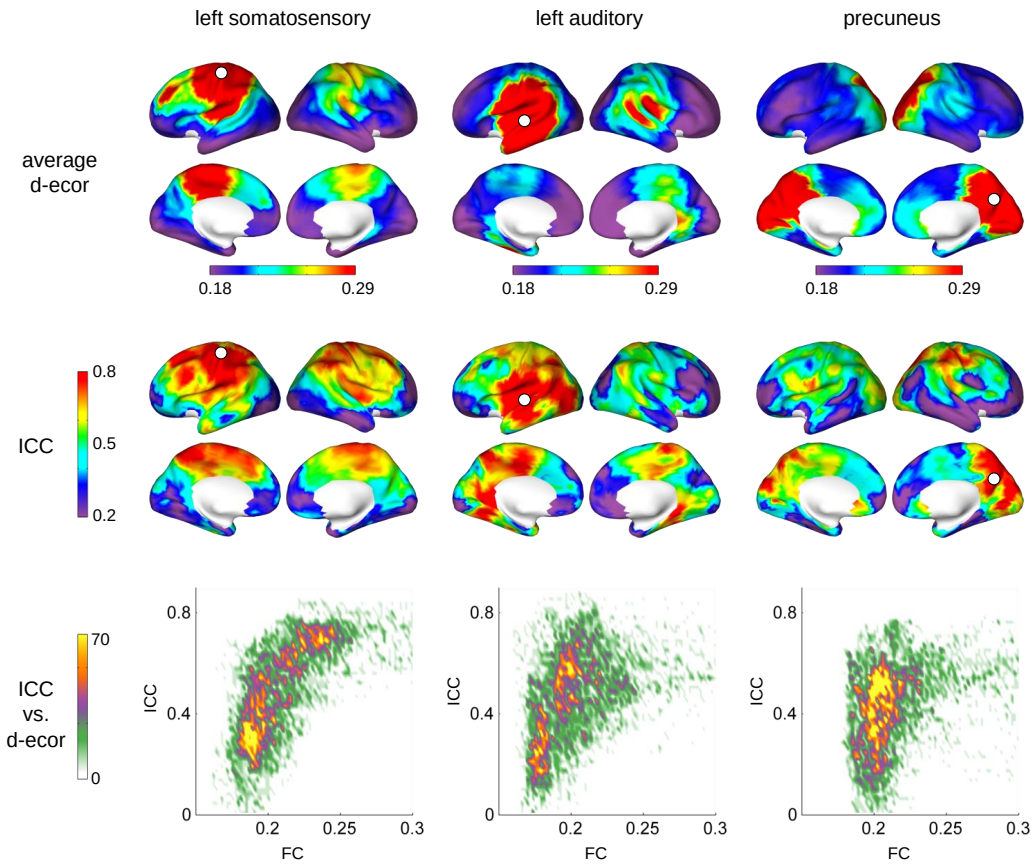

Figure E.1: FC and ICC for beta band resting-state eyes closed and d-ecor. For three selected seeds (left primary somatosensory, left primary auditory and precuneus), average FC maps (1st row), ICC (2nd row) and the normalized joint histogram of ICC and FC values (3rd row) are displayed. FC maps are averaged over all sessions and subjects. The seed location is indicated with a white circle.

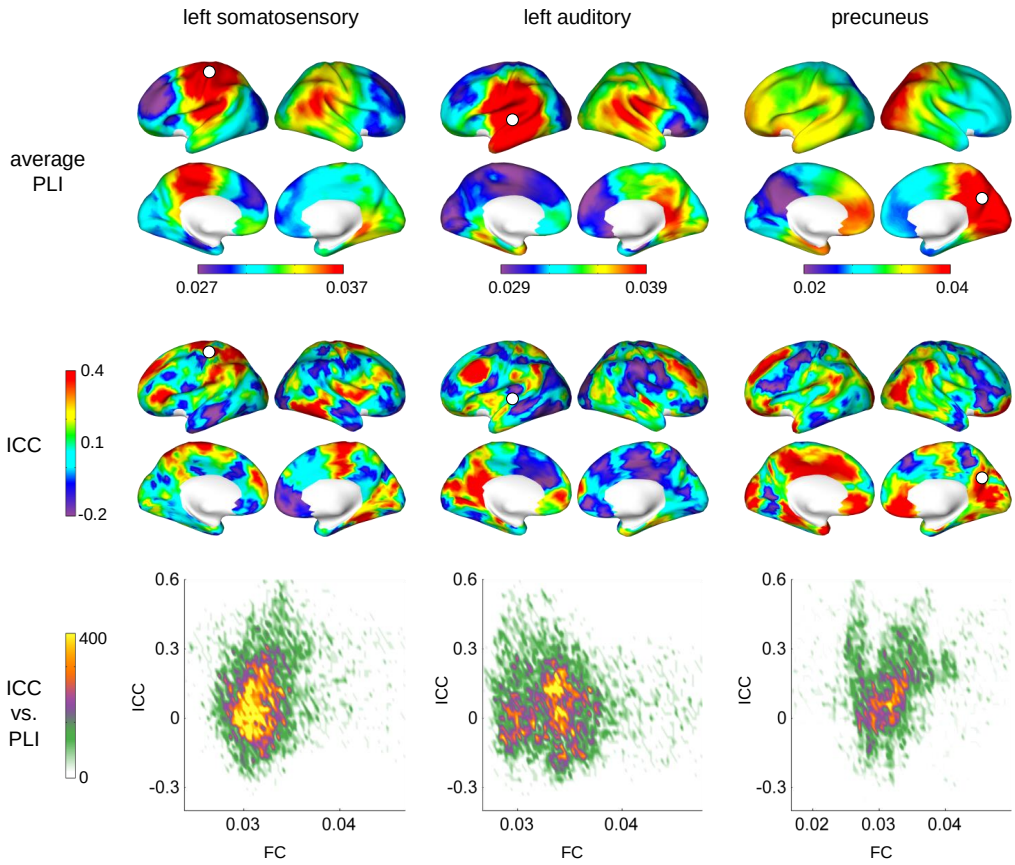

Figure E.2: FC and ICC for beta band resting-state eyes closed and PLI. For three selected seeds (left primary somatosensory, left primary auditory and precuneus), average FC maps (1st row), ICC (2nd row) and the normalized joint histogram of ICC and FC values (3rd row) are displayed. FC maps are averaged over all sessions and subjects. The seed location is indicated with a white circle.

Bibliography

Acar, Z. A. and Makeig, S. (2010). Neuroelectromagnetic forward head modeling toolbox. *Journal of neuroscience methods*, 190(2):258–70.

Acar, Z. A. and Makeig, S. (2013). Effects of forward model errors on EEG source localization. *Brain topography*, 26(3):378–96.

Adlard, P. A., Tran, B. A., Finkelstein, D. I., Desmond, P. M., Johnston, L. A., Bush, A. I., and Egan, G. F. (2014). A review of β-amyloid neuroimaging in Alzheimer's disease. *Frontiers in neuroscience*, 8.

Agosta, F., Pievani, M., Geroldi, C., Copetti, M., Frisoni, G. B., and Filippi, M. (2012). Resting state fMRI in Alzheimer's disease: beyond the default mode network. *Neurobiology of Aging*, 33(8):1564–78.

Albert, M. S., DeKosky, S. T., Dickson, D., Dubois, B., Feldman, H. H., Fox, N. C., Gamst, A., Holtzman, D. M., Jagust, W. J., Petersen, R. C., Snyder, P. J., Carrillo, M. C., Thies, B., and Phelps, C. H. (2013). The Diagnosis of Mild Cognitive Impairment due to Alzheimer's Disease: Recommendations from the National Institute on Aging-Alzheimer's Association Workgroups on Diagnostic Guidelines for Alzheimer's Disease. *FOCUS*, 11(1):96–106.

Alexander, A. L., Lee, J. E., Lazar, M., and Field, A. S. (2007). Diffusion tensor imaging of the brain. *Neurotherapeutics : the journal of the American Society for Experimental NeuroTherapeutics*, 4(3):316–29.

Alzheimer's Association (2011). 2011 Alzheimer's disease facts and figures. *Alzheimer's & dementia*, 7(2):208–44.

American Psychiatric Association (2000). *Diagnostic and statistical manual of mental disorders, Fourth Edition, Text Revision*. Washington, DC.

American Psychiatric Association (2013). *Diagnostic and Statistical Manual of Mental Disorders, Fifth Edition*. Arlington, VA.

Androulidakis, A. G., Doyle, L. M. F., Gilbertson, T. P., and Brown, P. (2006). Corrective movements in response to displacements in visual feedback are more effective during periods of 13-35 Hz oscillatory synchrony in the human corticospinal system. *The European journal of neuroscience*, 24(11):3299–304.

Aoki, F., Fetz, E., Shupe, L., Lettich, E., and Ojemann, G. (1999). Increased gamma-range activity in human sensorimotor cortex during performance of visuomotor tasks. *Clinical Neurophysiology*, 110(3):524–37.

Apostolova, L. G., Dutton, R. A., Dinov, I. D., Hayashi, K. M., Toga, A. W., Cummings, J. L., and Thompson, P. M. (2006). Conversion of mild cognitive impairment to Alzheimer disease predicted by hippocampal atrophy maps. *Archives of neurology*, 63(5):693–9.

Atcherson, S. R., Gould, H. J., Pousson, M. a., and Prout, T. M. (2006). Long-term stability of N1 sources using low-resolution electromagnetic tomography. *Brain topography*, 19(1-2):11–20.

Axmacher, N., Henseler, M. M., Jensen, O., Weinreich, I., Elger, C. E., and Fell, J. (2010). Cross-frequency coupling supports multi-item working memory in the human hippocampus. *Proceedings of the National Academy of Sciences of the United States of America*, 107(7):3228–33.

Başar, E., Başar-Eroglu, C., Karakaş, S., and Schürmann, M. (2001). Gamma, alpha, delta, and theta oscillations govern cognitive processes. *International journal of psychophysiology : official journal of the International Organization of Psychophysiology*, 39(2-3):241–8.

Babiloni, C., Binetti, G., Cassetta, E., Cerboneschi, D., Dal Forno, G., Del Percio, C., Ferreri, F., Ferri, R., Lanuzza, B., Miniussi, C., Moretti, D. V., Nobili, F., Pascual-Marqui, R. D., Rodriguez, G., Romani, G. L., Salinari, S., Tecchio, F., Vitali, P., Zanetti, O., Zappasodi, F., and Rossini, P. M. (2004). Mapping distributed sources of cortical rhythms in mild Alzheimer's disease. A multicentric EEG study. *NeuroImage*, 22(1):57–67.

Babiloni, C., Carducci, F., Lizio, R., Vecchio, F., Baglieri, A., Bernardini, S., Cavedo, E., Bozzao, A., Buttinelli, C., Esposito, F., Giubilei, F., Guizzaro, A., Marino, S., Montella, P., Quattrocchi, C. C., Redolfi, A., Soricelli, A., Tedeschi, G., Ferri, R., Rossi-Fedele, G.,

Ursini, F., Scrascia, F., Vernieri, F., Pedersen, T. J., Hardemark, H.-G., Rossini, P. M., and Frisoni, G. B. (2013). Resting state cortical electroencephalographic rhythms are related to gray matter volume in subjects with mild cognitive impairment and Alzheimer's disease. *Human brain mapping*, 34(6):1427–46.

Babiloni, C., Frisoni, G. B., Pievani, M., Vecchio, F., Lizio, R., Buttiglione, M., Geroldi, C., Fracassi, C., Eusebi, F., Ferri, R., and Rossini, P. M. (2009). Hippocampal volume and cortical sources of EEG alpha rhythms in mild cognitive impairment and Alzheimer disease. *NeuroImage*, 44(1):123–35.

Babiloni, C., Frisoni, G. B., Vecchio, F., Lizio, R., Pievani, M., Cristina, G., Fracassi, C., Vernieri, F., Rodriguez, G., Nobili, F., Ferri, R., and Rossini, P. M. (2011). Stability of clinical condition in mild cognitive impairment is related to cortical sources of alpha rhythms: an electroencephalographic study. *Human brain mapping*, 32(11):1916–31.

Bai, O., Lin, P., Vorbach, S., Floeter, M. K., Hattori, N., and Hallett, M. (2008). A high performance sensorimotor beta rhythm-based brain-computer interface associated with human natural motor behavior. *Journal of neural engineering*, 5(1):24–35.

Baillet, S., Mosher, J., and Leahy, R. (2001). Electromagnetic brain mapping. *IEEE Signal Processing Magazine*, 18(6):14–30.

Bajo, R., Castellanos, N. P., Cuesta, P., Aurtenetxe, S., Garcia-Prieto, J., Gil-Gregorio, P., Del-Pozo, F., and Maestu, F. (2012). Differential patterns of connectivity in progressive mild cognitive impairment. *Brain connectivity*, 2(1):21–4.

Baldassarre, A., Lewis, C. M., Committeri, G., Snyder, A. Z., Romani, G. L., and Corbetta, M. (2012). Individual variability in functional connectivity predicts performance of a perceptual task. *Proceedings of the National Academy of Sciences of the United States of America*, 109(9):3516–21.

Ballard, C., Gauthier, S., Corbett, A., Brayne, C., Aarsland, D., and Jones, E. (2011). Alzheimer's disease. *Lancet*, 377(9770):1019–31.

Barnes, D. E. and Yaffe, K. (2011). The projected effect of risk factor reduction on Alzheimer's disease prevalence. *Lancet neurology*, 10(9):819–28.

Barnhart, H. X., Haber, M. J., and Lin, L. I. (2007). An overview on assessing agreement with continuous measurements. *Journal of biopharmaceutical statistics*, 17(4):529–69.

Barry, R. J., Clarke, A. R., and Johnstone, S. J. (2003). A review of electrophysiology in attention-deficit/hyperactivity disorder: I. Qualitative and quantitative electroencephalography. *Clinical Neurophysiology*, 114(2):171–83.

Bartlett, J. W. and Frost, C. (2008). Reliability, repeatability and reproducibility: analysis of measurement errors in continuous variables. *Ultrasound in obstetrics & gynecology : the official journal of the International Society of Ultrasound in Obstetrics and Gynecology*, 31(4):466–75.

Bate, C. and Williams, A. (2011). Amyloid-β-induced synapse damage is mediated via cross-linkage of cellular prion proteins. *The Journal of biological chemistry*, 286(44):37955–63.

Belardinelli, P., Ortiz, E., and Braun, C. (2012). Source activity correlation effects on LCMV beamformers in a realistic measurement environment. *Computational and mathematical methods in medicine*, 2012.

Benjamini, Y. and Yekutieli, D. (2001). The control of the false discovery rate in multiple testing under dependency. *Annals of statistics*, 29(4):1165–88.

Bennett, C. M. and Miller, M. B. (2010). How reliable are the results from functional magnetic resonance imaging? *Annals of the New York Academy of Sciences*, 1191:133–55.

Berendse, H., Verbunt, J., Scheltens, P., van Dijk, B., and Jonkman, E. (2000). Magnetoencephalographic analysis of cortical activity in Alzheimer's disease: a pilot study. *Clinical Neurophysiology*, 111(4):604–12.

Berger, H. (1929). Uber das elektrenkephalogramm des menschen. *Arch. Psychiatr*, 87:527–70.

Bero, A. W., Bauer, A. Q., Stewart, F. R., White, B. R., Cirrito, J. R., Raichle, M. E., Culver, J. P., and Holtzman, D. M. (2012). Bidirectional relationship between functional connectivity and amyloid-β deposition in mouse brain. *The Journal of neuroscience : the official journal of the Society for Neuroscience*, 32(13):4334–40.

Bhattacharya, B. S., Coyle, D., and Maguire, L. P. (2011). A thalamo-cortico-thalamic neural mass model to study alpha rhythms in Alzheimer's disease. *Neural networks : the official journal of the International Neural Network Society*, 24(6):631–45.

Binnewijzend, M. A. a., Schoonheim, M. M., Sanz-Arigita, E., Wink, A. M., van der Flier, W. M., Tolboom, N., Adriaanse, S. M., Damoiseaux, J. S., Scheltens, P., van Berckel,

B. N. M., and Barkhof, F. (2012). Resting-state fMRI changes in Alzheimer's disease and mild cognitive impairment. *Neurobiology of aging*, 33(9):2018–28.

Biswal, B., Zerrin Yetkin, F., Haughton, V. M., and Hyde, J. S. (1995). Functional connectivity in the motor cortex of resting human brain using echo-planar mri. *Magnetic Resonance in Medicine*, 34(4):537–41.

Bland, J. M. and Altman, D. G. (2010). Statistical methods for assessing agreement between two methods of clinical measurement. *International Journal of Nursing Studies*, 47(8):931–36.

Bollimunta, A., Chen, Y., Schroeder, C. E., and Ding, M. (2008). Neuronal mechanisms of cortical alpha oscillations in awake-behaving macaques. *The Journal of neuroscience : the official journal of the Society for Neuroscience*, 28(40):9976–88.

Bollimunta, A., Mo, J., Schroeder, C. E., and Ding, M. (2011). Neuronal mechanisms and attentional modulation of corticothalamic α oscillations. *The Journal of neuroscience : the official journal of the Society for Neuroscience*, 31(13):4935–43.

Bonnefond, M. and Jensen, O. (2013). The role of gamma and alpha oscillations for blocking out distraction. *Communicative & integrative biology*, 6(1).

Boutros, N. N., Arfken, C., Galderisi, S., Warrick, J., Pratt, G., and Iacono, W. (2008). The status of spectral EEG abnormality as a diagnostic test for schizophrenia. *Schizophrenia research*, 99(1):225–37.

Bozoki, A. C., Korolev, I. O., Davis, N. C., Hoisington, L. A., and Berger, K. L. (2012). Disruption of limbic white matter pathways in mild cognitive impairment and Alzheimer's disease: a DTI/FDG-PET study. *Human brain mapping*, 33(8):1792–802.

Bozzali, M. (2002). White matter damage in Alzheimer's disease assessed in vivo using diffusion tensor magnetic resonance imaging. *Journal of Neurology, Neurosurgery & Psychiatry*, 72(6):742–46.

Brier, M. R., Thomas, J. B., Snyder, A. Z., Benzinger, T. L., Zhang, D., Raichle, M. E., Holtzman, D. M., Morris, J. C., and Ances, B. M. (2012). Loss of intranetwork and internetwork resting state functional connections with Alzheimer's disease progression. *The Journal of neuroscience : the official journal of the Society for Neuroscience*, 32(26):8890–9.

Brookes, M. J., Hale, J. R., Zumer, J. M., Stevenson, C. M., Francis, S. T., Barnes, G. R., Owen, J. P., Morris, P. G., and Nagarajan, S. S. (2011a). Measuring functional

connectivity using MEG: methodology and comparison with fcMRI. *NeuroImage*, 56(3):1082–104.

Brookes, M. J., Vrba, J., Robinson, S. E., Stevenson, C. M., Peters, A. M., Barnes, G. R., Hillebrand, A., and Morris, P. G. (2008). Optimising experimental design for MEG beamformer imaging. *NeuroImage*, 39(4):1788–802.

Brookes, M. J., Woolrich, M., Luckhoo, H., Price, D., Hale, J. R., Stephenson, M. C., Barnes, G. R., Smith, S. M., and Morris, P. G. (2011b). Investigating the electrophysiological basis of resting state networks using magnetoencephalography. *Proceedings of the National Academy of Sciences of the United States of America*, 108(40):16783–8.

Brookes, M. J., Woolrich, M. W., and Barnes, G. R. (2012). Measuring functional connectivity in MEG: a multivariate approach insensitive to linear source leakage. *NeuroImage*, 63(2):910–20.

Brookes, M. J., Woolrich, M. W., and Price, D. (2014). An introduction to MEG connectivity measurements. In Supek, S. and Aine, C. J., editors, *Magnetoencephalography, from signals to dynamic cortical networks*, pages 321–358. Springer-Verlag, Berlin Heidelberg.

Brookmeyer, R., Johnson, E., Ziegler-Graham, K., and Arrighi, H. M. (2007). Forecasting the global burden of Alzheimer's disease. *Alzheimer's & dementia : the journal of the Alzheimer's Association*, 3(3):186–91.

Brown, M. A. and Semelka, R. C. (2003). *MRI. Basic principles and applications*. John Wiley and Sons, Inc.

Buckner, R. L., Andrews-Hanna, J. R., and Schacter, D. L. (2008). The brain's default network: anatomy, function, and relevance to disease. *Annals of the New York Academy of Sciences*, 1124:1–38.

Burgess, A. and Gruzelier, J. (1993). Individual reliability of amplitude distribution in topographical mapping of EEG. *Electroencephalography and Clinical Neurophysiology*, 86(4):219–23.

Buzsáki, G. (2002). Theta Oscillations in the Hippocampus Review. *Neuron*, 33:325–40.

Buzsáki, G., Anastassiou, C. A., and Koch, C. (2012). The origin of extracellular fields and currents–EEG, ECoG, LFP and spikes. *Nature reviews. Neuroscience*, 13(6):407–20.

Buzsáki, G. and Draguhn, A. (2004). Neuronal oscillations in cortical networks. *Science (New York, N.Y.)*, 304(5679):1926–9.

Buzsáki, G. and Moser, E. I. (2013). Memory, navigation and theta rhythm in the hippocampal-entorhinal system. *Nature neuroscience*, 16(2):130–8.

Cannon, R. L., Baldwin, D. R., Shaw, T. L., Diloreto, D. J., Phillips, S. M., Scruggs, A. M., and Riehl, T. C. (2012). Reliability of quantitative EEG (qEEG) measures and LORETA current source density at 30 days. *Neuroscience letters*, 518(1):27–31.

Canolty, R. T. and Knight, R. T. (2010). The functional role of cross-frequency coupling. *Trends in cognitive sciences*, 14(11):506–15.

Cashdollar, N., Malecki, U., Rugg-Gunn, F. J., Duncan, J. S., Lavie, N., and Duzel, E. (2009). Hippocampus-dependent and -independent theta-networks of active maintenance. *Proceedings of the National Academy of Sciences of the United States of America*, 106(48):20493–8.

Cavanagh, J. F. and Frank, M. J. (2014). Frontal theta as a mechanism for cognitive control. *Trends in cognitive sciences*, 18(8):414–21.

Celone, K. A., Calhoun, V. D., Dickerson, B. C., Atri, A., Chua, E. F., Miller, S. L., DePeau, K., Rentz, D. M., Selkoe, D. J., Blacker, D., Albert, M. S., and Sperling, R. A. (2006). Alterations in memory networks in mild cognitive impairment and Alzheimer's disease: an independent component analysis. *The Journal of neuroscience : the official journal of the Society for Neuroscience*, 26(40):10222–31.

Chechko, N., Drexler, E. I., Voss, B., Kellermann, T., Finkelmeyer, A., Schneider, F., and Habel, U. (2014). Neural Correlates of Unsuccessful Memory Performance in MCI. *Frontiers in Aging Neuroscience*, 6.

Chiang, a. K. I., Rennie, C. J., Robinson, P. a., Roberts, J. a., Rigozzi, M. K., Whitehouse, R. W., Hamilton, R. J., and Gordon, E. (2008). Automated characterization of multiple alpha peaks in multi-site electroencephalograms. *Journal of neuroscience methods*, 168(2):396–411.

Chiang, a. K. I., Rennie, C. J., Robinson, P. a., van Albada, S. J., and Kerr, C. C. (2011). Age trends and sex differences of alpha rhythms including split alpha peaks. *Clinical neurophysiology : official journal of the International Federation of Clinical Neurophysiology*, 122(8):1505–17.

Clarke, D. D. and Sokoloff, L. (1999). Regulation of Cerebral Metabolic Rate. In *Basic Neurochemistry: Molecular, Cellular and Medical Aspects*. Lippincott-Raven, Philadelphia, 6th edition.

Cohen, D. (1968). Magnetoencephalography: evidence of magnetic fields produced by alpha-rhythm currents. *Science (New York, N.Y.)*, 161(3843):784–6.

Congedo, M., John, R. E., De Ridder, D., and Prichep, L. (2010). Group independent component analysis of resting state EEG in large normative samples. *International Journal of Psychophysiology*, 78:89–99.

Cornew, L., Roberts, T. P. L., Blaskey, L., and Edgar, J. C. (2012). Resting-State Oscillatory Activity in Autism Spectrum Disorders. *Journal of Autism and Developmental Disorders*, 42(9):1884–94.

Crone, N. E., Boatman, D., Gordon, B., and Hao, L. (2001). Induced electrocorticographic gamma activity during auditory perception. *Clinical Neurophysiology*, 112(4):565–82.

Cuesta, P., Garcés, P., Castellanos, N. P., López, M. E., Aurtenetxe, S., Bajo, R., Pineda-Pardo, J. A., Bruña, R., Marín, A. G., Delgado, M., Barabash, A., Ancín, I., Cabranes, J. A., Fernandez, A., Del Pozo, F., Sancho, M., Marcos, A., Nakamura, A., and Maestú, F. (2015). Influence of the APOE ϵ4 Allele and Mild Cognitive Impairment Diagnosis in the Disruption of the MEG Resting State Functional Connectivity in Sources Space. *Journal of Alzheimer's disease : JAD*, 44(2):493–505.

Dalal, S. S., Baillet, S., Adam, C., Ducorps, A., Schwartz, D., Jerbi, K., Bertrand, O., Garnero, L., Martinerie, J., and Lachaux, J.-P. (2009). Simultaneous MEG and intracranial EEG recordings during attentive reading. *NeuroImage*, 45(4):1289–304.

Dale, A. M. and Halgren, E. (2001). Spatiotemporal mapping of brain activity by integration of multiple imaging modalities. *Current Opinion in Neurobiology*, 11(2):202–8.

Damoiseaux, J. S., Prater, K. E., Miller, B. L., and Greicius, M. D. (2012). Functional connectivity tracks clinical deterioration in Alzheimer's disease. *Neurobiology of Aging*, 33(4):828.e19–828.e30.

Dannhauer, M., Lanfer, B., Wolters, C. H., and Knösche, T. R. (2011). Modeling of the human skull in EEG source analysis. *Human brain mapping*, 32(9):1383–99.

Darvas, F., Pantazis, D., Kucukaltun-Yildirim, E., and Leahy, R. M. (2004). Mapping human brain function with MEG and EEG: methods and validation. *NeuroImage*, 23:S289–99.

de Lange, F. P., Jensen, O., Bauer, M., and Toni, I. (2008). Interactions between posterior gamma and frontal alpha/beta oscillations during imagined actions. *Frontiers in human neuroscience*, 2.

de Pasquale, F., Della Penna, S., Snyder, A. Z., Lewis, C., Mantini, D., Marzetti, L., Belardinelli, P., Ciancetta, L., Pizzella, V., Romani, G. L., and Corbetta, M. (2010). Temporal dynamics of spontaneous MEG activity in brain networks. *Proceedings of the National Academy of Sciences of the United States of America*, 107(13):6040–5.

de Pasquale, F., Della Penna, S., Snyder, A. Z., Marzetti, L., Pizzella, V., Romani, G. L., and Corbetta, M. (2012). A cortical core for dynamic integration of functional networks in the resting human brain. *Neuron*, 74(4):753–64.

Deiber, M.-P., Missonnier, P., Bertrand, O., Gold, G., Fazio-Costa, L., Ibañez, V., and Giannakopoulos, P. (2007). Distinction between perceptual and attentional processing in working memory tasks: a study of phase-locked and induced oscillatory brain dynamics. *Journal of cognitive neuroscience*, 19(1):158–72.

Desikan, R. S., Ségonne, F., Fischl, B., Quinn, B. T., Dickerson, B. C., Blacker, D., Buckner, R. L., Dale, A. M., Maguire, R. P., Hyman, B. T., Albert, M. S., and Killiany, R. J. (2006). An automated labeling system for subdividing the human cerebral cortex on MRI scans into gyral based regions of interest. *NeuroImage*, 31(3):968–80.

Deuker, L., Bullmore, E. T., Smith, M., Christensen, S., Nathan, P. J., Rockstroh, B., and Bassett, D. S. (2009). Reproducibility of graph metrics of human brain functional networks. *NeuroImage*, 47(4):1460–8.

Dickerson, B. C., Sperling, R. A., Hyman, B. T., Albert, M. S., and Blacker, D. (2007). Clinical prediction of Alzheimer disease dementia across the spectrum of mild cognitive impairment. *Archives of general psychiatry*, 64(12):1443–50.

Dubois, B., Feldman, H. H., Jacova, C., Dekosky, S. T., Barberger-Gateau, P., Cummings, J., Delacourte, A., Galasko, D., Gauthier, S., Jicha, G., Meguro, K., O'brien, J., Pasquier, F., Robert, P., Rossor, M., Salloway, S., Stern, Y., Visser, P. J., and Scheltens, P. (2007). Research criteria for the diagnosis of Alzheimer's disease: revising the NINCDS-ADRDA criteria. *Lancet neurology*, 6(8):734–46.

Dustman, R., Shearer, D., and Emmerson, R. (1993). EEG and event-related potentials in normal aging. *Progress in Neurobiology*, 41(3):369–401.

Eickhoff, S. B., Stephan, K. E., Mohlberg, H., Grefkes, C., Fink, G. R., Amunts, K., and Zilles, K. (2005). A new SPM toolbox for combining probabilistic cytoarchitectonic maps and functional imaging data. *NeuroImage*, 25(4):1325–35.

Ekstrom, A. D., Caplan, J. B., Ho, E., Shattuck, K., Fried, I., and Kahana, M. J. (2005). Human hippocampal theta activity during virtual navigation. *Hippocampus*, 15(7):881–9.

Elekta-Neuromag (2005). Elekta Neuromag® System Hardware User Manual. Technical report.

Engel, A. K. and Fries, P. (2010). Beta-band oscillations–signalling the status quo? *Current opinion in neurobiology*, 20(2):156–65.

Ergenoglu, T., Demiralp, T., Bayraktaroglu, Z., Ergen, M., Beydagi, H., and Uresin, Y. (2004). Alpha rhythm of the EEG modulates visual detection performance in humans. *Brain research. Cognitive brain research*, 20(3):376–83.

Evans, A. C., Janke, A. L., Collins, D. L., and Baillet, S. (2012). Brain templates and atlases. *NeuroImage*, 62(2):911–22.

Ewers, M., Sperling, R. A., Klunk, W. E., Weiner, M. W., and Hampel, H. (2011). Neuroimaging markers for the prediction and early diagnosis of Alzheimer's disease dementia. *Trends in neurosciences*, 34(8):430–42.

Fehr, T., Kissler, J., Moratti, S., Wienbruch, C., Rockstroh, B., and Elbert, T. (2001). Source distribution of neuromagnetic slow waves and MEG-delta activity in schizophrenic patients. *Biological psychiatry*, 50(2):108–16.

Fell, J. and Axmacher, N. (2011). The role of phase synchronization in memory processes. *Nature reviews. Neuroscience*, 12(2):105–18.

Fellgiebel, A., Müller, M. J., Wille, P., Dellani, P. R., Scheurich, A., Schmidt, L. G., and Stoeter, P. (2005). Color-coded diffusion-tensor-imaging of posterior cingulate fiber tracts in mild cognitive impairment. *Neurobiology of aging*, 26(8):1193–8.

Fernández, A., Arrazola, J., Maestú, F., Amo, C., Gil-Gregorio, P., Wienbruch, C., and Ortiz, T. (2003). Correlations of hippocampal atrophy and focal low-frequency magnetic activity in Alzheimer disease: volumetric MR imaging-

magnetoencephalographic study. *AJNR. American journal of neuroradiology*, 24(3):481–7.

Fernández, A., Hornero, R., Mayo, A., Poza, J., Gil-Gregorio, P., and Ortiz, T. (2006). MEG spectral profile in Alzheimer's disease and mild cognitive impairment. *Clinical neurophysiology : official journal of the International Federation of Clinical Neurophysiology*, 117(2):306–14.

Fernández, T., Harmony, T., Rodríguez, M., Bernal, J., Silva, J., Reyes, A., and Marosi, E. (1995). EEG activation patterns during the performance of tasks involving different components of mental calculation. *Electroencephalography and Clinical Neurophysiology*, 94(3):175–82.

Fingelkurts, A., Fingelkurts, A., Ermolaev, V., and Kaplan, A. (2006). Stability, reliability and consistency of the compositions of brain oscillations. *International journal of psychophysiology : official journal of the International Organization of Psychophysiology*, 59(2):116–26.

Fischer, P., Jungwirth, S., Zehetmayer, S., Weissgram, S., Hoenigschnabl, S., Gelpi, E., Krampla, W., and Tragl, K. H. (2007). Conversion from subtypes of mild cognitive impairment to Alzheimer dementia. *Neurology*, 68(4):288–91.

Fischl, B. and Dale, A. M. (2000). Measuring the thickness of the human cerebral cortex from magnetic resonance images. *Proceedings of the National Academy of Sciences of the United States of America*, 97(20):11050–5.

Fischl, B., Salat, D. H., Busa, E., Albert, M., Dieterich, M., Haselgrove, C., van der Kouwe, A., Killiany, R., Kennedy, D., Klaveness, S., Montillo, A., Makris, N., Rosen, B., and Dale, A. M. (2002). Whole Brain Segmentation. *Neuron*, 33(3):341–55.

Fischl, B., Van Der Kouwe, A., Destrieux, C., Halgren, E., Ségonne, F., Salat, D. H., Busa, E., Seidman, L. J., Goldstein, J., Kennedy, D., Caviness, V., Makris, N., Rosen, B., and Dale, A. M. (2004). Automatically Parcellating the Human Cerebral Cortex. *Cerebral Cortex*, 14:11–22.

Fishbine, B. (2003). SQUID magnetometry. In *Los Alamos Research Quarterly*, pages 4–11.

Flint, A. C. and Connors, B. W. (1996). Two types of network oscillations in neocortex mediated by distinct glutamate receptor subtypes and neuronal populations. *J Neurophysiol*, 75(2):951–57.

Fries, P. (2005). A mechanism for cognitive dynamics: neuronal communication through neuronal coherence. *Trends in cognitive sciences*, 9(10):474–80.

Frisoni, G. B. (2012). Alzheimer disease: biomarker trajectories across stages of Alzheimer disease. *Nature reviews. Neurology*, 8(6):299–300.

Friston, K. J. (2011). Functional and effective connectivity: a review. *Brain connectivity*, 1(1):13–36.

Fu, J.-L., Liu, Y., Li, Y.-M., Chang, C., and Li, W.-B. (2013). Use of Diffusion Tensor Imaging for Evaluating Changes in the Microstructural Integrity of White Matter Over 3 Years in Patients with Amnesic-Type Mild Cognitive Impairment Converting to Alzheimer's Disease. *Journal of neuroimaging : official journal of the American Society of Neuroimaging*, 24(4):343–8.

Garcés, P., Angel Pineda-Pardo, J., Canuet, L., Aurtenetxe, S., López, M. E., Marcos, A., Yus, M., Llanero-Luque, M., Del-Pozo, F., Sancho, M., and Maestú, F. (2014). The Default Mode Network is functionally and structurally disrupted in amnestic mild cognitive impairment - a bimodal MEG-DTI study. *NeuroImage. Clinical*, 6:214–21.

Garcés, P., Vicente, R., Wibral, M., Pineda-Pardo, J. A., López, M. E., Aurtenetxe, S., Marcos, A., de Andrés, M. E., Yus, M., Sancho, M., Maestú, F., and Fernández, A. (2013). Brain-wide slowing of spontaneous alpha rhythms in mild cognitive impairment. *Frontiers in Aging Neuroscience*, 5.

Gasser, T., Bächer, P., Steinberg, H., and Bacher, P. (1985). Test-retest reliability of spectral parameters of the EEG. *Electroencephalography and Clinical Neurophysiology*, 60(4):312–19.

Gilbertson, T., Lalo, E., Doyle, L., Di Lazzaro, V., Cioni, B., and Brown, P. (2005). Existing motor state is favored at the expense of new movement during 13-35 Hz oscillatory synchrony in the human corticospinal system. *The Journal of neuroscience : the official journal of the Society for Neuroscience*, 25(34):7771–9.

Gisev, N., Bell, J. S., and Chen, T. F. (2013). Interrater agreement and interrater reliability: key concepts, approaches, and applications. *Research in social & administrative pharmacy : RSAP*, 9(3):330–8.

Gloor, P., Ball, G., and Schaul, N. (1977). Brain lesions that produce delta waves in the EEG. *Neurology*, 27(4):326–26.

Goh, J. O., An, Y., and Resnick, S. M. (2012). Differential trajectories of age-related changes in components of executive and memory processes. *Psychology and aging*, 27(3):707–19.

Gramfort, A., Kowalski, M., and Hämäläinen, M. (2012). Mixed-norm estimates for the M/EEG inverse problem using accelerated gradient methods. *Physics in medicine and biology*, 57(7):1937–61.

Gramfort, A., Luessi, M., Larson, E., Engemann, D. A., Strohmeier, D., Brodbeck, C., Parkkonen, L., and Hämäläinen, M. S. (2014). MNE software for processing MEG and EEG data. *NeuroImage*, 86:446–60.

Greicius, M. D., Krasnow, B., Reiss, A. L., and Menon, V. (2003). Functional connectivity in the resting brain: a network analysis of the default mode hypothesis. *Proceedings of the National Academy of Sciences of the United States of America*, 100(1):253–8.

Greicius, M. D., Srivastava, G., Reiss, A. L., and Menon, V. (2004). Default-mode network activity distinguishes Alzheimer's disease from healthy aging: evidence from functional MRI. *Proceedings of the National Academy of Sciences of the United States of America*, 101(13):4637–42.

Gross, J., Baillet, S., Barnes, G. R., Henson, R. N., Hillebrand, A., Jensen, O., Jerbi, K., Litvak, V., Maess, B., Oostenveld, R., Parkkonen, L., Taylor, J. R., van Wassenhove, V., Wibral, M., and Schoffelen, J.-M. (2013). Good practice for conducting and reporting MEG research. *NeuroImage*, 65:349–63.

Gross, J., Kujala, J., Hamalainen, M., Timmermann, L., Schnitzler, A., and Salmelin, R. (2001). Dynamic imaging of coherent sources: Studying neural interactions in the human brain. *Proceedings of the National Academy of Sciences of the United States of America*, 98:694–9.

Grundman, M., Petersen, R. C., Ferris, S. H., Thomas, R. G., Aisen, P. S., Bennett, D. a., Foster, N. L., Jack, C. R., Galasko, D. R., Doody, R., Kaye, J., Sano, M., Mohs, R., Gauthier, S., Kim, H. T., Jin, S., Schultz, A. N., Schafer, K., Mulnard, R., van Dyck, C. H., Mintzer, J., Zamrini, E. Y., Cahn-Weiner, D., and Thal, L. J. (2004). Mild cognitive impairment can be distinguished from Alzheimer disease and normal aging for clinical trials. *Archives of neurology*, 61(1):59–66.

Gudmundsson, S., Runarsson, T. P., Sigurdsson, S., Eiriksdottir, G., and Johnsen, K. (2007). Reliability of quantitative EEG features. *Clinical neurophysiology : official*

journal of the International Federation of Clinical Neurophysiology, 118(10):2162–71.

Haegens, S., Nácher, V., Luna, R., Romo, R., and Jensen, O. (2011). α-Oscillations in the monkey sensorimotor network influence discrimination performance by rhythmical inhibition of neuronal spiking. *Proceedings of the National Academy of Sciences of the United States of America*, 108(48):19377–82.

Hagmann, P., Cammoun, L., Gigandet, X., Meuli, R., Honey, C. J., Wedeen, V. J., and Sporns, O. (2008). Mapping the structural core of human cerebral cortex. *PLoS biology*, 6(7):e159.

Hall, E. L., Woolrich, M. W., Thomaz, C. E., Morris, P. G., and Brookes, M. J. (2013). Using variance information in magnetoencephalography measures of functional connectivity. *NeuroImage*, 67:203–12.

Hämäläinen, M., Hari, R., Ilmoniemi, R. J., Knuutila, J., and Lounasmaa, O. V. (1993). Magnetoencephalography—theory, instrumentation, and applications to noninvasive studies of the working human brain. *Reviews of Modern Physics*, 65(2):413–97.

Hämäläinen, M. S. and Sarvas, J. (1987). Feasibility of the homogeneous head model in the interpretation of neuromagnetic fields. *Physics in Medicine and Biology*, 32(1):91–7.

Hämäläinen, M. S. and Sarvas, J. (1989). Realistic conductivity geometry model of the human head for interpretation of neuromagnetic data. *IEEE transactions on biomedical engineering*, 36(2):165–71.

Hardmeier, M., Hatz, F., Bousleiman, H., Schindler, C., Stam, C. J., and Fuhr, P. (2014). Reproducibility of Functional Connectivity and Graph Measures Based on the Phase Lag Index (PLI) and Weighted Phase Lag Index (wPLI) Derived from High Resolution EEG. *PloS one*, 9(10).

Hardy, J. and Selkoe, D. J. (2002). The amyloid hypothesis of Alzheimer's disease: progress and problems on the road to therapeutics. *Science (New York, N.Y.)*, 297(5580):353–6.

Hari, R. and Salmelin, R. (1997). Human cortical oscillations: a neuromagnetic view through the skull. *Trends in neurosciences*, 20(1):44–9.

Harmony, T. (2013). The functional significance of delta oscillations in cognitive processing. *Frontiers in integrative neuroscience*, 7.

Harmony, T., Fernández, T., Silva, J., Bernal, J., Díaz-Comas, L., Reyes, A., Marosi, E., Rodríguez, M., and Rodríguez, M. (1996). EEG delta activity: an indicator of attention to internal processing during performance of mental tasks. *International Journal of Psychophysiology*, 24(1-2):161–71.

Haueisen, J. and Knösche, T. R. (2014). Forward modeling and tissue conductivities. In Supek, S. and Aine, C. J., editors, *Magnetoencephalography, from signals to dynamic cortical networks*, pages 107–27. Springer-Verlag, Berlin Heidelberg.

Hauk, O., Wakeman, D. G., and Henson, R. (2011). Comparison of noise-normalized minimum norm estimates for MEG analysis using multiple resolution metrics. *NeuroImage*, 54(3):1966–74.

Hebert, L. E., Weuve, J., Scherr, P. A., and Evans, D. A. (2013). Alzheimer disease in the United States (2010-2050) estimated using the 2010 census. *Neurology*, 80(19):1778–83.

Hedden, T., Van Dijk, K. R. A., Becker, J. A., Mehta, A., Sperling, R. A., Johnson, K. A., and Buckner, R. L. (2009). Disruption of functional connectivity in clinically normal older adults harboring amyloid burden. *The Journal of neuroscience : the official journal of the Society for Neuroscience*, 29(40):12686–94.

Heller, L. and van Hulsteyn, D. B. (1992). Brain stimulation using electromagnetic sources: theoretical aspects. *Biophysical journal*, 63(1):129–38.

Helmholtz, H. (1853). Ueber einige Gesetze der Vertheilung elektrischer Ströme in körperlichen Leitern mit Anwendung auf die thierisch-elektrischen Versuche. *Annalen der Physik und Chemie*, 165(6):211–233.

Hillebrand, A., Barnes, G. R., Bosboom, J. L., Berendse, H. W., and Stam, C. J. (2012). Frequency-dependent functional connectivity within resting-state networks: an atlas-based MEG beamformer solution. *NeuroImage*, 59(4):3909–21.

Hillebrand, A., Singh, K. D., Holliday, I. E., Furlong, P. L., and Barnes, G. R. (2005). A new approach to neuroimaging with magnetoencephalography. *Human brain mapping*, 25(2):199–211.

Hindriks, R. and van Putten, M. J. (2013). Thalamo-cortical mechanisms underlying changes in amplitude and frequency of human alpha oscillations. *NeuroImage*, 70:150–63.

Hipp, J. F., Hawellek, D. J., Corbetta, M., Siegel, M., and Engel, A. K. (2012). Large-scale cortical correlation structure of spontaneous oscillatory activity. *Nature neuroscience*, 15(6):884–90.

Honey, C. J., Sporns, O., Cammoun, L., Gigandet, X., Thiran, J. P., Meuli, R., and Hagmann, P. (2009). Predicting human resting-state functional connectivity. *Proceedings of the National Academy of Sciences*, 106(6):2035–40.

Hoogenboom, N., Schoffelen, J.-M., Oostenveld, R., Parkes, L. M., and Fries, P. (2006). Localizing human visual gamma-band activity in frequency, time and space. *NeuroImage*, 29(3):764–73.

Howard, M. W. (2003). Gamma Oscillations Correlate with Working Memory Load in Humans. *Cerebral Cortex*, 13(12):1369–74.

Huang, C., Wahlund, L.-O., Dierks, T., Julin, P., Winblad, B., and Jelic, V. (2000). Discrimination of Alzheimer's disease and mild cognitive impairment by equivalent EEG sources: a cross-sectional and longitudinal study. *Clinical Neurophysiology*, 111(11):1961–7.

Huang, M. X., Mosher, J. C., and Leahy, R. M. (1999). A sensor-weighted overlapping-sphere head model and exhaustive head model comparison for MEG. *Physics in Medicine and Biology*, 44(2):423–40.

Hughes, S. W. and Crunelli, V. (2005). Thalamic mechanisms of EEG alpha rhythms and their pathological implications. *The Neuroscientist : a review journal bringing neurobiology, neurology and psychiatry*, 11(4):357–72.

Iversen, J. R., Repp, B. H., and Patel, A. D. (2009). Top-down control of rhythm perception modulates early auditory responses. *Annals of the New York Academy of Sciences*, 1169:58–73.

Jack, C. R. and Holtzman, D. M. (2013). Biomarker modeling of Alzheimer's disease. *Neuron*, 80(6):1347–58.

Jack, C. R., Shiung, M. M., Weigand, S. D., O'Brien, P. C., Gunter, J. L., Boeve, B. F., Knopman, D. S., Smith, G. E., Ivnik, R. J., Tangalos, E. G., and Petersen, R. C. (2005). Brain atrophy rates predict subsequent clinical conversion in normal elderly and amnestic MCI. *Neurology*, 65(8):1227–31.

Jack, C. R., Weigand, S. D., Shiung, M. M., Przybelski, S. A., O'Brien, P. C., Gunter, J. L., Knopman, D. S., Boeve, B. F., Smith, G. E., and Petersen, R. C. (2008). Atrophy rates accelerate in amnestic mild cognitive impairment. *Neurology*, 70(19 Pt 2):1740–52.

Jack, C. R., Wiste, H. J., Vemuri, P., Weigand, S. D., Senjem, M. L., Zeng, G., Bernstein, M. A., Gunter, J. L., Pankratz, V. S., Aisen, P. S., Weiner, M. W., Petersen, R. C., Shaw, L. M., Trojanowski, J. Q., and Knopman, D. S. (2010). Brain beta-amyloid measures and magnetic resonance imaging atrophy both predict time-to-progression from mild cognitive impairment to Alzheimer's disease. *Brain : a journal of neurology*, 133(11):3336–48.

Jafarpour, a., Horner, a. J., Fuentemilla, L., Penny, W. D., and Duzel, E. (2013). Decoding oscillatory representations and mechanisms in memory. *Neuropsychologia*, 51(4):772–80.

Jasper, H. and Penfield, W. (1949). Zur Deutung des normalen Elektrencephalogramms und selner Veriinderungen . Electroeorticograms in man : Effect of voluntary movement upon the electrical activity of the preeentral gyrus *. *Archiv für Psychiatrie und Zeitschrift Neurologie*, 174(307):163–74.

Jbabdi, S. and Johansen-Berg, H. (2011). Tractography: where do we go from here? *Brain connectivity*, 1(3):169–83.

JCGM (2008). International Vocabulary of Metrology–Basic and General Concepts and Associated Terms. Technical Report 6, Joint Committee for Guides in Metrology, 3rd edition.

Jenkinson, M., Beckmann, C. F., Behrens, T. E. J., Woolrich, M. W., and Smith, S. M. (2012). FSL. *NeuroImage*, 62(2):782–90.

Jenks, W. G., Sadeghi, S. S. H., and Wikswo, J. P. (1997). SQUIDs for nondestructive evaluation. *Journal of Physics D: Applied Physics*, 30(3):293–323.

Jensen, O., Kaiser, J., and Lachaux, J.-P. (2007). Human gamma-frequency oscillations associated with attention and memory. *Trends in neurosciences*, 30(7):317–24.

Jensen, O. and Lisman, J. E. (2000). Position Reconstruction From an Ensemble of Hippocampal Place Cells: Contribution of Theta Phase Coding. *J Neurophysiol*, 83(5):2602–9.

Jerbi, K., Ossandón, T., Hamamé, C. M., Senova, S., Dalal, S. S., Jung, J., Minotti, L., Bertrand, O., Berthoz, A., Kahane, P., and Lachaux, J.-P. (2009). Task-related

gamma-band dynamics from an intracerebral perspective: review and implications for surface EEG and MEG. *Human Brain Mapping*, 30(6):1758–71.

Jin, S.-H., Seol, J., Kim, J. S., and Chung, C. K. (2011). How reliable are the functional connectivity networks of MEG in resting states? *Journal of neurophysiology*, 106(6):2888–95.

Johansen-Berg, H., Behrens, T. E. J., Robson, M. D., Drobnjak, I., Rushworth, M. F. S., Brady, J. M., Smith, S. M., Higham, D. J., and Matthews, P. M. (2004). Changes in connectivity profiles define functionally distinct regions in human medial frontal cortex. *Proceedings of the National Academy of Sciences of the United States of America*, 101:13335–40.

John, E. R., Ahn, H., Prichep, L., Trepetin, M., Brown, D., and Kaye, H. (1980). Developmental equations for the electroencephalogram. *Science*, 210(4475):1255–8.

Jones, D. K., Knösche, T. R., and Turner, R. (2013). White matter integrity, fiber count, and other fallacies: The do's and don'ts of diffusion MRI. *NeuroImage*, 73:239–54.

Jones, D. T., Machulda, M. M., Vemuri, P., McDade, E. M., Zeng, G., Senjem, M. L., Gunter, J. L., Przybelski, S. A., Avula, R. T., Knopman, D. S., Boeve, B. F., Petersen, R. C., and Jack, C. R. (2011). Age-related changes in the default mode network are more advanced in Alzheimer disease. *Neurology*, 77(16):1524–31.

Jurysta, F., van de Borne, P., Lanquart, J.-P., Migeotte, P.-F., Degaute, J.-P., Dumont, M., and Linkowski, P. (2005). Progressive aging does not alter the interaction between autonomic cardiac activity and delta EEG power. *Clinical neurophysiology : official journal of the International Federation of Clinical Neurophysiology*, 116(4):871–7.

Kahana, M. J. (2006). The cognitive correlates of human brain oscillations. *The Journal of neuroscience : the official journal of the Society for Neuroscience*, 26(6):1669–72.

Kamerlingh Onnes, H. (1911). The superconductivity of mercury. *Leiden Commun*, 120b, 122b.

Kamiński, J., Brzezicka, A., Gola, M., and Wróbel, A. (2012). β band oscillations engagement in human alertness process. *International journal of psychophysiology : official journal of the International Organization of Psychophysiology*, 85(1):125–8.

Kaplan, P. W. (2004). The EEG in metabolic encephalopathy and coma. *Journal of clinical neurophysiology*, 21(5):307–18.

Katz, M. J., Lipton, R. B., Hall, C. B., Zimmerman, M. E., Sanders, A. E., Verghese, J., Dickson, D. W., and Derby, C. A. (2012). Age-specific and sex-specific prevalence and incidence of mild cognitive impairment, dementia, and Alzheimer dementia in blacks and whites: a report from the Einstein Aging Study. *Alzheimer disease and associated disorders*, 26(4):335–43.

Khader, P. H., Jost, K., Ranganath, C., and Rösler, F. (2010). Theta and alpha oscillations during working-memory maintenance predict successful long-term memory encoding. *Neuroscience letters*, 468(3):339–43.

Khalsa, S., Mayhew, S. D., Chechlacz, M., Bagary, M., and Bagshaw, A. P. (2014). The structural and functional connectivity of the posterior cingulate cortex: Comparison between deterministic and probabilistic tractography for the investigation of structure–function relationships. *NeuroImage*, 102:118–27.

Khosla, D., Singh, M., and Don, M. (1997). Spatio-temporal EEG source localization using simulated annealing. *IEEE Transactions on Biomedical Engineering*, 44(11):1075–91.

Kircher, T. T., Weis, S., Freymann, K., Erb, M., Jessen, F., Grodd, W., Heun, R., and Leube, D. T. (2007). Hippocampal activation in patients with mild cognitive impairment is necessary for successful memory encoding. *Journal of neurology, neurosurgery, and psychiatry*, 78(8):812–8.

Kiuchi, K., Morikawa, M., Taoka, T., Nagashima, T., Yamauchi, T., Makinodan, M., Norimoto, K., Hashimoto, K., Kosaka, J., Inoue, Y., Inoue, M., Kichikawa, K., and Kishimoto, T. (2009). Abnormalities of the uncinate fasciculus and posterior cingulate fasciculus in mild cognitive impairment and early Alzheimer's disease: a diffusion tensor tractography study. *Brain research*, 1287:184–91.

Klimesch, W. (1999). EEG alpha and theta oscillations reflect cognitive and memory performance: a review and analysis. *Brain research. Brain research reviews*, 29(2-3):169–95.

Knyazev, G. G. (2007). Motivation, emotion, and their inhibitory control mirrored in brain oscillations. *Neuroscience and biobehavioral reviews*, 31(3):377–95.

Knyazev, G. G. (2012). EEG delta oscillations as a correlate of basic homeostatic and motivational processes. *Neuroscience and biobehavioral reviews*, 36(1):677–95.

Knyazev, G. G., Slobodskoj-Plusnin, J. Y., Bocharov, A. V., and Pylkova, L. V. (2011). The default mode network and EEG α oscillations: an independent component analysis. *Brain research*, 1402:67–79.

Kondacs, A. and Szabó, M. (1999). Long-term intra-individual variability of the background EEG in normals. *Clinical neurophysiology : official journal of the International Federation of Clinical Neurophysiology*, 110(10):1708–16.

Korb, A. S., Cook, I. A., Hunter, A. M., and Leuchter, A. F. (2008). Brain electrical source differences between depressed subjects and healthy controls. *Brain topography*, 21(2):138–46.

Lachaux, J. P., Rodriguez, E., Martinerie, J., and Varela, F. J. (1999). Measuring phase synchrony in brain signals. *Human brain mapping*, 8:194–208.

Laird, A. R., Fox, P. M., Eickhoff, S. B., Turner, J. A., Ray, K. L., McKay, D. R., Glahn, D. C., Beckmann, C. F., Smith, S. M., and Fox, P. T. (2011). Behavioral interpretations of intrinsic connectivity networks. *Journal of cognitive neuroscience*, 23(12):4022–37.

Lalancette, M., Quraan, M., and Cheyne, D. (2011). Evaluation of multiple-sphere head models for MEG source localization. *Physics in medicine and biology*, 56(17):5621–35.

Landau, S. M., Harvey, D., Madison, C. M., Reiman, E. M., Foster, N. L., Aisen, P. S., Petersen, R. C., Shaw, L. M., Trojanowski, J. Q., Jack, C. R., Weiner, M. W., and Jagust, W. J. (2010). Comparing predictors of conversion and decline in mild cognitive impairment. *Neurology*, 75(3):230–8.

Lazar, M., Weinstein, D. M., Tsuruda, J. S., Hasan, K. M., Arfanakis, K., Meyerand, M. E., Badie, B., Rowley, H. a., Haughton, V., Field, A., and Alexander, A. L. (2003). White matter tractography using diffusion tensor deflection. *Human brain mapping*, 18(4):306–21.

Le Bihan, D., Mangin, J. F., Poupon, C., Clark, C. A., Pappata, S., Molko, N., and Chabriat, H. (2001). Diffusion tensor imaging: concepts and applications. *Journal of magnetic resonance imaging : JMRI*, 13(4):534–46.

Le Van Quyen, M., Foucher, J., Lachaux, J.-P., Rodriguez, E., Lutz, A., Martinerie, J., and Varela, F. J. (2001). Comparison of Hilbert transform and wavelet methods for the analysis of neuronal synchrony. *Journal of Neuroscience Methods*, 111(2):83–98.

Legendre, P. (2005). Species associations: the Kendall coefficient of concordance revisited. *Journal of Agricultural, Biological, and Environmental Statistics*, 10(2):226–245.

Lin, F.-H., Witzel, T., Ahlfors, S. P., Stufflebeam, S. M., Belliveau, J. W., and Hämäläinen, M. S. (2006). Assessing and improving the spatial accuracy in MEG source localization by depth-weighted minimum-norm estimates. *NeuroImage*, 31(1):160–71.

Lodder, S. S. and van Putten, M. J. a. M. (2011). Automated EEG analysis: characterizing the posterior dominant rhythm. *Journal of neuroscience methods*, 200(1):86–93.

Lopes da Silva, F. (2010). Electrophysiological Basis of MEG Signals. In Hansen, P. C., Kringelbach, M. L., and Salmelin, R., editors, *MEG: An Introduction to Methods*, pages 1–23. Oxford University Press.

Lopes da Silva, F. (2013). EEG and MEG: relevance to neuroscience. *Neuron*, 80(5):1112–28.

López, M. E., Bruña, R., Aurtenetxe, S., Pineda-Pardo, J. A., Marcos, A., Arrazola, J., Reinoso, A. I., Montejo, P., Bajo, R., and Maestú, F. (2014). Alpha-band hypersynchronization in progressive mild cognitive impairment: a magnetoencephalography study. *The Journal of neuroscience : the official journal of the Society for Neuroscience*, 34(44):14551–9.

Lőrincz, M. L., Kékesi, K. A., Juhász, G., Crunelli, V., and Hughes, S. W. (2009). Temporal Framing of Thalamic Relay-Mode Firing by Phasic Inhibition during the Alpha Rhythm. *Neuron*, 63(5):683–96.

Luckhoo, H., Hale, J. R., Stokes, M. G., Nobre, A. C., Morris, P. G., Brookes, M. J., and Woolrich, M. W. (2012). Inferring task-related networks using independent component analysis in magnetoencephalography. *NeuroImage*, 62(1):530–41.

Luckhoo, H. T., Brookes, M. J., and Woolrich, M. W. (2014). Multi-session statistics on beamformed MEG data. *NeuroImage*, 95:330–5.

Lynall, M.-E., Bassett, D. S., Kerwin, R., McKenna, P. J., Kitzbichler, M., Muller, U., and Bullmore, E. (2010). Functional connectivity and brain networks in schizophrenia. *The Journal of neuroscience : the official journal of the Society for Neuroscience*, 30(28):9477–87.

Maldjian, J. A., Davenport, E. M., and Whitlow, C. T. (2014). Graph theoretical analysis of resting-state MEG data: Identifying interhemispheric connectivity and the default mode. *NeuroImage*, 96:88–94.

Mann, E. O. and Paulsen, O. (2007). Role of GABAergic inhibition in hippocampal network oscillations. *Trends in neurosciences*, 30(7):343–9.

Maris, E. and Oostenveld, R. (2007). Nonparametric statistical testing of EEG- and MEG-data. *Journal of neuroscience methods*, 164(1):177–90.

Marple, S. L. (1999). Computing the discrete-time "analytic" signal via FFT. *Signal Processing, IEEE Transactions on Signal Processing*, 47(9):2600–3.

Matsuda, H. (2001). Cerebral blood flow and metabolic abnormalities in Alzheimer's disease. *Annals of Nuclear Medicine*, 15(2):85–92.

Mayhew, S. D., Ostwald, D., Porcaro, C., and Bagshaw, A. P. (2013). Spontaneous EEG alpha oscillation interacts with positive and negative BOLD responses in the visual-auditory cortices and default-mode network. *NeuroImage*, 76:362–72.

McEvoy, L. K., Smith, M. E., and Gevins, A. (2000). Test-retest reliability of cognitive EEG. *Clinical neurophysiology : official journal of the International Federation of Clinical Neurophysiology*, 111(3):457–63.

McGraw, K. and Wong, S. (1996). Forming inferences about some intraclass correlation coefficients. *Psychological methods*, 1(1).

Meissner, W. and Ochsenfeld, R. (1933). Ein neuer Effekt bei Eintritt der Supraleitfähigkeit. *Die Naturwissenschaften*, 21(44):787–88.

Menon, R. S. (2001). Imaging function in the working brain with fMRI. *Current Opinion in Neurobiology*, 11(5):630–36.

Milstein, J. N. and Koch, C. (2008). Dynamic moment analysis of the extracellular electric field of a biologically realistic spiking neuron. *Neural computation*, 20(8):2070–84.

Mintun, M. A., Larossa, G. N., Sheline, Y. I., Dence, C. S., Lee, S. Y., Mach, R. H., Klunk, W. E., Mathis, C. A., DeKosky, S. T., and Morris, J. C. (2006). [11C]PIB in a nondemented population: potential antecedent marker of Alzheimer disease. *Neurology*, 67(3):446–52.

Moretti, D. V., Fracassi, C., Pievani, M., Geroldi, C., Binetti, G., Zanetti, O., Sosta, K., Rossini, P. M., and Frisoni, G. B. (2009a). Increase of theta/gamma ratio is associated with memory impairment. *Clinical neurophysiology : official journal of the International Federation of Clinical Neurophysiology*, 120(2):295–303.

Moretti, D. V., Frisoni, G. B., Fracassi, C., Pievani, M., Geroldi, C., Binetti, G., Rossini, P. M., and Zanetti, O. (2011). MCI patients' EEGs show group differences between those who progress and those who do not progress to AD. *Neurobiology of aging*, 32(4):563–71.

Moretti, D. V., Paternicò, D., Binetti, G., Zanetti, O., and Frisoni, G. B. (2012). EEG markers are associated to gray matter changes in thalamus and basal ganglia in subjects with mild cognitive impairment. *NeuroImage*, 60(1):489–96.

Moretti, D. V., Pievani, M., Fracassi, C., Binetti, G., Rosini, S., Geroldi, C., Zanetti, O., Rossini, P. M., and Frisoni, G. B. (2009b). Increase of theta/gamma and alpha3/alpha2 ratio is associated with amygdalo-hippocampal complex atrophy. *Journal of Alzheimer's disease : JAD*, 17(2):349–57.

Mori, S. and van Zijl, P. C. M. (2002). Fiber tracking: principles and strategies - a technical review. *NMR in biomedicine*, 15(7-8):468–80.

Mosher, J., Leahy, R., and Lewis, P. (1999). EEG and MEG: forward solutions for inverse methods. *IEEE Transactions on Biomedical Engineering*, 46(3):245–59.

Mosher, J. C. and Leahy, R. M. (1998). Recursive MUSIC: a framework for EEG and MEG source localization. *IEEE transactions on bio-medical engineering*, 45(11):1342–54.

Murakami, S. and Okada, Y. (2006). Contributions of principal neocortical neurons to magnetoencephalography and electroencephalography signals. *The Journal of physiology*, 575:925–36.

Myles, P. S. and Cui, J. (2007). Using the Bland-Altman method to measure agreement with repeated measures. *British journal of anaesthesia*, 99(3):309–11.

Nakasatp, N., Levesque, M. F., Barth, D. S., Baumgartner, C., Rogers, R. L., and Sutherling, W. W. (1994). Comparisons of MEG, EEG, and ECoG source localization in neocortical partial epilepsy in humans. *Electroencephalography and Clinical Neurophysiology*, 91(3):171–78.

Naveh-Benjamin, M. (2000). Adult age differences in memory performance: tests of an associative deficit hypothesis. *Journal of experimental psychology. Learning, memory, and cognition*, 26(5):1170–87.

Niso, G., Bruña, R., Pereda, E., Gutiérrez, R., Bajo, R., Maestú, F., and Del-Pozo, F. (2013). HERMES: towards an integrated toolbox to characterize functional and effective brain connectivity. *Neuroinformatics*, 11(4):405–34.

Noachtar, S. and Rémi, J. (2009). The role of EEG in epilepsy: a critical review. *Epilepsy & behavior : E&B*, 15(1):22–33.

Nolte, G. (2003). The magnetic lead field theorem in the quasi-static approximation and its use for magnetoencephalography forward calculation in realistic volume conductors. *Physics in Medicine and Biology*, 48(22):3637–52.

Nunez, P. L., Wingeier, B. M., and Silberstein, R. B. (2001). Spatial-temporal structures of human alpha rhythms: theory, microcurrent sources, multiscale measurements, and global binding of local networks. *Human brain mapping*, 13(3):125–64.

O'Keefe, J. and Recce, M. L. (1993). Phase relationship between hippocampal place units and the EEG theta rhythm. *Hippocampus*, 3(3):317–30.

Olde Dubbelink, K. T. E., Stoffers, D., Deijen, J. B., Twisk, J. W. R., Stam, C. J., and Berendse, H. W. (2013). Cognitive decline in Parkinson's disease is associated with slowing of resting-state brain activity: a longitudinal study. *Neurobiology of aging*, 34(2):408–18.

Oostenveld, R., Fries, P., Maris, E., and Schoffelen, J. M. (2011). FieldTrip: Open source software for advanced analysis of MEG, EEG, and invasive electrophysiological data. *Computational intelligence and neuroscience*, 2011.

Osipova, D., Ahveninen, J., Jensen, O., Ylikoski, A., and Pekkonen, E. (2005). Altered generation of spontaneous oscillations in Alzheimer's disease. *NeuroImage*, 27(4):835–41.

Osipova, D., Rantanen, K., Ahveninen, J., Ylikoski, R., Häppölä, O., Strandberg, T., and Pekkonen, E. (2006). Source estimation of spontaneous MEG oscillations in mild cognitive impairment. *Neuroscience letters*, 405(1-2):57–61.

Papanicolaou, A. C. (2009). Part i: the method. In *Clinical Magnetoencephalography and Magnetic Source Imaging*, pages 3–58. Cambridge University Press.

Parkkonen, L. (2010). Instrumentation and Data Preprocessing. In Hansen, P. C., Kringelbach, M. L., and Salmelin, R., editors, *MEG: An Introduction to Methods*, pages 24–65. Oxford University Press.

Pascual-Marqui, R., Michel, C., and Lehmann, D. (1994). Low resolution electromagnetic tomography: a new method for localizing electrical activity in the brain. *International Journal of Psychophysiology*, 18(1):49–65.

Pasqualotto, E., Federici, S., and Belardinelli, M. O. (2012). Toward functioning and usable brain-computer interfaces (BCIs): a literature review. *Disability and rehabilitation. Assistive technology*, 7(2):89–103.

Passero, S., Rocchi, R., Vatti, G., Burgalassi, L., and Battistini, N. (1995). Quantitative EEG Mapping, Regional Cerebral Blood Flow, and Neuropsychological Function in Alzheimer's Disease. *Dementia and Geriatric Cognitive Disorders*, 6(3):148–56.

Penny, W. D., Friston, K. J., Ashburner, J. T., Kiebel, S. J., and Nichols, T. E. (2011). *Statistical Parametric Mapping: The Analysis of Functional Brain Images: The Analysis of Functional Brain Images*. Academic Press.

Pereda, E., Quiroga, R. Q., and Bhattacharya, J. (2005). Nonlinear multivariate analysis of neurophysiological signals. *Progress in neurobiology*, 77(1-2):1–37.

Pesaran, B., Pezaris, J. S., Sahani, M., Mitra, P. P., and Andersen, R. A. (2002). Temporal structure in neuronal activity during working memory in macaque parietal cortex. *Nature neuroscience*, 5(8):805–11.

Petersén, I. and Eeg-Olofsson, O. (1971). The Development of the Electroencephalogram in Normal Children from the Age of 1 Through 15 Years – Non-paroxysmal activity. *Neuropediatrics*, 2(3):247–304.

Petersen, R. C. (2001). Current Concepts in Mild Cognitive Impairment. *Archives of Neurology*, 58(12):1985–92.

Petersen, R. C. (2011). Clinical practice. Mild cognitive impairment. *The New England journal of medicine*, 364(23):2227–34.

Petersen, R. C., Jack, C. R., Xu, Y.-C., Waring, S. C., O'Brien, P. C., Smith, G. E., Ivnik, R. J., Tangalos, E. G., Boeve, B. F., and Kokmen, E. (2000). Memory and MRI-based hippocampal volumes in aging and AD. *Neurology*, 54(3):581.

Petersen, R. C. and Negash, S. (2008). Mild cognitive impairment: an overview. *CNS spectrums*, 13(1):45–53.

Petrella, J. R., Sheldon, F. C., Prince, S. E., Calhoun, V. D., and Doraiswamy, P. M. (2011). Default mode network connectivity in stable vs progressive mild cognitive impairment. *Neurology*, 76(6):511–7.

Platt, B. and Riedel, G. (2011). The cholinergic system, EEG and sleep. *Behavioural brain research*, 221(2):499–504.

Pogosyan, A., Gaynor, L. D., Eusebio, A., and Brown, P. (2009). Boosting cortical activity at Beta-band frequencies slows movement in humans. *Current biology*, 19(19):1637–41.

Pollock, V., Schneider, L., and Lyness, S. (1991). Reliability of topographic quantitative EEG amplitude in healthy late-middle-aged and elderly subjects. *Electroencephalography and Clinical Neurophysiology*, 79(1):20–26.

Portier, C. J. and Wolfe, M. S. (1998). Assessment of health effects from exposure of power-line frequency electric and magnetic fields. Technical report, National Institute of Environmental Health Sciences.

Prestia, A., Caroli, A., van der Flier, W. M., Ossenkoppele, R., Van Berckel, B., Barkhof, F., Teunissen, C. E., Wall, A. E., Carter, S. F., Schöll, M., Choo, I. H., Nordberg, A., Scheltens, P., and Frisoni, G. B. (2013). Prediction of dementia in MCI patients based on core diagnostic markers for Alzheimer disease. *Neurology*, 80(11):1048–56.

Prince, M., Bryce, R., Albanese, E., Wimo, A., Ribeiro, W., and Ferri, C. P. (2013). The global prevalence of dementia: a systematic review and metaanalysis. *Alzheimer's & dementia : the journal of the Alzheimer's Association*, 9(1):63–75.

Qi, Z., Wu, X., Wang, Z., Zhang, N., Dong, H., Yao, L., and Li, K. (2010). Impairment and compensation coexist in amnestic MCI default mode network. *NeuroImage*, 50(1):48–55.

Qiu, C., Kivipelto, M., and von Strauss, E. (2009). Epidemiology of Alzheimer's disease: occurrence, determinants, and strategies toward intervention. *Dialogues in clinical neuroscience*, 11(2):111–28.

Raichle, M. E. and Gusnard, D. A. (2002). Appraising the brain's energy budget. *Proceedings of the National Academy of Sciences of the United States of America*, 99(16):10237–9.

Raichle, M. E., MacLeod, A. M., Snyder, A. Z., Powers, W. J., Gusnard, D. A., and Shulman, G. L. (2001). A default mode of brain function. *Proceedings of the National Academy of Sciences of the United States of America*, 98(2):676–82.

Raichle, M. E. and Snyder, A. Z. (2007). A default mode of brain function: A brief history of an evolving idea. *NeuroImage*, 37(4):1083–90.

Reddy, P. H. and Beal, M. F. (2008). Amyloid beta, mitochondrial dysfunction and synaptic damage: implications for cognitive decline in aging and Alzheimer's disease. *Trends in molecular medicine*, 14(2):45–53.

Rihs, T. A., Michel, C. M., and Thut, G. (2009). A bias for posterior alpha-band power suppression versus enhancement during shifting versus maintenance of spatial attention. *NeuroImage*, 44(1):190–9.

Roberson, E. D. and Mucke, L. (2006). 100 years and counting: prospects for defeating Alzheimer's disease. *Science (New York, N.Y.)*, 314(5800):781–4.

Roberts, T. P. and Poeppel, D. (1996). Latency of auditory evoked M100 as a function of tone frequency. *Neuroreport*, 7(6):1138–40.

Rombouts, S. A. R. B., Barkhof, F., Goekoop, R., Stam, C. J., and Scheltens, P. (2005). Altered resting state networks in mild cognitive impairment and mild Alzheimer's disease: an fMRI study. *Human brain mapping*, 26(4):231–9.

Romei, V., Gross, J., and Thut, G. (2010). On the role of prestimulus alpha rhythms over occipito-parietal areas in visual input regulation: correlation or causation? *The Journal of neuroscience : the official journal of the Society for Neuroscience*, 30(25):8692–7.

Rosazza, C. and Minati, L. (2011). Resting-state brain networks: literature review and clinical applications. *Neurological sciences : official journal of the Italian Neurological Society and of the Italian Society of Clinical Neurophysiology*, 32(5):773–85.

Rosen, W. G., Terry, R. D., Fuld, P. A., Katzman, R., and Peck, A. (1980). Pathological verification of ischemic score in differentiation of dementias. *Annals of neurology*, 7(5):486–8.

Rosenblum, M. and Pikovsky, A. (2003). Synchronization: From pendulum clocks to chaotic lasers and chemical oscillators. *Contemporary Physics*, 44(5):401–16.

Rosenblum, M., Pikovsky, A., Kurths, J., Schäfer, C., and Tass, P. (2001). *Neuro-Informatics and Neural Modelling*, volume 4 of *Handbook of Biological Physics*. Elsevier.

Sakkalis, V. (2011). Review of advanced techniques for the estimation of brain connectivity measured with EEG/MEG. *Computers in biology and medicine*, 41(12):1110–7.

Salmelin, R. (2010). Multi-dipole modelling in MEG. In Hansen, P. C., Kringelbach, M. L., and Salmelin, R., editors, *MEG: An Introduction to Methods*, pages 124–155. Oxford University Press.

Sambataro, F., Murty, V. P., Callicott, J. H., Tan, H.-Y., Das, S., Weinberger, D. R., and Mattay, V. S. (2010). Age-related alterations in default mode network: Impact on working memory performance. *Neurobiology of Aging*, 31(5):839–52.

Samson-Dollfus, D., Delapierre, G., Do Marcolino, C., and Blondeau, C. (1997). Normal and pathological changes in alpha rhythms. *International journal of psychophysiology : official journal of the International Organization of Psychophysiology*, 26(1-3):395–409.

Sarvas, J. (1987). Basic mathematical and electromagnetic concepts of the biomagnetic inverse problem. *Physics in Medicine and Biology*, 32(1):11–22.

Sauseng, P. and Klimesch, W. (2008). What does phase information of oscillatory brain activity tell us about cognitive processes? *Neuroscience and biobehavioral reviews*, 32(5):1001–13.

Schaefer, M., Mühlnickel, W., Grüsser, S. M., and Flor, H. (2002). Reproducibility and Stability of Neuroelectric Source Imaging in Primary Somatosensory Cortex. *Brain Topography*, 14(3):179–89.

Scher, M. S. (2008). Ontogeny of EEG-sleep from neonatal through infancy periods. *Sleep medicine*, 9(6):615–36.

Schoffelen, J. M. and Gross, J. (2009). Source connectivity analysis with MEG and EEG. *Human Brain Mapping*, 30:1857–65.

Scholtes, V. A., Terwee, C. B., and Poolman, R. W. (2011). What makes a measurement instrument valid and reliable? *Injury*, 42(3):236–40.

Sederberg, P. B., Kahana, M. J., Howard, M. W., Donner, E. J., and Madsen, J. R. (2003). Theta and Gamma Oscillations during Encoding Predict Subsequent Recall. *J. Neurosci.*, 23(34):10809–14.

Ségonne, F., Pacheco, J., and Fischl, B. (2007). Geometrically accurate topology-correction of cortical surfaces using nonseparating loops. *IEEE transactions on medical imaging*, 26(4):518–29.

Sekihara, K. and Nagarajan, S. S. (2008). *Adaptive Spatial Filters for Electromagnetic Brain Imaging*. Springer.

Serra, L., Cercignani, M., Lenzi, D., Perri, R., Fadda, L., Caltagirone, C., Macaluso, E., and Bozzali, M. (2010). Grey and white matter changes at different stages of Alzheimer's disease. *Journal of Alzheimer's disease : JAD*, 19(1):147–59.

Shao, J., Myers, N., Yang, Q., Feng, J., Plant, C., Böhm, C., Förstl, H., Kurz, A., Zimmer, C., Meng, C., Riedl, V., Wohlschläger, A., and Sorg, C. (2012). Prediction of Alzheimer's disease using individual structural connectivity networks. *Neurobiology of aging*, 33(12):2756–65.

Shechtman, O. (2013). The Coefficient of Variation as an Index of Measurement Reliability. In Doi, S. A. R. and Williams, G. M., editors, *Methods of Clinical Epidemiology*, pages 39–49. Springer Berlin Heidelberg.

Shehzad, Z., Kelly, A. M. C., Reiss, P. T., Gee, D. G., Gotimer, K., Uddin, L. Q., Lee, S. H., Margulies, D. S., Roy, A. K., Biswal, B. B., Petkova, E., Castellanos, F. X., and Milham, M. P. (2009). The resting brain: unconstrained yet reliable. *Cerebral cortex (New York, N.Y. : 1991)*, 19(10):2209–29.

Sheline, Y. I. and Raichle, M. E. (2013). Resting State Functional Connectivity in Preclinical Alzheimer's Disease. *Biological Psychiatry*, 74(5):340–7.

Sheline, Y. I., Raichle, M. E., Snyder, A. Z., Morris, J. C., Head, D., Wang, S., and Mintun, M. A. (2010). Amyloid Plaques Disrupt Resting State Default Mode Network Connectivity in Cognitively Normal Elderly. *Biological Psychiatry*, 67(6):584–7.

Shrout, P. E. and Fleiss, J. L. (1979). Intraclass correlations: uses in assessing rater reliability. *Psychological bulletin*, 86(2):420–8.

Simpson, J. R. (2014). DSM-5 and neurocognitive disorders. *The journal of the American Academy of Psychiatry and the Law*, 42(2):159–64.

Singer, W. (1999). Neuronal synchrony: a versatile code for the definition of relations? *Neuron*, 24(1):49–65.

Smith, S. M. (2002). Fast robust automated brain extraction. *Human brain mapping*, 17(3):143–55.

Smith, S. M., Fox, P. T., Miller, K. L., Glahn, D. C., Fox, P. M., Mackay, C. E., Filippini, N., Watkins, K. E., Toro, R., Laird, A. R., and Beckmann, C. F. (2009). Correspondence of the brain's functional architecture during activation and rest. *Proceedings of the National Academy of Sciences of the United States of America*, 106(31):13040–5.

Sokolov, A., Pavlova, M., Lutzenberger, W., and Birbaumer, N. (2004). Reciprocal modulation of neuromagnetic induced gamma activity by attention in the human visual and auditory cortex. *NeuroImage*, 22(2):521–9.

Sorg, C., Riedl, V., Mühlau, M., Calhoun, V. D., Eichele, T., Läer, L., Drzezga, A., Förstl, H., Kurz, A., Zimmer, C., and Wohlschläger, A. M. (2007). Selective changes of resting-state networks in individuals at risk for Alzheimer's disease. *Proceedings of the National Academy of Sciences of the United States of America*, 104(47):18760–5.

Sperling, R. a., Laviolette, P. S., O'Keefe, K., O'Brien, J., Rentz, D. M., Pihlajamaki, M., Marshall, G., Hyman, B. T., Selkoe, D. J., Hedden, T., Buckner, R. L., Becker, J. A., and Johnson, K. a. (2009). Amyloid deposition is associated with impaired default network function in older persons without dementia. *Neuron*, 63(2):178–88.

Spironelli, C. and Angrilli, A. (2009). EEG delta band as a marker of brain damage in aphasic patients after recovery of language. *Neuropsychologia*, 47(4):988–94.

Stam, C. J., Nolte, G., and Daffertshofer, A. (2007). Phase lag index: assessment of functional connectivity from multi channel EEG and MEG with diminished bias from common sources. *Human brain mapping*, 28(11):1178–93.

Stenroos, M., Hunold, A., and Haueisen, J. (2014). Comparison of three-shell and simplified volume conductor models in magnetoencephalography. *NeuroImage*, 94:337–48.

Stenroos, M. and Sarvas, J. (2012). Bioelectromagnetic forward problem: isolated source approach revis(it)ed. *Physics in medicine and biology*, 57(11):3517–35.

Steriade, M., Gloor, P., Llinás, R., Lopes da Silva, F., and Mesulam, M.-M. (1990). Basic mechanisms of cerebral rhythmic activities. *Electroencephalography and Clinical Neurophysiology*, 76(6):481–508.

Taulu, S. (2008). *Processing of weak magnetic multichannel signals: the signal space separation method*. Doctoral dissertation, Helsinki University of Technology.

Taulu, S. and Kajola, M. (2005). Presentation of electromagnetic multichannel data: The signal space separation method. *Journal of Applied Physics*, 97(12).

Taulu, S. and Simola, J. (2006). Spatiotemporal signal space separation method for rejecting nearby interference in MEG measurements. *Physics in medicine and biology*, 51(7):1759–68.

Taulu, S., Simola, J., and Kajola, M. (2005). Applications of the signal space separation method. *IEEE Transactions on Signal Processing*, 53(9):3359–72.

Thut, G., Nietzel, A., Brandt, S. A., and Pascual-Leone, A. (2006). Alpha-band electroencephalographic activity over occipital cortex indexes visuospatial attention bias and predicts visual target detection. *The Journal of neuroscience : the official journal of the Society for Neuroscience*, 26(37):9494–502.

Tiihonen, J., Kajola, M., and Hari, R. (1989). Magnetic mu rhythm in man. *Neuroscience*, 32(3):793–800.

Tort, A. B. L., Kramer, M. A., Thorn, C., Gibson, D. J., Kubota, Y., Graybiel, A. M., and Kopell, N. J. (2008). Dynamic cross-frequency couplings of local field potential oscillations in rat striatum and hippocampus during performance of a T-maze task. *Proceedings of the National Academy of Sciences of the United States of America*, 105(51):20517–22.

Tzourio-Mazoyer, N., Landeau, B., Papathanassiou, D., Crivello, F., Etard, O., Delcroix, N., Mazoyer, B., and Joliot, M. (2002). Automated anatomical labeling of activations in SPM using a macroscopic anatomical parcellation of the MNI MRI single-subject brain. *NeuroImage*, 15(1):273–89.

Uludağ, K. and Roebroeck, A. (2014). General overview on the merits of multimodal neuroimaging data fusion. *NeuroImage*, 102:3–10.

Uutela, K., Hämäläinen, M., and Salmelin, R. (1998). Global optimization in the localization of neuromagnetic sources. *IEEE transactions on bio-medical engineering*, 45(6):716–23.

Uutela, K., Hämäläinen, M., and Somersalo, E. (1999). Visualization of magnetoencephalographic data using minimum current estimates. *NeuroImage*, 10(2):173–80.

Uutela, K., Taulu, S., and Hämäläinen, M. (2001). Detecting and correcting for head movements in neuromagnetic measurements. *NeuroImage*, 14(6):1424–31.

van den Heuvel, M. P. and Hulshoff Pol, H. E. (2010). Exploring the brain network: a review on resting-state fMRI functional connectivity. *European neuropsychopharmacology : the journal of the European College of Neuropsychopharmacology*, 20(8):519–34.

Van Der Meer, M. L., Tewarie, P., Schoonheim, M. M., Douw, L., Barkhof, F., Polman, C. H., Stam, C. J., and Hillebrand, a. (2013). Cognition in MS correlates with resting-state oscillatory brain activity: An explorative MEG source-space study. *NeuroImage: Clinical*, 2:727–34.

Van Essen, D. C., Drury, H. A., Dickson, J., Harwell, J., Hanlon, D., and Anderson, C. H. (2001). An integrated software suite for surface-based analyses of cerebral cortex. *Journal of the American Medical Informatics Association : JAMIA*, 8(5):443–59.

Van Veen, B. D., van Drongelen, W., Yuchtman, M., and Suzuki, A. (1997). Localization of brain electrical activity via linearly constrained minimum variance spatial filtering. *IEEE transactions on bio-medical engineering*, 44(9):867–80.

Varela, F., Lachaux, J. P., Rodriguez, E., and Martinerie, J. (2001). The brainweb: phase synchronization and large-scale integration. *Nature reviews. Neuroscience*, 2(4):229–39.

Verghese, P. B., Castellano, J. M., and Holtzman, D. M. (2011). Apolipoprotein E in Alzheimer's disease and other neurological disorders. *The Lancet. Neurology*, 10(3):241–52.

Vierling-Claassen, D., Cardin, J. A., Moore, C. I., and Jones, S. R. (2010). Computational modeling of distinct neocortical oscillations driven by cell-type selective optogenetic drive: separable resonant circuits controlled by low-threshold spiking and fast-spiking interneurons. *Frontiers in human neuroscience*, 4:198.

Visser, P. J., Verhey, F., Knol, D. L., Scheltens, P., Wahlund, L.-O., Freund-Levi, Y., Tsolaki, M., Minthon, L., Wallin, A. K., Hampel, H., Bürger, K., Pirttila, T., Soininen, H., Rikkert, M. O., Verbeek, M. M., Spiru, L., and Blennow, K. (2009). Prevalence and prognostic value of CSF markers of Alzheimer's disease pathology in patients with subjective cognitive impairment or mild cognitive impairment in the DESCRIPA study: a prospective cohort study. *The Lancet. Neurology*, 8(7):619–27.

von Stein, A. and Sarnthein, J. (2000). Different frequencies for different scales of cortical integration: from local gamma to long range alpha/theta synchronization. *International Journal of Psychophysiology*, 38(3):301–13.

Vos, S. J. B., van Rossum, I. A., Verhey, F., Knol, D. L., Soininen, H., Wahlund, L.-O., Hampel, H., Tsolaki, M., Minthon, L., Frisoni, G. B., Froelich, L., Nobili, F., van der Flier, W., Blennow, K., Wolz, R., Scheltens, P., and Visser, P. J. (2013). Prediction of

Alzheimer disease in subjects with amnestic and nonamnestic MCI. *Neurology*, 80(12):1124–32.

Vrba, J. (2002). Magnetoencephalography: the art of finding a needle in a haystack. *Physica C: Superconductivity*, 368(1-4):1–9.

Vrba, J. and Robinson, S. E. (2001). Signal processing in magnetoencephalography. *Methods*, 25(2):249–71.

Wang, L., Li, H., Liang, Y., Zhang, J., Li, X., Shu, N., Wang, Y. Y., and Zhang, Z. (2013). Amnestic mild cognitive impairment: topological reorganization of the default-mode network. *Radiology*, 268(2):501–14.

Wang, X. (2010). Neurophysiological and computational principles of cortical rhythms in cognition. *Physiological reviews*, pages 1195–1268.

Wee, C.-Y., Yap, P.-T., Zhang, D., Denny, K., Browndyke, J. N., Potter, G. G., Welsh-Bohmer, K. A., Wang, L., and Shen, D. (2012). Identification of MCI individuals using structural and functional connectivity networks. *NeuroImage*, 59(3):2045–56.

Weir, J. P. (2005). Quantifying test-retest reliability using the intraclass correlation coefficient and the SEM. *Journal of strength and conditioning research / National Strength & Conditioning Association*, 19(1):231–40.

Wens, V., Bourguignon, M., Goldman, S., Marty, B., Op de Beeck, M., Clumeck, C., Mary, A., Peigneux, P., Van Bogaert, P., Brookes, M. J., and De Tiège, X. (2014). Inter- and intra-subject variability of neuromagnetic resting state networks. *Brain topography*, 27(5):620–34.

Wienbruch, C., Paul, I., Bauer, S., and Kivelitz, H. (2005). The influence of methylphenidate on the power spectrum of ADHD children - an MEG study. *BMC psychiatry*, 5:29.

Wood, C. C. (1982). Application of dipole localization methods to source identification of human evoked potentials. *Annals of the New York Academy of Sciences*, 388:139–155.

Worden, M. S., Foxe, J. J., Wang, N., and Simpson, G. V. (2000). Anticipatory biasing of visuospatial attention indexed by retinotopically specific alpha-band electroencephalography increases over occipital cortex. *The Journal of neuroscience : the official journal of the Society for Neuroscience*, 20(RC63).

Yamashita, M., Kawato, M., and Imamizu, H. (2015). Predicting learning plateau of working memory from whole-brain intrinsic network connectivity patterns. *Scientific reports*, 5:7622.

Yesavage, J. A., Brink, T. L., Rose, T. L., Lum, O., Huang, V., Adey, M., and Leirer, V. O. (1982). Development and validation of a geriatric depression screening scale: A preliminary report. *Journal of Psychiatric Research*, 17(1):37–49.

Ziegler, E., Chellappa, S. L., Gaggioni, G., Ly, J. Q. M., Vandewalle, G., André, E., Geuzaine, C., and Phillips, C. (2014). A finite-element reciprocity solution for EEG forward modeling with realistic individual head models. *NeuroImage*, 103:542–51.

Zijlmans, J. C. M., Pasman, J. W., Horstink, M. W. I. M., Stegeman, D. F., van't Hof, M. A., Poortvliet, D. J. C., Notermans, S. L. H., and Jonkman, E. J. (1998). EEG findings in patients with vascular parkinsonism. *Acta Neurologica Scandinavica*, 98(4):243–7.